THÈSE

En vue de l'obtention du

DOCTORAT DE L'UNIVERSITÉ DE TOULOUSE

Délivré par :

Institut National Polytechnique de Toulouse (Toulouse INP)

Discipline ou spécialité :

Dynamique des fluides

Présentée et soutenue par :

M. OTMAN MAALAL

le mercredi 7 octobre 2020

Titre :

Porométrie liquide-liquide, évaporométrie et simulations sur réseau de pores.

Ecole doctorale :

Mécanique, Energétique, Génie civil, Procédés (MEGeP)

Unité de recherche :

Institut de Mécanique des Fluides de Toulouse (IMFT)

Directeur(s) de Thèse :

M. MARC PRAT

M. DIDIER LASSEUX

Rapporteurs :

M. DENIS BOUYER, UNIVERSITE MONTPELLIER 2

M. PASCAL ROYER, Laboratoire de Mécanique et Génie Civil

Membre(s) du jury :

Mme CORINNE CABASSUD, INSA TOULOUSE, Président

M. ANTHONY SZYMCZYK, UNIVERSITE RENNES 1, Membre

M. DIDIER LASSEUX, CNRS AQUITAINE, Membre

M. MARC PRAT, CNRS TOULOUSE, Membre

Remerciements

Je tiens à remercier chaleureusement toutes les personnes qui ont contribué de prés ou de loin à l'élaboration et la réussite de ce travail de thèse.

Je remercie d'emblée mes directeurs de thèse Marc Prat et Didier Lasseux pour leurs conseils ainsi que leur grande disponibilité qui a permis à ce travail de se dérouleur dans les meilleures conditions.

Ce travail n'aurait pas pu aboutir sans le soutien de l'Institut de la Filtration et des Techniques Séparatives (IFTS) qui s'est amplement investi dans ce projet. Dans ce sens, je tiens à remercier M. Vincent Edery, directeur général de l'IFTS, pour sa confiance et son engagement dans ce projet. Je remercie également René Peinador, ingénieur de recherche à l'IFTS, pour son encadrement et son implication dans l'aspect expérimental de la thèse. J'en profite aussi pour remercier Pascal Ginisty, Nicolas Petillon, Isabelle Durand, Cecile Mutti ainsi que tout le personnel de l'IFTS.

Je tiens aussi à exprimer ma profonde gratitude à Manuel Marcoux, enseignant-chercheur à L'IMFT pour son engagement dans ce travail. Je remercie également mes collègues Malick Niang et Marouane Talbi pour les discussions enrichissantes sur le sujet.

Mes derniers remerciements vont à ma famille. En particulier, ma mère Nouzha, ma sœur Dounia et mon frère Mohamed pour leurs encouragements.

Finalement, je dédie ce modeste travail à la mémoire de mon père Abdelahad.

Résumé

Les milieux nanoporeux (milieux dont les tailles de pores sont submicroniques) sont des objets de haute technologie utilisés dans les techniques de séparation ou encore dans les piles à combustible. La distribution de taille de pores (PSD) de ces milieux, en particulier quand ils sont minces, est une information cruciale pour les applications concernées. La porométrie fluide-fluide et l'évapoporométrie sont deux techniques intéressantes de mise en œuvre relativement simple visant à obtenir cette information. Les deux méthodes exploitent les propriétés de capillarité des milieux qui contrôlent la hiérarchie dans les classes de pores selon laquelle se fait l'invasion progressive du milieu lors d'un déplacement fluide-fluide immiscible (cas de la porométrie fluide-fluide) ou le séchage du milieu (cas de l'évapoporométrie). Toutefois, l'exploitation des données obtenues (seuil de pression versus débit ou masse évaporée versus humidité relative) passe par un modèle pour obtenir les données visées. Les modèles actuellement utilisées considèrent le milieu poreux comme un faisceau de tubes parallèles. Ceci convient parfaitement à certains types de membranes poreuses utilisées en filtration par exemple où la nanostructure est similaire à un arrangement de tubes parallèles. En revanche, beaucoup d'autres milieux présentent des nanostructures enchevêtrées considérablement plus complexes, rendant très critiquables ou pour le moins douteuses l'exploitation des données expérimentales selon le modèle de tubes parallèles. Dans ce contexte, l'objectif de la thèse est de développer des modèles et des simulations numériques permettant d'assoir l'exploitation des données des deux techniques de porométrie sur une base plus solide dans le cas des milieux à nanostructures complexes. L'idée est de s'appuyer sur des modélisations de type réseau de pores des processus concernés : évaporation ou déplacement fluide-fluide immiscible en milieu nanoporeux. Les méthodes réseau de pores s'appuient sur des représentations simplifiées de l'espace des pores permettant des calculs rapides (comparé à des méthodes de calcul directes) tout en prenant en compte les propriétés morphologiques de la nanostructure. Ces méthodes sont utilisées pour l'étude des écoulements diphasiques en milieu poreux. Une première étape consistera à réaliser la simulation de drainage pour la porométrie fluide-fluide et la simulation de séchage pour la technique d'évapoporométrie. Cela revient à simuler, à l'aide de la méthode des réseaux poreux, les écoulements diphasiques qui ont lieu lors de l'utilisation de chacune des deux techniques. Nous évaluerons le modèle de tubes parallèles considéré dans l'analyse par le poromètre fluide-fluide ainsi que les résultats obtenus par l'évapoporomètre. Dans un second temps, nous tenterons de proposer un algorithme d'optimisation pour obtenir la PSD en considérant le modèle de réseau de pores adaptable à différentes classes de nanostructures (milieux fibreux, assemblages de particules sphériques, etc.). Enfin, nous exploiterons l'algorithme d'optimisation pour déterminer la fraction de mouillabilité d'un milieu avec une caractéristique de mouillabilité mixte en utilisant les informations qui peuvent être recueillies à partir du poromètre fluide-fluide.

Abstract

Nanoporous media (media with submicron pore sizes) are high-tech objects used in separation techniques or even in fuel cells. The pore size distribution (PSD) of these media, especially when they are thin, is crucial information for the applications concerned. Fluid-fluid porometry and evapoporometry are two interesting relatively simple techniques to obtain this information. The two methods exploit the properties of capillarity of the media which control the hierarchy in the classes of pores according to which the progressive invasion of the medium takes place during an immiscible fluid-fluid displacement (case of fluid-fluid porometry) or drying (case of evapoporometry). However, the use of the data obtained (pressure threshold versus flow rate or evaporated mass versus relative humidity) requires a model to obtain the targeted data. The models currently in use consider the porous medium as a bundle of parallel tubes. This is perfectly suited to certain types of porous membranes used in filtration, for example where the nanostructure is similar to an arrangement of parallel tubes. On the other hand, many other environments present considerably more complex entangled nanostructures, making it very questionable or at least doubtful the exploitation of experimental data according to the parallel tube model. In this context, the objective of the thesis is to develop models and numerical simulations allowing the exploitation of the data from the two porometry techniques on a more solid basis in the case of media with complex nanostructures. The idea is to rely on pore network type modeling of the processes involved: evaporation or immiscible fluid-fluid displacement in a nanoporous medium. Pore lattice methods are based on simplified representations of pore space allowing fast calculations (compared to direct calculation methods) while taking into account the morphological properties of the nanostructure. These methods are used for the study of two-phase flows in porous media. A first step will consist in performing the simulation of drainage for the fluid-fluid porometry and drying simulation for the evapoporometry technic. This amounts to simulating, using the pore networks method, the two-phase flows that take place during the use of each of the two techniques. We will evaluate the parallel tubes model considered in the analysis by the fluid-fluid porometer as well as the results obtained by the evapoporometer. In a second step, we will try to propose an optimization algorithm to get the PSD by considering the pore network model that can be adapted to different classes of nanostructures (fibrous media, assemblies of spherical particles, etc.). Finally, we will exploit the optimization algorithm to determine the wettability fraction of a medium with a mixed wettability characteristic using the information that can be gathered from the fluid-fluid porometer.

Table des matières

Introduction 6

Determination of the throat size distribution of a porous medium as an inverse optimization problem combining pore network modeling and genetic and hill climbing algorithms 16

Pore network simulations of fluid-fluid displacement porosimetry for evaluation of pore size distribution 56

Pore network model of drying with kelvin effect 90

Membrane characterization by evapoporometry and liquid-liquid displacement porosimetry: assessment from pore network simulation 125

Identification of local contact angle distribution inside a porous medium as an inverse optimization problem 164

Conclusion 191

Perspectives 193

Introduction

L'utilisation des milieux poreux est très répandue dans le domaine industriel. Parmi les applications faisant intervenir un ou des milieux poreux, on peut par exemple citer le séchage de matières alimentaires, le séchage du bois, la synthèse de produits cosmétiques et de médicaments, la récupération d'hydrocarbures, les piles à combustibles ou encore les matériaux de construction. Un milieu poreux est par définition un milieu solide comprenant des interstices pouvant permettre le passage d'un fluide ou plusieurs fluides. Ces interstices sont appelés pores.

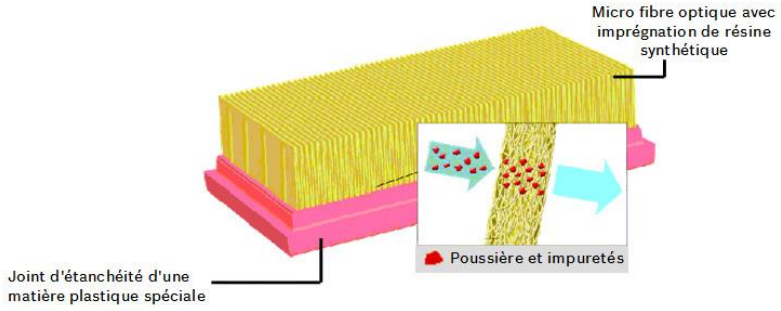
Les processus de séparation et de filtration sont un autre exemple d'application faisant intervenir des membranes poreuses et plus généralement des filtres. La performance de ces derniers est mesurée à travers la caractérisation de l'espace poreux permettant la capture des particules à filtrer. Parmi ces filtres, on trouve par exemple comme illustré sur la Fig.1, les filtres à sable, les filtres en papier et les filtres à air.



a) Filtre à sable pour filtrer l'eau [1]



b) Filtre à papier pour une cafetière [2]



c) Filtre à air [3]

Figure 1: Exemples de filtres

La filtration par membrane peut être classifiée suivant les tailles des pores constituants la membrane : On parle de microfiltration pour des tailles de pores entre 0.1 et 5 µm, d'ultrafiltration pour des tailles entre 1 et 100 nm, de nanofiltration pour des tailles entre 0.5 et 10 nm. Pour ces membranes de filtration,

comme pour les autres milieux poreux en général, une caractéristique essentielle est la distribution des tailles de pores. L'importance de cette caractéristique en pratique explique pourquoi de nombreuses techniques de porosimétrie ont été développées afin de la déterminer. Ces techniques sont généralement classées en deux catégories principales :

- Les techniques de caractérisation directes basées sur la visualisation d'images réelles du milieu poreux. Ces images peuvent être obtenues par microscopie en utilisant la microscopie électronique (SEM) et la microscopie à sonde locale (SPM) ou par spectroscopie. Les principaux inconvénients de ces méthodes sont :
    - La résolution des images obtenues est faible (ce qui génère des erreurs dans la détermination des tailles de pores surtout pour les membranes d'ultrafiltration et de nanofiltration)
    - Le volume du milieu caractérisé est petit et peut ne pas représenter toute la membrane.
    - Le coût de ces matériels.
- Des techniques de caractérisation indirectes qui sont fondées sur l'application de processus physiques sur la membrane en question et l'utilisation de lois théoriques pour déterminer les tailles des pores. Ces méthodes peuvent être divisées en deux catégories :
    - Des techniques utilisant le déplacement immiscible d'un fluide mouillant par un autre fluide non mouillant (drainage) à travers le milieu poreux. Ces méthodes comprennent la porosimétrie mercure et la porosimétrie fluide-fluide. Ces méthodes relient la taille du pore envahi à la différence de pression appliquée à travers l'équation de Young-Laplace, la répartition des tailles de pores est estimée via la perméabilité effective (pour le cas de la porosimétrie fluide-fluide) ou via le volume envahi (pour le cas de la porosimétrie au mercure). Tandis que la porosimétrie fluide-fluide détermine uniquement les pores continus, la porosimétrie mercure détermine également les pores en cul de sac (« dead end ») en mesurant le volume du mercure envahi. Cette différence est due au fait que les pores en cul de sac contribuent au volume total du fluide non-mouillant alors qu'ils ne contribuent pas à la chute de pression dans l'écoulement et donc à la perméabilité apparente.

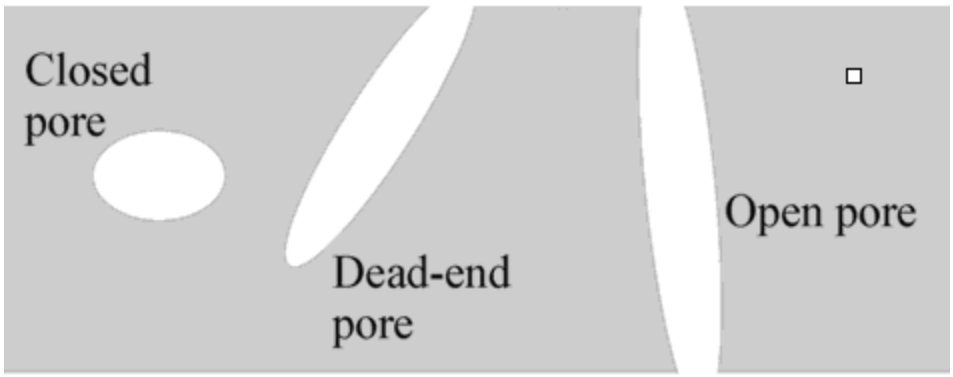


Figure 2: Types de pores dans un milieu poreux [4]

Lorsque les pores sont de très petites tailles, la différence de pression pour envahir un pore est élevée et de nature à déformer les pores lorsque l'on considère la porosimétrie mercure et la

porosimétrie gaz-liquide. La porosimétrie liquide-liquide vise à limiter ce type de problème via le choix d'un couple de liquides ayant une faible tension superficielle permettant d'envahir les pores de très petite taille pour une différence de pression comparativement bien plus faible.

- Une autre catégorie regroupe toutes les techniques basées sur un changement de phase. Par exemple : l'évapoporosimétrie qui consiste au suivi de l'évaporation à partir d'une membrane initialement saturée par un liquide volatile en mesurant la masse évaporée en fonction du temps. La distribution des tailles de pores (PSD selon l'acronyme anglais pour Pore Size Distribution) est ensuite déterminée en utilisant le taux d'évaporation mesuré et l'équation de Kelvin. La technique d'adsorption / désorption de gaz consiste à saturer le milieu poreux par un gaz d'adsorption par condensation capillaire, puis la désorption du gaz est réalisée. Le volume du gaz désorbé ainsi que la pression de désorption permet d'obtenir la PSD en considérant l'équation de Kelvin. La thermoporosimétrie consiste à faire fondre un liquide initialement congelé saturant le milieu poreux en augmentant progressivement la température. Cette méthode est basée sur l'équation de Gibbs-Thompson pour déterminer la PSD.

La figure ci-dessous résume les principales techniques existantes pour la caractérisation des membranes. Bien que non-exhaustive, cette étude illustre bien que la détermination de la PSD a motivé de nombreux développements. L'existence de ces différentes techniques est aussi une indication qu'aucune méthode n'est parfaite. Chacune a ses avantages et ses inconvénients. Il est clair qu'une étude comparative détaillée de l'ensemble constitue un travail très lourd. Dans cette thèse, on s'intéresse à deux techniques : la porosimétrie fluide-fluide et l'évapoporosimétrie. La première technique est utilisée surtout pour les membranes de microfiltration et d'ultrafiltration, elle est utilisée aussi pour les membranes de nanofiltration en considérant un couple de fluides mouillant/non-mouillant liquide-liquide. L'évapoporométrie est utilisée uniquement pour les membranes de nanofiltration. Le choix d'étudier plus particulièrement ces deux techniques est donc pleinement cohérent avec les activités de l'IFTS. L'IFTS commercialise un poromètre (illustré sur la Fig.4) mettant en œuvre la porosimétrie fluide-fluide. Il est donc important de bien caractériser ce qui est réellement obtenu avec le poromètre. La question de développer un dispositif d'évapoporosimétrie s'est aussi posée à l'IFTS notamment via des contacts avec l'université de Singapour où un tel dispositif existe. Dans ce contexte un des attendus de la thèse est d'aider à mieux cerner les performances de l'évapoporosimétrie.

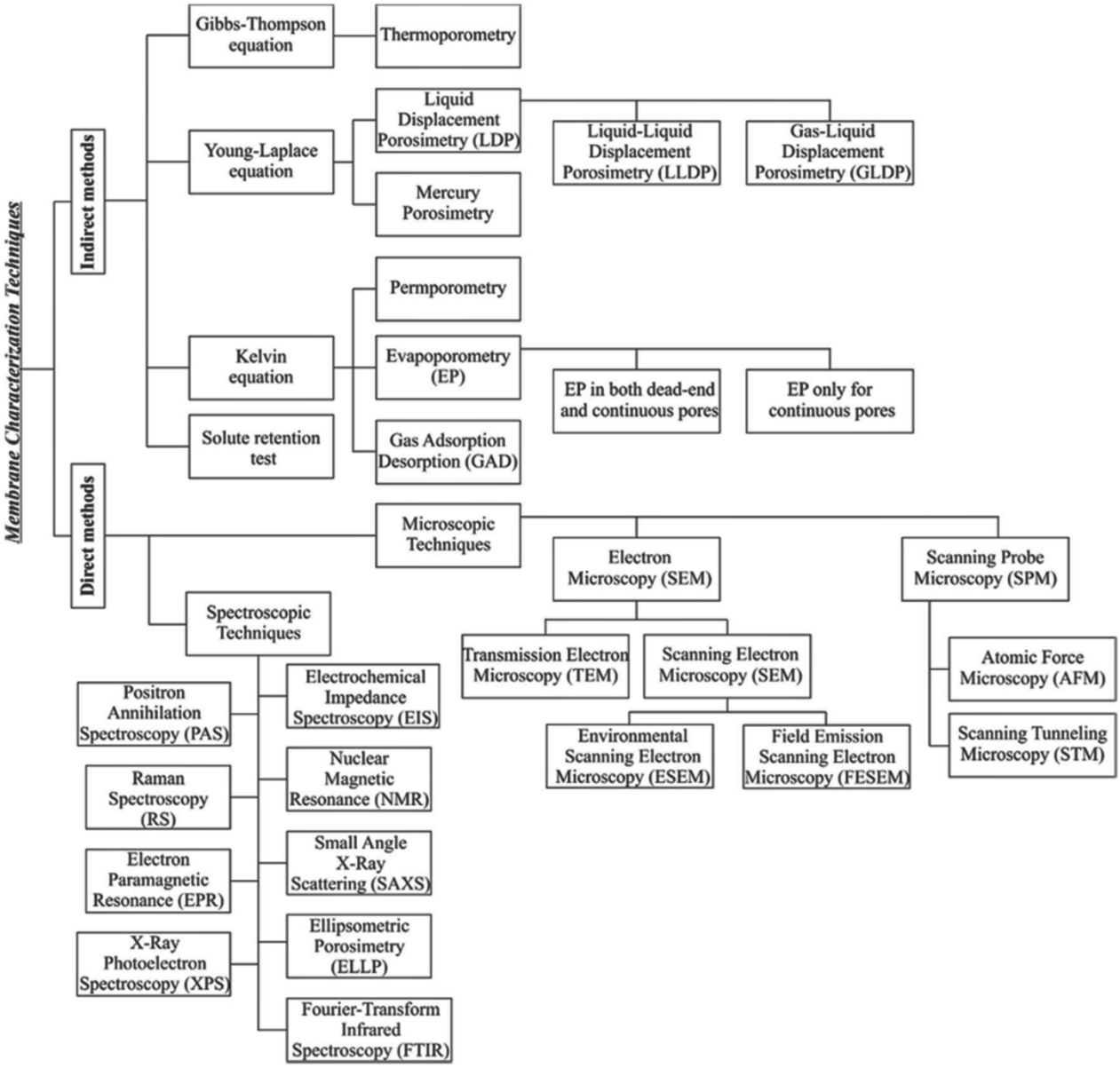


Figure 3: Liste de techniques de caractérisation de membrane [5]



Figure 4: Poromètre IFTS [6]

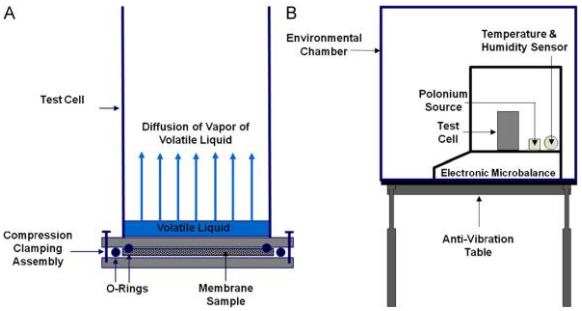


Figure 5: Evapoporométre [7]

Comme mentionné plus haut, la porosimétrie fluide-fluide réside dans l'analyse de données mesurées lors du drainage. Ces données sont la différence de pression entre l'entrée et la sortie de la membrane et le débit en fluide non-mouillannt. Selon le protocole généralement utilisé, l'exploitation de ces données est basée sur une modélisation simpliste consistant à considérer le milieu poreux comme un faisceau de tubes parallèles de taille différente.

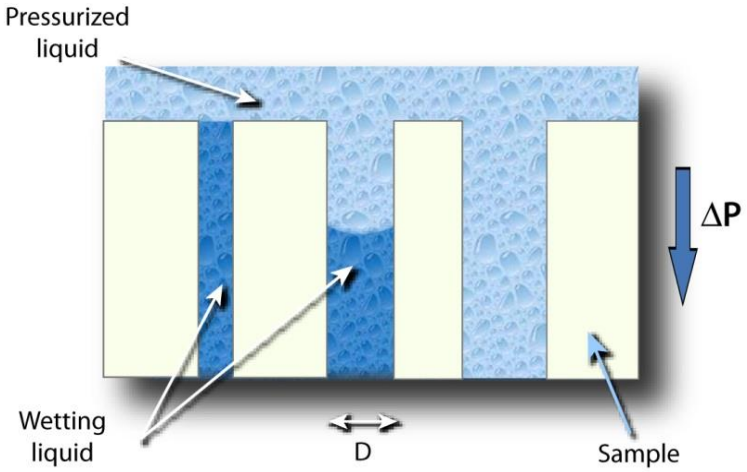


Figure 6: Représentation de l'espace poreux par la porométrie [6]

Cette représentation ne correspond, en réalité, qu'à un nombre très limité de membranes. Comme illustré sur la Fig.6, les membranes peuvent avoir en réalité des pores interconnectés et enchevêtrés.

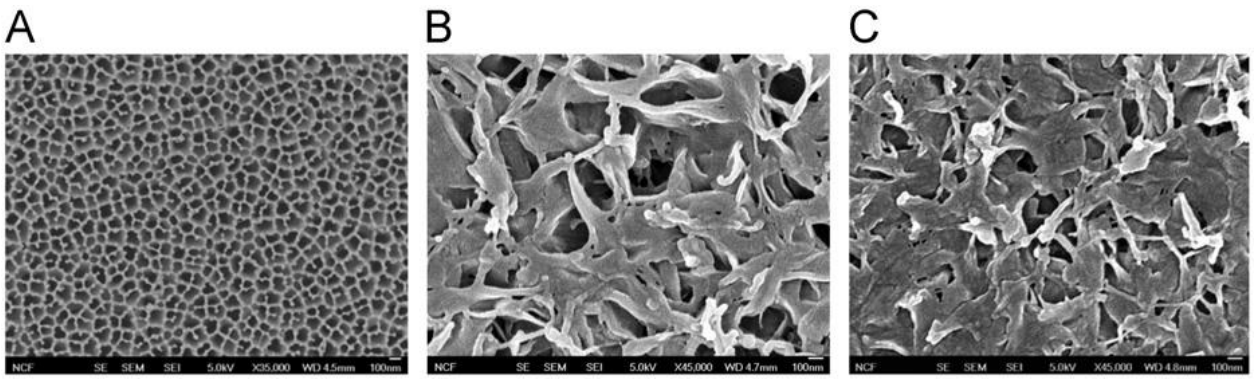


Figure 7: Images FESEM pour différentes membranes [7]

La figure 6A est un exemple de membrane avec des pores cylindriques non-connectés. La structure de l'espace poreux pour les deux autres membranes est clairement différente de pores cylindriques. Compte tenu de ces microstructures, exploiter les données du porométre via un modèle de tubes parallèles semble raisonnable pour la membrane de la Fig.6A mais totalement inapproprié pour les deux autres membranes. Dans ces conditions, l'idée est tout d'abord d'évaluer ce qui est réellement obtenu en terme de PSD lorsque le modèle de tubes parallèles est appliqué au cas des réseaux poreux interconnectés. Pour cela, on s'appuie sur des représentations-modèles de l'espace des pores appelées classiquement réseau de pores (ou PNM en anglais pour Pore Network Model).

La modélisation par réseaux de pores s'est beaucoup développée depuis son introduction par Fatt (1956). Cette modélisation est basée sur une représentation de l'espace pore en un réseau de cavités, appelées « pore bodies », connectées entre elles par des canaux de plus petites tailles appelés « pore throats ». Ces canaux correspondent aux constrictions locales dans l'espace des pores.

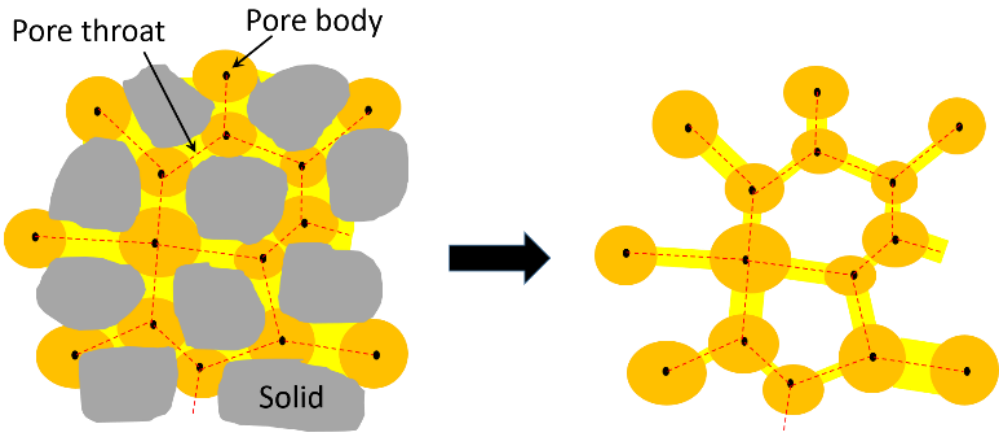


Figure 8: Représentation de l'espace poreux par un modèle de réseau de pores

Les « pore bodies » ainsi que les « pore throats » peuvent avoir différentes formes géométriques. La forme circulaire est choisie pour les « pore bodies » et les « pores throats » dans ce travail. Ce choix est justifié pour simplifier les calculs. En effet, lorsque deux fluides (fluides mouillant et non mouillant) coexistent dans un « pore body » ou « pore throat » de forme anguleuse, le fluide mouillant occupe les coins tandis que le fluide non mouillant occupe le centre. La considération d'éléments cylindriques (pore body ou pore throat) conduit à négliger ces effets de coins, dont la prise en compte est jugée peu importante, du moins au premier ordre, pour évaluer les deux techniques de porosimétrie considérée.

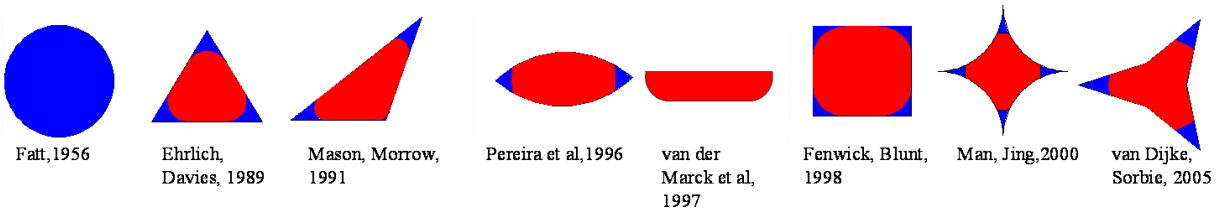


Figure 9: Différentes coupes transversales de pore bodies et pore throats [8]

Un réseau de pores est dit structuré lorsque les centres des « pore bodies » sont répartis spatialement de façon régulière. La connectivité est le nombre moyen de « pore throats » connectés à un « pore body ». Dans ce travail, on choisit un réseau 2D carré (connectivité de 4) et un réseau 3D cubique (connectivité de 6). Le pas du réseau est la distance qui sépare les centres de deux « pore bodies » voisins.

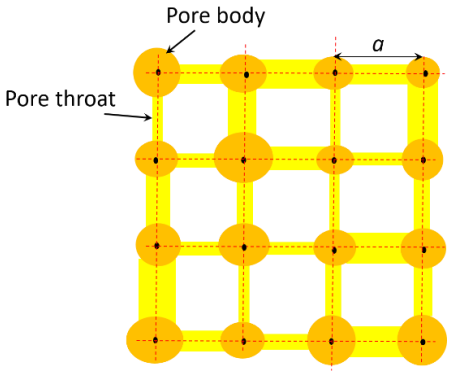
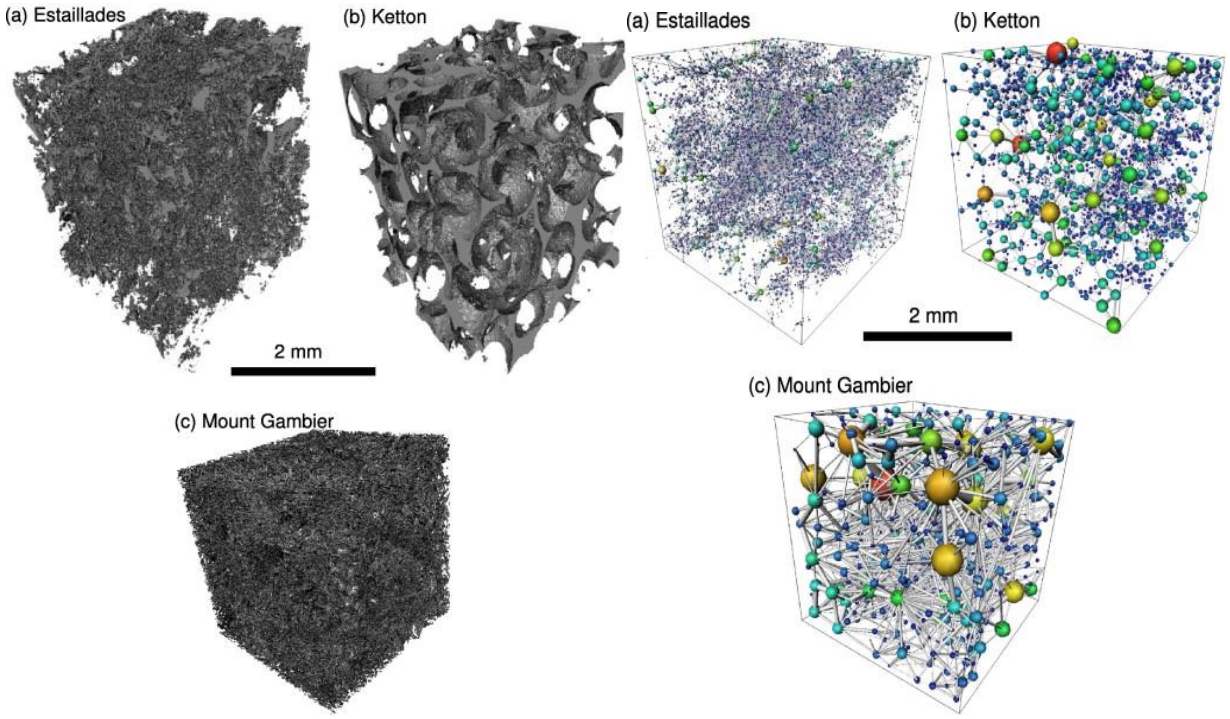


Figure 10: Exemple de réseau carré

Comme illustré sur la Figure 10, il est possible d'extraire le réseau de pores à partir des images issues des méthodes directes de caractérisation des membranes présentées précédemment. Les réseaux illustrés sur la figure 10 pour différents milieux poreux ont été extraits à partir d'images 3D obtenues par la technique de micro-tomographie par rayons X. Nous avons pour notre part néanmoins travaillé avec des réseaux modèles structurés car obtenir des réseaux issus des images est une tache lourde et prenante, en particulier pour les membranes d'ultra et nano-filtrations qui ne peuvent être imagées avec des tomographes à rayon X en raison des tailles de pores mises en jeu. Par ailleurs, l'utilisation de réseaux réguliers simples constitue une première étape importante vers la prise en compte de réseaux éventuellement plus complexes.



a) X-ray micro-CT de 3 milieux poreux différents b) Réseaux de pores correspondants

Figure 11: Réseaux de pores extraits à partir d'image X-ray micro-CT [9]

Une fois le réseau obtenu ou défini, l'étape suivante est de simuler dans le réseau les écoulements et les processus physiques à la base des deux techniques de porosimétrie considérées, à savoir des déplacements diphasiques non miscibles (pour la porosimétrie fluide–fluide) et l'évaporation (pour l'évapoporosimétrie). On peut distinguer ici deux approches principales : la simulation directe (type Lattice-Boltzmann ou basée sur la résolution des équations de Navier-Stokes à l'échelle des pores) et la simulation PNM. Comme cela sera détaillé plus loin dans le manuscrit, la simulation PNM utilise des lois de transferts simplifiés dans les « pore throats ». Bien que moins précis, ce type de simulation est de ce fait beaucoup moins coûteux en temps de calcul que les simulations directes. Pour cette raison, notre choix s'est orienté vers des simulations de type PNM.

Ce manuscrit est divisé en 5 chapitres :

Le premier chapitre concerne la simulation numérique par la méthode de percolation d'invasion dans un réseau de pores selon une approche quasi-statique du drainage. Le but de cette partie est de simuler une première situation se rapprochant de celle correspondant à la porosimétrie fluide-fluide et d'examiner les résultats trouvés en considérant le modèle de tubes parallèles. Ce chapitre présente aussi une méthode d'analyse des données obtenues en considérant le modèle de réseau de pores au lieu de la modélisation par tubes parallèles.

Le deuxième chapitre est dédié à une analyse de la porosimétrie liquide-liquide proprement dite. Du point de vue algorithmique, la différence clé avec le chapitre précédent est la prise en compte des effets visqueux lors de l'invasion en complément de l'approche uniquement quasi-statique considérée dans le premier chapitre.

Le troisième chapitre est dédié à l'explication de l'algorithme de simulation de l'évaporation dans un réseau de pores avec effet Kelvin.

Le quatrième chapitre est consacré à la comparaison des résultats numériques obtenus par l'évapoporosimétrie et la porosimétrie fluide-fluide.

A la différence des chapitres précédents, le cinquième chapitre n'est pas motivé par la problématique de la porosimétrie. Il s'intéresse au problème de la caractérisation de la distribution de l'angle de contact local au sein du réseau poreux. Le lien avec les chapitres précédents est méthodologique. Des méthodes de calcul et d'exploitation des données via des techniques d'optimisation très similaires y sont utilisées.

Référence des figures

[1] https://www.piscine-center.net/charge-filtrante-pour-filtres-a-sable-piscines.html

[2] https://maisonemile.fr/products/filtre-en-papier-naturel-pour-dripper-v60-hario%C2%AE-1-a-6-tasses

[3] www.partauto.fr/blog/2019/03/20/quand-faut-il-remplacer-le-filtre-a-air/

[4] T. Karppinen, Characterizing physical properties of wetting paper by air coupled ultrasound and light, University of Helsinki.

[5] M.B. Tanis-Kanbur, R.I. Peinador, X. Hu, J.I. Calvo, J.W. Chew, Membrane characterization via evapoporometry (EP) and liquid-liquid displacement porosimetry (LLDP) techniques, Journal of Membrane Science, 586, 248-258 (2019).

[6] https://www.ifts-sls.com/fichier_article/files/ArticlePorometreFluideFluideFrjuil2015.pdf

[7] W.B. Krantz, A.R. Greenberg, E. Kujundzic, A. Yeo, and S. S. Hosseini, Evapoporometry: A novel technique for determining the pore-size distribution of membranes Journal of Membrane Science, 438, 153-166 (2013).

[8] Joekar-Niasar, V., Hassanizadeh – "Dynamics of Two-Phase Flow in Porous Media; From Pore

Scale to Darcy Scale" journal of Critical Reviews in Environmental Science and Technology, 2010.

[9] M. J. Blunt, B. Bijeljic ,H. Dong, O. Gharbi, S. Iglauer, P. Mostaghimi, A. Paluszny, C. Pentland, Pore-scale imaging and modelling, Advances in Water Resources, 51, 197-216 (2013).

Determination of the throat size distribution of a porous medium as an inverse optimization problem combining pore network modeling and genetic and hill climbing algorithms.

Otman Maalal[a,b], Marc Prat[a*], René Peinador[b], Didier Lasseux[c]

Institut de Mécanique des Fluides de Toulouse (IMFT), Université de Toulouse, CNRS, Toulouse, France.
Institut de La Filtration et des Techniques Séparatives (IFTS), Rue Marcel Pagnol, 47510, Foulayronnes, France
I2M, UMR 5295, CNRS, Univ. Bordeaux – Esplanade des Arts et Métiers, 33405 Talence, CEDEX, France

[*] *Corresponding author:mprat@imft.fr (+33534322883)*

Abstract

The pore size distribution (PSD) of a porous medium is often estimated from the retention curve or the invading fluid flow rate curve using simple relationships more or less explicitly based on the consideration that the porous medium is made of a bundle of cylindrical parallel tubes. This type of determination is tested using pore network simulations. Starting from two- or three-dimensional networks, which characteristics are known a priori, the estimation of the throat size distribution (TSD) is performed using the standard methods in the case of drainage. Results show a significant discrepancy with the input data, The disagreement is more pronounced when the fluid flow rate curve is employed together with the parallel tube assumption. The physical origins of these shortcomings are identified. A new method, based on pore network simulations combined with a genetic algorithm and the hill climbing algorithm is designed, which makes simultaneous use of the non-wetting fluid flow rate curve and the retention curve of the medium. Very significant improvement is achieved in the estimation of the TSD using this procedure which reveals to be very effective and opens wide perspectives.

Keywords: Pore size distribution; Throat size distribution; Pore network model; Genetic algorithm; Hill climbing algorithm

1 Introduction

The pore size distribution (PSD) is a key structure characteristic of a porous medium of major importance to model flow and transport processes. A simple method for determining the PSD is to use the retention curve, i.e. the fluid potential to saturation relationship [1]. As discussed for instance in [2], this is often performed assuming more or less explicitly that the pore system can be represented by a bundle of parallel cylindrical capillary tubes of circular cross section with a random distribution of radii. However, except for a few particular systems, for example the Anopore^{TM} membrane discussed in [3], the microstructure of a porous medium is generally significantly different from a simple bundle of parallel cylindrical tubes. Most porous materials are rather characterized by a system of highly interconnected pores. As a result, the information on the PSD obtained from simple interpretation based on this representation is questionable and must be cautiously assessed. Another issue is that the PSD obtained in this way makes no difference between the throats, i.e. the constrictions in the pore space, and the "pores", defined here as the local larger cavities. Making such a distinction between throats and pores is a classical feature of pore network models (PNM) [4]. This is justified by the fact that constrictions are largely controlling the capillary effects since menisci tend to get preferentially pined in constrictions as well as transport phenomena since, for example, the pressure drop between two adjacent pores can be essentially controlled by the constriction connecting them when this constriction is sufficiently narrow compared to the pore size [5, 6]. This leads to distinguish the pore size distribution (PSD), which corresponds to the pores in the PNM partition of the pore space, from the throat size distribution (TSD), i.e. the distribution of constriction sizes. In this context, the question arises as to whether it is possible to identify both the PSD and TSD, or at least the TSD, from relatively basic information such as the retention curve or the flow rate curve, the latter denoting the flow-rate to fluid potential relationship. With the development of imaging techniques, e.g. micro X-ray tomography, this approach may be itself questioned since the TSD and the PSD can be determined by means of various algorithms applied to segmented images of the microstructure [7, 8]. However, imaging devices are expensive and the segmentation of the pore space in pores and throats is rarely straightforward, requiring the treatment of a huge amount of data. Moreover, obtaining reliable images for materials with pores and throats in the submicronic range is not an easy task. As a result, cheaper and more routine characterization techniques are still quite desirable.

In what follows, the focus is laid on the TSD. The intrinsic permeability and porosity, together with the retention and non-wetting fluid flow rate curves are supposed to be known, i.e. are available from measurement for a pair of fluids for which the wetting fluid is perfectly wetting. In addition to the assessment of two classical TSD extraction methods, the objective of the paper is to explore whether this information is sufficient to characterize the TSD. Taking into account the non-wetting fluid flow rate is motivated by the fact that the evaluation of a porosimetry technique, referred to as the fluid-fluid displacement porosimetry (FFDP) [9, 10], is also of interest. In this technique, a perfectly wetting liquid is displaced by a non-wetting liquid through a series of pressure steps and the non-wetting flow rate through the sample is recorded for each pressure step. The flow rate vs pressure curve is then harnessed to extract the TSD [9]. In the context of FFDP, the situation under study in the present paper can actually be seen as a quasi-static version, referred to as QSFFDP, where QS stands for quasi-static. Contrary to the classical FFDP technique where the viscous pressure drop across the sample in the non-wetting fluid is on the order of the capillary pressure, the viscous pressure drop remains small compared to the capillary pressure. Actually, this corresponds to the situation considered in practice for determining the non-wetting fluid relative permeability. Considering the flow rate curve so as to use the same convention as in the FFDP or the non-wetting fluid relative permeability curve is strictly equivalent in the quasi-static limit under consideration here. The classical FFDP (as opposed to the QSFFDP) will be the object of a future study.

On this basis, the idea is then to rely on pore network simulations. Starting from a perfectly known microstructure with interconnected pores, referred to as the reference network, an immiscible displacement is performed numerically for conditions similar to the ones employed for the classical retention curve measurement. The TSD is extracted from the retention curve and flow rate data using classical extraction methods based on the bundle of capillary tubes model. The TSD obtained with this procedure is compared to the actual TSD. The decisive feature here is that the TSD is perfectly known a priori for the reference medium. This allows illustrating and assessing the limitations of the classical methods for the TSD determination. Then, the question arises as to how the use of the immiscible displacement data can be improved when the microstructure is clearly not a simple system of parallel tubes. This amounts to considering an ill-posed inverse problem in which the objective is to determine the TSD. Regarding the method used to compute the displacement in the network, direct simulations like Lattice Boltzmann Methods (LBM) [11],

Volume of Fluid (VOF) models [12], etc., and pore network models (PNM) [4] are nowadays interesting techniques. As will be explained below, the TSD identification method requires computing the immiscible displacement many times. In this respect, PNM are well adapted as this technique requires much shorter computational time compared to direct simulations.

The present paper is organized as follows. In section 2, two classical methods for determining the PSD (more exactly the TSD) from the non-wetting fluid flow rate curve or the retention curve are recalled. The pore network models are presented in Section 3. The algorithms used to simulate the displacement and compute the flow rate and retention curves are presented in Section 4. The assessment of the TSD determination from the classical methods is presented in Section 5. In Section 6, a method to determine the TSD from both the non-wetting fluid normalized flow-rate and retention curves using PNM simulations combined to an optimization method is presented. A short discussion is presented in Section 7. Conclusions are drawn in Section 8.

2 Flow-rate porosimetry and retention curve porosimetry

Suppose the retention curve, $P_c(S)$, flow rate curve, $Q_{nw}(P_c)$, and the porosity are known, where $P_c(S)$ is the capillary pressure, Q_{nw} is the non-wetting fluid flow rate for the quasi-static fluid distribution corresponding to $P_c(S)$ while S is the wetting fluid saturation. Considering generalized Darcy's law implies,

$$Q_{nw} = \frac{k k_r(P_c)}{\mu} \frac{\Delta P}{L} \tag{1}$$

where μ is the non-wetting fluid viscosity, L is the sample length, k is the porous medium intrinsic permeability and k_r is the non-wetting fluid relative permeability. In addition, ΔP is the pressure difference between the inlet and outlet in the non-wetting fluid. In the quasi-static limit under consideration here, ΔP is small compared to the capillary pressure. Throughout the article, a constant ΔP is considered independently of the capillary pressure.

To extract the TSD from the retention curve, a pore size r is associated with a value of P_c using the Young Laplace equation

$$P_c = \frac{2\gamma \cos\theta}{r} \tag{2}$$

where the contact angle is $\theta = 0$ in our case (perfectly wetting displaced fluid) and γ is the interfacial tension. For simplicity, trapping phenomena [13] are assumed negligible so that *S* varies in the interval [0,1]. The wetting fluid saturation *S* corresponding to *r* is then simply defined as [14],

$$S = \frac{\int_0^r f(r)dr}{\int_0^{+\infty} f(r)dr} \tag{3}$$

where $f(r)$ is the pore size distribution, i.e. the pore size probability density function (p.d.f.). Deriving Eq. (3) with respect to r yields,

$$\frac{dS}{dr} = \frac{f(r)}{\int_0^{+\infty} f(r)dr} \tag{4}$$

Since, by definition, $\int_0^{+\infty} f(r)dr = 1$, this leads to

$$f(r) = \frac{dS}{dr} \tag{5}$$

In discrete form, Eq. (5) can be expressed as

$$f_k(r_{AB}) = \frac{S(P_{cB}) - S(P_{cA})}{r_B - r_A} \tag{6}$$

where P_{cA} and P_{cB} are two close values of P_c and $r_{AB} = (r_A + r_B)/2$, r_A and r_B being determined from Eq. (2). The value of f_k is then normalized according to

$$d_k(r_{AB}) = \frac{f_k}{\sum_{i=1}^{n} f_i} \tag{7}$$

Here, *n* is the number of classes considered to compute the discrete p.d.f.

The method for determining the TSD from the flow-rate $Q_{nw}(P_c)$ is somewhat similar but explicitly relies on the model of a bundle of parallel cylindrical tubes. It is also similar to the one used in the

FFDP technique [9]. In the bundle of tubes model, the flow-rate is computed applying Poiseuille's law in each tube containing the non-wetting fluid.

$$Q_{nw} = \frac{\Delta P \pi}{8 \mu L} \int_{r_{min}}^{+\infty} r^4 f_Q(r) dr \tag{8}$$

where the tube length is L assuming straight tubes and

$$r_{min} = \frac{2\gamma \cos\theta}{P_c} \tag{9}$$

f_Q being again the TSD. In principle, $f_Q = f$. However, a different notation is used since it is not obvious that both PSDs will be the same when the porous medium microstructure is different from a bundle of parallel tubes.

Combining Eqs. (1) and (9), assuming ΔP = constant $\ll P_c$ independently of the capillary pressure and deriving the ensuing equation with respect to r lead to

$$\frac{dQ_{nw}}{dr} = -\frac{\Delta P \pi}{8 \mu L} r^4 f_Q(r) \tag{10}$$

and thus

$$f_Q(r) = -\frac{8 \mu L}{\Delta P \pi} r^{-4} \frac{dQ_{nw}}{dr} \tag{11}$$

Equation (11) can be expressed in discrete form as [9]

$$f_{Qk}(r_{AB}) = -\frac{8 \mu L}{\Delta P \pi} r_{AB}^{-4} \left(\frac{Q_{nw_B} - Q_{nw_A}}{r_B - r_A} \right) \tag{12}$$

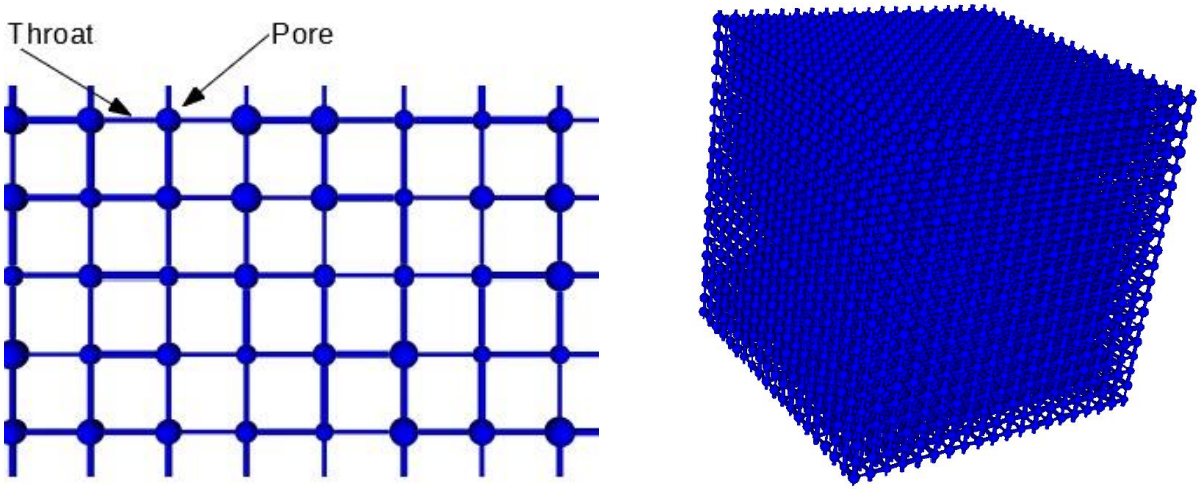
The value of f_{Qk} is then normalized as,

$$d_{Qk}(r_{AB}) = \frac{f_{Qk}}{\sum_{i=1}^{n} f_{Qi}} \tag{13}$$

In what follows, water is considered as the wetting fluid and air as the displacing fluid. Thus γ = 0.072 N/m and $\mu = \mu_{nw} = 10^{-5}$ Pa.s.

3 Interconnected model porous medium

The QS immiscible displacement is simulated considering simple model porous media referred to as pore network models (PNM). In a PNM, the pore space is represented as a network of pores connected by narrower channels. The pores correspond to locally larger volumes whereas the channels correspond to the throats of the pore space, i.e. the narrower passages, also referred to as the constrictions, between pores. Although it is possible to construct the network from digital images of real microstructures, (see e.g. [15]), simpler networks are sufficient for testing the QSFFDP. In what follows, square (2D) and cubic (3D) networks are considered. As illustrated in Fig. 1, pores are spheres of radius r_p located at the nodes of a regular grid. The distance between two adjacent nodes is the lattice spacing a with a = 350 μm in the simulations presented below. The size of the network is the number of nodes (pores) in each direction (for example, Fig. 1a shows a 8×5 square network). Throats are cylindrical channels of radius r_t. The throat size is randomly distributed according to a given probability density function (p.d.f.). Similarly, the pore size can be distributed according to a given p.d.f with the constraint that the pore size is equal or greater than the largest throat to which it is connected. In what follows, several types of p.d.f. will be considered, namely uniform, Gaussian, log-normal and bimodal. Also, it can be noted that the network coordinance, i.e. the number of throats connected to a pore, is 4 for the 2D square network and 6 for the 3D cubic network.



a) b)

Fig. 1. Square (2D) (a) and cubic (3D) (b) pore networks. Pores and nodes are randomly distributed. The lattice spacing is a = 350 μm.

4 Fluid – fluid immiscible quasi-static displacement simulation

Modeling of immiscible two-phase flow displacements on a network has been the subject of many works and the reader is referred to [4, 16] for reviews. Here, the interest is on the displacement of a wetting fluid by a non-wetting one in the network. This process is known as drainage. In the quasi-static limit considered for the present study, it was shown that drainage can be simulated using a simple algorithm referred to as the invasion percolation algorithm [17, 18]. This algorithm can be summarized as follows. A pressure difference, P_{ck}, between the two phases is applied by imposing a pressure increment in the non-wetting phase in contact with one face of the network, identified as the inlet face. The opposite face is the outlet, whereas all the other faces of the network are kept impervious. At each pressure increment, all the throats containing a meniscus for which the capillary pressure, P_{cth}, as expressed in Eq. (2) such that $P_{ck} \geq P_{cth}$, are identified. They are referred to as interfacial throats. The throat for which $(P_{ck} - P_{cth})/P_{ck}$ is maximum, hence corresponding to the interfacial throat of maximum diameter among the interfacial throats such that $\frac{(P_{ck}-P_{cth})}{P_{ck}} > 0$, is invaded together with the adjacent pore if the latter was not already invaded in a previous step. If this pore was occupied by the wetting fluid, new menisci are then positioned at the entrance of the throats occupied by the wetting fluid and connected to the newly invaded pore. In other words, the list of interfacial throats is updated so as to remove the invaded throat and add the throats connected to the newly invaded pore and occupied by the wetting fluid. This procedure is repeated until there is no unstable menisci remaining in the network, i.e. until there exists no throat for which $\frac{(P_{ck}-P_{cth})}{P_{ck}} > 0$. The resulting wetting - non-wetting fluid distribution corresponds to the equilibrium distribution at the specified value of P_{ck}. For a sufficiently low pressure difference between the two fluids, the wetting phase displacement is not sufficient for the invading phase to reach the network outlet. The first equilibrium for which the invading fluid reaches the outlet corresponds to the breakthrough (BT) and is characterized by $P_{ck} = P_{cBT}$. While incrementing the displacing fluid pressure, the fluid distribution at BT is the first for which the non-wetting fluid can flow through the network, which means that $Q_{nw} = 0$ for $P_{ck} < P_{cBT}$ while $Q_{nw} > 0$ for $P_{ck} \geq P_{cBT}$. Note that the invasion rules described above correspond to a quasi-static drainage process without trapping. This means that an element, pore or throat, occupied by the wetting fluid is assumed to be always connected to the outlet face, possibly through liquid films

[19] present in the pore and throat surface roughness and/or in a subnetwork of small crevices at the throat and pore walls. Trapping rules could be implemented (see for instance [13]), but, for simplicity, they are not considered in what follows.

Each pressure increment provides a point in the graph of the retention curve, the fluid potential being the capillary pressure (i.e. the pressure difference between the non-wetting and wetting fluids) and the saturation being computed from the equilibrium fluid distribution. Next, the computation of the non-wetting fluid flow rate, Q_{nw}, after breakthrough is performed as follows [4]. At each saturation equilibrium, a pressure difference, ΔP, much smaller than the capillary pressure characterizing this equilibrium, is applied in the non-wetting fluid between the network inlet and outlet. For the resulting flow, the mass conservation equation is expressed at each invaded pore *i*

$$\sum Q_{nw\,i,j} = 0 \tag{14}$$

where $Q_{nw\,i,j}$ is the non-wetting fluid volume flow rate between pore *i* and adjacent pore *j*. If the throat between pores *i* and *j* is occupied by the wetting fluid then $Q_{nw\,i,j} = 0$. If the throat is occupied by the non-wetting fluid, then

$$Q_{nw\,i,j} = \frac{\pi r_{t\,i,j}^4}{8\mu_{nw} l_{i,j}} \Delta P_{i,j} \tag{15}$$

where $r_{t\,i,j}$ and $l_{i,j}$ are the radius and length of the throat linking the two pores respectively, while $\Delta P_{i,j}$ is the pressure drop in the non-wetting phase between the two neighboring pores. Taking into account the pressure boundary conditions at the inlet ($P_{inlet} = \Delta P + P_{outlet}$) and outlet ($P_{outlet} = Cte$) and the zero flux condition imposed on the lateral faces of the network, Eqs. (14) and (15) lead to a linear system for the pressure field in the non-wetting fluid. This system is numerically solved using the conjugate gradient method. Once the pressure field is obtained, Q_{nw}, can be computed either at the outlet or inlet using Poiseuille's law applied to all non-wetting fluid throats connected to the outlet or inlet, respectively.

In summary, the fluid-fluid distribution is computed, in a first step, neglecting the viscous pressure drop in each fluid-phase on the grounds that capillary effects are dominant. For this given fluid–fluid distribution, the flow is computed in a second step as indicated above. This is carried out by sampling the capillary pressure, P_c, with successive increasing values, P_{ck}, the former step allowing the determination of the retention curve and the latter the flow rate curve. Examples of fluid distribution in a 2D network are reported in Fig. 2.

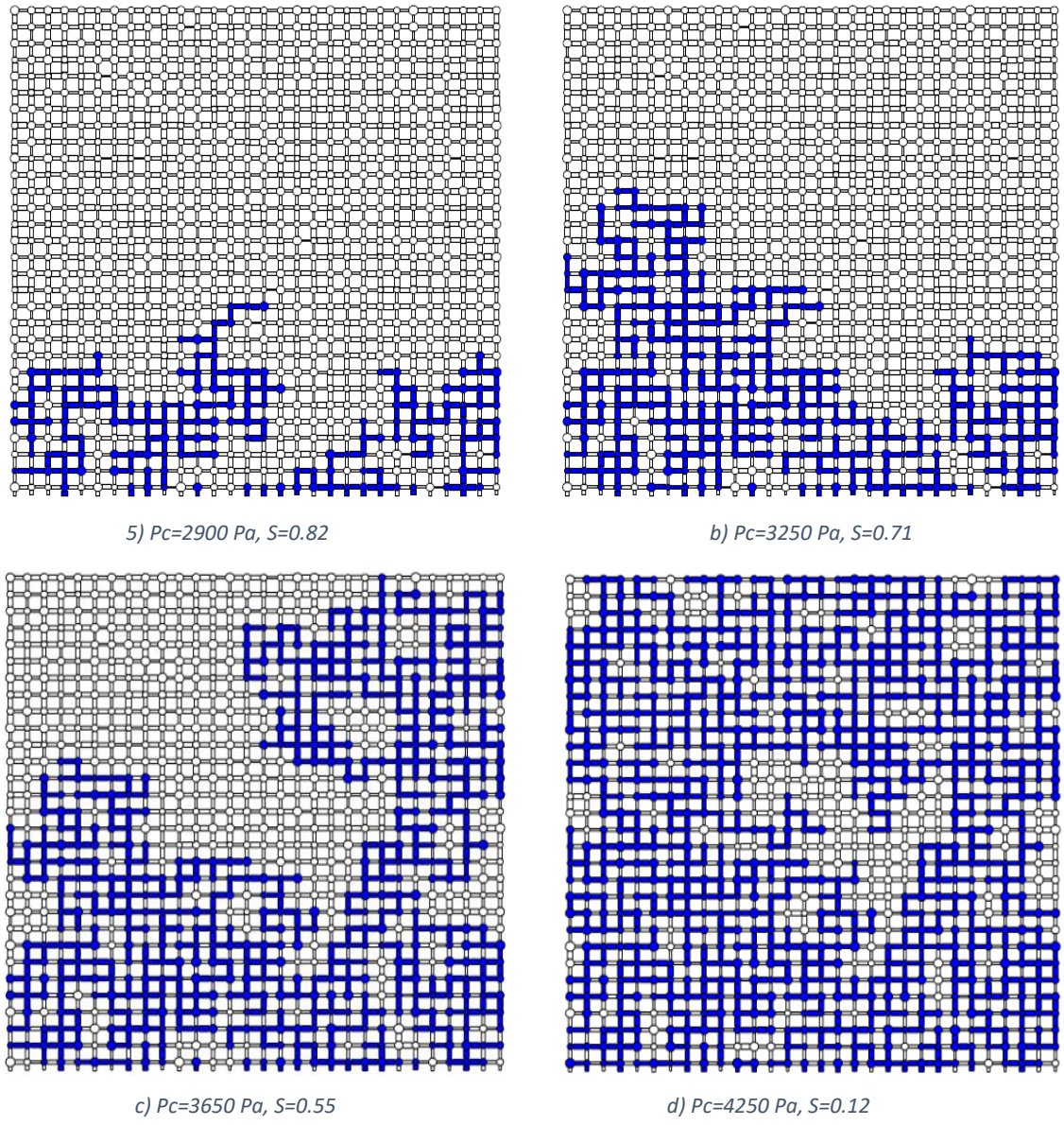
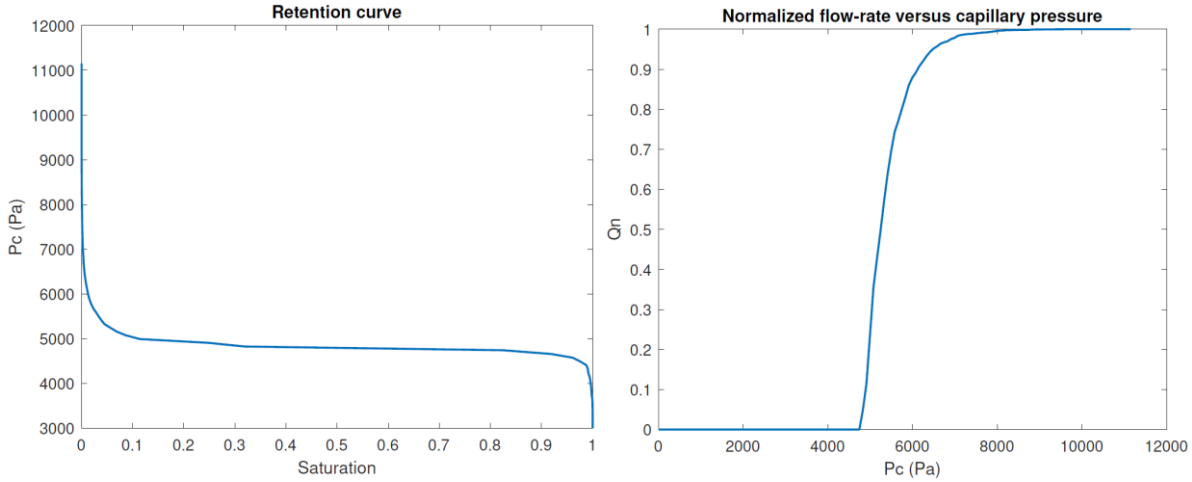


Fig. 2. Examples of fluid-fluid distribution computed in a 30 × 30 2D network with a uniform TSD characterized by r_{min} = 20 μm and r_{max} = 60 μm. Invading fluid in blue enters the network at the bottom face.

Figure 3 shows the retention curve and the non-wetting fluid normalized flow-rate $Q_n = \frac{Q_{nw}}{Q_{max}}$ obtained with the above algorithm for a 50 × 50 square network with Gaussian distributions for both the TSD and PSD having mean radii of 30 µm and 90 µm and standard deviations of 5 µm and 10 µm, respectively. Here, Q_{max} is the flow rate that would be obtained when the network is fully invaded and the same ΔP as the one used to compute Q_{nw} is applied, which means that $Q_{max} = \frac{k}{\mu}\frac{\Delta P}{L}$, and thus, from Eq.(1), that $Q_n = k_r$.



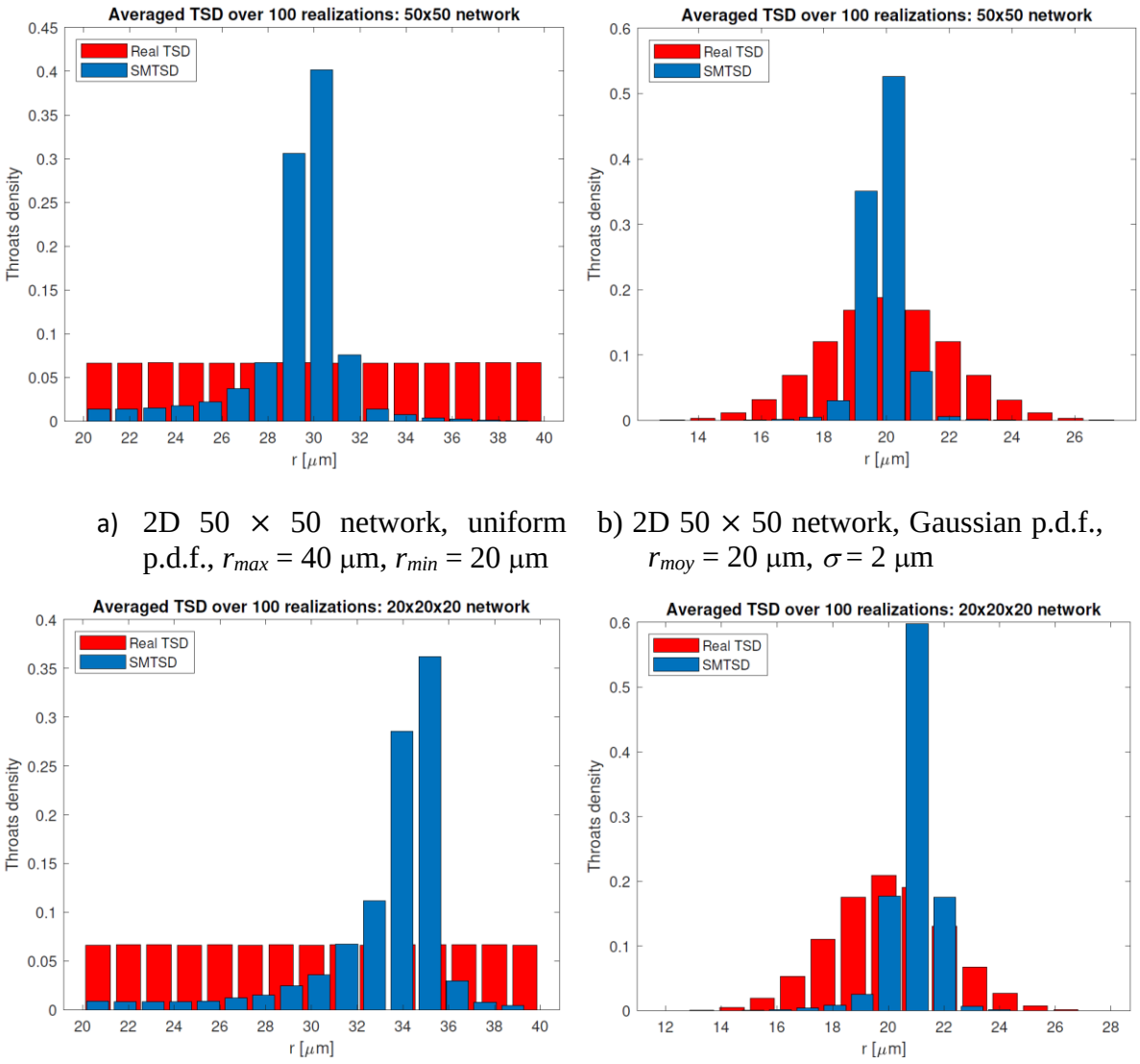
a) b)

Fig.3. Example of computed retention curve (i.e. capillary pressure versus the wetting fluid saturation) (a) and non-wetting fluid normalized flow-rate curve; (b) for a 50 × 50 square network with Gaussian PSD (mean radius: 90 µm, standard deviation: 10 µm) and TSD (mean radius: 30 µm, standard deviation: 5 µm).

5 Assessment of TSD extraction from simple models

As illustrated in Fig. 3, the PNM, allows simulating the flow-rate and retention (or capillary) curves with the decisive advantage that the TSD (and the PSD) of the medium is perfectly known a priori; it is referred to as the reference TSD in the following. Then, starting from the computed curves, the standard determination procedures can be used, i.e. Eqs. (6) and (12), in order to extract the TSD (or PSD) and compare the result with the reference TSD (or PSD). Since the throats control the displacement process, it is reasonable to expect that only the TSD can be determined. The TSD

obtained either from Eq. (6) or Eq. (12) is referred to as the simple model TSD, i.e. the SMTSD. A 2D square 50 × 50 and 3D cubic 20 × 20 × 20 networks were considered for the comparison. For each network, the $Q_n(P_c)$ and $P_c(S)$ curves were computed and the SMTSD extracted using Eqs. (6) and (12). In order to get smoother results, the extracted data, for a given type of network, were averaged over 100 realizations of the network. This corresponds to a 100 realizations of each network type for which throat and pore sizes are randomly assigned according of the given p.d.f.. This means that the fluid-fluid displacement was computed 100 times for each case under consideration. Then the SMTSD was extracted from each flow rate curve and each retention curve, yielding 2 ×100 TSD. Then, for either the flow rate curves or the retention curves, the average TSD is computed from the 100 TSD. This average is presented and discussed below. A "case" is defined by the dimensionality of the network, i.e. square or cubic, the size of the network, the selected p.d.f., i.e. uniform or Gaussian, and the parameters of the p.d.f., namely, the minimum and maximum radii, r_{min} and r_{max}, respectively, for the uniform distribution or the mean size and standard deviation, r_{moy} and σ, respectively, for the pores and the throats in the case of a Gaussian p.d.f..



a) 2D 50 × 50 network, uniform p.d.f., r_{max} = 40 μm, r_{min} = 20 μm

b) 2D 50 × 50 network, Gaussian p.d.f., r_{moy} = 20 μm, σ = 2 μm

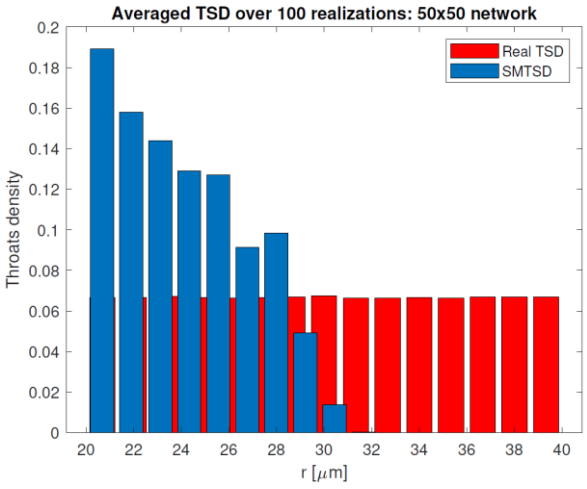
c) 3D 20 × 20 × 20 network, uniform p.d.f., r_{max} = 40 μm, r_{min} = 20 μm

d) 3D 20 × 20× 20 network, Gaussian p.d.f., r_{moy} = 20 μm, σ = 2 μm

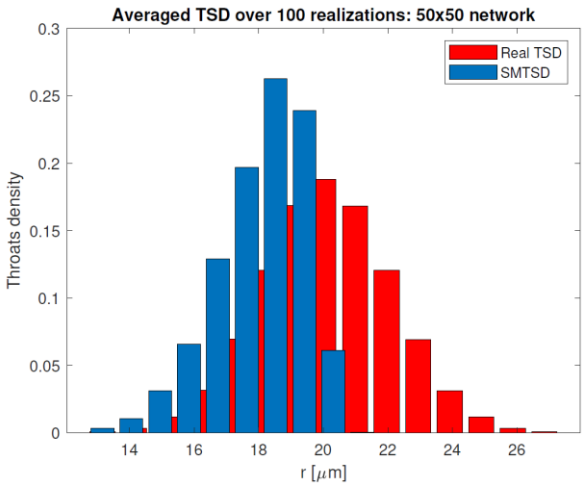
Fig.4. Comparison of the TSD obtained from the simple model (SMTSD), i.e. Eq.(6), and the reference TSD for various cases using the retention curve information.

The comparison between the reference TSD and the SMTSD for various cases when the retention curve information (Eq. (6)) is used is presented in Figure 4 and Table 1. As can be seen, the SMTSD does not match the reference TSD, in particular for the uniform distribution for which the uniform nature is not retrieved. For the 3D networks, it can be seen that the SM procedure introduces

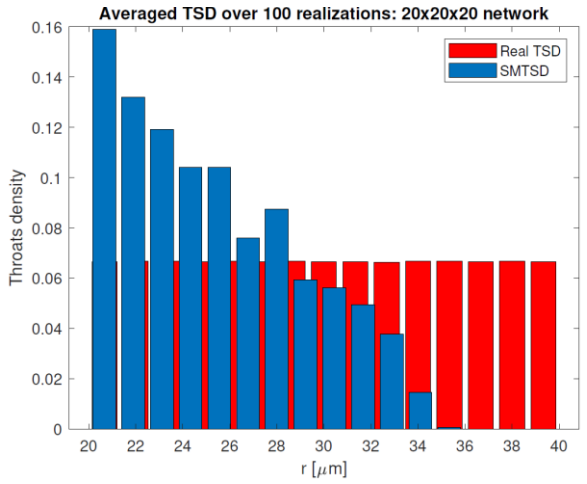
skewness towards large throat size. In brief, the simple model (SM) does not contain the necessary information to predict the reference TSD.



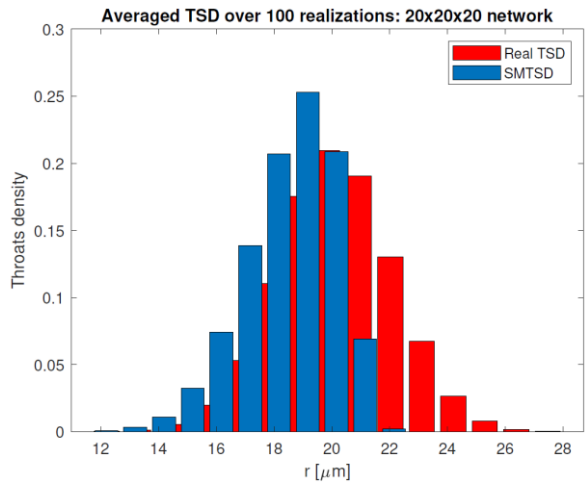
a) 2D 50 × 50 network, uniform p.d.f., r_{max} = 40 μm, r_{min} = 20 μm, r_c = 30 μm.



b) 2D 50 × 50 network, Gaussian p.d.f., r_{moy} = 20 μm, σ = 2 μm, r_c = 20 μm.



c) 3D 20 × 20× 20 network, uniform p.d.f., r_{max} = 40 μm, r_{min} = 20 μm, r_c = 35 μm.



d) 3D 20 × 20× 20 network, Gaussian p.d.f., r_{moy} = 20 μm, σ = 2 μm, r_c = 21.4 μm.

Fig. 5. Comparison of the TSD obtained from the parallel tube model (SMTSD) and the reference TSD for various cases using the flow-rate information, Eq. (12). r_c is the critical radius corresponding to the network percolation threshold.

As illustrated in Fig. 5 and Table1, the SMTSD is somewhat well estimated from the flow rate curve compared to the case where the capillary curve information is used. Indeed, the shape of the TSD is approximately similar to the reference TSD. The discrepancy is noted for the larger throats that are not represented.

Table1. Comparison between the reference TSD and the SMTSD obtained from the Young-Laplace equation and the capillary pressure (or retention) curve, Eq. (6), or from the parallel tube model and the normalized flow-rate curve, Eq. (12), for various cases.

			Young –Laplace and $P_c(S)$		Parallel tubes model and $Q_n(S)$	
	Statistical Moments (μm)	Reference TSD	SMTSD	Relative Error (%)	SMTSD	Relative Error (%)
Uniform p.d.f. 2D network	Mean	30	29.29	2.36	24.14	19.53
	Standard deviation	5.75	2.26	60.75	2.72	52.64
Gaussian p.d.f. 2D network	Mean	20	19.92	0.39	18.08	9.58
	Standard deviation	2	0.69	65.62	1.4	30.1
Uniform p.d.f. 3D network	Mean	30	33.32	11.06	25.38	15.4
	Standard deviation	5.75	2.92	49.2	3.77	34.44
Gaussian p.d.f. 3D network	Mean	20	20.95	4.76	18.6	7
	Standard deviation	2	0.84	58.09	1.59	20.3

A major shortcoming is that some throat sizes are not retrieved at all. In the case of the 2D network with a uniform distribution for instance, the throat sizes in the upper half of the distribution are not retrieved, in particular while employing the flow rate curve. Thus, only half of the throat sizes is

actually identified. The same problem can be noticed with the 3D network, but to a lesser extent since the range of non-identified throat sizes is narrower (but here again the larger throats are not identified). Insights on this result can be gained from percolation theory [20]. In the percolation theory, a certain fraction, p, of throats are "active". This fraction of active throats (or "bonds" in the language of percolation theory) is distributed randomly. Suppose p is progressively increased starting from p =0. For a particular value, p_c, of this fraction, a percolating path (a path of interconnected active throats connecting the inlet to the outlet) forms for the first time in the network. The quantity p_c is the percolation threshold of the network which value depends on the network [20]. For a square network in bond percolation, p_c = 0.5 whereas $p_c \approx 0.25$ for a cubic network.

In the present context, an active throat is a throat that can be invaded, i.e. a throat such that $P_{ck} \geq P_{cth}$ and the breakthrough corresponds to the percolation threshold since there is no non-wetting fluid path flowing through the network before breakthrough. The percolation threshold can thus be related to the TSD

$$p_c = \int_{r_c}^{\infty} f(r)dr = 1 - \int_0^{r_c} f(r)dr = 1 - F(r_c) \tag{16}$$

where r_c is the percolation radius, i.e. the radius given by $P_{cth} = P_{cBT}$, f being the reference TSD p.d.f., and F the corresponding cumulative distribution function [21].

Thus, the threshold or percolation radius, r_c, represents the critical radius above which the flow-rate is non-zero. This means that, when the bundle of parallel tubes model is considered, all the throats of the network having radii greater than the threshold radius, which are hence invaded by the non-wetting fluid prior to the BT, cannot be determined by the parallel tube model.

From Eq. (16), r_c is given by

$$r_c = r_{max}(1 - p_c) + p_c\, r_{min} \tag{17}$$

for a uniform p.d.f., where r_{max} and r_{min} are the maximum and the minimum radii of the (reference) TSD respectively. For a Gaussian TSD, the threshold radius is given by

$$r_c = r_{moy} + \sqrt{2}\,\sigma\, erf^{-1}(1 - 2p_c) \quad (18)$$

where erf^{-1} is the inverse error function.

For a square lattice (p_c = 0.5), the above relationships give $r_c = \frac{r_{max}+r_{min}}{2}$ and $r_c = r_{moy}$ for the uniform and Gaussian p.d.f. respectively. For a cubic lattice ($p_c \approx 0.25$), one obtains $r_c = \frac{3}{4}r_{max} + \frac{1}{4}r_{min}$ and $r_c = r_{moy} + \frac{\sqrt{2}}{2}\sigma$ for the uniform and Gaussian p.d.f. respectively. The values are reported in Fig. 5. The analytical threshold radii are perfectly consistent with the results shown in the TSD comparisons in Fig. 5. In summary, the parallel tube model is not the appropriate representation able to identify the throat sizes greater than the critical radius corresponding to the network percolation threshold. The greater the percolation threshold, the larger the range of missing throats in the TSD determination with the parallel tube model.

6 Beyond the TSD extraction simple models

The observation above calls upon more sophisticated procedures to extract the TSD of a porous material from data available from a primary drainage process. As shown in the previous section, the standard and commonly used models to extract the TSD do not allow determining the reference TSD from the $Q_n(P_c)$ or $P_c(S)$ data. This unsatisfactory situation is explained by two reasons. First, for a given pressure step, all the newly invaded throats, regardless their sizes, are assigned to a single throat size value corresponding to the imposed pressure difference related to the Young-Laplace equation (2). Second, when the determination of the TSD is based on the flow rate curve, all the radius values larger than the percolation radius cannot be determined since the flow rate is zero until breakthrough is reached, hence providing no information on all the throats of radius larger than the critical value. Thus, the question arises as to whether a better use of the $Q_n(P_c)$ and $P_c(S)$ curves can be performed in order to predict the reference TSD. An attempt in this direction is presented in the following.

6.1 TSD determination as an inverse problem

In essence, the problem to be solved is an inverse problem relying on the question: knowing the $Q_n(P_c)$ and $P_c(S)$ curves, can the TSD of the corresponding medium be reliably predicted? In this

procedure, the direct problem is of course to predict the $Q_n(P_c)$ and $P_c(S)$ curves of the porous medium under consideration. In addition, the inverse problem is solved using again PNM and the direct problem is solved as in the previous section using the invasion percolation (IP) algorithm in the absence of trapping, considering the pressure and no flux boundary conditions already mentioned in section 4. Actually, a somewhat simplified version of this inverse problem is employed, assuming that the pore network structure is known. This means that the minimization procedure to fit $Q_n(P_c)$ and $P_c(S)$ is carried out for a given type of network, i.e. square or cubic for instance. In other words, for a given type of network (a 50×50 2D square network for instance), the objective is to correctly identify the TSD. The assumption that the pore network structure is known a priori is further commented in the discussion section 7 below. To build and test the procedure, a particular realization of the network, with specified p.d.f. parameters, is used as the reference network which TSD is hence known. It shall be viewed as the porous medium to be characterized for which the experimental measurement of $Q_n(P_c)$ and $P_c(S)$ would have been performed in practice and which TSD is to be determined.

The inverse problem is solved using an optimization method based on a searching algorithm which is a hybrid version of the genetic [22] and hill climbing [24] [24][24] algorithms. The genetic algorithm is a searching algorithm based on the biological evolution laws including reproduction, mutation and natural selection. A population of individuals is first defined. In our case, the individuals are realizations of the pore network. Every individual has genes. A gene in a pore network is either a throat (or a pore) characterized by its size. The algorithm is relying on a fitness function which value is estimated from a direct solution for each individual. The fitness function, denoted $fit(\mathbf{r}_t)$ in its generic form, is an objective function comparing the curve obtained by direct simulation for the individual to the reference one, $\mathbf{r}_t$ being a vector which components are the individual throat radii. The genetic algorithm aims at minimizing this fitness function [23].

The overall algorithm can be summarized by the following steps:

The first step consists in generating a series of N_0 parent realizations ($N_0 = 16$ in this work) to which evolutionary laws and natural selection are applied. In the most general case, both the throat and pore sizes vary from one element (pore or throat) to the other in the network. Referring for instance to the computation of the normalized flow-rate, it is clear from Eq. (15) that the local

volume flow rate through a throat depends not only on the throat radius, but also on the adjacent pores radii. Indeed, by construction, the length of a throat $l_{i,j}$ is expressed as

$$l_{i,j} = a - r_{pi,j} - r_{pi+1,j} \tag{19}$$

where a is the lattice spacing and $r_{pi,j}$ and $r_{pi+1,j}$ are the radii of the two adjacent pores. As a result, the $Q_n(P_c)$ and $P_c(S)$ curves depend not only on the TSD but also on the PSD. Thus, the pore size should be kept as a variable in the optimization process in order to keep generality. However, as already mentioned, the drainage process is essentially sensitive to the TSD and the impact of the PSD on the flow rate can be reasonably neglected. Thus, the pore size is taken as constant (equal to 80 µm) in what follows. Consequently, generation of individuals is carried by only varying the TSD which remains uniform. The minimum and maximum radii of the distribution are determined from the invasion percolation procedure carried out on the reference network. The minimum throat radius, $r_{min\,0}$, is given by Eq. (2) at the corresponding pressure step when the saturation becomes equal to zero. Conversely, the maximum throat radius, $r_{max\,0}$, cannot be as exactly determined as $r_{min\,0}$. It is approximately specified by multiplying by a factor 1.3 the radius corresponding to the first pressure step at which the saturation is no longer equal to one.

In order to introduce diversity in the initial population, individuals are then generated within N_{0b} class intervals. The i^{th} interval has also a uniform p.d.f. with minimum and maximum radii, $r_{min\,i}$ and $r_{max\,i}$ respectively given by $r_{min\,i} = \frac{(N_{0b}+i)r_{min\,0}+(N_{0b}-i)r_{max\,0}}{2N_{0b}}$ and $r_{max\,i} = \frac{(N_{0b}-i)r_{min\,0}+(N_{0b}+i)r_{max\,0}}{2N_{0b}}$. The number of individuals generated in the i^{th} interval is N_{0i} so that $N_0 = \sum_{i=1}^{N_{0b}} N_{0i}$. Here, $N_{0b} = 4$ and $N_{0i} = 4$. The normalized non-wetting fluid flow rate and capillary pressure retention curves, together with the corresponding fitness function of interest, are computed for each individual parent. After this initialization procedure, the genetic algorithm is executed according to the following steps.

1. The natural selection is applied following a tournament method [22]. This is achieved by randomly choosing a subset of N_1 individuals among the generation of individuals (here, $N_1 = 5$) and the two ones featuring the best fitness values are selected. Consequently, the generation is reduced by two individuals.

2. Two evolutionary operators, namely crossover and mutation, are applied to the two parent individuals. Crossover is the process by which the two selected parent individuals give birth to a child realization by exchanging randomly throat sizes (genes). Mutation is an operation applied separately to both selected parent realizations. It consists in altering genes (the sizes of randomly chosen throats). Mutations are generally supposed to happen rarely. In the present case, the mutation rate is taken equal to 0.01.
3. The $Q_n(P_c)$ and $P_c(S)$ curves and the fitness values for the two children are computed and, among the four individuals (the two parents and the two children), the two individuals having the best fitness values are selected. They are kept to form the new generation.
4. Steps 1 to 3 are repeated until there is no more individuals in the parent population and a new generation of N_0 individuals is formed.
5. The process made of steps 1 to 4 is iterated until convergence is reached. By convergence, it is meant that the fitness of all the individuals from one generation to the following one does not change by more than about 0.1%.

For all the cases under study in this work, 200 generations (iterations) were enough to reach convergence at which the solution is estimated to be close to the global solution. Then a new step is performed using the hill climbing algorithm.

The solution obtained from the genetic algorithm is global in the sense that the population of all the individuals is optimized by adjusting their overall genes content. When considering a network with its given TSD, the genetic algorithm, which operates on randomly selected throats, keeps in fact this TSD. A network with a Gaussian TSD, for example, is such that throat radii close to the mean radius are more likely to be selected than others. This limits the population diversity. The objective of the hill climbing algorithm, which, like the genetic algorithm is a searching algorithm, is to gradually modify the throat size p.d.f. within a single individual so as to converge toward the TSD of the reference network. To this purpose, the hill climbing algorithm is operated on the best fitted individual in the population once the genetic algorithm ends. It attempts to find a better solution by adjusting only a single variable among all the variables. By contrast to the genetic algorithm, the variables that are adjusted are not the throat radii, but rather the throat densities. Once the lower and upper bounds of the TSD are specified at the starting point of the optimization process, the distribution can be divided into class intervals, or bins. Then the density of throat sizes belonging to each bin, i.e. the fraction of throats having a size within the radius interval

corresponding to the bin can be determined. The hill climbing algorithm aims at determining the optimal density of each bin. To summarize, the genetic algorithm is a multi-directional search algorithm operating on radii belonging to different distribution bins, whereas the hill climbing algorithm is a unidirectional algorithm that operates only on radii belonging to a pair of defined bins. Actually, as the sum of all distribution bin densities must be equal to one, the hill climbing algorithm operates on two bin densities by increasing one (the positive bin) and decreasing the other (the negative bin) with the same amount. Thus, two bins must be selected. In our case, the two bins of the best fitted individual resulting from the genetic algorithm are randomly chosen. A relatively small randomly chosen number of throats are interchanged between the negative and positive bins. If the fitness function is improved, the modified individual replaces the individual in the population and the hill climbing process is repeated until the fitness function does not improve. When it is not improved, another test is performed by randomly choosing a different couple of bins. The fitness function for the hill climbing algorithm is equivalent to the one considered for the genetic algorithm and is denoted by *fit(***d***)* in its generic form, where **d** is the distribution density vector. The difference between the genetic and hill climbing algorithms lies in the variables to control for minimizing the objective function. Fitness functions are detailed in the following section.

6.2 Fitness functions

The direct problem solution provides the $Q_n(P_c)$ and $P_c(S)$ curves of the reference network, i.e. the one for which the TSD from either the normalized flow rate curve or the capillary pressure curve data, or both, is to be determined. As indicated above, the network is a 2D, 50 × 50 square network, with a lattice spacing of 350 μm and a chosen TSD as will be further presented in the results section. The initial N_{0i} individuals (also 2D, 50 × 50 square networks with a lattice spacing of 350 μm) are generated in the N_{0b} class intervals having a uniform TSD with their own minimum and maximum radii as mentioned above.

For the same pressure steps as the ones considered for the reference $Q_n(P_c)$ and $P_c(S)$ curves, the optimization process, following the genetic and hill climbing algorithms, is performed. Again, this implies to solve the direct problem for every individual considered in the optimization process. The

TSD at each step of the optimization procedure is compared to the reference one by evaluating the fitness function, which is defined as the cumulative error function. If the optimization is based on the normalized flow rate $Q_n = \frac{Q_{nw}}{Q_{max}}$, this fitness function is given by

$$fit_{Q_n}(\boldsymbol{\omega}) = \sum_{j=1}^{n} \left| Q_{n-refj} - Q_{n-indj}(\boldsymbol{\omega}) \right| \qquad \boldsymbol{\omega} = \boldsymbol{r}_t, \boldsymbol{d} \tag{20}$$

where *n* is the total number of pressure steps, Q_{n-refj} and Q_{n-indj} are respectively the reference and individual normalized flow rates corresponding to the j^{th} pressure increment and $\boldsymbol{\omega} = \boldsymbol{r}_t, \ \boldsymbol{d}$ depending on whether the algorithm is at the genetic or hill climbing stage. Again, flow rates are considered so as to use the same convention as for the FFDP [19]. However, it should be clear that $Q_n = k_r$ in the quasi-static limit under consideration, where k_r is the non-wetting fluid relative permeability.

Similarly, if the optimization is based on the capillary pressure curve, the fitness function is defined as

$$fit_{\varepsilon P_c}(\boldsymbol{\omega}) = \sum_{j=1}^{n} \left| \varepsilon_{ref} S_{refj} - \varepsilon_{ind} S_{indj}(\boldsymbol{\omega}) \right| \qquad \boldsymbol{\omega} = \boldsymbol{r}_t, \boldsymbol{d} \tag{21}$$

where S_{refj} and S_{indj} are the reference and individual saturations at the j^{th} pressure increment, respectively. As can be inferred from Eq. (21), where ε_{ref} and ε_{ind} are respectively the reference and individual porosities, the porosity is actually also considered as a variable to optimize. By definition, εS is computed as

$$\varepsilon S = \frac{V_{non-inv}}{V_{total}} \tag{22}$$

where $V_{non-inv}$ is the volume of pores not invaded at the j^{th} step and V_{total} is the total volume of the porous medium. This quantity is the wetting fluid volume fraction which does not involve the total pore space volume V_{pores} but only the volume of the non-invaded pores as a variable to adjust. This is preferable to the saturation as the latter depends on both $V_{non-inv}$ and V_{pores} that can have

different impact on the fitness function. Actually, the variable that is adjusted is the porosity when the saturation is equal to one, otherwise, it is the saturation function.

When both the flow-rate and the capillary pressure curves are considered, then the fitness function is defined as,

$$fit_{Q_n-\varepsilon P_c}(\boldsymbol{\omega}) = \sum_{j=1}^{n}\left|Q_{n-refj} - Q_{n-indj}(\boldsymbol{\omega})\right| + f_p \sum_{j=1}^{n}\left|\varepsilon_{ref} S_{refj} - \varepsilon_{indk} S_{indj}(\boldsymbol{\omega})\right| \quad \boldsymbol{\omega} = \boldsymbol{r}_t, \boldsymbol{d} \qquad (23)$$

where f_p is a penalization factor that is taken as constant and computed as

$$f_p = \frac{1}{\varepsilon_{ref}} \qquad (24)$$

The idea with the weighted definition in Eq; (23) is actually to give more importance to the capillary pressure curve in the optimization process.

6. 3 Results

Results are first discussed for a reference network with a Gaussian TSD having a mean radius of 40 μm and a standard deviation of 10 μm. This reference TSD is shown in Fig. 6a. As mentioned in section 6.2, the initial population that must be generated at the beginning of the optimization process is composed of realizations with uniform distributions, thus with a type of p.d.f. different from the Gaussian one of the reference network.

Results on optimized TSDs when the target data are only the capillary pressure curve (Eq. (21)) (left column), only the normalized flow-rate curve (Eq. (20)) (middle column) and both the retention and normalized flow-rate curves (Eq. (23)) (right column) are represented in Fig 7. Corresponding quantitative results are reported in Table 2.

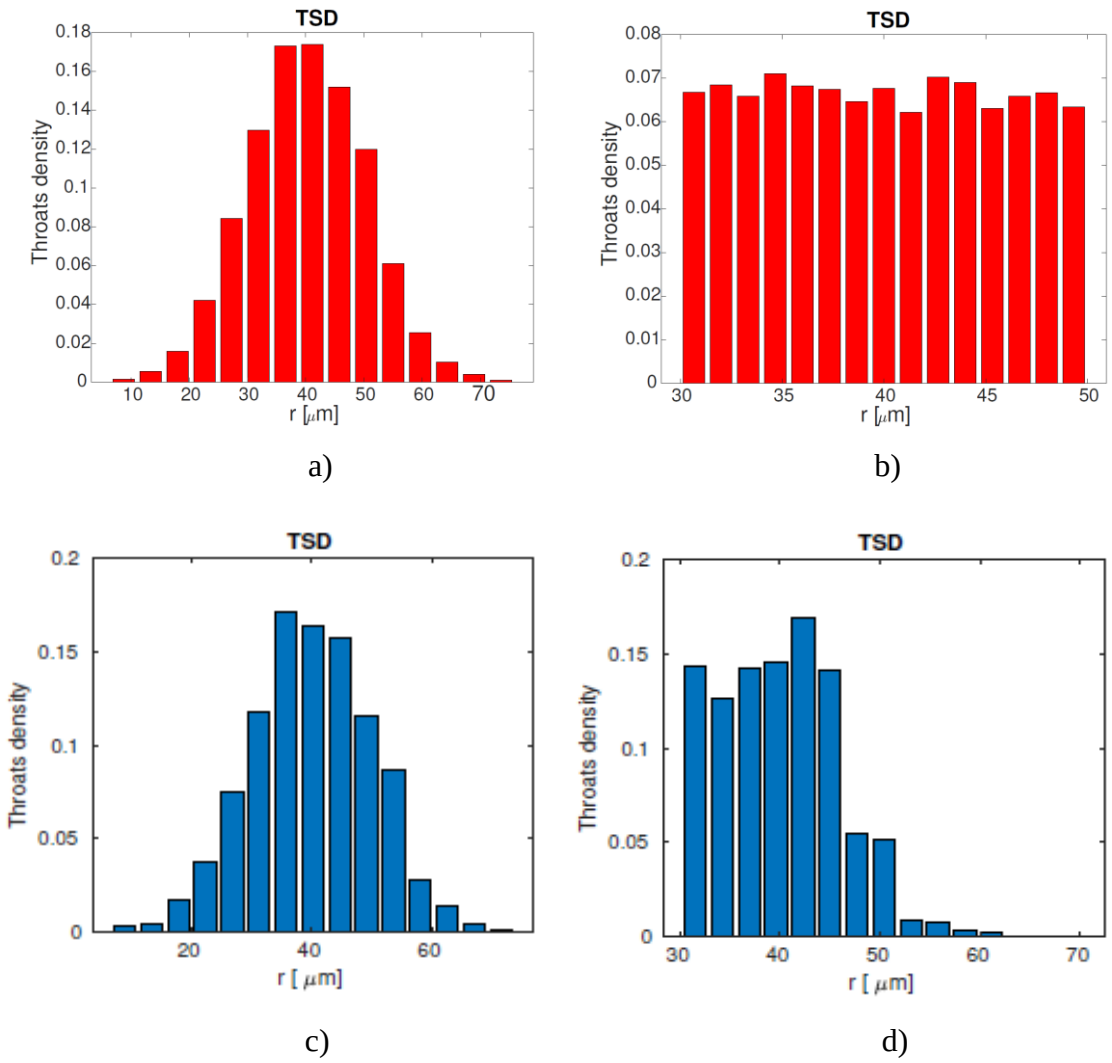


Fig. 6. Top: Reference Gaussian TSD (a) and reference uniform TSD (b) (for a 50 × 50 square network). Bottom: TSD obtained from the optimization procedure using both the normalized flow-rate and capillary pressure curve as target data. The TSDs in (c) and (d) are to be compared with the TSDs in (a) and (b), respectively.

As can be seen from Fig. 7 and Table 2, using the capillary pressure leads to a better result than when only the normalized flow rate curve is employed. Not surprisingly, the best result is obtained when both the retention curve and the normalized flow rate curve are used in the optimization process. Indeed, comparing the reference TSD in Fig. 6.a to the optimized one obtained with this

procedure in Fig. 6c shows a very good agreement. This is also confirmed by the results in Table 2. As illustrated in Fig. 7 (right column), the retention and normalized flow rate curves resulting from the optimization procedure reproduce very well the corresponding curves of the reference case.

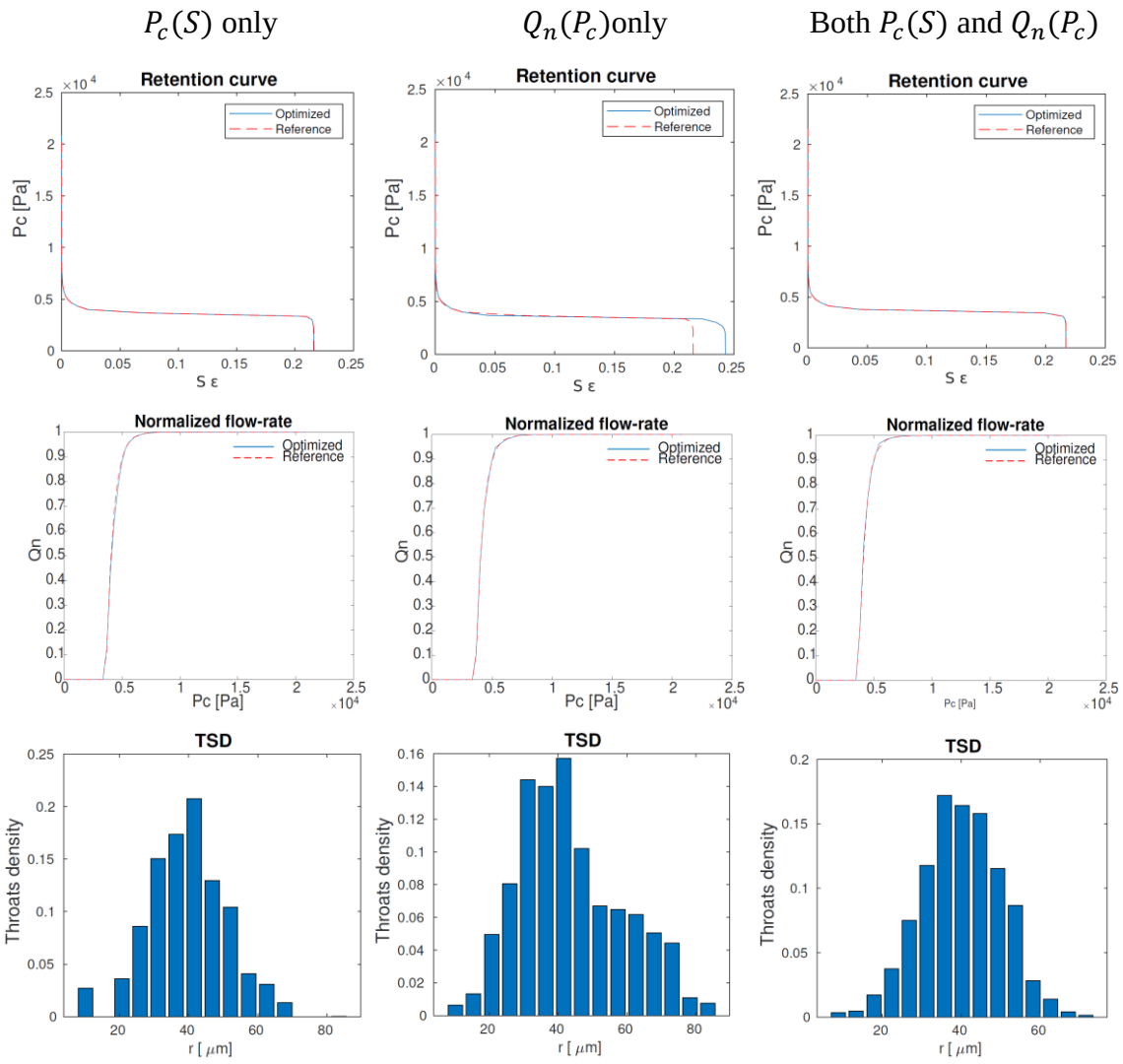


Fig.7. Results of optimization procedure considering the capillary pressure curve only as target data (left column), the normalized flow rate curve only (middle column) and both the normalized flow rate (equivalent to k_r) and capillary pressure curves (right column). Case when the reference p.d.f. is Gaussian (as depicted in Fig. 6a).

Table 2. Comparison between the reference and optimized TSDs when the reference TSD is the Gaussian TSD depicted in Fig. 6a.

		$P_c(S)$ only		$Q_n(P_c)$ only		Both $P_c(S)$ and $Q_n(P_c)$	
Statistical Moments (μm)	Reference TSD	Optimized TSD	Relative Error (%)	Optimized TSD	Relative Error (%)	Optimized TSD	Relative Error (%)
Mean	40	39.57	1.08 %	43.53	8.83	40.24	0.6
Standard deviation	9.9	11.37	14.85	15.18	53.33	9.77	1.31
Skewness	-0.01	0.06	-	0.45	-	0.043	-
Kurtosis	3	3.275	9.16	2.57	14.33	2.77	7.67

A similar test was performed when the reference TSD is uniform (Fig. 6b). The results are represented in Fig. 8 and quantitative data in Table 3. Here again, the TSD obtained considering the capillary pressure curve only is closer to the reference one than when the optimization is based on the normalized flow-rate curve only. The best result is again obtained when both the capillary pressure and the normalized flow-rate curves are used in the optimization procedure. However, as illustrated in Fig.6b and d, the optimization is less performant than in the case of a Gaussian TSD for the reference medium. This discrepancy can be explained by the uncertainty on the distribution upper bound associated to the difficulty of accurately determining the maximum throat radius, $r_{max\,0}$, as mentioned in section 6.1. This inaccuracy leads to introduce some throats greater than the maximum radius (50 μm) in the reference distribution during the optimization procedure. This effect is of course much less sensitive in the case of distributions of Gaussian or Log-normal types for which the relative density of throats close to the distribution upper bound is much lower than in a uniform distribution.

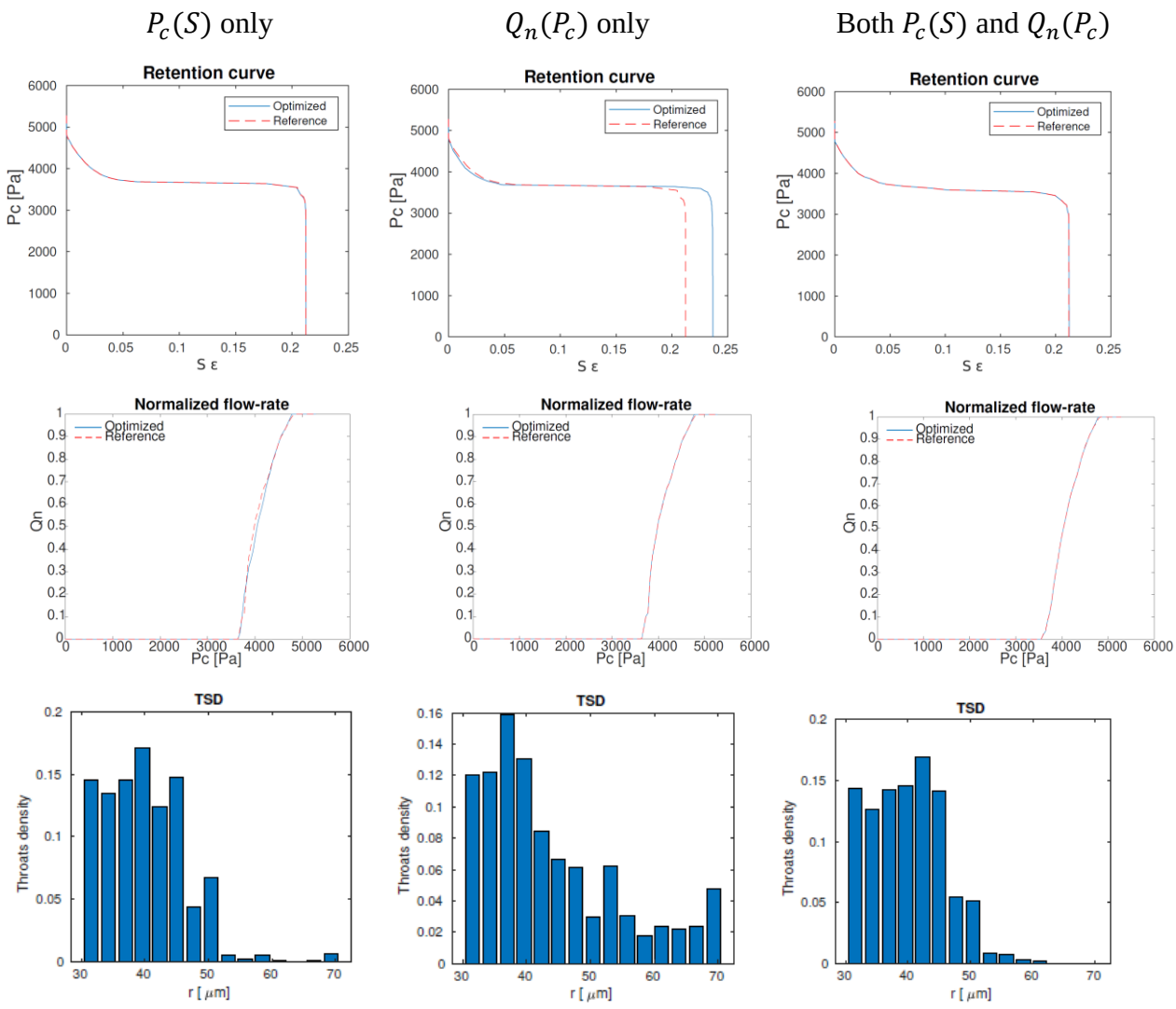


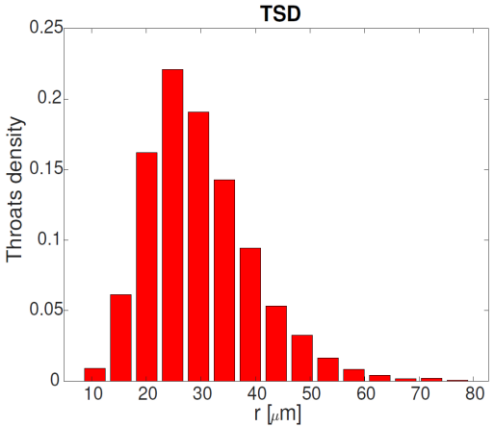
Fig.8. Optimization results considering only the capillary pressure curve as target data (left column), only the normalized flow-rate curve (middle column) and both the normalized flow-rate and capillary pressure curves (right column). The reference p.d.f. is the uniform one reported in Fig. 6b.

As also shown in Fig. 8, the capillary and normalized flow rate curves of the optimized network almost perfectly match the ones of the reference network. However, the match for the capillary curve is not satisfactory for the lower values of the capillary pressure when only the normalized flow rate data are used in the optimization procedure. This also holds in the case of the Gaussian reference TSD (see Fig.7). This is an additional illustration of the impact of the distribution upper bound specification and also of the percolation threshold issue discussed in section 5.

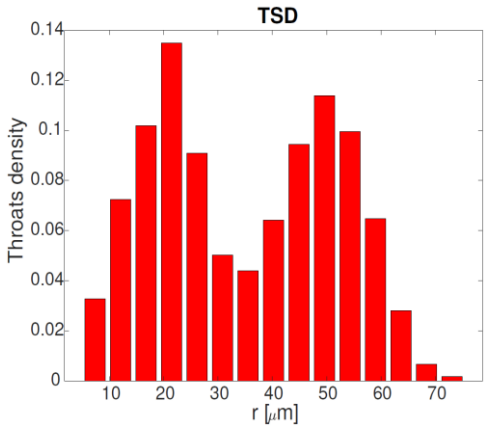
Table 3. Comparison between the reference TSD and the obtained TSD. Case where the reference TSD is the uniform TSD depicted in Fig. 6b.

		$P_c(S)$ only		$Q_n(P_c)$ only		Both $P_c(S)$ and $Q_n(P_c)$	
Statistical Moments (μm)	Reference TSD	Optimized TSD	Relative Error (%)	Optimized TSD	Relative Error (%)	Optimized TSD	Relative Error (%)
Mean	40	39.88	0.29 %	43.67	9.18	39.93	0.18
Standard deviation	5.77	6.36	10.22	10.72	85.79	5.97	3.47
Skewness	0.01	0.91	-	0.97	-	0.42	-
Kurtosis	1.8	5.06	181	2.99	66.1	2.93	62.78

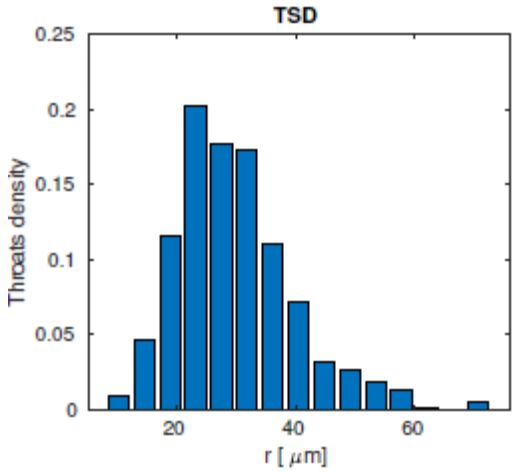
Two additional tests were performed considering a reference log-normal distribution (as depicted in Fig. 9a) and the expected more challenging bimodal distribution depicted in Fig. 9b. For these cases, only the full optimization procedure, i.e. the one based on both $P_c(S)$ and $Q_n(P_c)$, was used. As can be seen from Fig. 9 and Table 4, results are quite satisfactory. Here also, the match between the reference capillary pressure and the normalized flow rate curves and the curves resulting from the optimization procedure is excellent. Finally, among the four reference TSDs considered here, results obtained for the uniform one are the less accurate, mainly because of the uncertainty associated with the distribution upper bound specification.


TSD
Throats density
r [μm]

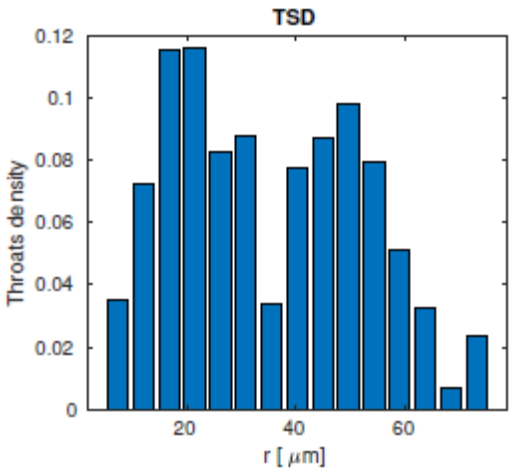
a)


TSD
Throats density
r [μm]

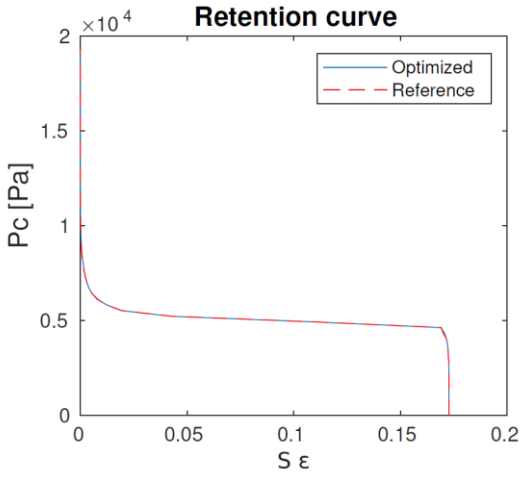
b)


TSD
Throats density
r [μm]

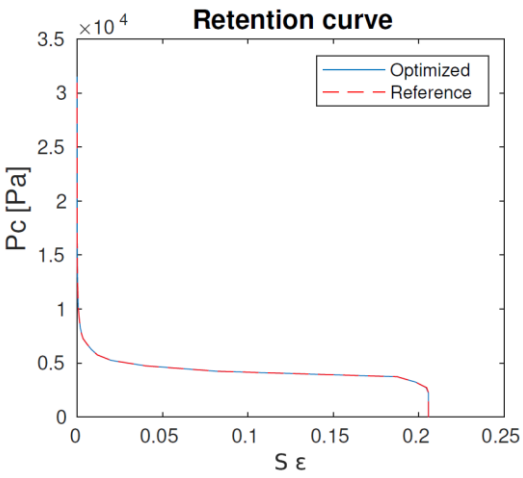
c)


TSD
Throats density
r [μm]

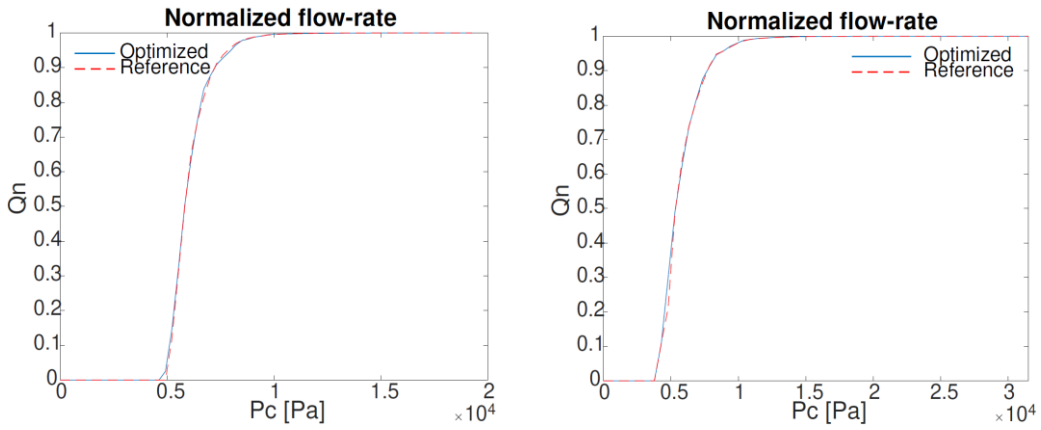
d)


Retention curve
×10^4
Optimized
Reference
Pc [Pa]
S ε

e)


Retention curve
×10^4
Optimized
Reference
Pc [Pa]
S ε

f)



g) h)

Fig.9. Results of the optimization procedure using both the normalized flow-rate and capillary pressure curves as target data for a 50 × 50 square network having a reference Log-normal TSD (a) and bimodal TSD (b). Figures in the left and right columns are for the Log-normal and bimodal distributions, respectively. The optimized TSDs in (c) and (d) are to be compared with the reference TSDs in (a) and (b) respectively. Comparison of the reference and optimized capillary (or retention) curves ((e) and (f)) and normalized flow-rate (or relative permeability) curves ((f) and (g)).

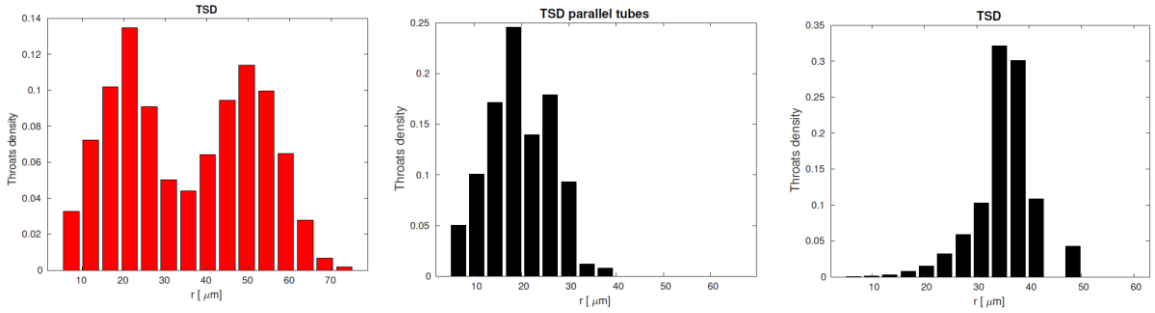
Table 4. Comparison between the reference and optimized TSDs using both the capillary pressure and normalized flow-rate curves as target data. Cases where the reference TSD is the Log-normal one depicted in Fig. 9a or the bimodal one depicted in Fig.9b.

	Log-normal TSD			Bimodal TSD		
Statistical Moments (μm)	Reference TSD	Optimized TSD	Relative Error (%)	Reference TSD	Optimized TSD	Relative Error (%)
Mean	39.84	39.85	0.003	35.3	35.09	0.6
Standard deviation	9.83	9.8	0.3	16.61	17.07	2.8
Skewness	0.63	0.58	7.94	0.06	0.245	-

Kurtosis	3.48	3.33	4.31	1.71	2.01	17.54

7 Discussion

To further illustrate the interest of the optimization approach compared to the conventional approaches based on the consideration of the parallel tube model and the normalized flow-rate curve (Eq. (12)) or just the Young-Laplace equation and the retention curve (Eq. (6)), the conventional approaches was applied to the bimodal reference network (Fig. 9b). The results are represented in Fig. 10 and reported in Table 5.



a) b) c)

Fig. 10. Reference bimodal TSD (a), TSD identified using Eq. (12), i.e. the normalized flow-rate curve and the parallel tube model (b), TSD identified using Eq. (6), i.e. the capillary pressure curve combined with the Young-Laplace equation (c).

As can be seen, the bimodal nature of the distribution cannot be identified using the conventional approaches. The approach based on the normalized flow-rate curve and the parallel tube model, i.e. Eq. (12), only captures the throat sizes below the percolation threshold (as discussed in Section 5). As a result, only throats in the range of the lower peak distribution are retrieved. When the capillary pressure curve combined with the Young Laplace equation is used, i.e. Eq. (6), throats over a larger range of size are identified but the bimodal nature of the distribution is not at all retrieved. However, as indicated in Table 5, the procedure based on the capillary pressure curve, i.e. Eq. (6), leads to a satisfactory estimate of the throat size mean value. Actually, as can be seen also from Table 1, the use of the capillary pressure curve information in conjunction with the Young – Laplace equation leads to the same result, i.e. the throat size mean value is reasonably well predicted. Note from

Tables 2 and 3 that it is also the case with the optimization procedure: the throat size mean value is well predicted when the capillary pressure curve information is used (and also when both the $P_c(S)$ and $Q_n(P_c)$ information are used as can be seen from Tables 2-5). An explanation of this fact, i.e. the fact that the use of the retention curve in conjunction with the Young – Laplace equation always lead to a good estimate of the mean throat size, is proposed in the Appendix.

Table 5. Comparison of the throat size mean values of the reference TSD with those obtained using the parallel tube model and normalized flow-rate curve, Eq. (12), or the capillary pressure curve combined with the Young –Laplace equation, Eq. (6), for the reference bimodal TSD depicted in Fig. 9b.

Reference TSD	// tube model using $Q_n(P_c)$		Young-Laplace and $P_c(S)$	
Mean (μm)	Mean (μm)	Relative error (%)	Mean (μm)	Relative error (%)
35.3	19.6	44.48	35.3	0.3

As a matter of prospective, the above results call upon the following remarks. Although the TSD identification based on the optimization procedure clearly leads to much better results than the conventional approaches, several points are worth being recalled or discussed. Firstly, trapping phenomena were ignored. It would be interesting to investigate the possible impact of this phenomenon on the TSD determination. Secondly, the optimization procedure has been tested considering only the throat size variability. In other words, the pore size variability (the PSD, was not considered. In this respect, it would be interesting to explore the ability of the optimization procedure to capture both the PSD and the TSD. Thirdly, the optimization procedure has been performed for given pore network structures, i.e. square or cubic in our simulations. It can certainly be argued that, in general, the network structure is unknown a priori. In addition, the pore network that can represent a real porous medium is rarely structured but rather unstructured. This means that the distance between two adjacent pores may vary, as well as the local coordinance, i.e. the number of pores to which a given pore is directly connected. Therefore, an interesting question to address will be to test the impact of the structure. In other words, if cubic networks are used, for

instance, in the optimization procedure with reference data obtained from a medium whose 3D pore network is obviously not cubic, will the procedure still be relevant, or at least provide significantly better results than those obtained using the much simpler procedures making use of Eq. (6) or Eq. (12). Since the microstructures of porous media can be quite diverse, it can be surmised that the quality of the results will also be quite diverse depending on the medium pore network structure and how close it is from a cubic network. In principle, the optimization procedure can of course be used for pore networks different from cubic. However, this may be cumbersome, keeping in mind that many realizations of the network must be generated. Here the use of stochastic network generators [24] might be an option. From a practical point of view, a simpler option may be to create a catalog of various pore network structures (cubic, Voronoi...) and choose the one which seems the closest to the structure of the porous medium to be characterized. This choice could be guided by images from the microstructure or partial information on this structure. However, when detailed digital 3D images of the microstructure are available, it is probably simpler to try to extract the PSD and/or the TSD directly from the images [7, 8]. Nevertheless, it would be interesting to test whether the use of the $Q_n(P_c)$ and $P_c(S)$ curves with the optimization procedure might help characterize the microstructure by testing different pore network structures available in the catalog. Another type of situation is when the throat or pore sizes change due to some coupled phenomena (particle trapping, dissolution or precipitation, biofilm development). Using the optimization procedure to characterize the pore network evolution can be much simpler than repeated 3D imaging. In this case, one could use a stochastic pore network generator based on data obtained on initial images of the microstructure. Nevertheless, this requires determining the retention curves and the non-wetting fluid normalized flow rate (as well as the porosity and the permeability) repeatedly. Finally, the network size considered in this work remains quite small, and this was mainly motivated by the interest which was focused on the characterization of thin porous media with only few pores over their thickness [25] . One can wonder whether increasing the network size might affect the results. Although tests in this direction could be interesting, it can be noted, for instance, that the problem associated with the network percolation threshold, when the flow rate information is used, will still be present whatever the network size. As a consequence, the standard methods (based on Eqs (6) or (12)) are not expected to perform better whatever the network size.

8 Conclusion

Pore network simulations were developed to assess the performance of two conventional and simple methods aiming at the determination of the throat size distribution (TSD) of a porous medium from macroscopic data such as the retention curve and/or the normalized flow rate curve. It was shown that using the normalized flow rate curve alone, which is roughly an information similar to the one used in the fluid-fluid porosimetry displacement (FFPD) technique [9], is not satisfactory since all the throats greater than the critical throat corresponding to the network percolation threshold cannot be identified. On the whole, the procedure based on the capillary pressure curve combined with the Young-Laplace equation leads to better determination of the mean radius than the procedure based on the normalized flow-rate curve combined with the parallel tube model. However, all the invaded pores at a given pressure step in both procedures are assigned to one pore size corresponding to the specified capillary pressure regardless of their actual sizes. Thus, these simple procedures do not make any distinction between the throat size distribution (TSD) and the pore size distribution (PSD). In order to alleviate the limitations of the conventional TSD identification methods, a procedure combining pore network simulations and an optimization technique based on a genetic algorithm and the hill climbing algorithm was developed. This algorithm leads to much better results compared to the simpler methods. Referring again to the FFPD, the study also indicates that the knowledge of the non-wetting fluid normalized flow rate is not sufficient to determine the TSD. Using the porosity and the retention curve as additional information are necessary to obtain satisfactory results.

However, the optimization procedure is significantly more intense in terms of computational resources and computer programming compared to the conventional procedures. Also, a somewhat simple situation has been considered to test the optimization procedure. Only the TSD was considered and no variability in the pore size was envisaged. The network structure and size were the same in the reference network and the various networks generated during the optimization procedure. Certainly, more work is needed to fully explore the capability of the approach proposed in the present work with the aim of solving the ill-posed problem consisting in identifying the TSD (and the PSD) from macroscopic data such as the normalized flow rate and capillary pressure curves. Nevertheless, results obtained here are very encouraging and suggest to further investigate the way opened by the methodology developed in this work.

Acknowledgements

This research was supported by the Project "PEMFC – SUDOE" – SOE1/P1/E0293 which is co-financed by the European Regional Development Fund in the framework of the Interreg Sudoe programme.

Appendix

Some explanation of the fact that the use of the retention curve in conjunction with the Young – Laplace equation always lead to a satisfactory estimate of the mean throat size is proposed in this Appendix.

By definition the mean throat size is given by

$$\bar{r} = \int_0^{+\infty} r f(r) dr = \int_{r_{min}}^{r_{max}} r f(r) dr \quad \text{(A-1)}$$

Combining Eq. (A-1) with Eqs. (6) and (5) for $\theta = 0$ and recalling that trapping phenomena are neglected (thus S varies between 0 and 1) yields

$$\bar{r} = \int_0^1 r(S) dS \quad \text{(A-2)}$$

and

$$\bar{r} = 2\gamma \int_0^1 \frac{dS}{P_c} \quad \text{(A-3)}$$

The Brooks and Corey representation [27] for the retention curve may be invoked, which in our case takes the form

$$S = \left(\frac{P_c}{P_M}\right)^{-\lambda} \quad \text{(A-4)}$$

where P_M and λ are two parameters that must be fitted to represent the retention curve.

Using Eq. (A-4) in Eq. (A-3) yields

$$\bar{r} = r_M \frac{\lambda}{\lambda+1} \quad \text{(A-5)}$$

where $r_M = \frac{2\gamma}{P_M}$, r_M actually corresponding to the radius of the largest throat at the network inlet. Fitting the values of P_M and λ for the networks featuring a Gaussian and uniform TSD explored in this work (see section) and applying Eq. (A-5) lead to the results presented in Table A-1.

Table A-1 Comparison between the mean throat radius in the TSD and the radius predicted by Eq.(A-5)

p.d.f	$\bar{r}$ (from p.d.f)	$\bar{r}$ (from Eq.(A-5)	r_M	λ
Uniform 2D (Table 1)	29.6 μm	29.65 μm	30.91 μm	23.5
Gaussian 2D (Table 1)	19.9 μm	19.86 μm	20.42 μm	35.3
Uniform 3D (Table 1)	33.32 μm	33.61 μm	35.85 μm	15
Gaussian 3D (Table 1)	20.98 μm	20.99 μm	21.64 μm	32.5

These results justify why the capillary curve contains the required information that can restitute a relevant value of the mean throat radius.

References

[1] E. H. D'Hollander, Estimation of the pore size distribution from the moisture characteristic, Water Resources Research, 15, 107–112 (1979).

[2] L. R. Stingaciu, L. Weihermüller, S. Haber-Pohlmeier, S. Stapf, H. Vereecken, and A. Pohlmeier, Determination of pore size distribution and hydraulic properties using nuclear magnetic resonance relaxometry: A comparative study of laboratory methods, Water Resources Research, 46, W11510 (2010).

[3] W.B. Krantz, A.R.Greenberg, E. Kujundzic, A.Yeo, S. S.Hosseini, Evapoporometry: A novel technique for determining the pore-size distribution of membranes, Journal of Membrane Science, 438, 153-166 (2013).

[4] M.J. Blunt, M.D. Jackson, M. Piri, P.H. Valvatne, Detailed physics, predictive capabilities and macroscopic consequences for pore-network models of multiphase flow, Advances in Water Resources, 25 (8-12), 1069-1089 (2002).

[5] F. Plouraboué, S. Geoffroy, M. Prat, Conductances between confined rough walls, Physics of Fluids, 16, 615-624 (2004).

[6] F. Plouraboué, F. Flukiger, M. Prat, P. Crispel, Geodesic network method for flows between two rough surfaces in contact, Physical review, E 73, 1-12 (2006).

[7] R. Ziel, A. Haus, A. Tulke, Quantication of the pore size distribution (porosity profiles) in microfiltration membranes by SEM, TEM and computer image analysis, Journal of Membrane Science, 323, 241-246 (2008).

[8] H. Dong, M.J. Blunt, Pore-network extraction from micro-computerized-tomography images, Physical Review, E, 80, 036307 (2009).

[9] K.R. Morison, A comparison of liquid-liquid porosimetry equations for evaluation of pore size distribution, Journal of Membrane Science, 325, 301-310 (2008).

[10] R.I. Peinador, J.I. Calvo, P. Prádanos, L. Palacio, A. Hernández, Characterisation of polymeric UF membranes by liquid{liquid displacement porosimetry, Journal of Membrane Science, 348, 238-244 (2010).

[11] C. Pan, M. Hilpert, C. T. Miller, Lattice-Boltzmann simulation of two-phase flow in porous media, Water Resources Research, 40, W01501 (2004).

[12] A.Q. Raeini, M.J. Blunt, B.Bijeljic, Direct simulations of two-phase flow on micro-CT images of porous media and upscaling of pore-scale forces, Advances in Water Resources, 74, 116-126 (2014).

[13] V. Joekar-Niasar, S.M. Hassanizadeh and A. Leijnse, Insights into the relationships among capillary pressure, saturation, interfacial area and relative permeability using pore-network modelling, Transport in Porous Media, 74, 201-219 (2008).

[14] Y. Mualem, A new model for predicting the hydraulic conductivity of unsaturated porous media, Water Resources Research, 12, 513-522 (1976).

[15] T. Agaesse, A. Lamibrac, F. Buechi, J. Pauchet, M. Prat, Validation of pore network simulations of ex-situ water distributions in a gas diffusion layer of proton exchange membrane fuel cells with X-ray tomographic images, Journal of Power Sources, 331, 462-474, (2016).

[16] M.J. Blunt, Flow in porous media-pore-network models and multiphase flow, Current Opinion in Colloid & Interface Science, 6, 197-207 (2001).

[17] R Lenormand, E Touboul, C Zarcone, Numerical models and experiments on immiscible displacements in porous media, Journal of fluid mechanics, 189, 165-187 (1988).

[18] D. Wilkinson and J.F. Willemsen, Invasion percolation: a new form of percolation theory, Journal of Physics A: Mathematical and General, 16, 3365-3376 (1983).

[19] D. Zhou, M. Blunt, F.M. Orr Jr, Hydrocarbon drainage along corners of noncircular capillaries, Journal of Colloid and Interface Science, 187, 11-21 (1997).

[20] D Stauffer, A. Aharony, Introduction to percolation theory, Taylor & Francis, London, (1992).

[21] C.W. Gardiner, Handbook of stochastic methods, Springer, (1985).

[22] E. Unsal, J. H. Dane, and G. V. Dozier, A genetic algorithm for predicting pore geometry based on air permeability measurements, Vadose Zone Journal, 4, 389-397 (2005).

[23] J. McCall, Genetic algorithms for modelling and optimization, Journal of Computational and Applied Mathematics, 184, 205-222 (2005).

[24] S.C. Su, C.J. Lin and C.K. Ting, An effective hybrid of hill climbing and genetic algorithm for 2D triangular protein structure prediction, Proteome Science, 9, (Suppl 1): S19 (2011).

[25] L. Mosser, O. Dubrule, M.J. Blunt, Reconstruction of three-dimensional porous media using generative adversarial neural networks, Physical Review E, 96, 043309 (2017).

[26] M. Prat, T. Agaësse, Thin porous media, Handbook of Porous Media 3rd Edition, Edited by K.Vafai, CRC Press, Chapter 4, 89-112 (2015).

[27] R.H. Brooks, A.T. Corey, Properties of porous media affecting fluid flow. Journal of the Irrigation and Drainage Division, 92, 61-88 (1966).

Pore network simulations of fluid-fluid displacement porosimetry for evaluation of pore size distribution

Otman Maalal[a,b], Marc Prat[a*], René Peinador[b], Didier Lasseux[c]

Institut de Mécanique des Fluides de Toulouse (IMFT), Université de Toulouse, CNRS, Toulouse, France.
Institut de La Filtration et des Techniques Séparatives (IFTS), Rue Marcel Pagnol, 47510, Foulayronnes, France
CNRS, I2M, UMR 5295 – Esplanade des Arts et Métiers, 33405 Talence, CEDEX, France

[*] *Corresponding author:mprat@imft.fr (+33534322883)*

Abstract

Fluid-fluid displacement porosimetry (FFDP) is a method for determining the pore size distribution of a porous medium from fluid-fluid immiscible displacement (drainage) results. The method leads to unambiguous results when the porous medium microstructure is strongly anisotropic and akin to a bundle of parallel cylindrical tubes. The information obtained from this technique is however less simple to interpret for less simple microstructures. This is illustrated from pore network simulations. For the interconnected microstructures considered in this study, the simulations indicate that the method leads to a shift in the distribution toward unrealistic small pore sizes. Then, it is shown that the situation can be improved by considering the pore size distribution characterization as an inverse optimization problem. The latter is solved from pore network simulations combined with a genetic algorithm and the hill climbing algorithm.

Keywords: Fluid-fluid displacement porosimetry; Pore size distribution; Throat size distribution; Pore network model; Genetic algorithm; Hill climbing algorithm

1 Introduction

Fluid-fluid displacement porosimetry (FFDP) [1-4] is a technique for characterizing the pore size distribution of a porous medium. The method is notably used for the characterization of thin porous media such as ultrafiltration and microfiltration membranes, e.g. [2-4], and is more commonly referred to as the Liquid-Liquid Displacement Porosimetry (LLDP) technique because the two fluids commonly used are liquids. However, the technique can be extended to Gas-Liquid Displacement Porosimetry. For this reason, this technique is more simply referred to as the fluid-fluid displacement porosimetry (FFDP) technique in the current study. In this method, the membrane is wetted by a liquid and another immiscible liquid or a gas is forced through the pores. This is accomplished through a series of pressure steps resulting in the immiscible displacement of the wetting liquid by the injected fluid. The pressure in the injected fluid at the membrane inlet is measured as well as the injected fluid flow rate through the membrane. The link with the pore size distribution is via the local capillary pressure invasion threshold which must be overcome for a displacement to occur in a pore and also through the dependency of the local flow conductances with the pore size. However, as pointed out in [1], practically all the determinations of the pore size distribution with the FFDP technique have been made considering a simplified representation of the membrane as a bundle of parallel cylindrical tubes. This is a quite questionable simplification of the microstructure of most membranes. Owing to this simplification, the question arises as to whether this technique really allows determining the pore size distribution in thin porous layers markedly different from a simple system of cylindrical pores in parallel. Clarifying this question is the main objective of the present article. To this end, the FFDP is simulated numerically for given microstructures. This means that the pore size distribution is perfectly known for each considered microstructure. Then, the pore size distribution (PSD) is determined from the FFDP simulation, i.e. from the simulated two-phase immiscible displacement in the considered microstructure under the same conditions as in the FFDP experimental devices. The FFDP PSD can finally be compared to the real PSD in order to evaluate the possible bias and errors associated with the FFDP. According to these simulations, significant discrepancies are found between the FFDP PSD and the real PSD. In order to improve the PSD determination from the FFDP raw data, the PSD extraction model based on the parallel cylindrical tube simplification is abandoned and a more sophisticated approach is developed. The latter considers the PSD determination as an inverse

optimization problem, which is solved using a genetic algorithm [5-6] combined with the hill climbing algorithm [5,7]. This approach is tested for various PSD, namely, uniform, Gaussian, Log-normal and bimodal. Both steps, i.e. the evaluation and assessment of the commonly used FFDP approach and the inverse optimization approach, rely on numerical simulations of the immiscible fluid-fluid displacement in the pore space of the considered thin porous media. The latter are performed within the classical framework of pore network modeling [8-10]. Typically, pore network models consider a simplified representation of the pore space as a system of nodes connected by narrower channels. The nodes are local larger volumes in the pore space. Within the framework of pore network modelling, these local larger volumes are referred to as pore bodies whereas the narrower channels between pores are referred to as pore throats or simply throats. In what follows, simple two-dimensional square pore networks are considered.

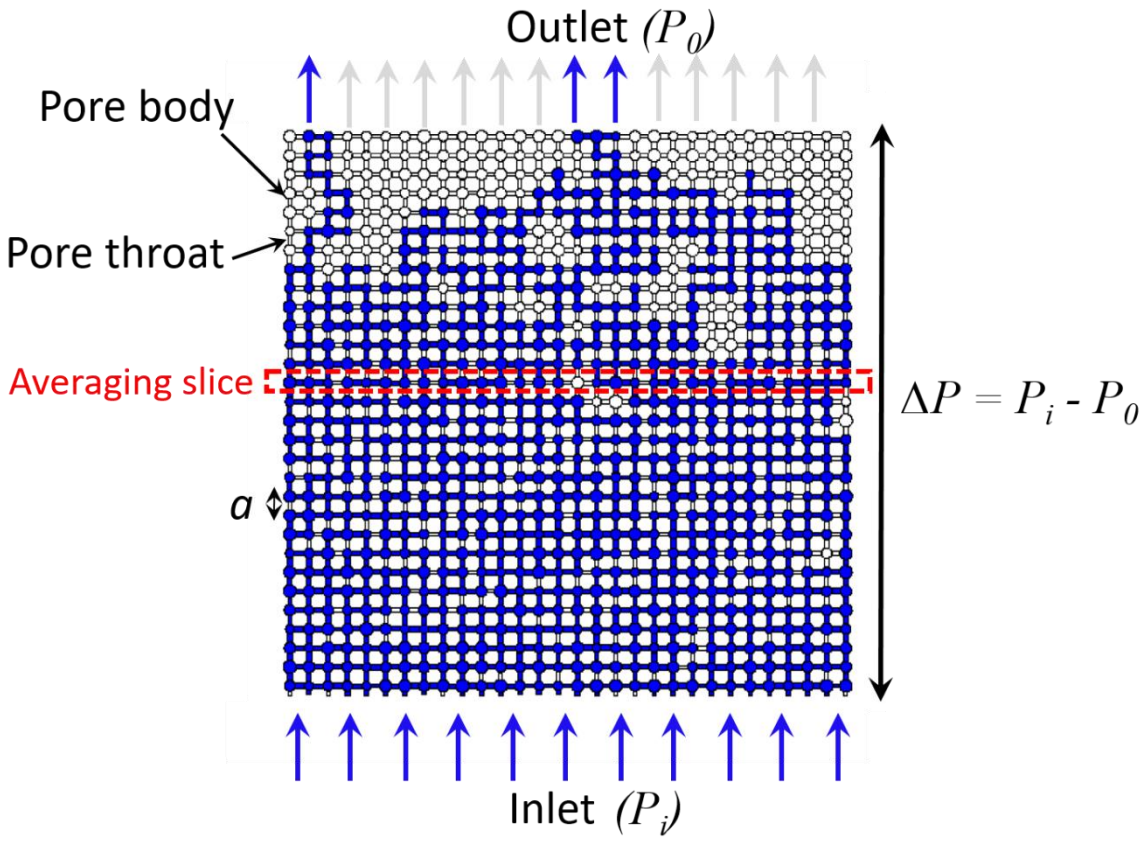


Fig.1. Square pore network and sketch of immiscible displacement in FFDP (displacing fluid in blue, displaced fluid in light grey). The red dashed box corresponds to an exemplary network slice used for spatially averaging the pressure.

As illustrated in Fig.1, the pore bodies are located at the nodes of a square regular grid and the throats correspond to the segments between nodes. The morphology of pore networks extracted from real porous media microstructures is obviously more complex than a regular grid, e.g. [11-12]. However, it is expected that the crucial ingredients for assessing the FFDP are the pore space interconnectivity (the fact that a pore body is connected to several pore bodies) and the disordered nature of the pore space (the fact that the local geometrical dimensions vary from one pore body or throat to the other). These two ingredients are present in the simple pore networks considered in the present study. In other words, it is our belief that the main results obtained from this study also apply to the unstructured networks representative of the pore space of real porous media.

The consideration of pore network models leads to distinguish two main microstructure elements: the throats and the pore bodies. A distribution is associated with each element category, which leads to distinguish the pore body size distribution (PBSD) from the throat size distribution (TSD). The constrictions in the pore space, which correspond to the throats, play an important role since the menisci tend to get pinned in the constrictions due to capillary effects and the local viscous pressure drops are highly dependent on the flow through the throats (the narrower the passage, the greater is the pressure drop between two pore bodies for an identical flow rate). For these reasons, the focus will be on the TSD determination.

The present paper is organized as follows. In section 2, the commonly used method for determining the TSD from the FFDP raw data is recalled. The pore network model is presented in Section 3. The algorithms used to simulate the displacement and compute the FFDP data is presented in Section 4. The assessment of the TSD determination from the commonly used FFDP method is presented in Section 5. In Section 6, a method to determine the TSD from the FFDP curve using PNM simulations combined to an optimization method is presented. Section 7 presents results obtained with the optimization method when both the FFDP and retention curves are used as target data. A short discussion is presented in Section 8. Conclusions are drawn in Section 9.

2 Fluid-fluid displacement porosimetry

As indicated above and sketched in Fig.1, the FFDP is based on the measurements of the pressure P_i in the displacing fluid at the inlet and the corresponding displacing fluid flow rate $Q(P_i)$. The

pressure P_o at the outlet is fixed and considered to be the same in the displacing and displaced fluids. The commonly used method [1] for determining the TSD from the flow-rate data $Q(P_i)$ in the FFDP explicitly relies on the model of a bundle of parallel cylindrical tubes. In the tube bundle model, the flow-rate is computed by applying Poiseuille law in each tube containing the non-wetting fluid.

$$Q_i = \frac{\Delta P \pi}{8\mu L} \int_{r_{min}}^{+\infty} r^4 f_Q(r) dr \tag{1}$$

where L is the tube length, $\Delta P = P_i - P_o$, μ is the displacing fluid viscosity, the radius of a tube is denoted by r and f_Q is the sought TSD. Radius r_{min} is determined from Young-Laplace equation as

$$r_{min} = \frac{2\gamma \cos\theta}{\Delta P} \tag{2}$$

where the contact angle is $\theta = 0$ (a perfectly wetting displaced fluid is assumed) and γ is the interfacial tension. Eq.(2) expresses that all the tubes greater or equal to r_{min} are invaded by the displacing fluid. The greater the inlet pressure, the lower is the threshold radius r_{min}. Combining Eq.(1) and Eq.(2) leads to

$$Q_i = \frac{\pi 2\gamma \cos\theta}{8\mu L r_{min}} \int_{r_{min}}^{+\infty} r^4 f_Q(r) dr \tag{3}$$

Deriving Eq(3) with respect to r lead to

$$\frac{dQ_i}{dr} = -\frac{Q_i}{r} - \frac{\pi 2\gamma \cos\theta}{8\,\mu L} r^3 f_Q(r) \tag{4}$$

and thus to

$$f_Q(r) = -\frac{8\,\mu L}{\pi 2\gamma \cos\theta} r^{-3} \left(\frac{dQ_i}{dr} + \frac{Q_i}{r}\right) \tag{5}$$

Equation (5) can be expressed in discrete form as [1]

$$f_{Qk}(r_{AB}) = -\frac{8\,\mu L}{\pi 2\gamma\, cos\theta} r_{AB}^{-3}\left(\frac{Q_{iB}-Q_{iA}}{r_B-r_A}+\frac{Q_{iAB}}{r_{AB}}\right) \quad (6)$$

where Q_{iA} and Q_{iB} are two close values of Q_i corresponding to two close values of the inlet pressure P_{iA} and P_{iB} , $Q_{iAB} = \frac{Q_{iB}+Q_{iA}}{2}$ and $r_{AB} = (r_A + r_B)/2$, r_A and r_B being determined from Eq. (2).

The value of f_{Qk} is then normalized as,

$$d_{Qk}(r_{AB}) = \frac{f_{Qk}}{\sum_{i=1}^{n} f_{Qi}} \quad (7)$$

where *n* is the number of classes considered to compute the throat size distribution. In what follows, water is considered as the wetting fluid and air as the displacing fluid. Thus γ = 0.072 N/m and $\mu = \mu_{air} = 10^{-5}$ Pa.s.

3 Interconnected model porous medium

The FFDP immiscible displacement is simulated in the model porous medium depicted in Fig.1 using the pore network modeling (PNM) approach [8]. As illustrated in Fig. 1, pore bodies in this model are spheres of radius r_p located at the nodes of a regular square grid. The distance between two adjacent nodes is the lattice spacing *a* with *a* = 350 μm in all the simulations presented below. The size of the network is the number of nodes (pores) in each direction (for example, Fig. 1 shows a 30 × 30 square network). Throats are cylindrical channels of radius r_t. The throat size is randomly distributed according to a given probability density function (p.d.f.). Similarly, the pore body sizes are distributed according to a given p.d.f with the constraint that the size of a pore body is equal or greater than the size of the largest throat to which it is connected. The same type of p.d.f., i.e. Gaussian, uniform, etc, is considered for the pore bodies and the throats. In what follows, several types of p.d.f. will be considered, namely uniform, Gaussian, log-normal and bimodal. Also, it can be noted that the network coordination number, i.e. the number of throats connected to a pore body, is 4 in the 2D square network.

4 Fluid – fluid immiscible displacement simulation

The modeling of immiscible two-phase flow displacements on a network has been the subject of many works and the reader is referred to [8, 13] for reviews. In the FFDP, a wetting fluid is displaced by a non-wetting one. This process is called a drainage process. It is analyzed in detail in [14], where it is shown that the resulting flow pattern depends on the competition between the capillary and viscous forces. The method for computing the flow is similar to the one described in [14]. Since the inlet pressure variation between two pressure steps is small, a simplification is to consider that the pressure in the displaced fluid is uniform and equal to P_o. This means that the viscous flow is only computed in the fraction of the network occupied by the displacing fluid. The displacing fluid flow computation consists in expressing the mass conservation equation at each network node (pore body) j

$$\sum Q_{i-j,k} = 0 \tag{8}$$

where $Q_{i-\,j,k}$ is the non-wetting fluid volume flow rate between pore body j and adjacent pore body k. If the throat between pore bodies j and k is occupied by the wetting fluid, then $Q_{i-\,j,k} = 0$. If the throat is occupied by the non-wetting fluid, then

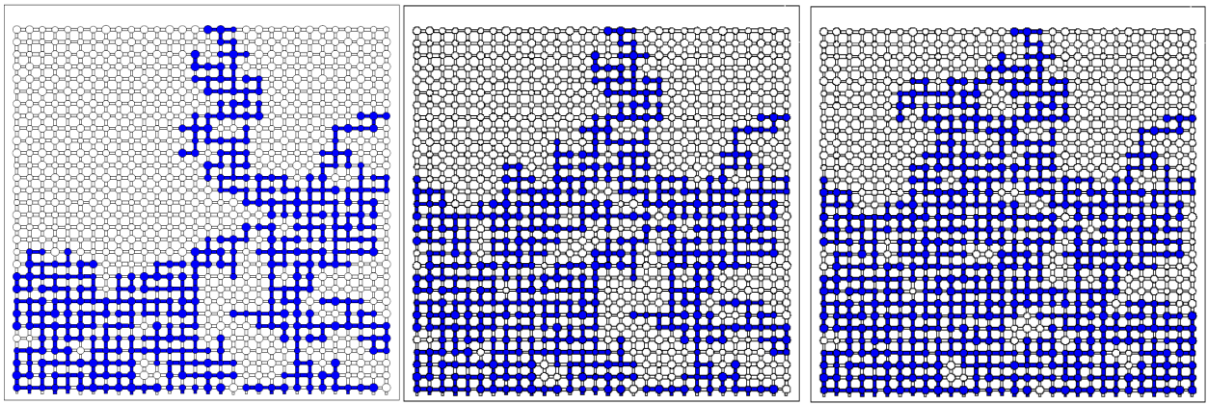
$$Q_{i-\,j,k} = \frac{\pi r_{t\,j,k}^4}{8\mu_{nw} l_{j,k}} \Delta P_{j,k} \tag{9}$$

where $r_{t\,j,k}$ and $l_{j,k}$ are the radius and length of the throat linking the two pore bodies respectively, while $\Delta P_{j,k}$ is the pressure drop in the displacing fluid between the two neighboring pore bodies. The boundary conditions at the inlet and outlet are $P = P_i$ and $P = P_0 = Cte$, respectively. A zero-flux condition is imposed on the lateral faces of the network. This leads to a linear system for the pressure field in the non-wetting fluid. This system is numerically solved using the conjugate gradient method. Once the pressure field is obtained, the displacing fluid flow rate Q_i is computed at the inlet using Poiseuille law applied to all displacing fluid throats connected to the inlet.

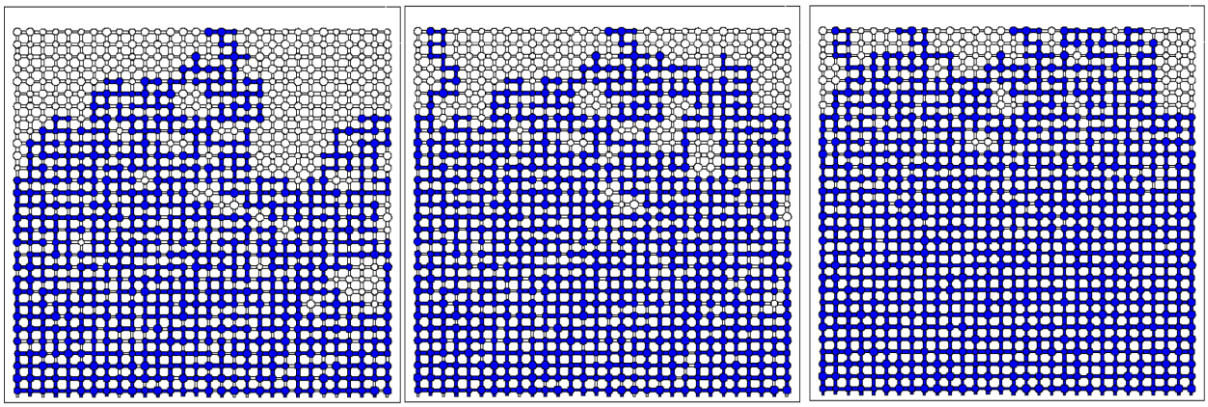
The flow computation method described above applies for a given fluid distribution in the network. It must be coupled with an algorithm allowing the determination of the fluid distribution. To this end, a meniscus at the entrance of a throat is defined as stable when the pressure difference between each side of the meniscus is less than the capillary pressure threshold of the considered throat (such a throat is referred to as an interfacial throat),

$$P_{i-j,k} - P_0 < P_{cth} \tag{10}$$

where $P_{cth} = \frac{2\gamma\, cos\theta}{r_t}$ and $P_{i-j,k}$ is the pressure in the displacing fluid pore body adjacent to the considered throat (of radius r_t). Starting from the fluid configuration obtained at the previous step, the pressure field in the displacing fluid for the new pressure step is computed as indicated above. Then all unstable menisci are identified. This corresponds to all menisci such that $P_{i-j,k} - P_0 \geq P_{cth}$. Then the interfacial throat for which $(P_{i-j,k} - P_0) - P_{cth}$ is maximum is invaded together with the adjacent pore body if the latter was not already invaded in a previous step. If this pore body was occupied by the displaced fluid, new menisci are then positioned at the entrance of the throats occupied by the displaced fluid and connected to the newly invaded pore body. Thus, the list of interfacial throats is updated so as to remove the invaded throat and add the throats connected to the newly invaded pore body and occupied by the displaced fluid. This procedure is repeated until there is no unstable menisci remaining in the network, i.e. until there exists no interfacial throat for which $P_{i-j,k} - P_0 \geq P_{cth}$. The resulting fluid distribution corresponds to the equilibrium distribution at the specified value of P_i.



***6**) ΔP=3653 Pa, S=0.6* *b) ΔP =3681 Pa, S=0.5* *c) ΔP =3722 Pa, S=0.4*



d) ΔP =3743 Pa, S=0.3 *e) ΔP =3768 Pa, S=0.2* *f) ΔP =3781 Pa, S=0.1*

Fig.2. Example of fluid-fluid distributions computed in a 30 × 30 2D network with a uniform TSD between r_{tmin} = 30 μm and r_{tmax} = 50 μm and a uniform PSD between r_{pmin} = 80 μm and r_{pmax} = 120 μm for an increasing pressure difference. The displacing fluid in blue enters the network at the bottom. *S* is the displaced fluid saturation, i.e. the network volume fraction occupied by the displaced fluid.

The above procedure is enforced after the breakthrough (BT). The breakthrough corresponds to the minimum inlet pressure P_{iBT} for which the displacing fluid reaches the outlet. For inlet pressures lower than P_{iBT}, the displacing fluid has not reached the outlet and therefore there is no flow when the steady state is reached. The procedure to compute the fluid distribution before BT is similar to the one described above. The important difference is that the pressure is spatially uniform and equal to P_i in the displacing fluid since there is no flow before BT when the capillary equilibrium is reached. The invasion rules described above correspond to a drainage process without trapping. An element, pore body or throat, occupied by the displacing fluid is thus assumed to be always connected to the outlet face, possibly through liquid films [15] present in the pore and throat surface roughness and/or in a subnetwork of small crevices at the pore walls. Implementation of trapping rules is possible (see for instance [16]), but, for simplicity, trapping is not considered in what follows.

Examples of fluid distribution in a 30 × 30 2D network obtained with the procedure described above are displayed in Fig.2 whereas the corresponding displacing fluid pressure profiles are shown in Fig.3. The first pattern in Fig.2 corresponds to breakthrough. The pressure plotted in Fig.3 is the

displacing fluid pressure averaged over slices containing one row of pores. Such a slice is illustrated in Fig.1. The average displacing fluid pressure in a slice is computed as,

$$< P >= \frac{\sum_{j=1}^{m} \frac{4\pi r_{pj}^3}{3} P_{i-j}}{\sum_{j=1}^{m} \frac{4\pi r_{pj}^3}{3}} \tag{11}$$

where *m* is the number of pores occupied by the displacing fluid in the slice.

As can be seen from Fig.2, the displacement occurs in comparatively more throats and pore bodies in the lower region of the network, that is the region adjacent to the inlet, than in the upper region of the network. This is fully consistent with the existence of the viscous pressure (non-linear) drop in the displacing fluid illustrated in Fig.3. Consider two interfacial throats of same radius. Such a throat is invaded by the displacing fluid when $P_{i-j,k} - P_0 \geq P_{cth}$. The closer the throat to the inlet, the greater is the local pressure $P_{i-j,k}$ (Fig.3). As a result, in the sequence of pressure steps, a throat closer to the inlet is invaded before a throat of comparable radius located further away in the network. This also means that throats of different radius are invaded when the inlet pressure is incremented. For a given inlet pressure, since $P_{i-j,k}$ decreases on average with the increasing distance from the inlet, the critical invasion threshold radius given by the equation $P_{i-j,k} - P_0 = P_{cth} = \frac{2\gamma cos\theta}{r_t}$ increases with the increasing distance from the inlet. In other words, contrary to the common FFDP assumption consisting in associating a single pore radius with each inlet pressure through the Young-Laplace equation (2), the simulation results illustrated in Figs. (2) and (3) clearly indicate that this is not correct.

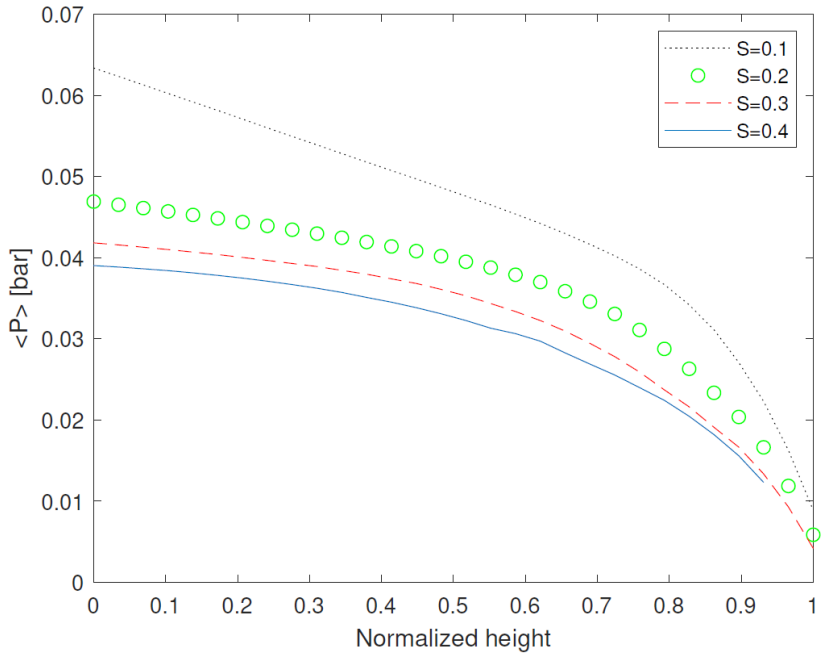


Fig.3. Displacing fluid slice average pressure profiles in the 30x30 network corresponding to the fluid distributions depicted in Fig.2. Note that the pressure is averaged over 30 realizations whereas only one realization is of course shown in Fig.2. The inlet is on the left. The outlet on the right (normalized height = 1).

The corresponding FFDP curve is shown in Fig.4. Note that the curve in Fig.4 is for one realization of the network and not an average curve over several realizations (contrary to the pressure curves in Fig.3). This curve typically shows the displacing fluid flow rate as a function of the inlet pressure. Throughout the article, the displacing fluid flow rate Q_i is normalized. The quantity $\frac{Q_i}{P_i - P_0}$ is considered and normalized by $\frac{Q_{if}}{P_{if} - P_0}$ where Q_{if} and P_{if} are the final displacing fluid flow rate and inlet pressure. Thus, the quantity

$$\chi = \frac{Q_i\,(P_{if} - P_0)}{Q_{if}(P_i - P_0)} \tag{12}$$

is considered. χ should not be mistaken with the displacing fluid relative permeability (k_r) in the classical theory of two-phase flow in porous media [17]. χ would correspond to k_r if the fluid distributions were quasi-static. Owing to the viscous pressure drop in the displacing fluid, this is

obviously not the case in the situation under study. In that sense, χ can be seen as a "dynamic" relative permeability.

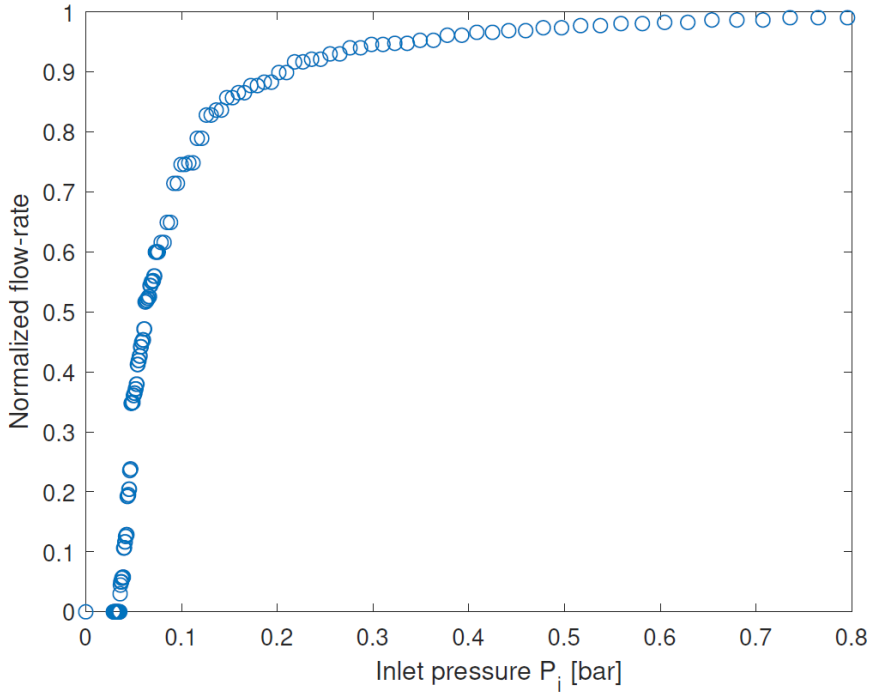


Fig.4. FFDP curve: displacing fluid flow rate (χ) as a function of inlet pressure.

5 Assessment of TSD extraction from FFDP

As illustrated in Fig.4, the FFDP curve can be obtained with the decisive advantage that the TSD of the considered porous medium is perfectly known. The latter is referred to as the real TSD. The next step is to apply the commonly used FFDP TSD extraction procedure, i.e. Eqs. (1-7) starting from the computed FFDP curve and see how the TSD so obtained compares with the real TSD. The TSD obtained from Eq. (6) is thus referred to as the FFDP TSD. A 2D square 50 × 5, a 2D square 50 × 25 and a 2D square 30 × 30 networks were considered for the comparison. For each network, the $\chi(\Delta P)$ curve was computed and the FFDP TSD extracted using Eq. (6). For a given network, the results were averaged over 100 realizations of the network so as to get smoother results. A realization of the network corresponds to throat size randomly assigned according to the given p.d.f.. For a given network size, the FFDP TSD was extracted from each $\chi(\Delta P)$ curve yielding 100 TSD. Then, the average TSD is computed as the average of the 100 TSD. The comparison was performed for two types of p.d.f.: uniform or Gaussian. The p.d.f. parameters are

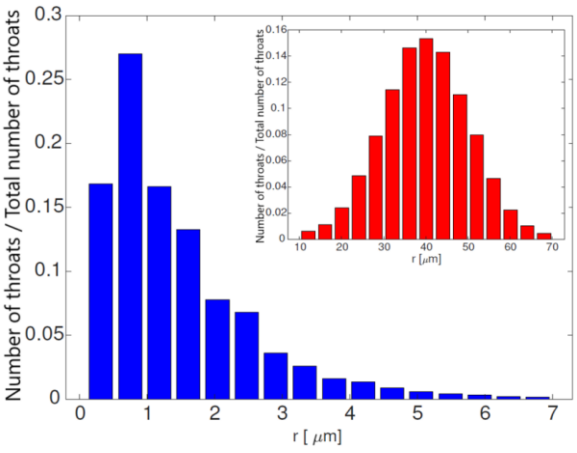
the minimum and maximum radii, r_{min} and r_{max} for a uniform distribution or the mean size and standard deviation, r_{moy} and σ, the throats in the case of a Gaussian p.d.f.. The p.d.f. parameters considered in this section are given in Table 1.

Table 1. PBSD and TSD parameters considered in section 5.

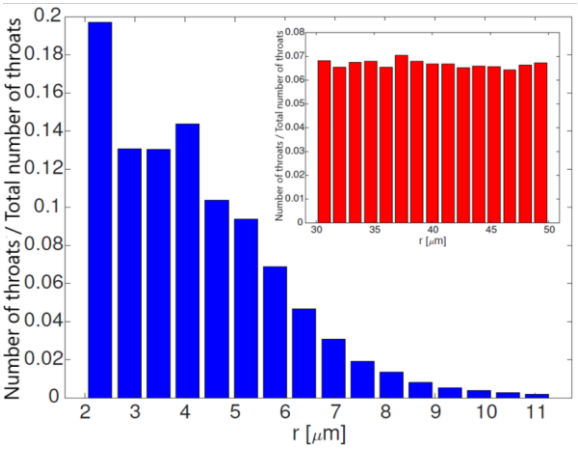
p.d.f	Pore bodies	Throats
uniform	r_{pmax} = 80 μm, r_{pmin} = 120 μm	r_{tmax} = 50 μm, r_{tmin} = 30 μm
Gaussian	r_{pmoy} = 120 μm, σ = 10 μm	r_{tmoy} = 40 μm, σ = 10 μm

The comparison between the reference (or real) TSD and the FFDP TSD for various cases is presented in Figure 5 and Table 2.

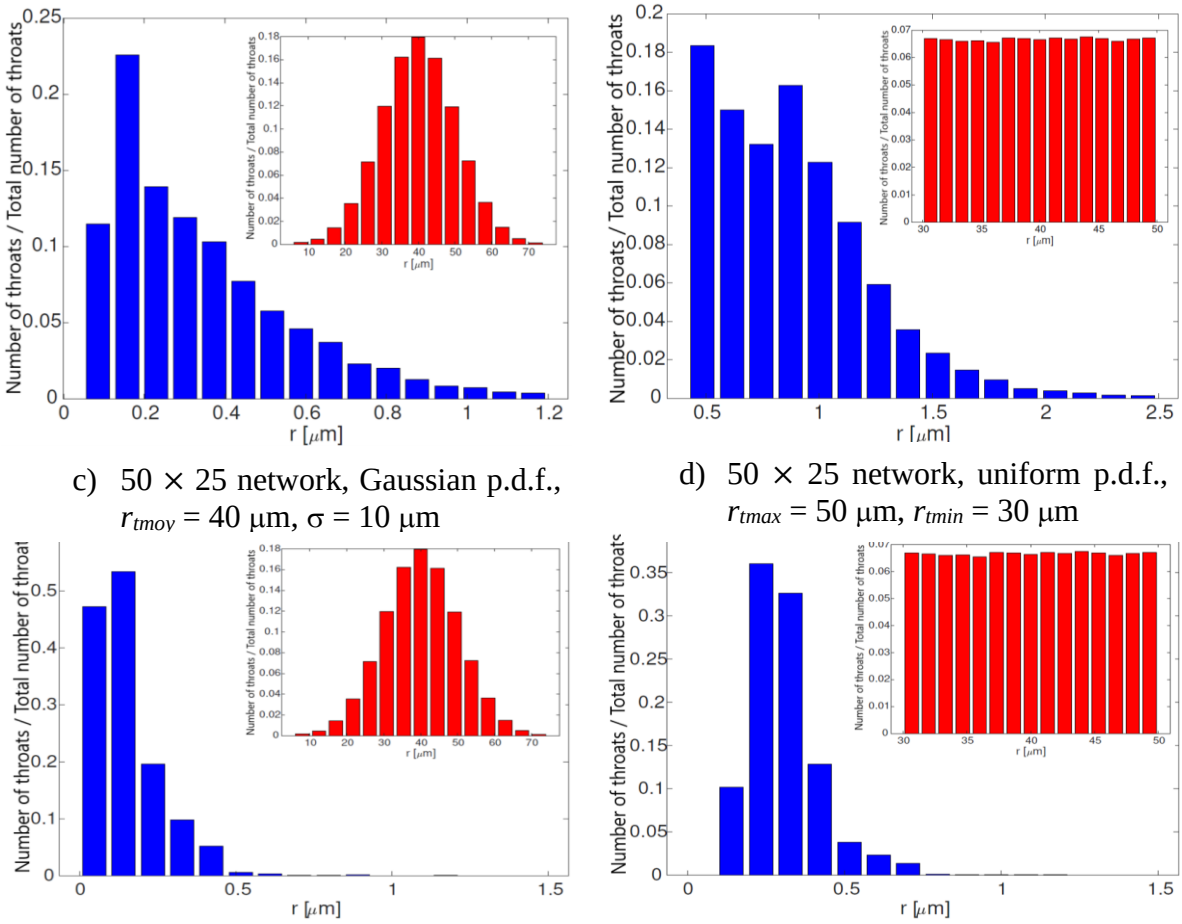
As can be seen, the FFDP TSD is significantly different from the reference TSD for all considered cases. The FFDP procedure introduces a significant positive skewness. In addition to the noticeable asymmetry, it can be seen that the FFDP procedure leads to identify throat sizes smaller than in the real TSD. As reported in Table 2, the errors associated with the parallel cylindrical tube simplification is significant. In summary, the nature of the distribution, uniform or Gaussian, is not retrieved and the identified sizes are too small. The comparison between the results for the two networks in Fig.5 shows that the shift in the distribution toward unrealistic small throat sizes depends on the network width (measured in lattice spacing unit, i.e. in number of elements (pores or throats) over the network width). This is an indication that the commonly used FFDP TSD extraction method should not be used for the characterisation of thick porous systems.



a) 50 × 5 network, Gaussian p.d.f., r_{tmoy} = 40 μm, σ = 10 μm



b) 50 × 5 network, uniform p.d.f., r_{tmax} = 50 μm, r_{tmin} = 30 μm



c) 50 × 25 network, Gaussian p.d.f., r_{tmoy} = 40 μm, σ = 10 μm

d) 50 × 25 network, uniform p.d.f., r_{tmax} = 50 μm, r_{tmin} = 30 μm

d) 30 × 30 network, Gaussian p.d.f., r_{tmoy} = 40 μm, σ = 10 μm

e) 30 × 30 network, uniform p.d.f., r_{tmax} = 50 μm, r_{tmin} = 30 μm

Fig.5. Comparison of the TSD obtained from the commonly used FFDP procedure, Eq.(6), and the real TSD for various cases.

Table 2. Comparison between the reference TSD and the TSD obtained from the commonly used FFDP procedure (Eq.(6)).

			FFDP TSD	
	Statistical Moments (μm)	Real TSD	Obtained TSD	Relative Error (%)
Uniform p.d.f. 50x5 network	Mean	39.95	4.21	89.47
	Standard deviation	5.74	1.67	70.83
	Mean	39.97	1.44	96.41

Gaussian p.d.f. 50x5 network	Standard deviation	10.28	1.1	89.29
Uniform p.d.f. 50x25 network	Mean	40.01	0.88	97.8
	Standard deviation	5.76	0.34	94.1
Gaussian p.d.f. 50x25 network	Mean	40.02	0.34	99.16
	Standard deviation	10.2	0.22	97.82
Uniform p.d.f. 30x30 network	Mean	39.99	0.31	99.23
	Standard deviation	5.75	0.12	97.89
Gaussian p.d.f. 30x30 network	Mean	40.01	0.15	99.62
	Standard deviation	10.29	0.12	98.86

The results presented in Fig.5 and Table 2 are consistent with the fluid distributions and the pressure profiles depicted in Figs. 2 and 3. As discussed previously, the existence of the pressure drop across the network is not consistent with the identification of a single throat size from the Young-Laplace equation contrary to the assumption considered in the commonly used FFDP procedure. In order to fully invade the network, the pressure difference between the two fluids in the outlet region of the network must be comparable (slightly greater) to the throat capillary pressure thresholds. Since the displacing fluid pressure is significantly higher in the network inlet region, using the inlet pressure P_i together with the Young-Laplace equation leads necessarily to underestimate the throat sizes. Since the viscous pressure drop increases with the network width, greater inlet pressures are necessary to fully invade the network when the network width is increased. This is consistent with the increase in the shift toward smaller throat sizes with an increasing network size reported in Fig.5.

6 The FFDP TSD extraction as an inverse optimization problem

6.1 Method of solution

Owing to the serious shortcomings of the commonly used FFDP TSD extraction procedure, the question arises as to whether a better procedure can be devised. As shown in the previous section, the standard and commonly used FFDP TSD extraction procedure does not allow determining the reference TSD from the $Q_i(\Delta P)$ curve. The main reason explaining this unsatisfactory situation lies in the fact that throats of various sizes are invaded when the pressure is incremented due to the displacing fluid pressure variation across the porous medium whereas only a single throat size is assigned via the Young-Laplace equation (2) to all the newly invaded throats with the commonly used FFDP procedure, regardless of their actual sizes. This notably introduces a shift toward (unrealistic) small throat sizes.

In order to improve this situation, the TSD identification problem is addressed as an inverse problem. The direct problem is the determination of the $Q_i(\Delta P)$ curve for a given microstructure. The inverse problem consists in identifying the TSD from the $Q_i(\Delta P)$ curve. In what follows, this inverse problem is studied as an optimization problem. The general idea is to gradually modify the microstructure (more precisely the sizes assigned to the throats for a given network structure) so as to retrieve the $Q_i(\Delta P)$ curve accurately. To this end, a genetic algorithm [5-6] is combined with the hill climbing algorithm [5,7]. The approach is similar to the one presented in [18] where the objective was to identify the TSD from the displacing fluid relative permeability and the retention curve. As in [18], it is assumed that the pore network structure is known. This means that the optimization procedure is performed for a given type of network, i.e. a square network in the present study. Again, the unknown is the TSD. The pore body sizes are not considered in the optimization procedure on the ground that the FFDP flow is essentially controlled by the throats. Thus, the pore size is taken as constant (equal to 80 μm) in what follows. A particular realization of the network, with specified p.d.f. parameters, is used as the reference network which TSD is hence known. This reference network is the equivalent of the porous medium to be characterized in practice, that is the one for which the experimental measurement of $Q_i(\Delta P)$ would have been performed in practice and which TSD is to be determined.

Since the inverse optimization approach is described in [18], only a summary is given below with the adaptations to the problem considered in the present study. A population of individuals is first defined. The individuals are realizations of the pore network. Every individual has genes. A gene in the pore network is a throat characterized by its size. A fitness function, denoted by $fit(\mathbf{r}_t)$, is

introduce in order to compare the $\chi(\Delta P)$ curve obtained by direct simulation for the individuals to the reference one. $\mathbf{r}_t$ is the vector of the individual throat radii. The aim is to minimize the fitness function (defined below by Eq. (13)).

The inverse optimization algorithm can be summarized as follows. A series of N_0 parent realizations ($N_0 = 16$ in this work) is generated using a uniform p.d.f.. This requires specifying the minimum and maximum radii of the distribution. To this end, a quasi-static drainage is performed on the reference network using the classical invasion percolation algorithm [19]. The maximum throat radius, $r_{max\,0}$ is approximately specified by multiplying by a factor 1.3 the radius corresponding to the first pressure step at which the displaced fluid saturation is no longer equal to one. The factor 1.3 is introduced because the biggest throat at the inlet can be expected to be smaller than the biggest throat in the whole network. The minimum throat radius, $r_{min\,0}$, is given by Eq. (2) at the pressure step corresponding to the full invasion of the network.

Individuals are then generated within N_{0b} class intervals. The i^{th} interval has also a uniform p.d.f. with minimum and maximum radii, $r_{min\,i}$ and $r_{max\,i}$ given by $r_{min\,i} = \frac{(N_{0b}+i)r_{min\,0}+(N_{0b}-i)r_{max\,0}}{2N_{0b}}$ and $r_{max\,i} = \frac{(N_{0b}-i)r_{min\,0}+(N_{0b}+i)r_{max\,0}}{2N_{0b}}$ respectively. The number of individuals generated in the i^{th} interval is N_{0i} so that $N_0 = \sum_{i=1}^{N_{0b}} N_{0i}$ with $N_{0b} = 4$ and $N_{0i} = 4$ in the simulations presented below. The normalized FFDP curve, $\chi(\Delta P)$, and the corresponding fitness function, are computed for each parent individual. Then, the main steps of the genetic algorithm are the following:

6. The natural selection is performed by randomly choosing a subset of N_1 individuals in the individuals' generation (with $N_1 = 5$). The two individuals with the best fitness values are selected. Consequently, the generation is reduced by two individuals.
7. Crossover and mutation operators are applied to the two parent individuals. Crossover is the evolutionary operator in which the two selected parent individuals give birth to two child realizations by exchanging randomly throat sizes (genes). Mutation is an evolutionary operation consisting in altering genes (the sizes of randomly chosen throats). Mutation is applied separately to both selected parent realizations. Mutations are generally supposed to be rare. In the present case, the mutation rate is equal to 0.01. In our case this means for instance for a 30 x 30 network that 4 throats are selected randomly in each direction. Then

the size of these 8 throats are specified randomly between r_{min} and r_{max} according to a uniform p.d.f.

8. The $\chi(\Delta P)$ curve and the fitness values are computed for the two children. The two individuals among the four individuals (the two parents and the two children) corresponding to the best fitness values are selected. They are kept to form the new generation.
9. Steps 1 to 3 are repeated until a new generation of N_0 individuals is formed.
10. Steps 1 to 4 are repeated until convergence is reached. Convergence means that the fitness of all the individuals from one generation to the following one does not change by more than about 0.1%.

200 generations (iterations) were typically enough for all the cases studied in this work to reach convergence at which the solution is estimated to be close to the global solution. Then a new step is performed using the hill climbing algorithm.

The genetic algorithm leads to a global solution in the sense that the population of all the individuals is optimized by adjusting their overall genes content. When considering a network of a given TSD type, i.e. uniform, Gaussian, etc, the genetic algorithm, which operates on randomly selected throats, keeps in fact this TSD. A network with a Gaussian TSD, for example, is such that throat radii close to the mean radius are more likely to be selected than others. This limits the population diversity. The objective of the hill climbing algorithm is to gradually modify the throat size p.d.f. within a single individual so as to converge toward the TSD of the reference network. To this end, the hill climbing algorithm is applied to the best fitted individual obtained at the end of the genetic algorithm step. By contrast to the genetic algorithm, the variables that are adjusted are not the throat radii, but the throat fractions. Once the lower and upper bounds of the TSD are specified at the starting point of the optimization process, the distribution can be divided into class intervals, or bins. Then the fraction of throats having a size within the radius interval corresponding to the bin can be determined. The hill climbing algorithm aims at determining the optimal fraction of each bin. In brief, the genetic algorithm is a multi-directional search algorithm operating on radii belonging to different distribution bins, whereas the hill climbing algorithm is an unidirectional algorithm that operates only on radii belonging to a pair of defined bins. Actually, as the sum of all distribution bin fractions must be equal to one, the hill climbing algorithm operates on two bin fractions by increasing one (the positive bin) and decreasing the other (the negative bin) with the

same amount. Two bins of the best fitted individual resulting from the genetic algorithm are randomly chosen. A relatively small randomly chosen number of throats are interchanged between the negative and positive bins. If the fitness function is improved, the modified individual replaces the individual in the population and the hill climbing process is repeated until the fitness function does not improve by more than 0.1%. When it is not improved, another test is performed by randomly choosing a different couple of bins. The fitness function for the hill climbing algorithm is equivalent to the one considered for the genetic algorithm and is denoted by *fit(***f***)* where **f** is the throat fraction vector. The fitness function is presented below.

The direct problem solution provides the FFDP curve, $\chi(\Delta P)$, of the reference network, i.e. the network for which the TSD is to be determined from the FFDP curve. The network is a 2D 30 × 30 square network, with a lattice spacing of 350 μm with a chosen TSD as will be further presented in the results section. The initial N_{0i} individuals (also 2D, 30 × 30 square networks with a lattice spacing of 350 μm) are generated in the N_{0b} class intervals considering a uniform TSD. Their own minimum and maximum radii is determined via the invasion percolation procedure mentioned previously.

The optimization process based on the genetic and hill climbing algorithms is performed for the same pressure steps as for the reference FFDP curve, $\chi_{ref}(\Delta P)$. This implies to solve the direct problem for every individual considered in the optimization process. The TSD at each step of the optimization procedure is compared to the reference one by evaluating the fitness function given by

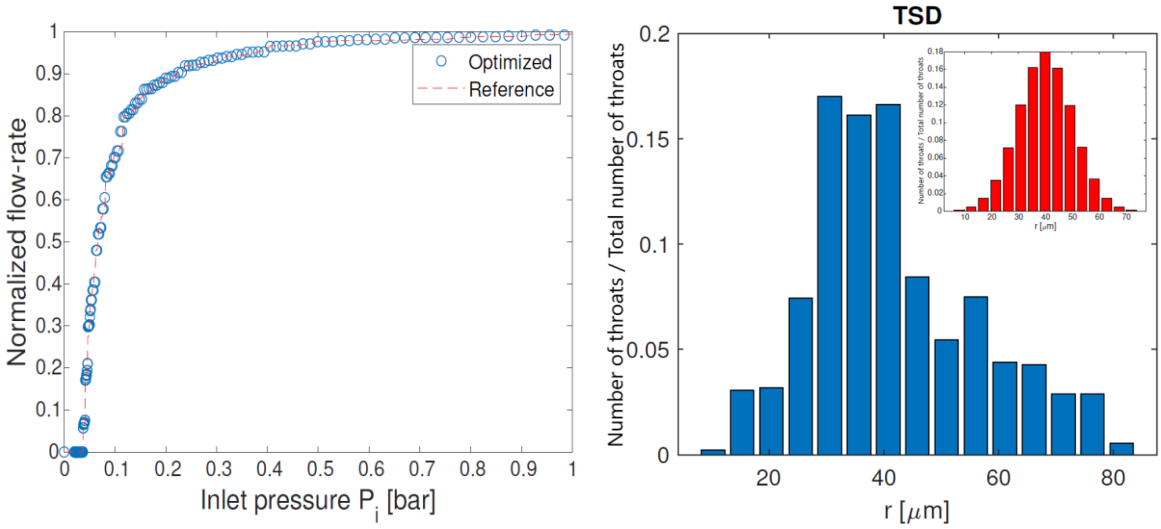
$$fit_{\chi}(\boldsymbol{\omega}) = \sum_{j=1}^{n} \left| \chi_{n-refj} - \chi_{n-indj}(\boldsymbol{\omega}) \right| \qquad \boldsymbol{\omega} = \boldsymbol{r}_t, \boldsymbol{f} \tag{13}$$

where *n* is the total number of pressure steps, χ_{n-refj} and χ_{n-indj} are respectively the reference and individual normalized flow rates (Eq.(12)) corresponding to the j^{th} pressure increment and $\boldsymbol{\omega} = \boldsymbol{r}_t, \boldsymbol{f}$ depending on whether the algorithm is at the genetic or hill climbing stage.

6. 2 Results

A reference network with a Gaussian TSD having a mean radius of 40 μm and a standard deviation of 10 μm is first considered. The corresponding reference TSD is shown in the inset of Fig. 6b.

Note that the initial network population in the optimization process is generated with uniform distributions, thus with a type of p.d.f. different from the Gaussian distribution of the reference network.



a) b)

Fig.6. Results of optimization procedure for a case when the reference p.d.f. is Gaussian: a) FFDP curve for the reference network and the optimized network, b) TSD of the optimized network (the inset shows the reference TSD).

Table 3. Comparison between the reference TSD and the obtained TSD. Case where the reference TSD is the Gaussian TSD depicted in the inset in Fig. 6a.

	Gaussian			uniform		
		Optimized network			Optimized network	
Statistical Moments (μm)	Real TSD	Obtained TSD	Relative Error (%)	Real TSD	Obtained TSD	Relative Error (%)
Mean	42.05	43.65	3.8	41.16	42.8	3.98
Standard deviation	10.2	13.16	33.33	6.08	7.19	18.25
Skewness	-0.22	0.41	-	-0.6	-0.34	-
Kurtosis	2.71	2.95	8.86	1.81	1.71	5.44

As shown in Fig.6a, the optimization procedure leads to an almost perfect agreement between the reference $\chi(\Delta P)$ curve and the corresponding curve for the optimized network. Compared to the commonly used FFDP procedure (Fig.5), the identified TSD is much closer to the reference (real) TSD. There is no shift toward unrealistic small throat sizes and the distribution is much closer to a Gaussian distribution. However, one can note a slight positive skewness. The values for the first four moments of the distribution reported in Table 3 are also in much better agreement with the corresponding values of the real TSD (as can be seen from the comparison with the values reported in Table 2 obtained for the commonly used FFDP procedure).

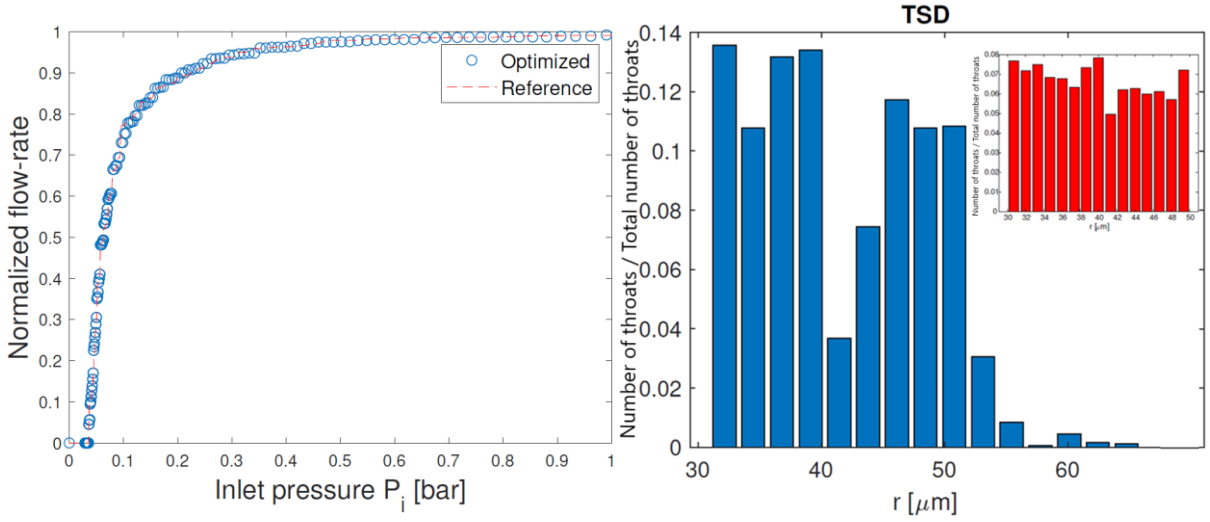


Fig.7. Results of optimization procedure for a case when the reference p.d.f. is uniform: a) FFDP curve for the reference network and the optimized network, b) TSD of the optimized network (the inset shows the reference TSD).

As reported in Fig.7 and Table 3, somewhat similar results are obtained when the reference p.d.f. is uniform. In both cases, it can be seen that a few throat sizes greater than the largest throat size in the real distribution are obtained through the optimization procedure. This is due to the specification of the maximum throat size with the factor 1.3 indicated in the previous sub-section. Nevertheless, the fraction of throat sizes in this too large range is quite low. This is an indication that the optimization procedure should lead to still better results with a more refined estimate of the maximum throat radius (via smaller pressure steps for example).

7 TSD extraction combining FFDP and retention curve

7.1 Method of solution

It was shown in [18] that the inversion optimization procedure considering the displacing fluid relative permeability and the retention curve led to better results than when only the displacing fluid relative permeability was considered. Thus, one can wonder whether considering the retention curve in addition to the FFDP curve could improve the TSD identification. The retention curve corresponds to a series of capillary quasi-static equilibria within the porous medium and is a classical characterization of a porous medium, also for the thin porous media of special interest for the present study, e.g. [20]. However, this implies in practice to perform an additional experiment since the FFDP devices are typically not adapted to measure the retention curve. Examples of specific measurement devices adapted to thin porous media are described for instance in [20-21]. To obtain the drainage retention curve, the procedure is somewhat similar to the FFDP procedure. The porous medium is initially saturated by a wetting fluid. Then a non-wetting fluid is injected through a series of pressure steps. An important difference compared to the FFDP devices is the presence of a porous membrane with smaller pores than in the medium of interest at the outlet preventing the non-wetting fluid to exit the porous medium. Thus, contrary to the FFDP, there is no displacing fluid flow in the porous medium when an equilibrium is reached. An important difference lies also in the fluid-fluid distribution. In the case of the retention curve, the fluid-fluid distributions are quasi-static, that is only controlled by capillary effects. By contrast, as illustrated in Fig.2, the fluid-fluid distributions are affected by the viscous pressure drop in the displacing fluid in the case of the FFDP. The retention curve is the plot of the pressure difference, $P_c = P_{nw} - P_w$, between the two fluids as a function of the wetting fluid saturation, S, where P_{nw} is the pressure in the non-wetting fluid and P_w is the pressure in the wetting fluid. S is the volume fraction of the pore space occupied by the wetting fluid. It should be clear that the wetting fluid (the non-wetting fluid respectively) corresponds to the displacing fluid (the displaced fluid respectively) in the FFDP. The couple of fluids is, however, not necessarily the same in the FFDP and the retention curve measurement since two separate measurement devices are used. In what follows, it is therefore assumed that both the FFDP curve, $\chi(\Delta P)$, and the retention curve, $P_c(S)$, were measured. For the present study, this means that the curve $P_c(S)$ can be computed for the reference network as well as for all the networks generated during the optimization procedures. The algorithm for

computing the retention curve in a network is described in [18] and therefore is not described here again. The optimization procedure is completely analogous to the one described in Section 6.1. The only difference lies in the fitness function since now both the retention curve and the FFDP flow rate curve are considered. The fitness function now reads

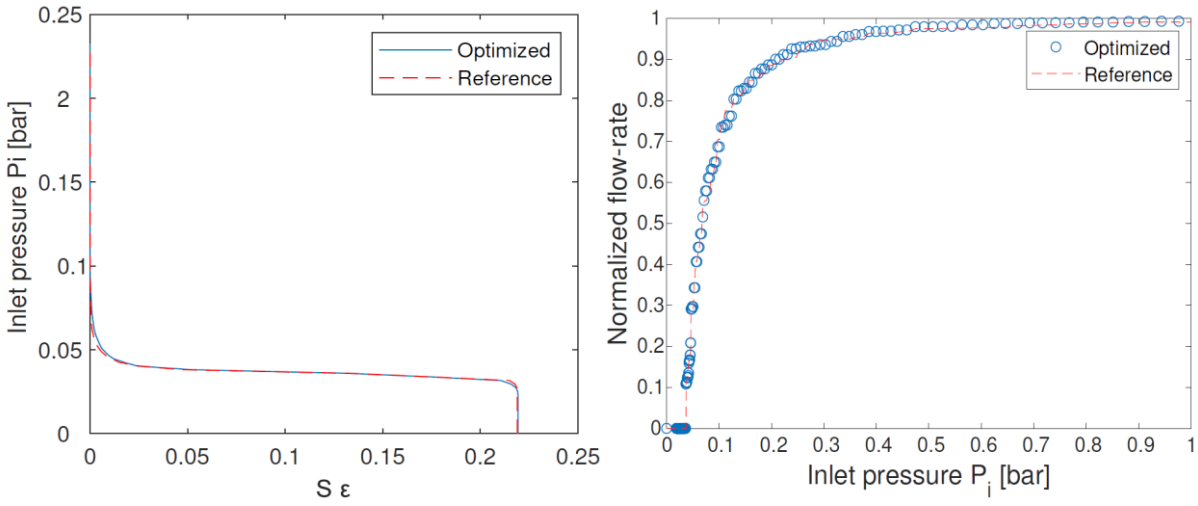
$$fit_{\chi-P_c}(\boldsymbol{\omega}) = \sum_{j=1}^{n}\left|\chi_{n-refj} - \chi_{n-indj}(\boldsymbol{\omega})\right| + f_p \sum_{j=1}^{n}\left|S_{refj}\varepsilon_{ref} - S_{indj}\varepsilon_{ind}(\boldsymbol{\omega})\right| \quad \boldsymbol{\omega} = \boldsymbol{r}_t, \boldsymbol{f} \tag{14}$$

where f_p is a penalization factor taken equal to $1/\varepsilon_{ref}$, where ε_{ref} is the porosity of the reference network.

7.2 Results

As can be seen from the comparison between Fig.6 and Fig. 8, using both the retention and FFDP curves in the optimization process leads to significantly better results. This is also confirmed by the results reported in Table 4. It can be also noted in Fig. 8 that the retention and FFDP curves resulting from the optimization procedure reproduce very well the corresponding curves of the reference case. As shown in [18], it is of course possible to develop the inverse optimization procedure using only the retention curve. The used fitness function is given in [18]. For completeness, the results obtained when only the retention curve is used are also indicated in Table 4. As can be seen, the results when only the retention curve is used are slightly better than when only the FFDP curve is used. However, the best results are obtained when both the retention curve and the FFDP curve are used.

Fig.9 and Table 5 present the results obtained for the case of the uniform distribution depicted in the inset of Fig.9b. Here again, significantly better results (compare Fig.7 and Fig.9) are obtained when the FFDP curve is used in conjunction with the retention curve in the optimization process. However, the results for the uniform distribution can be judged as slightly less good than for the Gaussian distribution. In particular, it can be noticed that the procedure leads to identify a few throat sizes greater than the greatest throat size in the reference distribution. Again, this is attributed to the procedure used to estimate the distribution maximum radius from the invasion percolation procedure with the factor 1.3 (as described in section 6.1).



a) b

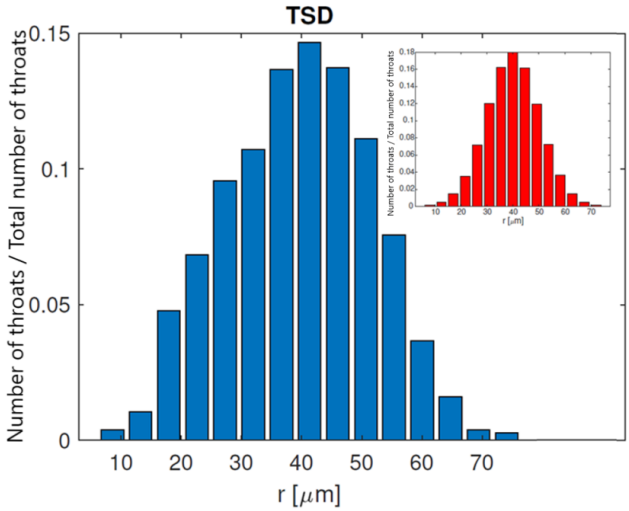


Fig.8. Results of optimization procedure when both the FFDD and the retention curves are used for a case where the reference p.d.f. is Gaussian (the mean radius and standard deviation are respectively equal to 40 μm and 10 μm): a) FFDP curve and retention curve for the reference network and the optimized network, b) TSD of the optimized network (the inset shows the reference TSD) .

Table 4. Comparison between the reference TSD and the obtained TSD. Case where the reference TSD is the Gaussian TSD depicted in the inset of Fig.8b.

		P_c only		$FFDP$ only		both $FDDP$ and P_c	
Statistical Moments (μm)	Real TSD	Obtained TSD	Relative Error (%)	Obtained TSD	Relative Error (%)	Obtained TSD	Relative Error (%)
Mean	42.05	41.11	2.3	43.65	3.8	41.96	0.21
Standard deviation	10.2	10.3	0.9	13.16	33.33	10.14	0.59
Skewness	-0.22	-0.42	-	0.41	-	-0.36	-
Kurtosis	2.71	2.93	7.66	2.95	8.86	2.86	5.54

Table 5. Comparison between the reference TSD and the obtained TSD. Case where the reference TSD is the uniform TSD depicted in the inset in Fig. 9b.

		P_c only		$FFDP$ only		both $FFDP$ and P_c	
Statistical Moments (μm)	Real TSD	Obtained TSD	Relative Error (%)	Obtained TSD	Relative Error (%)	Obtained TSD	Relative Error (%)
Mean	41.16	41.25	0.21	42.8	3.98	40.96	0.49
Standard deviation	6.08	6.14	1.01	7.19	18.25	5.85	3.78
Skewness	-0.6	-0.04	-	-0.34	-	-0.49	-
Kurtosis	1.81	2.9	60.17	1.71	5.44	2.6	43.65

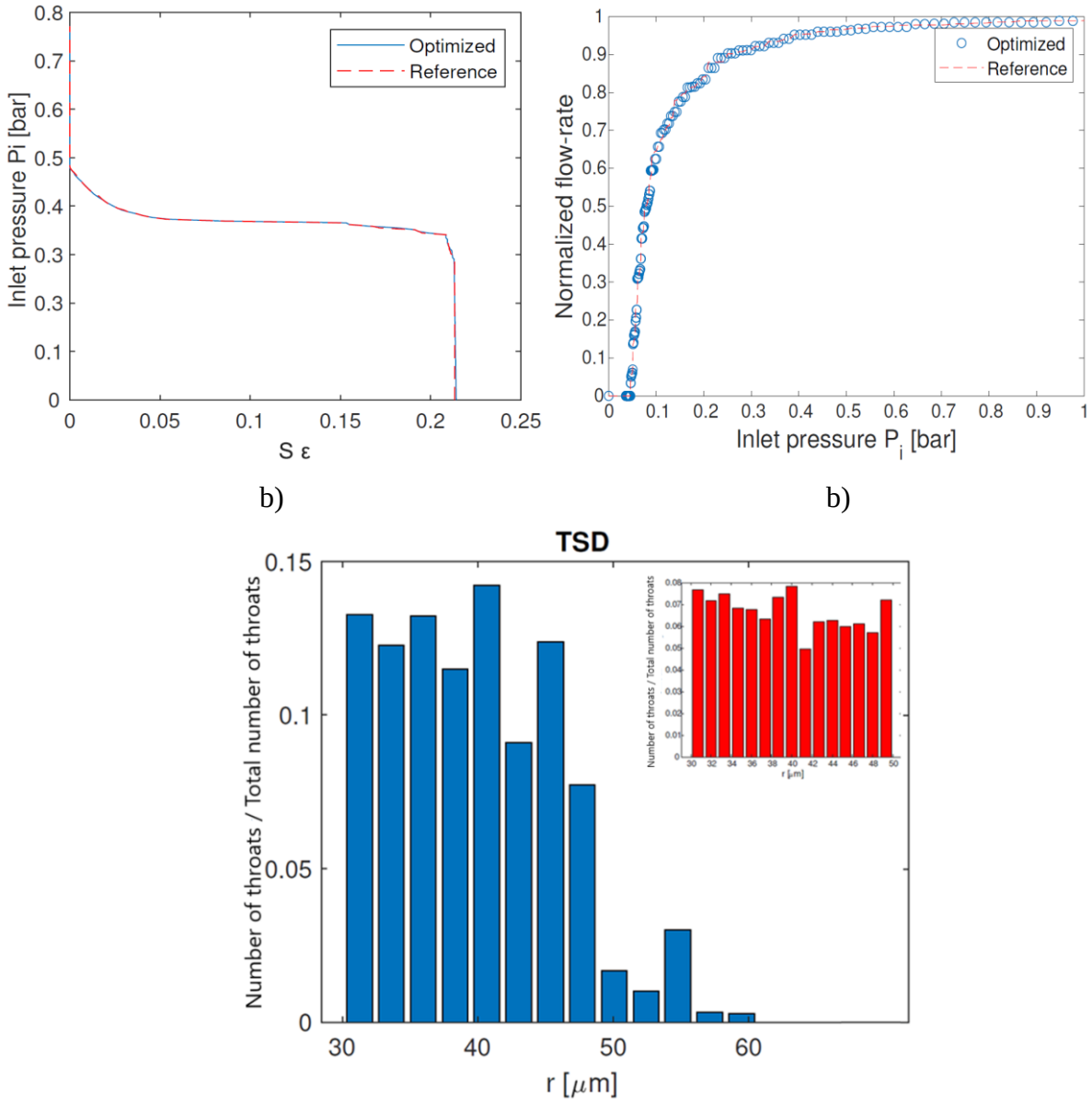


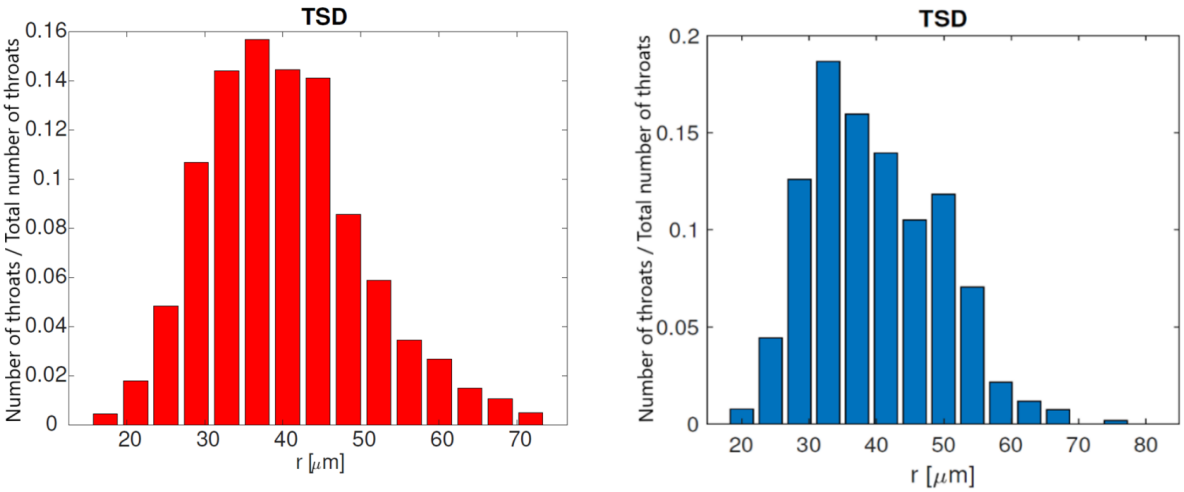
Fig.9. Results of optimization procedure when both the FFDD and the retention curves are used for a case where the reference p.d.f. is uniform (the maximum and minimum radius are respectively 50 μm and 30 μm): a) FFDP curve and retention curve for the reference network and the optimized network, b) TSD of the optimized network (the inset shows the reference TSD).

Nevertheless, to further illustrate the capabilities of the inverse optimization procedure as it is, two additional tests were performed considering a reference log-normal distribution (as depicted in Fig. 10a) and the expected more challenging bimodal distribution depicted in Fig. 11a. For these cases, only the full optimization procedure, i.e. the one combining both the $P_c(S)$ and $\chi(\Delta P)$ curves

was used. As can be seen from Figs. 10 and 11 and Table 6, results are quite satisfactory. Here also, the match between the reference capillary pressure and FFDP curves and the curves resulting from the optimization procedure is excellent (not shown). Finally, from the four reference tested TSD, the less good results were obtained for the uniform TSD, mainly because of the uncertainty associated with the distribution upper bound radius specification.

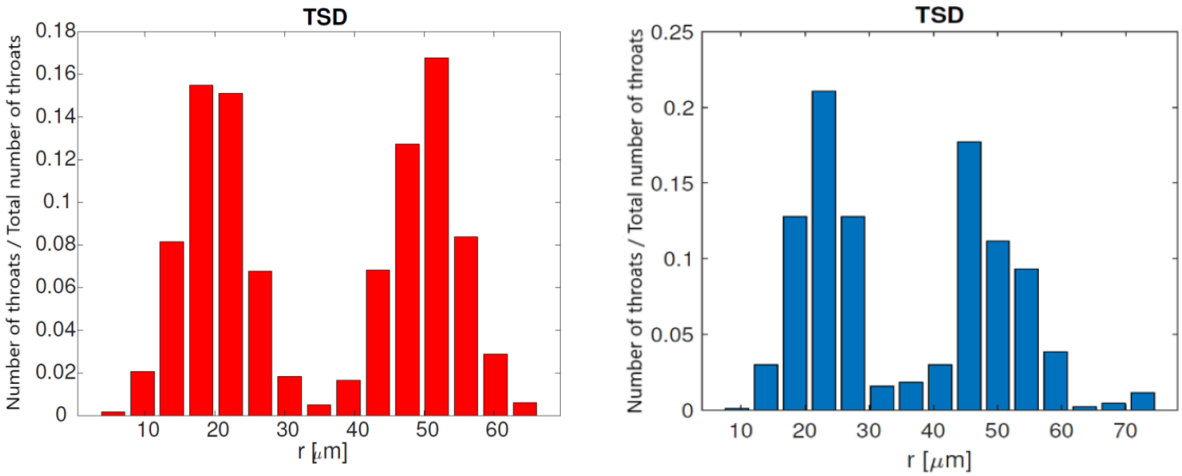
Table 6. Comparison between the reference TSD and the obtained TSD using both the capillary pressure and FFDP curves as target data. Cases where the reference TSD is the Log-normal TSD depicted in Fig. 10a or the bimodal TSD depicted in Fig.11a.

	Log-normal TSD			Bimodal TSD		
Statistical Moments (μm)	Real TSD	Obtained TSD	Relative Error (%)	Real TSD	Obtained TSD	Relative Error (%)
Mean	40.84	41.38	1.31	36.16	36.23	0.19
Standard deviation	9.33	10.01	7.25	16.06	14.63	8.92
Skewness	0.05	0.08	-	-0.22	0.11	-
Kurtosis	2.62	2.73	4.13	1.37	1.69	23.33



a) b)

Fig.10. Reference Log-normal TSD (a) for a 30 × 30 square network and TSD obtained from the optimization procedure using both the FFDP and capillary pressure curves as target data



a) b)

Fig.11. Reference bimodal TSD (a) (for a 30 × 30 square network) and TSD obtained from the optimization procedure using both the FFDP and capillary pressure curves as target data (b).

8 Discussion

The TSD identification based on the optimization procedure clearly leads to much better results than the conventional FFDP approach. However, several simplifications were introduced: trapping phenomena were ignored, a square network of identical size was considered for the reference network and the networks generated in the optimization procedure considering only the throat size distributions as the distribution to be identified (the pore size variability was neglected). These simplifications are discussed in [18] and therefore the corresponding discussion is not repeated here. Here, the focus is on the FFDP, which was not considered in [18], where it is recalled that the retention curve and the displacing fluid relative permeability were considered as input data for the optimization procedure. It was concluded in [18] that the combined used of the retention and relative permeability curves led to better results than the use of the relative permeability curve alone. Similarly, the combined use of the retention and FFDP curves led to the best results for all the distributions tested.

The combined use of the retention curve and FFDP curves is thus recommended. For the TSD identification of thin porous media with throats in the micronic range, such as the diffusion medium used in fuel cells for example [20-22], obtaining both curves should not be a problem. For thin

nanoporous media, the combined approach could be more difficult to use because the retention curve can be difficult to measure. In practice, the retention curve measurement implies to place a porous membrane at the outlet of the porous medium of interest. The pores in the outlet membrane must be smaller than the pores in the porous medium to be characterized in order to prevent the non-wetting fluid to exit the porous medium. It can be difficult to find a membrane with the required pore size when the pores in the porous medium of interest are in the nanoporous range. This problem is not encountered with the FFDP technique. Also, the FFDP technique can be performed using a pair of immiscible liquids with a relatively low interfacial tension so as to generate the displacement with reasonably low-pressure differences even with nano-pores. Thus, in this case, the FFDP technique combined with the optimization procedure is an interesting option to characterize the TSD.

However, the optimization procedure is significantly more complex than the commonly used FFDP TSD extraction method based on the parallel tube model. An alternative might be to try to introduce analytical corrections to the bias revealed by the simulations. This could be the subject of a future work.

9 Conclusion

Pore network simulations were developed in order to evaluate the fluid-fluid displacement porosimetry (FFDP) technique. It was suggested that two types of microstructure elements, namely pore bodies and pore throats, must be distinguished in the pore space. It was argued that the distribution commonly obtained with the FFDP technique was the throat size distribution (TSD) rather than the pore body size distribution (PBSD). The simulations indicate that the commonly used FFDP procedure for identifying the TSD from the FFDP curve introduces a bias toward unrealistic small sizes. The wider the porous medium, the greater is the bias. In practice, this means that the results obtained with the commonly used FFDP procedure should not be regarded as really representative of the real TSD when the pore space structure is significantly different from a system of straight non-interconnected quasi-cylindrical pores.

A significantly more sophisticated procedure combining pore network simulations of the immiscible displacement and an optimization technique based on the combination of a genetic algorithm and the hill climbing algorithm was then tested to improve the TSD identification from the FFDP raw data. This procedure leads to much better results than the usual FFDP procedure and

allows eliminating the bias toward unrealistic small throats. Furthermore, it was shown that the TSD identification could be still improved by considering the retention curve in addition to the FFDP curve in the optimization procedure.

However, the optimization procedure is significantly less simple that the commonly used FFDP procedure. The commonly used procedure is analytical whereas the optimization procedure implies repeated numerical simulations of the immiscible displacements in the pore space. Also, several simplifications were introduced to test the optimization procedure. In particular, identical network structure and size were considered in the reference network and the various networks generated during the optimization procedure. The variability in the pore size was neglected, considering only the throat size variability. Owing to these simplifications, solving the problem consisting in identifying the TSD (and the PBSD) from macroscopic data such as the FFDP and capillary pressure curves clearly requires further work. Nevertheless, it is our belief that the results obtained in the present study are an encouraging step.

Acknowledgements

This research was supported by the Project "PEMFC – SUDOE" – SOE1/P1/E0293 which is co-financed by the European Regional Development Fund in the framework of the Interreg Sudoe programme.

References

1. K.R. Morison, A comparison of liquid-liquid porosimetry equations for evaluation of pore size distribution, Journal of Membrane Science, 325, 301-310 (2008).
2. R.I. Peinador, J.I. Calvo, P. Prádanos, L. Palacio, A. Hernández, Characterization of polymeric UF membranes by liquid-liquid displacement porosimetry, Journal of Membrane Science, 348, 238-244 (2010).
3. J. I Calvo, R. I. Peinador, P. Prádanos, A. Bottino, A. Comite, R. Firpo, A. Hernández, Porosimetric characterization of polysulfone ultrafiltration membranes by image analysis and liquid–liquid displacement technique, Desalination, 357, 84-92 (2015).
4. M. B. Tanis-Kanbur, R.I. Peinador, X. Hu, J. I. Calvo, J. W. Chew, Membrane characterization via evapoporometry (EP) and liquid-liquid displacement porosimetry (LLDP) techniques, Journal of Membrane Science, 586, 248-258 (2019).

5. Skiena, Steven (2010). The Algorithm Design Manual (2nd ed.). Springer Science+Business Media.

6. E. Unsal, J. H. Dane, and G. V. Dozier, A genetic algorithm for predicting pore geometry based on air permeability measurements, Vadose Zone Journal, 4, 389-397 (2005).

7. S.C. Su, C.J. Lin and C.K. Ting, An effective hybrid of hill climbing and genetic algorithm for 2D triangular protein structure prediction, Proteome Science, 9, S19 (2011).

8. M.J. Blunt, M.D. Jackson, M. Piri, P.H. Valvatne, Detailed physics, predictive capabilities and macroscopic consequences for pore-network models of multiphase flow, Advances in Water Resources, 25 (8-12), 1069-1089 (2002).

9. Q. Xiong, T. G. Baychev, A. P. Jivkov, Review of pore network modelling of porous media: Experimental characterizations, network constructions and applications to reactive transport, Journal of Contaminant Hydrology, 192, 101-117 (2016).

10. I. Bondino, G. Hamon, W. Kallel, D. Kachuma: Relative permeabilities from simulation in 3D rock models and equivalent pore networks: critical review and way forward. Petrophysics 54(6), 538-46 (2013).

11. T. Agaesse, A. Lamibrac, F. Buechi, J. Pauchet, M. Prat, Validation of pore network simulations of ex-situ water distributions in a gas diffusion layer of proton exchange membrane fuel cells with X-ray tomographic images, Journal of Power Sources, 331, 462-474 (2016).

12. A.Q Raeini, B. Bijeljic, M.J Blunt, Generalized network modeling: network extraction as a coarse-scale discretization of the void space of porous media. Physical Review E, 96, 013312 (2017).

13. M.J. Blunt, Flow in porous media-pore-network models and multiphase flow, Current Opinion in Colloid & Interface Science, 6, 197-207 (2001).

14. R Lenormand, E Touboul, C Zarcone, Numerical models and experiments on immiscible displacements in porous media, Journal of fluid mechanics, 189, 165-187 (1988).

15. D. Zhou, M. Blunt, F.M. Orr Jr, Hydrocarbon drainage along corners of noncircular capillaries, Journal of Colloid and Interface Science, 187, 11-21 (1997).

16. V. Joekar-Niasar, S.M. Hassanizadeh and A. Leijnse, Insights into the relationships among capillary pressure, saturation, interfacial area and relative permeability using pore-network modelling, Transport in Porous Media, 74, 201-219 (2008).

17. F.A.L. Dullien Porous Media: Fluid Transport and Pore Structure, Academic Press 1991.

18. O. Maalal, M. Prat, R. Peinador, D. Lasseux, Determination of the throat size distribution of a porous medium as an inverse optimization problem combining pore network modeling and genetic and hill climbing algorithms. submitted to …

19. D. Wilkinson and J.F. Willemsen, Invasion percolation: a new form of percolation theory, Journal of Physics A: Mathematical and General, 16, 3365-3376 (1983).

20. J.D. Fairweather, P. Cheung, D.T. Schwartz, The effects of wetproofing on the capillary properties of proton exchange membrane fuel cell gas diffusion layers, Journal of Power Sources, 195, 787-793 (2010).

21. J. T. Gostick, M. A. Ioannidis, M. W.Fowler, M. D.Pritzker, Direct measurement of the capillary pressure characteristics of water–air–gas diffusion layer systems for PEM fuel cell, Electrochemistry Communications, 10, Issue 10, 1520-1523 (2008).

22. S. Park, J-W. Lee, B.N. Popov, A review of gas diffusion layer in PEM fuel cells: materials and designs. International Journal of Hydrogen Energy, 37, 5850–5865 (2012).

Pore network model of drying with kelvin effect

Otman Maalal[a,b], Marc Prat[a*], Didier Lasseux[c]

[a]Institut de Mécanique des Fluides de Toulouse (IMFT), Université de Toulouse, CNRS, Toulouse, France.

[b]Institut de La Filtration et des Techniques Séparatives (IFTS), Rue Marcel Pagnol, 47510, Foulayronnes, France

[c]I2M, UMR 5295, CNRS, Univ. Bordeaux – Esplanade des Arts et Métiers, 33405 Talence, CEDEX, France

[*] *Corresponding author:mprat@imft.fr (+33534322883)*

Abstract

A pore network model of isothermal drying is presented. The model takes into account the capillary effects, the transport of vapour by diffusion, including Knudsen effect, in the gas phase and the Kelvin effect. The model allows the simulation of drying in hygroscopic porous materials involving submicronic pores. The impact of Kelvin effect on the drying process is investigated, varying the relative humidity in the ambient air outside the medium. The simulations indicate that the Kelvin effect has a significant impact on the liquid distribution during drying. The evaporation rate is found to fluctuate due to the menisci curvature variations during drying. The simulations also highlight a noticeable non-local equilibrium effect.

Key words: Drying; Pore network model; Kelvin effect

1. Introduction

Pore network modelling (PNM) is now a classical technique to study transport phenomena in porous media. The technique has been applied to drying problems since the early 90's (see *e.g.*, (Prat 1993) and references therein). The first model of this type (Prat 1993), only took into account the vapour transport by diffusion in the gas phase, together with the capillary effects. Since then, many effects have been included in drying PNM and this is reviewed in (Prat 2011) and (Metzger 2019). However, to the best of our knowledge, all the PNM reported so far have been applied to capillary porous media characterized by pore sizes greater than 100 nm - 1 μm. This pore size range is characteristic of hygroscopic materials for which drying PNM is still lacking. The objective of the present article is therefore to contribute to filling this gap. A crucial difference between hygroscopic and capillary materials lies in the importance of adsorption phenomena. The fraction of the pore space volume that can be filled by liquid due to adsorption and/or capillary condensation of vapour (Adamson 1990) is significant in hygroscopic materials whereas this fraction is extremely small in capillary materials. This is related to the pore sizes, typically greater than 100 nm - 1μm in capillary materials, but rather less than 100 nm in purely hygroscopic materials. As a first step toward the detailed simulation of drying in hygroscopic materials, a PNM, taking into account the Kelvin effect, is presented in what follows. The Kelvin effect refers to the modification of the equilibrium vapour pressure, $P_{vequ.}$, due to the curvature of liquid-gas interfaces and can be computed from the Kelvin relationship which takes the following expression

$$RH_{equ.} = \frac{P_{vequ.}}{P_{vs}} = \exp\left(-\frac{M_v}{RT}\frac{2\gamma cos\theta}{\rho_\ell r}\right) \quad (1)$$

Here, P_{vs} is the saturation vapour pressure corresponding to a flat liquid – vapour interface, M_v is the vapour molecular weight, R the universal gas constant, T the temperature (assumed equal to 293K throughout the paper), γ is the surface tension, θ the contact angle, ρ_ℓ the liquid density; r is the radius of curvature of the liquid –gas interface considered as a spherical cap at the entrance of a cylindrical pore. The relationship expressed in Eq. (1) is classically used for modelling vapour capillary condensation (Adamson 1990).

As illustrated in Fig.1 representing $RH_{equ.}$ versus $d = 2r$ for water and $\theta = 0$, the Kelvin effect is only important for pore sizes smaller than 100 nm, and more specifically for diameters smaller than

about 20nm. Pore sizes in this range correspond to a very important class of materials, such as concrete, clay rocks, ultrafiltration membranes or catalyst layers of PEM fuel cells to only cite a few. For pore diameters larger than 100 nm, the effect becomes gradually negligible and the equilibrium vapor pressure is nearly equal to the saturation vapor pressure. However, the lower bound of applicability of the Kelvin relationship in terms of the pore diameter remains uncertain. A minimum diameter of 4 nm is often considered (see for instance (Takei et al. 1997)) and accuracy of Eq. (1) may be questionable below this value. In the remainder of this work, pore diameters larger than 4 nm will hence be considered in the simulations.

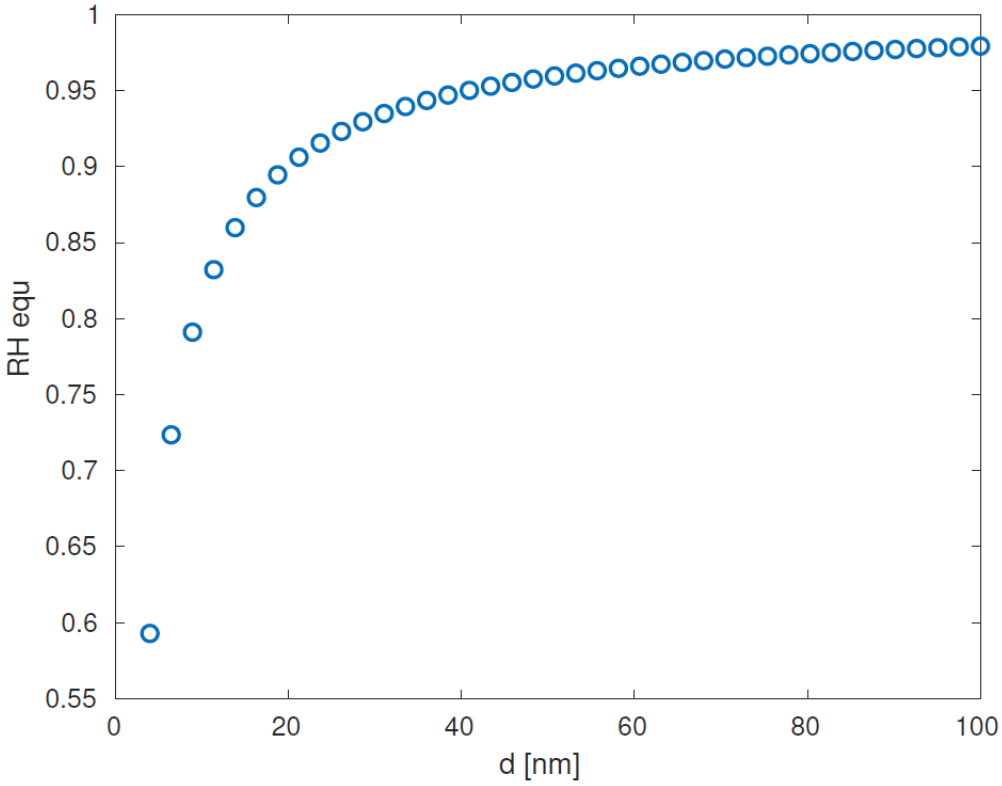


Fig.1. Variation of water activity (equilibrium relative humidity $RH_{equ.}$) as a function of pore equivalent diameter according to Kelvin relationship assuming $\theta = 0$ and a meniscus at maximum curvature at the pore entrance of diameter $d=2r$.

The development of drying PNM including Kelvin effect pertinent for material featuring pores in the above mentioned range of diameters is proposed in this article which is organized as follows. The main assumptions are presented in Section 2 while the pore network structure is briefly

discussed in Section 3. The drying PNM algorithm with Kelvin effect is presented in Section 4. Simulation are reported and discussed in Section 5. Section 6 is dedicated to a summary and conclusion of the analysis and some possible future works are presented.

2. Main assumptions

Throughout this work, the following assumptions are made regarding the drying process under consideration:

- the network is non-deformable;
- thermal effects are neglected on the ground that only slow drying is considered;
- the pressure in the gas phase remains uniform and constant, equal to the atmospheric pressure. This is also because only slow drying processes are considered;
- gravity effects are neglected. As a consequence of the range of pore size under concern, body forces can be expected to be negligible compared to viscous and/or capillary effects.
- the liquid is a perfectly wetting fluid ($\theta=0$);
- liquid films are neglected. These include the thick capillary films, (see *e.g.*, Yiotis *et al.* 2012; Chauvet *et al.* 2009; Prat 2007), as well as the thin films resulting from the attractive forces between the liquid molecules and the pore walls (Carey 1992).

To summarize, phenomena taken into account are vapour diffusion, including Knudsen effect, in the gas phase, capillary effects and the Kelvin effect.

3. Pore network model

While using PNM, two types of pore networks can be usually distinguished, namely structured and unstructured networks (Joekar et al. 2010). For simplicity, and as in most previous works on drying PNM, a structured model is considered here. It is made of a square network in 2D as depicted in Fig.2.

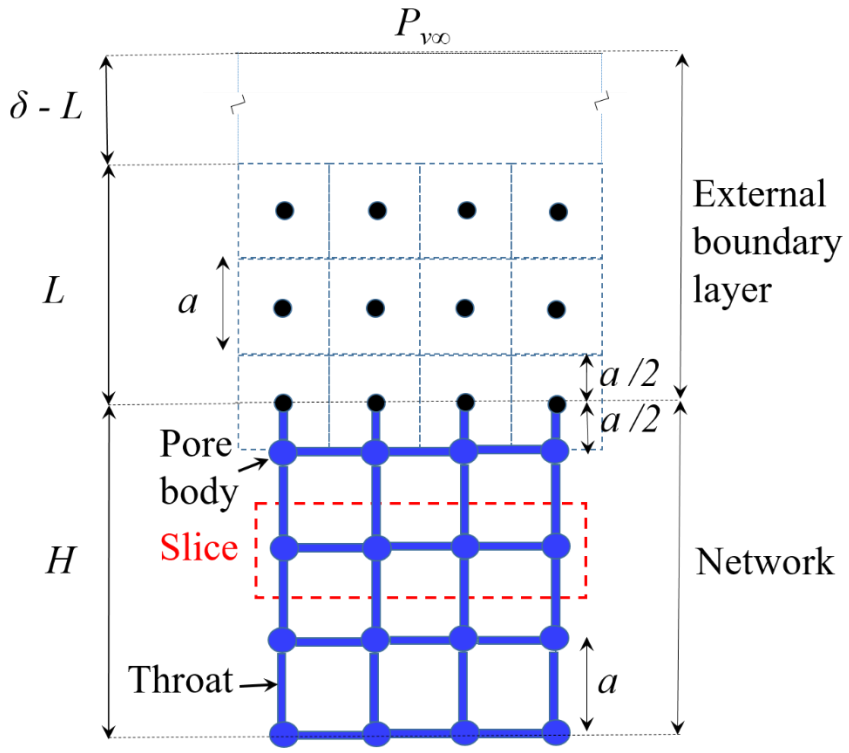


Fig.2 Square pore network. The red dashed box corresponds to an exemplary network slice used for spatially averaging the PNM simulation data. Black dots correspond to computational nodes in the sub-layer of the external boundary layer.

In this type of model, the pore space is conceptualized as a network of pore bodies located at the nodes (sites) of the network connected by smaller channels, or throats, corresponding to the constrictions between pore bodies. These channels correspond to the network bonds. Different options have been considered to distribute the pore space between the pore bodies (sites) and the channels (bonds). For instance, Metzger *et al.* (2007a) considered volumeless pore bodies, the pore space volume being only within the bonds. Alternatively, Prat (1993) distributed the pore space volume between pore bodies and bonds, whereas (Yiotis *et al.* 2001) considered volumeless throats (bonds), the pore space volume being only present in the pore bodies. In what follows, volumes are assigned to both throats and pore bodies as in (Prat 1993).

Spherical pore bodies of diameters d_p are placed at the network nodes. The lattice spacing, *i.e.*, the distance between two neighbouring pore bodies, is denoted by a. In the present work, this parameter is kept constant and is set to a = 300 nm. The pore body diameter is randomly distributed according

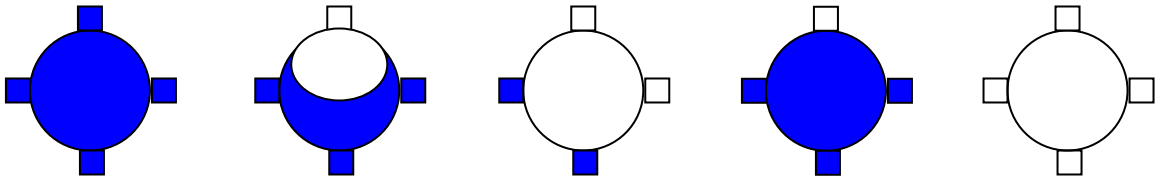
to a given probability density function (p.d.f.) in the range [d_{pmin}, d_{pmax}]. Bonds are cylindrical channels characterized by their diameter d_t, which is also randomly distributed according to a given p.d.f. in the range [d_{tmin}, d_{tmax}] with the constraint that the size of a bond is smaller than the smallest size of adjacent pore bodies. In the present analysis, uniform p.d.f. are considered. The pore body (the throat respectively) size distribution is referred to as the PSD (the TSD respectively).

4. Drying algorithm

The drying PNM presented in what follows can be seen as an extension of the model proposed earlier (Prat 1993). A key feature of the model is the full consideration of the fact that many liquid clusters can form during the drying process. This model is summarized below. The new features introduced for the present study are described afterwards.

At a given time during drying, a pore body or a throat can be either partially or fully invaded by the gas phase. As sketched in Fig.3, one can distinguish five situations regarding the pore bodies (or throats):

- pore bodies of type L, fully filled by liquid. All the four adjacent bonds are also saturated by the liquid phase;
- pore bodies of type PI, *i.e.*, partially invaded by the gas phase. Pore bodies PI contain a liquid/gas interface and are connected to only one gas saturated adjacent bond;
- pore bodies of type CI, *i.e.*, completely invaded, correspond to pore bodies containing gas only but connected to at least one liquid adjacent bond;
- pore bodies of type IF, *i.e.*, interfacial pore bodies, correspond to pore bodies containing liquid only but connected to only one gas saturated adjacent bond. In a cluster, only one IF pore body may exist. However, IF bonds may be multiple in a cluster;
- pore bodies of type G, containing only gas and with all connected gas filled adjacent bonds.



pore body L pore body PI pore body CI pore body IF pore body G

Fig.3. Sketch of various pore body types considered in the PNM (liquid in blue, gas in white).

The drying algorithm can be summarized as follows.

(1) Each liquid cluster in the network is identified and a label is attributed to them. This label is also given to each pore body and throat belonging to the cluster under consideration. This task is performed using the deep-search algorithm (see *e.g.*, Babalievski 1998).

(2) For clusters which include a PI pore body or throat, this pore body or throat is directly selected as the one to be invaded for this cluster. For the other clusters, the IF pore body or the IF bond of smallest capillary pressure threshold is identified. The capillary pressure threshold of a bond of diameter d_t is expressed according to Laplace's law as

$$p_{cap} \approx \frac{4\gamma \cos\theta}{d_t} \tag{2}$$

Thus, p_{cap} is the minimum pressure difference between the two fluids allowing the bond to be invaded by the gas phase. From Eq. (2), it is obvious that the selected IF bond in a given cluster is the one of largest diameter located at the cluster boundary. As pore body sizes are greater than bond sizes, if there exists an IF pore body, it is directly selected. Otherwise, the IF bond with the biggest diameter is identified.

(3) The diameter of the selected pore body or bond in cluster #*n* is denoted by d_{sn}. The volume of liquid in this throat or pore body at the considered time is V_{sn}. If the selected pore body (or throat) is a PI pore body (or throat), then V_{sn} is the volume of liquid remaining in the PI pore body (or throat). This choice is a consequence of the quasi-static approach. Since viscous effects are neglected, the pressure field is spatially uniform in the gas phase and in each liquid cluster. This implies that all the menisci located at a cluster boundary have the same curvature.

(4) The vapour partial pressure field is computed in the gas phase solving numerically the linear system resulting from the modelling of the diffusive transport (see below).

(5) The evaporation rate, F_n, at the boundary of each cluster is computed from the vapour partial pressure field computed in step (4) as

$$F_n = \sum_k \sum_j \phi_{kj} \tag{3}$$

where ϕ_{kj} is the evaporation rate through the interfacial bond connecting any pore body *k* at the boundary within the cluster (this can be a L, PI or IF pore body) to a gas saturated pore body *j* outside the cluster (*i.e.*, a CI or G pore body). The expression of ϕ_{kj} is detailed below (see Eqs. (4) and (8)).

(6) The time, t_n^*, needed to fully evaporate the liquid volume, V_{sn}, is computed for each cluster as $t_n^* = \rho_\ell V_{sn}/F_n$.

(7) The pore body or throat identified in step (2) for which the corresponding invading time is minimum, $t_{cmin}^* = \min(t_n^*)$, is fully invaded.

(8) The total elapsed time is computed as $t = t + t_{cmin}^*$.

(9) The phase distribution in the network is updated, including the partial drainage/evaporation of the liquid contained in the other elements (throats or PI pore bodies) identified in step 2 so that $V_{sn}(t + t_{cmin}) = V_{sn}(t) - \frac{F_n}{\rho_\ell} t_{cmin}$.

Compared to the algorithm for capillary porous media (Prat 1993), two modifications are introduced. The first one is straightforward and is related to the modelling of the vapour diffusion transport in small pores while considering the Knudsen diffusion. The second one is more important and is directly related to the consideration of the Kelvin effect. To begin with, modelling of the vapour diffusion transport shall be detailed.

The classical assumption to model diffusive transport of vapour in the gas phase is to make use of the quasi-steady assumption. This is based on the observation that the characteristic time of drying, *i.e.*, the time needed to reach the final liquid distribution in the network, is large compared to the characteristic time of diffusion at the pore scale. The mass rate between pore body *i* and pore body

j fully occupied by the gas phase (pore bodies G or CI) through the bond connecting them is expressed using Fick's law as

$$\phi_{ij} = D_{eff} \frac{M_v}{RT} \frac{\pi d_{tij}^2}{4} \left(\frac{P_{vj} - P_{vi}}{a} \right) \tag{4}$$

Here, P_v is the vapour partial pressure and D_{eff} is computed according to the following relationship (Bosanquet 1944)

$$\frac{1}{D_{eff}} = \frac{1}{D_v} + \frac{1}{D_{Knu}} \tag{5}$$

where D_v is the vapor molecular diffusion coefficient and D_{Knu} is the Knudsen diffusion coefficient. The Knudsen diffusion is considered here because the pore diameters are not large compared to the gas molecule mean free path (Kerkhof and Geboers 2005). The Knudsen diffusion coefficient is expressed as

$$D_{Knu} = \frac{d_{tij}}{3} \sqrt{\frac{8RT}{\pi M_v}} \tag{6}$$

A linear system of equations is obtained by expressing the mass conservation in each pore body i filled with gas (pore bodies G or CI),

$$\sum_j \varphi_{ij} = 0 \tag{7}$$

where index j refers to the neighbour pore bodies connected to pore body i by a gaseous bond. The resulting linear system is solved numerically to obtain the partial pressure at each gaseous or partially gaseous node of the network. However, to do so, boundary conditions must be specified and this is performed as follows. Let assume that the radius of curvature of each meniscus is known. The method for its determination is a crucial new feature of the present PNM and the way to compute it is described right after.

When pore body i is of PI type, then the vapour partial pressure is specified in this pore body from the Kelvin relationship (Eq. (1)) using the radius of curvature of the meniscus present in this pore

body. Thus, the vapour partial pressure in such pore body is not obtained from the solution of the linear system but is specified as a (Dirichlet) boundary condition.

When pore body *i* is of CI type, then the evaporation rate at a meniscus located at the entrance of an adjacent liquid throat (connecting pore body *i* to pore body *j*) is expressed as

$$\phi_{ij} = D_{eff} \frac{M_v}{RT} \frac{\pi d_{tij}^2}{4} \left(\frac{P_{vequ.j} - P_{vi}}{(d_{pi}/2)} \right) \tag{8}$$

The vapour partial pressure $P_{vequ.j}$ at the meniscus under consideration is determined from the Kelvin relationship using the radius of curvature of that meniscus. In Eq.(8), $d_{pi}/2$ corresponds to the distance between the meniscus and the pore body center whereas D_{eff} is computed by replacing d_{tij} by d_{pi} in Eq. (6).

The last step to form the linear system allowing the computation of the vapour partial pressure in each gaseous node of the network is to specify the boundary conditions at the surfaces limiting the porous domain. A zero flux condition is imposed on the impervious surfaces, *i.e.*, at the network lateral and bottom surfaces for the simulations carried out in this work. Then the boundary conditions at the open surface, *i.e.*, the surface through which the vapour can exit the porous medium, also need to be specified. In the present case, only the network top surface is open. To couple the network with the external gas, vapour partial pressure computational nodes are added on top of the network as sketched in Fig.2. As indicated in this figure, the vapour partial pressure is imposed ($P_v = P_{v\infty}$) at a distance δ from the network surface. This condition on the relative humidity is denoted as $RH_\infty = \frac{P_{v\infty}}{P_{vs}}$ in the following. In the layer of size *L* within δ, the mass flux between two nodes is given by an expression similar to Eq. (4), namely

$$\phi_{ij} = D_v \frac{M_v}{RT} a^2 \left(\frac{P_{vj} - P_{vi}}{a} \right) \tag{9}$$

The vertical flux between a node in the upper row of nodes within the layer *L* and the upper boundary where $P_v = P_{v\infty}$ is expressed as

$$\phi_{ij} = D_v \frac{M_v}{RT}\, a^2 \left(\frac{P_{v\infty} - P_{vi}}{\frac{a}{2} + \delta - L} \right) \quad (10)$$

For the nodes located at the interface between the network and the external diffusive layer (Fig.2), the vapour partial pressure is specified from the Kelvin relationship when the adjacent vertical throat is liquid. When the throat is gas saturated, the expression of the flux is given by Eq. (4).

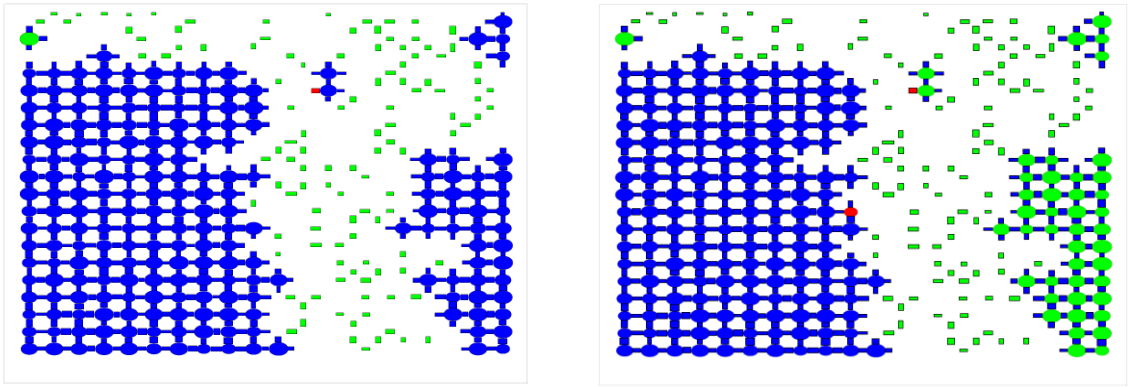
The use of an external diffusive layer made of a layer of thickness L which is discretized using the same mesh size, a, and the layer of thickness δ - L is motivated by the fact that it is of interest to account for situations where $\delta >> a$, representative of cases encountered in the porosimetry technique called evapo-porosimetry (Krantz *et al.* 2013). Actually, at the pore network surface and in its close neighbourhood, the vapour partial pressure field and the diffusive flux remains heterogeneous. The heterogeneity is then gradually damped out with an increasing distance from the surface. This explains why it is not necessary to set computational nodes all over the diffusive layer of thickness δ. In the layer sufficiently away from the surface, the diffusive transfer is unidirectional and an analytical formula, as given by Eq. (10), can then be used to model the transfer.

Kelvin effect implementation

As described above, the drying algorithm requires the determination of the menisci curvature at the boundary of each liquid cluster at each step of the drying process since this information is needed for computing the equilibrium vapour pressure from the Kelvin relationship. Computation of the curvature is actually a tricky part of the algorithm.

As simplified approaches, it could be appealing to first consider two options. Since the largest throat at the boundary of a cluster is the one to be invaded in the capillary limit envisaged in this work, the first obvious option, referred to as the "simple option", is to consider that the vapour pressure at the boundary of a cluster is given by the Kelvin relationship with $r = d_{tmax}/2$, where d_{tmax} is the diameter of the largest interfacial throat. However, since d_{tmax} varies from one cluster to the other, the vapour partial pressure at the boundary also differs from one cluster to the other. The net result of this procedure is the generation of a negative mass transfer rate, F_n, *i.e.*, "condensation", at the boundary of some clusters. This situation is illustrated in Fig. 4a. As a consequence, clusters featuring a negative mass transfer rate would grow and, therefore, the menisci radius of curvature

would be modified at their boundaries. This is in contradiction with the initial assumption that $r = d_{tmax}/2$. In other words, the assumption that the radius of curvature is simply given by $d_{tmax}/2$ does not lead to consistent results. A simple tempting correction, as a second option, is then to set F_n to zero for such clusters, for instance imposing a zero-flux condition at each meniscus of the cluster. As illustrated in Fig.4b, this also leads to inconsistency as negative mass rate may result at new clusters. Typically, with this option, the vapour partial pressure varies along the boundary of the cluster, which is not consistent with the Kelvin relationship combined with the capillary equilibrium condition, imposing that the meniscus curvature is the same for all the menisci belonging to the boundary of a given cluster. A more refined and physically consistent approach is hence needed. This means that the menisci curvature radius at the boundary of each cluster must be determined so that the evaporation rate F_n remains ≥ 0 for each cluster. The procedure implemented in the algorithm for this purpose is the following.



a) b)

Fig.4. a) Example of a situation where a negative mass transfer rate is obtained for a cluster (in green) when the simple option (see text) is used. b) If a zero evaporation rate is imposed at each interfacial throat of a cluster with a negative flux, then clusters which were with a positive evaporation rate can become clusters with a negative evaporation rate. Pore bodies and throats in red are PI (partially invaded) elements; clusters or single throats for which a negative mass transfer rate is computed, are shown in green. Vapour escapes from the network top edge.

Basically, the idea for eliminating the negative fluxes is to determine the equilibrium vapour pressure at the boundary of each cluster so that a zero or positive net overall flux is obtained, *i.e.*,

such that $F_n \geq 0$, for each cluster, including those formed by a single liquid throat. Contrary to the simpler (but inconsistent) procedure consisting in imposing a zero flux at each meniscus of the cluster, a zero overall flux is now achieved by exactly compensating condensation at some menisci by evaporation from the other menisci belonging to the same cluster. More specifically, the vapour pressure at the cluster boundary is obtained by using the following procedure. Let assume that *n* clusters with negative fluxes are identified among the *N* clusters present in the network. The vector, $\mathbf{F_n}$, of negative mass transfer rate components $F_{ni}(P_{ni})$, where P_{ni} is the equilibrium vapour pressure for cluster #*i* ($1 \leq i \leq n$), must be changed to zero. Newton's method is used to obtain the zero of vector $\mathbf{F_n}$. It is an iterative method that consists in imposing the zero flux condition through the following relationship

$$\mathbf{P_n}_k = \mathbf{P_n}_{k-1} - \mathbf{J_n}_k^{-1}\mathbf{F_n}_k \qquad (\mathbf{11})$$

where the subscript *k* denotes the k^{th} iteration, $\mathbf{P_n}$ is the equilibrium vapour pressure vector (of components P_{ni}, $1 \leq i \leq n$) for the *n* clusters, $\mathbf{J_n}$ is the Jacobian matrix of size $n \times n$ and components J_{nij} defined as

$$J_{nij} = \frac{\partial F_{ni}}{\partial P_{nj}} \qquad (12)$$

This matrix is computed using a finite difference method at the k^{th} iteration as

$$J_{nijk} = \frac{F_{nik} - F_{nik-1}}{P_{njk} - P_{njk-1}} \qquad (13)$$

where F_{nik} and F_{nik-1} (respectively P_{njk} and P_{njk-1}) are the mass transfer rate (the equilibrium vapour pressure respectively) at the boundary of cluster *i* (cluster *j* respectively) at iterations *k* and *k-1*.

In order to obtain the Jacobian matrix at each iteration, the vapour partial pressure field over the whole network must be computed *n* times. This means that the computational time increases with the number of clusters with negative fluxes. If the iteration number to reach the solution is *m*, then the necessary time is approximatively $m \times n \times t$ where *t* is the computational time of the vapour partial pressure field. For cluster *i*, the flux F_{ni} is related to the vapour partial pressure field around the cluster according to Eqs. (3) and (8). Because this flux to equilibrium vapour pressure

relationship is linear, Newton's method converges with only one iteration, and hence, the computational time is simply $n \times t$.

5. Results

Unless otherwise mentioned, results are presented for the following conditions. The network is a 20 × 20 square pore network with uniform probability density functions (p.d.f.) for the PSD and the TSD and a lattice spacing a=300 nm. The pore body radii are in the range [65 – 135 nm] whereas the throat radii vary from 2 to 48 nm. The total thickness of the external boundary layer is δ= 10 cm, which is consistent with the typical configuration encountered in the evapo-porosimetry technique (Krantz *et al.* 2013). The external boundary sub-layer, adjacent to the network where computational nodes are set, is of thickness L=50a (15 μm).

In Fig.5, the drying patterns obtained when the Kelvin effect is taken into account and when it is neglected, *i.e.*, when $P_v = P_{vs}$ is imposed at the surface of the menisci, are compared. The external relative humidity is $RH_\infty = 0$ in these simulations. As can be seen, the Kelvin effect does have an important impact on the pattern.

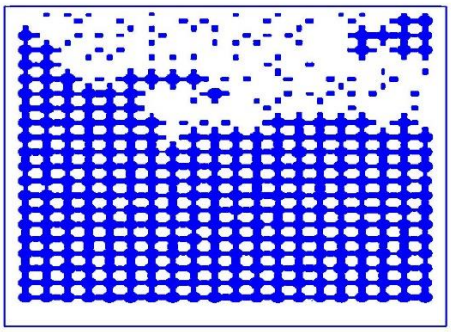
Whereas a drying zone develops in the top region of the network when Kelvin effect is neglected, it can be seen that this is not the case when the Kelvin effect is taken into account. Because of the Kelvin effect, the evaporation rate of a cluster in the network top region can be quite small. As a result, such a cluster can remain much longer in the top region than in a network where the Kelvin effect is neglected.

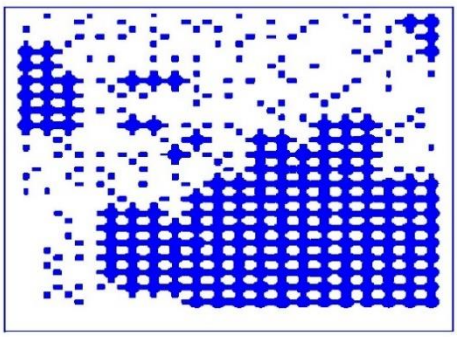
It should also be noted that in the presence of the Kelvin effect, many single liquid throats distributed all over the network remain while the drying process progresses. In a capillary porous material, a full drying is expected for any value of the external relative humidity RH_∞ lower than 1, except for a tiny volume of liquid confined in crevices, grain contacts or wall roughness corresponding to a very small fraction of the pore space. In a hygroscopic material, incomplete drying can be obtained depending on the pore size distribution and RH_∞. If the throat diameters are all greater than the "critical" throat diameter, d_c, given by the Kelvin relationship, *i.e.*, $d_c = \frac{M_v}{RT} \frac{4\gamma cos\theta}{\rho_\ell \ln\left(\frac{Pvequ.}{RH_\infty P_{vs}}\right)}$, then full drying is expected. When a fraction of the throats in the porous material have a diameter smaller than d_c, then drying should be incomplete since this fraction of throats

cannot be invaded (in the absence of significant viscous effects as considered in this work). This is illustrated in Fig.6. Naturally, if all the throats are lower than d_c, then no drying at all occurs.

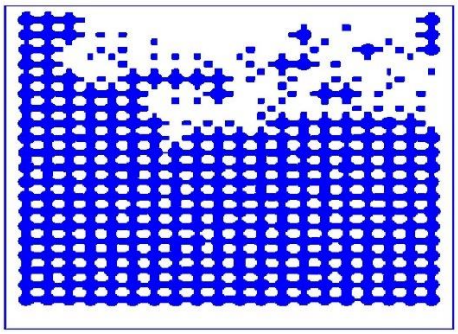
Drying pattern

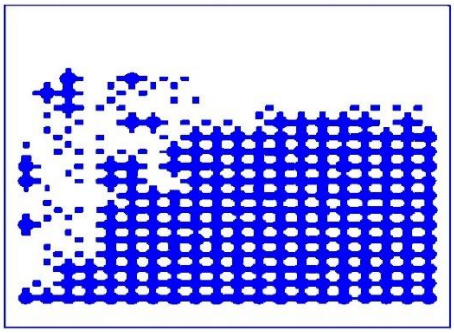
With Kelvin's effect





Without Kelvin's effect





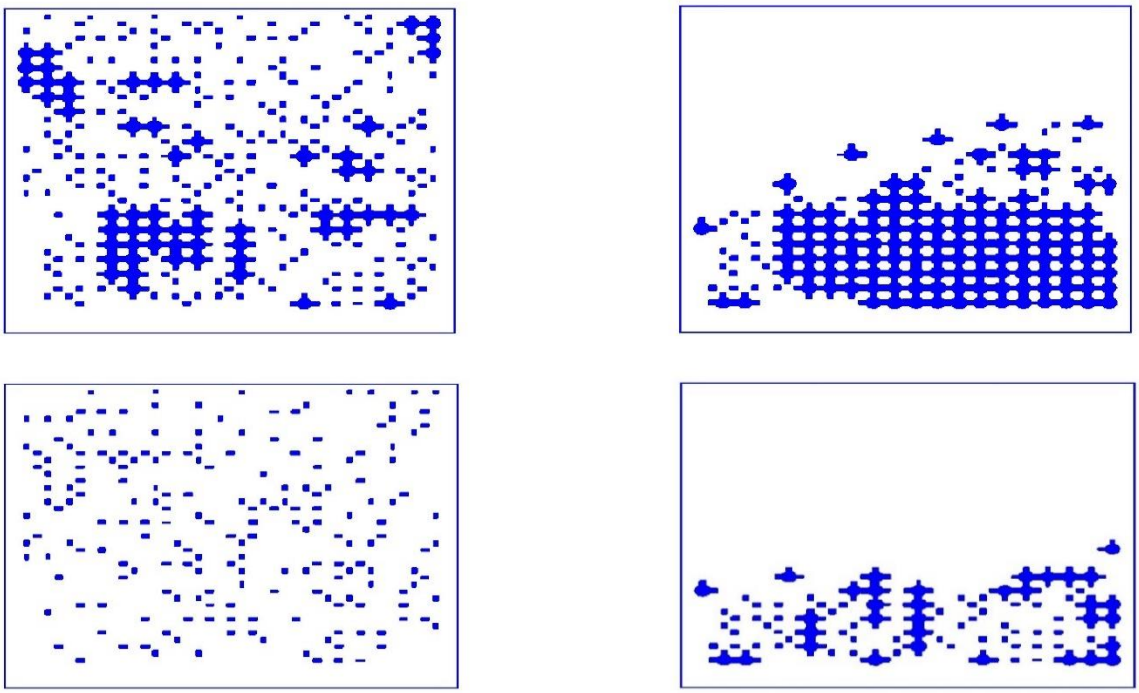


Fig.5. Liquid (in blue) and gas (in white) distributions in the network for a simulation with Kelvin effect (left) and without Kelvin effect (right). Patterns are shown for the same number of invaded pore bodies and throats. Vapour escapes from top the edge of the network. $RH_\infty = 0$.

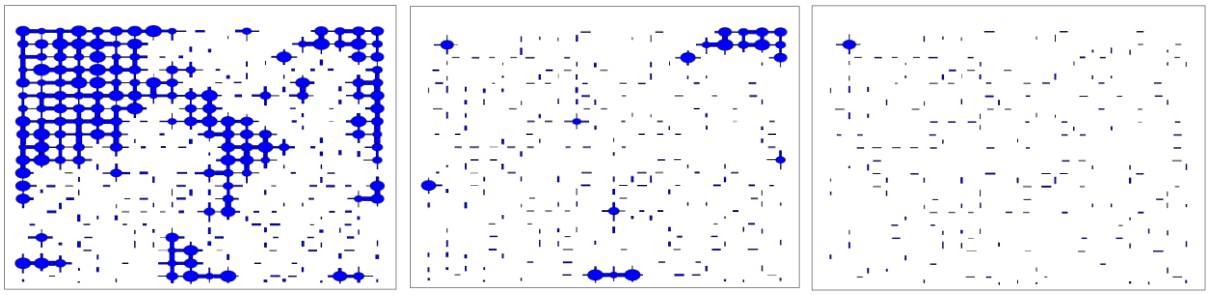


Fig.6. Final drying patterns for three different values of RH_∞: 0.96, 0.94 and 0.92 leading to incomplete final drying. The throat radii are distributed in the range [2 – 48 nm]. $RH_\infty = 0$.

Meniscus curvature distribution

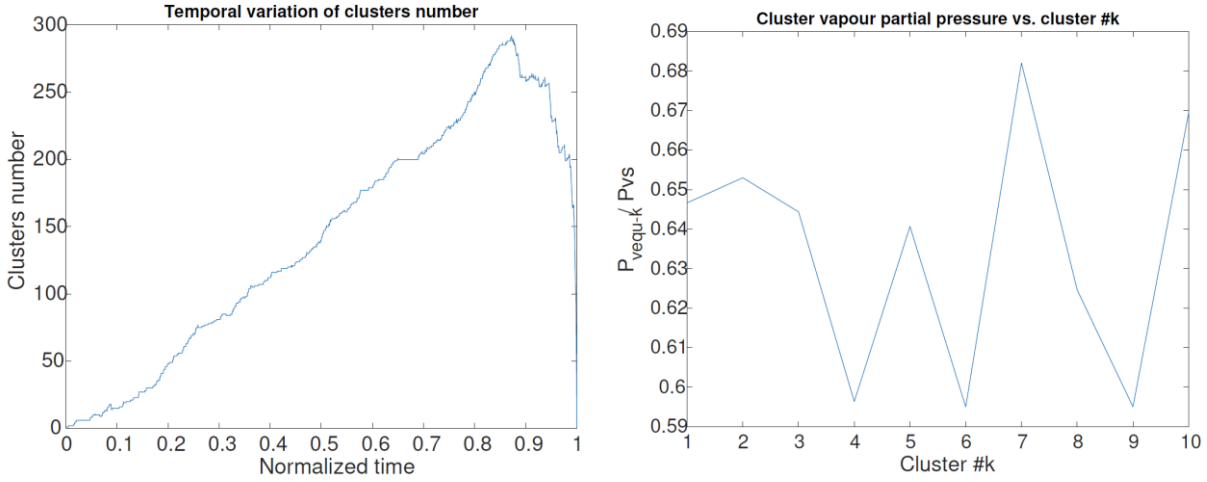
To characterize the fact that the meniscus curvature varies from one cluster to the other and thus also the equilibrium vapour partial pressure (the equilibrium vapour partial pressure is the vapour partial pressure computed at the boundary of a cluster), the average equilibrium vapour partial pressure and its standard deviation distribution were computed as follows

$$\bar{P}_{vequ.} = \frac{1}{N}\sum_{k=1}^{k=N} P_{vequ.-k} \tag{14}$$

$$\sigma_{P_{vequ.}} = \sqrt{\frac{\sum_{k=1}^{k=N}\left(P_{vequ.-k}-\bar{P}_{vequ.}\right)^2}{N}} \tag{15}$$

where N is the number of clusters in the network, $P_{vequ.-k}$ being the equilibrium vapour partial pressure at the boundary of cluster #k.

In Fig.7a, representing the variation of the number of clusters versus the normalized time, one can distinguish two main periods: a first period during which the number of clusters steadily increases up to a maximum and then a second period where the number of clusters present in the network decreases. These two periods are referred to as period 1 and period 2 respectively.



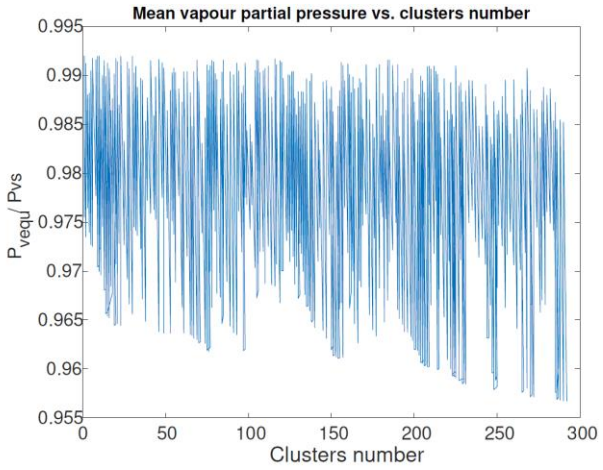
a) b)

Fig.7. a) Variation of the number of clusters present in the network during the drying process; b) illustration of the radius of curvature variation from one cluster to the other (case when 10 clusters are still present in the network).

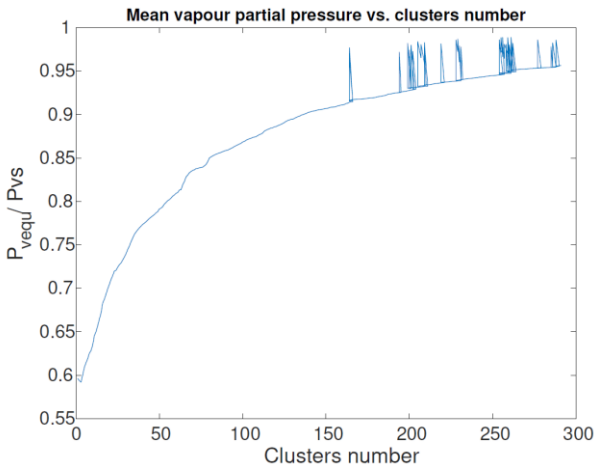
The fact that the equilibrium vapour pressure varies from one cluster to the other is illustrated in Fig.7b for the case where $\sigma_{P_{vequ.}}/P_{vs}$ is maximum (see Fig.8 below). In Fig.8, variations of the mean equilibrium vapour pressure and standard deviation (Eq. (15)) are represented as functions of the number of clusters present in the network in period 1 and period 2. As can be observed, the

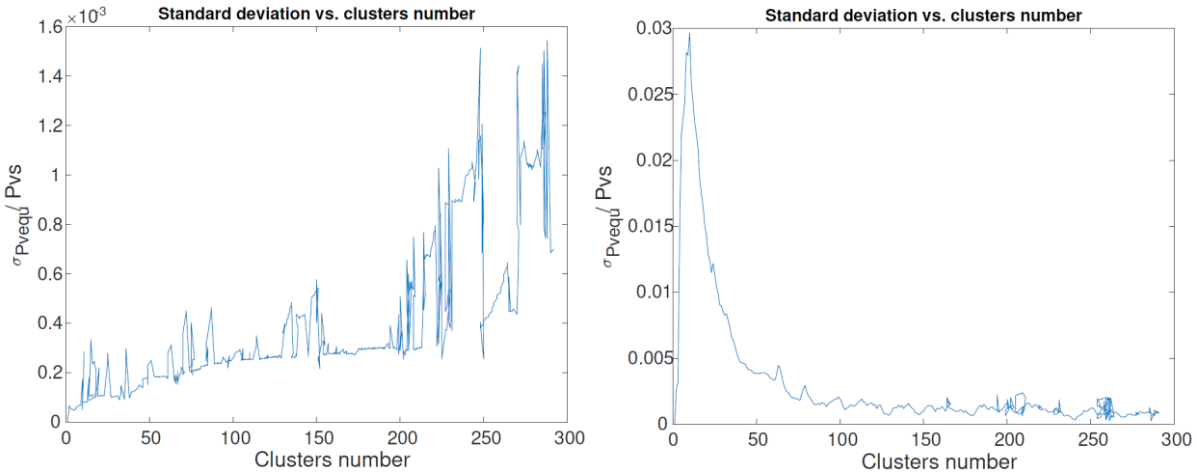
mean equilibrium vapour pressure fluctuates with the successive invasions in period 1. In period 2, fluctuations are damped out and the mean equilibrium vapour pressure gradually decreases with a decreasing number of clusters present in the network. This can be explained by the fact that only small clusters containing throats of small sizes are present in period 2 (as illustrated in Fig.5, the liquid is eventually distributed only in narrow throats toward the end of drying). As shown in Fig.8, the standard deviation (Eq. (15)) increases during most of the drying process until only a few clusters are present (10 in this example).

Period 1



Period 2



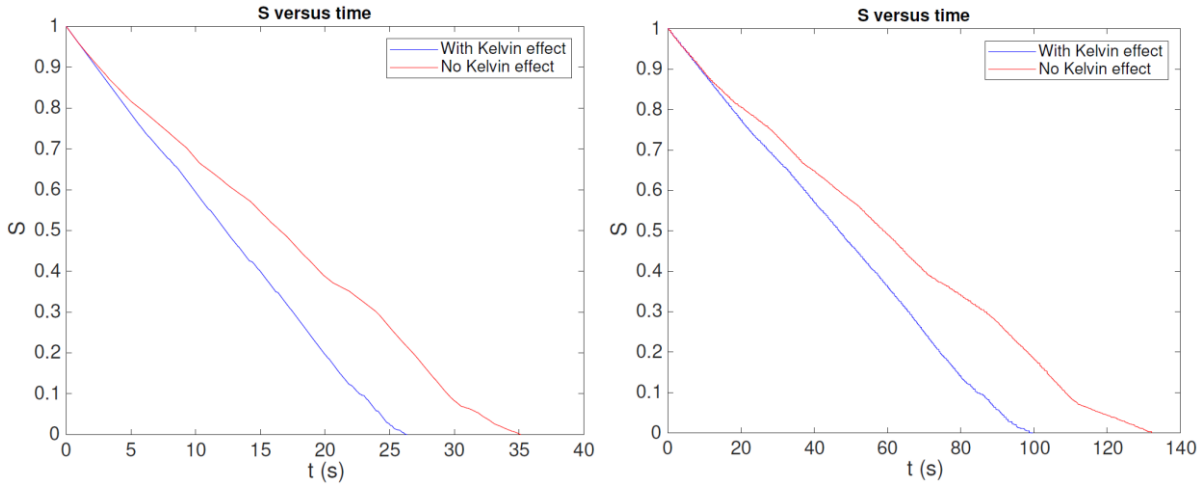


a) b)

Fig.8. a) Variation of the mean equilibrium vapour pressure in the network (Eq. (14)) as a function of the number of clusters in the network in period 1 and in period 2; b) variation of the cluster equilibrium vapour pressure standard deviation (Eq. (15)) as a function of the number of clusters in the network in period 1 and in period 2.

Drying kinetics

The drying kinetics in the presence of Kelvin effect and when the Kelvin effect is neglected are compared in Fig.9 for two values of the external relative humidity, namely $RH_\infty = 0$ and $RH_\infty = 0.6$.



a) b)

Fig.9. Variation of overall network saturation, *S*, as a function of time, *t*, for a simulation with Kelvin effect and without Kelvin effect for a) $RH_\infty = 0$; b) $RH_\infty = 0.6$.

As illustrated in Fig.9, drying in the presence of Kelvin effect can be faster than drying without Kelvin effect and the impact is not very sensitive to the applied relative humidity in the external gas phase (see Figs. 9a and 9b). It should be noted here that the conditions are exactly the same in both cases, in particular regarding the network which has the same pore body and throat size distributions. Such a comparison is practically impossible to perform experimentally since the Kelvin effect is directly related to the size of the pore bodies and throats. One option could be to vary the contact angle (strong Kelvin effect with a perfect wetting liquid versus a weaker Kelvin effect for a larger contact angle according to Eq. (1)) but then other factors, such as the effect of liquid films (Eijkel *et al.* 2005, Chauvet *et al.* 2009) or the impact of contact angle on the drying pattern (Chapuis and Prat 2007, Chraibi *et al.* 2009) might affect the comparison. In any case, the comparison shown in Fig.9 may be considered as paradoxical at first glance since the Kelvin effect reduces the vapour pressure at the menisci surface. Based on this observation, one would expect a slower drying in the presence of the Kelvin effect. However, the faster drying observed in the presence of the Kelvin effect is fully consistent with the patterns depicted in Fig.5. Indeed, this figure shows that the liquid phase is more evenly distributed, leading to a larger number of menisci exposed to evaporation in the presence of the Kelvin effect, whereas a dry zone develops in the upper region of the network when the Kelvin effect is not considered. The development of this dry zone is the main phenomenon explaining the slower drying when the Kelvin effect is neglected in the simulation.

In Fig.10, the total evaporation from the network versus time is reported. This figure highlights the effect of Knudsen diffusion, which reduces the evaporation rate compared to the case where only molecular diffusion is taken into account. This tendency was expected since the effective vapor diffusion coefficient, as expressed in Eq. (5), decreases with an increasing Knudsen diffusion effect. As illustrated in Fig.10, the impact is quite significant.

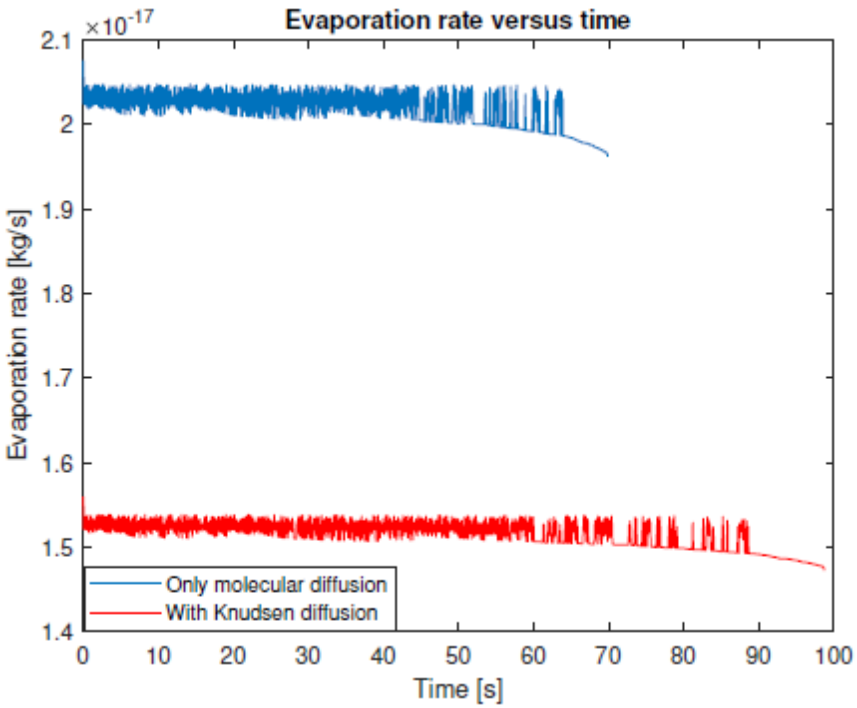


Fig.10. Impact of Knudsen diffusion on the evaporation rate for a 20 × 20 square network. The external relative humidity is fixed to RH_{∞} = 0 at δ = 10 cm. For this simulation, the pore body radii are in the range [60 – 100 nm] whereas the throat radii vary from 25 to 55 nm, both following a uniform p.d.f.

Evaporation rate fluctuations

As depicted in Fig.10, the evaporation rate fluctuates as a function of time. This is also a distinctive feature compared to drying PNM simulations when Kelvin effect are neglected. In the latter, the evaporation rate can only decrease. In the presence of a noticeable Kelvin effect, the vapour pressure at the boundary of each cluster fluctuates because of the menisci curvature fluctuations along the drying process (as illustrated in Fig.8). As a result, when, for instance, a larger throat becomes an interfacial throat, the menisci curvature decreases and therefore the menisci vapour pressure increases according to the Kelvin relationship. This, in turn, induces a larger evaporation rate.

Desorption isotherm

The desorption isotherm corresponds to the successive equilibrium saturations obtained when the relative humidity in the external gas, RH_∞, is gradually decreased with small increments, step by step. In Fig.11, the desorption isotherm, $\phi(S) = \frac{P_{vequ.}}{P_{vs}}$, is represented versus the overall network saturation, *S*. This result was obtained for a 20 × 20 square network and the nominal conditions, namely, a diffusion layer thickness δ = 10 cm, pore body and throat radii in the range [65 – 135 nm] and [2 - 48 nm] respectively, both following uniform p.d.f. The external relative humidity, RH_∞, is initially fixed equal to 1 and decreased with a step of 0.02 down to $RH_\infty = 0.6$. At this value of RH_∞, all the liquid in the network has evaporated.

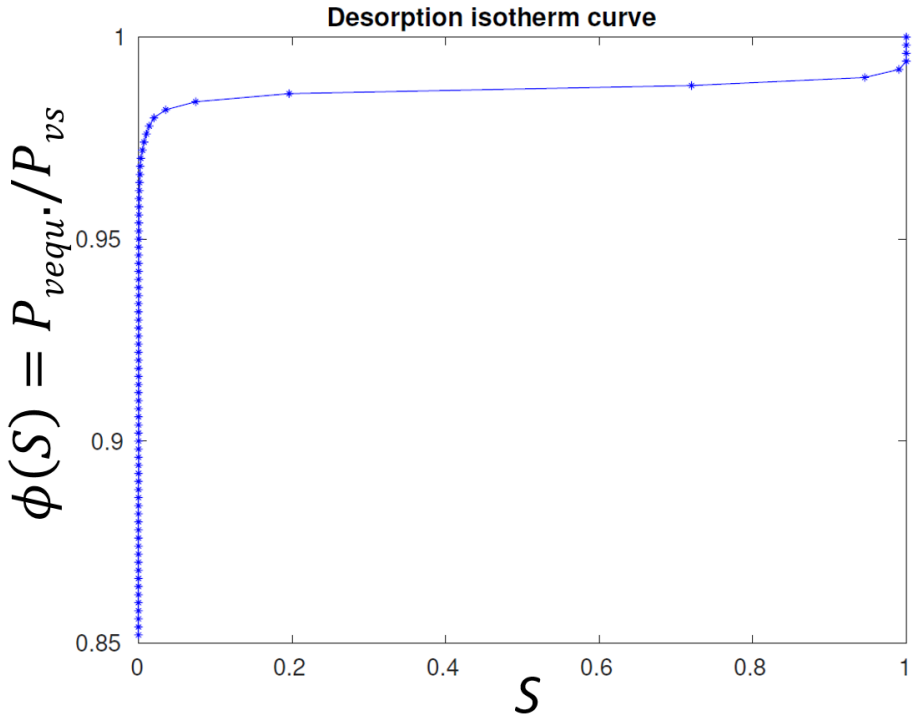


Fig.11. Simulated desorption isotherm with the drying model and with the desorption isotherm algorithm (see text). Both results are superimposed.

In the limit $\delta >> H$, (*H* denotes the network thickness, see Fig. 2), it is expected that this curve can be obtained in a simpler manner according to the following algorithm (El Hannach *et al.* 2014), which does not require solving the diffusion problem

1) The network is initially fully saturated and the external relative humidity is set to 1, *i.e.*, $RH_{\infty-0}$=1.

2) The external gas relative humidity is decreased $RH_{\infty-k+1} = RH_{\infty-k} - \Delta RH$ where ΔRH is a small relative humidity variation.
3) Kelvin equation, Eq. (1), is used to determine the critical diameter $d(RH_{\infty-k+1})$. All liquid pore bodies and throats having a diameter larger than $d(RH_{\infty-k+1})$ can be *potentially* invaded.
4) All the liquid pore bodies and throats identified in step #3 and accessible, *i.e.*, connected to the open surface of the network by a gaseous path, are identified.
5) The pore bodies and throats identified in step #4 are invaded.
6) Steps #4 and 5 are repeated until no liquid pore body or throat which diameter is greater than the critical diameter determined in step #3 is present and is accessible.
7) The network saturation is determined.
8) Steps #2 to #7 are repeated until $RH_{\infty-k+1} \leq 0$.

As expected, using this algorithm exactly leads to the same desorption curve (depicted in Fig.11) as the one obtained from the drying simulation.

Non-local equilibrium effect

As discussed for instance in (Moghaddam *et al.* 2017), the classical continuum models of drying, (see *e.g.*, (Whitaker 1977)), are based on the local equilibrium assumption. This means that the vapour pressure within a representative elementary volume (REV) is very close to the equilibrium vapour pressure. As a consequence, at the scale of the REV in which the average vapor pressure is denoted by $\langle P_v \rangle^g$, the equilibrium relationship to be considered is the desorption isotherm

$$\langle P_v \rangle^g = P_{vequ.} = P_{vs}\phi(S) \tag{16}$$

This assumption has been questioned, (see for instance (Chammari et al. 2008)) and it is therefore of interest to get some insights on this question from our drying PNM simulations including Kelvin effect. To this end, a procedure similar to the one described in (Moghaddam *et al.* 2017) is followed. The average vapour pressure is determined within a slice as

$$\langle P_v \rangle^g = \frac{\sum_1^{n_{g-slice}} \frac{\pi}{6} d_p^3 P_v + \sum_1^{n_{PI-slice}} \frac{\pi}{6} d_p^3 (1-S_p) P_v}{\sum_1^{n_{slice}} \frac{\pi}{6} d_p^3} \tag{17}$$

Similarly, the slice average saturation, S_s, is computed as

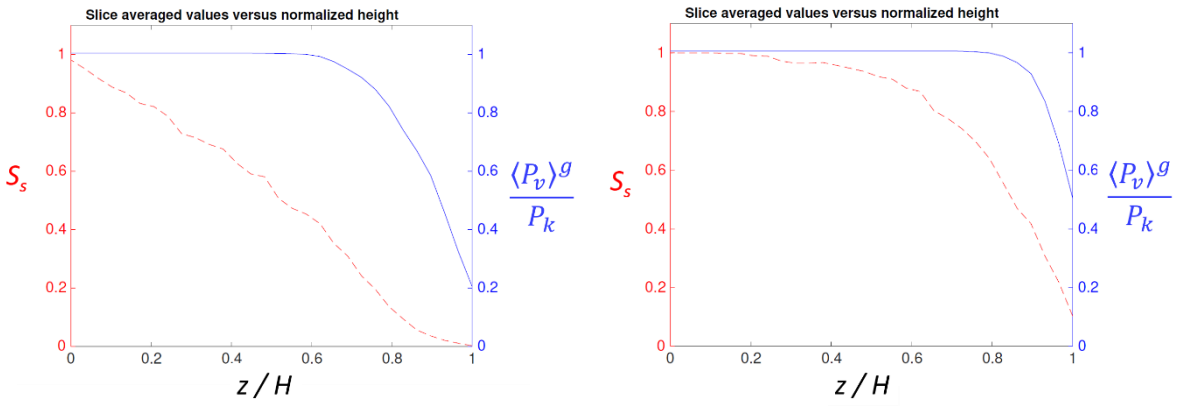
$$S_s = \frac{\sum_1^{n_{\ell-slice}} \frac{\pi}{6} d_p^3 + \sum_1^{n_{PI-slice}} \frac{\pi}{6} d_p^3 S_p}{\sum_1^{n_{slice}} \frac{\pi}{6} d_p^3} \tag{18}$$

In these two equations, $n_{g-slice}$, $n_{PI-slice}$ and $n_{\ell-slice}$ respectively denote the number of G, PI and L pore bodies in the slice, whereas n_{slice} represents the total number of pore bodies in the slice. Note that for simplicity, Eqs.(17) and (18) are written while assuming volumeless throats. When volumes are assigned to both throats and pore bodies, similar expressions are obtained.

The purpose is hence to analyse the average vapour pressure profiles together with the saturation profiles within the network (for $0 \leq z/H \leq 1$) for various overall saturations, *S*, *i.e.*, at various times.

For practical purposes, the slice average vapour pressure is normalized by the average equilibrium vapour pressure at all the clusters boundaries given by $P_k = \langle P_c \rangle = \frac{1}{N}\sum_1^N P_c$ where P_c refers to a cluster equilibrium vapour pressure, N being the number of clusters. As in (Moghaddam *et al.* 2017), and as illustrated in Fig.2, a slice is understood as a domain containing one horizontal line of pore bodies, all the horizontal throats and half the vertical throats adjacent to the pore bodies in the line.

Profiles resulting from this procedure for two values of the overall saturation, *S*, are reported in Fig.12. They were obtained after averaging results obtained over 25 realizations of a 30×30 square network and a relatively thin external boundary layer, namely $\delta = 10 \times a$. Other conditions are the nominal conditions, namely, pore body and throat radii in the range [65 – 135 nm] and [2 - 48 nm] respectively, using uniform p.d.f. The external relative humidity RH_∞ is equal to zero.



a) b)

Fig.12. Profiles of the slice-averaged normalized vapor partial pressure, $\frac{\langle P_v \rangle^g}{P_k}$, and the local saturation, S_s, versus the normalized network height, z/H, obtained from the drying PNM at network overall saturations S=0.5 a) and S=0.8 b). Both quantities are resulting from an average over 25 realizations of a 30×30 network.

As can be observed from Fig.12, the slice averaged vapour partial pressure is less than the slice averaged mean equilibrium vapour pressure, P_k , in slices where the slice averaged saturation, S_s, is non zero. More specifically, the difference between the two pressures becomes significant when S_s decreases below a threshold value (typically, this difference approximately exceeds 10% when $S_s \leq 0.2$ for S=0.5 (Fig.12a) and $S_s \leq 0.4$ for S=0.8 (Fig.12b)). This is an indication of a non-local equilibrium (NLE) effect.

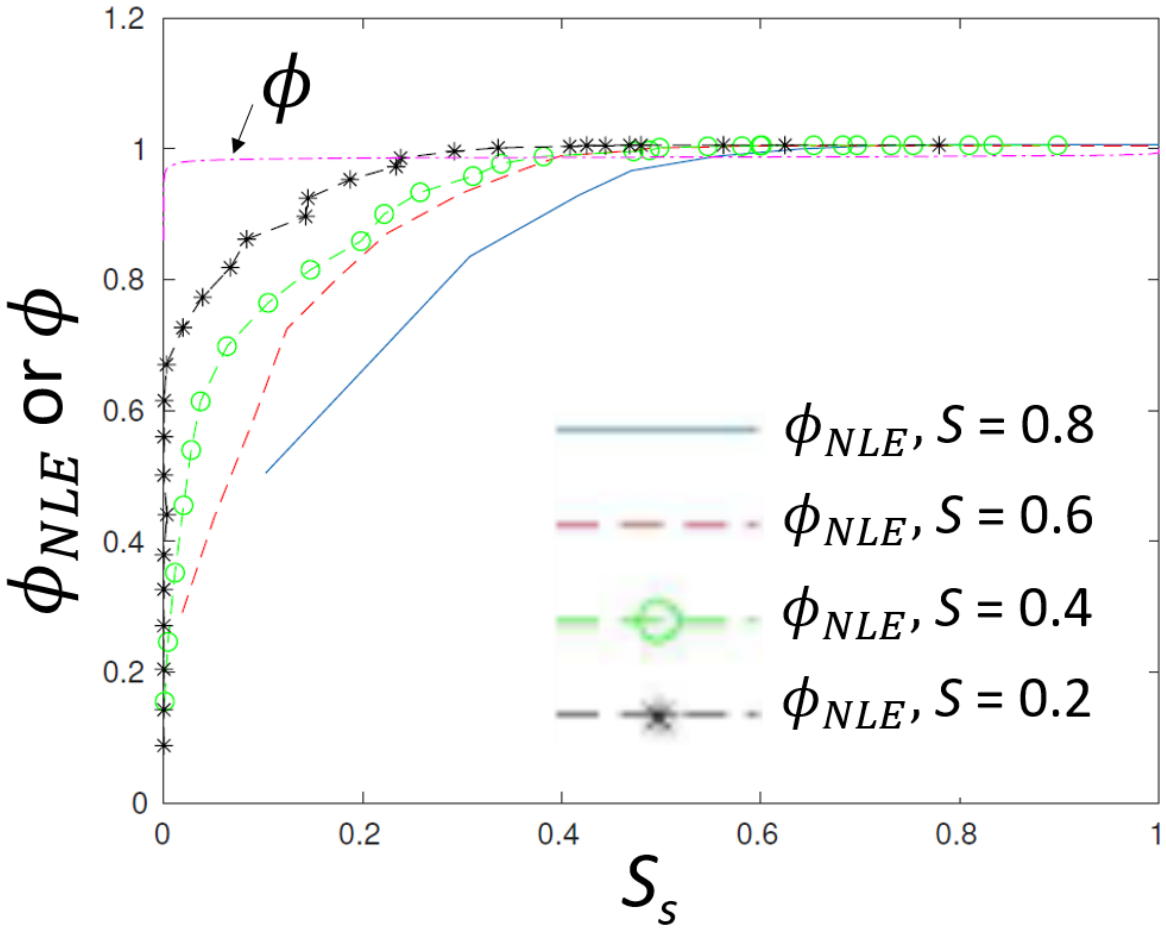


Fig.113. Internal NLE function (ϕ_{NLE}) obtained from the PN drying simulations as a function of local saturation, S_s, for different network overall saturation, S. The desorption isotherm is the curve labelled "ϕ".

To further illustrate this effect, a NLE function, $\phi_{NLE} = \langle P_v \rangle^g / P_{vs}$, may be defined which variation with the slice average saturation, S_s, is represented in Fig.13 for four values of the overall network saturation. In this figure, the desorption isotherm, $\phi(S)$, (see Fig.11), is also reported for comparison purposes.

As can be seen, the NLE function is significantly different from the desorption isotherm, confirming a noticeable NLE effect. This is in agreement with the discussions in (Chammari *et al.* 2008), claiming that NLE effects must be considered in the modelling of drying within the framework of the continuum approach in porous media. It can also be seen that the NLE function

varies with the overall network saturation. The variations with S are qualitatively similar to the results reported in (Moghaddam *et al.* 2017) in the absence of Kelvin effect. Even if it may be argued that the network under consideration is quite small and that a slice was not proven to be an acceptable REV, results exemplified in Fig.13 are an additional indication in favor of the consideration of NLE effects in drying. Certainly, it would be interesting to perform similar computations over much larger networks and preferentially with 3D networks.

Drying for $\delta >> H$

As a final investigation, it is interesting to analyse the time-evolution of the evaporation rate for various values of $\delta >> H$. At each time step, the vapour pressure is governed by the menisci curvature in the network. Thus, in this limit, one can assume that

$$P_{vI} = P_{vs}\phi(S) \tag{19}$$

where P_{vI} denotes the vapor pressure at the interface and $\phi(S)$ is the desorption isotherm (see Fig.11). The evaporation rate would then be given by

$$E = AD_v \frac{M_v}{RT} \frac{(P_{vI} - P_{v\infty})}{\delta} = AD_v \frac{M_v}{RT} P_{vs} \frac{(\phi(S) - RH_\infty)}{\delta} \tag{20}$$

in which A is the top surface area of the porous medium. Using the evaporation rate at $t = 0$, given by $E_0 = AD_v \frac{M_v}{RT} P_{vs} \frac{(1 - RH_\infty)}{\delta}$, as the reference, the normalized evaporation rate can be expressed, from Eq. (20), as

$$\frac{E}{E_0} = \frac{(\phi(S) - RH_\infty)}{(1 - RH_\infty)} \tag{21}$$

Results on $\frac{E}{E_0}$ obtained for a 30 × 30 square network are reported in Fig.14 versus the network saturation, S. Here again, pore body diameters are in the range [65 – 135 nm] whereas throat diameters vary from 2 to 48 nm, both following uniform p.d.f. The external relative humidity RH_∞ is taken equal to zero, which, from Eq. (21), simply leads to $\frac{E}{E_0} = \phi(S)$. Three values of the diffusive layer thickness are considered: $\delta = 10 \times a$, $\delta = 1000 \times a$ and $\delta = 10000 \times a$.

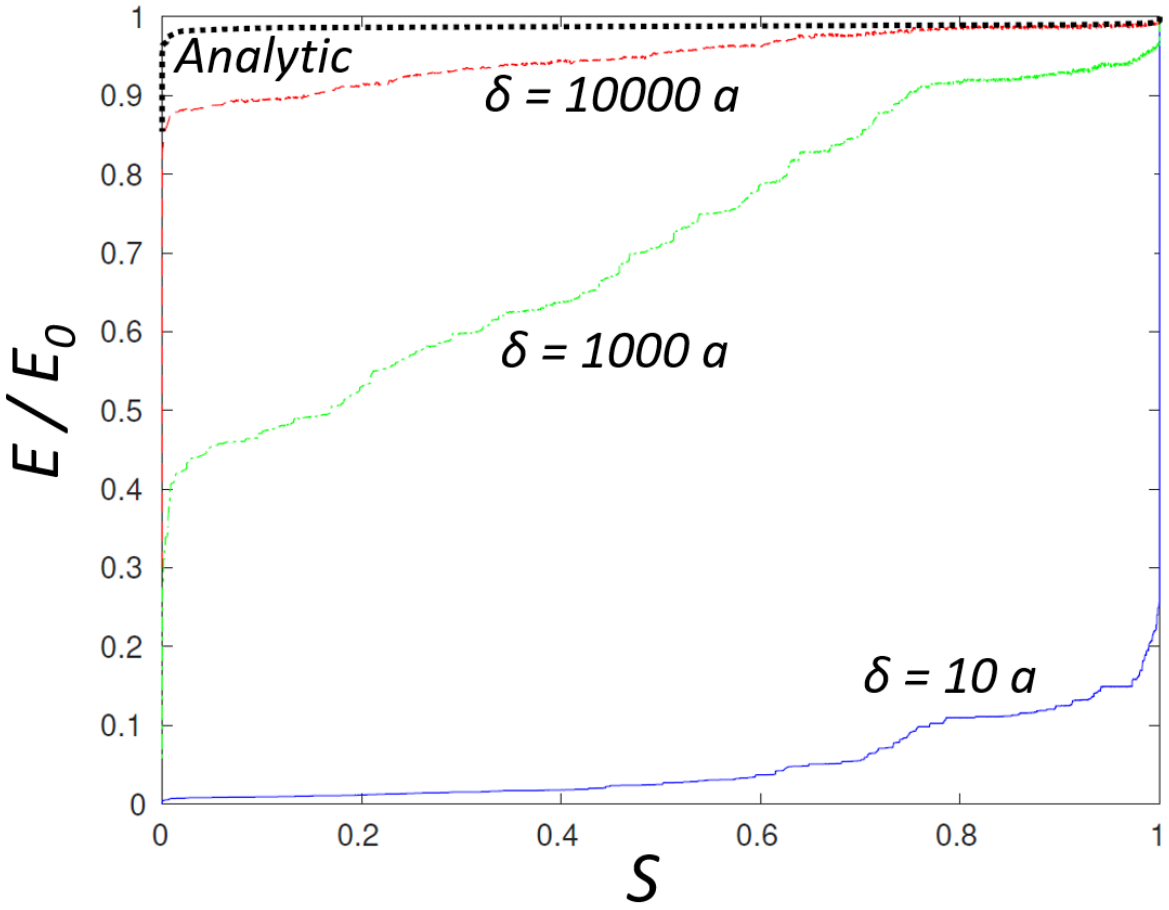


Fig.14. Impact of the external diffusive layer thickness, δ, on the drying curve. The curve labelled "analytic" corresponds to Eq. (21) (or, since $RH_\infty = 0$, to $\phi(S)$).

As can be seen from Fig.14, the drying curve tends toward the curve obtained from the desorption isotherm (Eq. (21)) when the external diffusive layer thickness δ is increased to very large values compared to H. This is expected on the ground that the diffusive transfer resistance within the network must gradually become negligible compared to the external transfer resistance when δ is increased. However, it can be seen that the convergence is quite slow. For the largest value under investigation, which corresponds to a ratio $\frac{H}{\delta}$ as low as 3×10^{-3}, evaporation rates are still noticeably different. This may be related to the impact of the NLE effect previously discussed,

indicating again that the mean vapour pressure in the network is different from the equilibrium vapour pressure.

6. Conclusions

A pore network model of isothermal drying, taking into account the Kelvin effect, was presented. This effect is noticeable for porous media with pore sizes in the sub-micronic range, typically with sizes varying between a few nanometers and, say, 100 nm. The model also takes into account the rarefaction effects on the vapour diffusion process with the consideration of Knudsen diffusion together with the usual molecular diffusion.

The drying PNM algorithm with Kelvin effect is noticeably more complicated than the drying PNM algorithm for capillary porous media for which the Kelvin effect can be ignored. The main point is to determine the curvature of the menisci at the boundary of the liquid clusters forming during the drying process. In the quasi-static limit considered in this work, the meniscus curvature is uniform at the boundary of a given cluster but can vary from one cluster to the other. The meniscus curvature for each cluster is determined through an iterative procedure using Kelvin relationship so that the net mass transfer rate from each liquid cluster in the network is zero (evaporation at some regions of the cluster boundary is exactly balanced by condensation in the complementary regions of the cluster boundary) or greater than zero (due to net evaporation) at each step of the drying process.

Simulations were performed so as to illustrate the impact of the Kelvin effect. It was shown that this effect has an impact on the drying pattern, *i.e.*, the liquid distribution in the network, compared to the situation where the Kelvin effect is neglected. The liquid distribution tends to be spatially more uniform compared to the situation with negligible Kelvin effect, with the presence of many isolated small cluster for which evaporation is not possible.

Depending on the pore size distribution (more exactly, the throat size distribution) and the relative humidity in the external gas phase, three main situations can be distinguished: no drying, partial drying and full drying. Partial drying is obtained when the relative humidity in the gas phase external to the medium is smaller than the equilibrium vapour pressure corresponding to the largest throats in the network but larger than the equilibrium vapour pressure corresponding to the smallest throats in the network. Full drying is obtained when the relative humidity in the external gas phase is smaller than the equilibrium vapour pressure corresponding to the smallest throats in the network

whereas no drying occurs when the relative humidity in the external gas phase is larger than the equilibrium vapour pressure corresponding to the largest throats in the network.

When drying is partial, the saturation is non-zero in the sample at the end of drying process. An interesting question is whether this saturation is directly given by the desorption isotherm. Our simulations indicate that this is indeed the case in the purely capillary limit considered in the article. In the presence of significant viscous effects, it is expected that the final saturation be different form the one given by the desorption isotherm. More precisely, it is expected that the greater the viscous effects, the smaller the final saturation since viscous effects must allow invading throats that cannot be invaded when capillary effects are fully dominant. In this respect, it would be interesting to extent the present model so as to take into account the viscous effects by first adapting the algorithm developed in the absence of Kelvin effect (see *e.g.*, Metzger *et al.* 2007b).

Simulations performed in this work indicate that the evaporation rate fluctuates with possible local (in time) slight re-increase as a result of menisci curvature variations during the drying process. This feature is directly related to the Kelvin effect and not observed in PNM simulations neglecting the Kelvin effect. One might argue that the simulations reported in the present analysis were performed on networks of relatively small size. The question may then arise as to whether fluctuations will be damped out in larger networks. Exploring this question is left for a future work. Simulations reported here also indicate a noticeable NLE effect. This certainly needs to be confirmed by simulations over much larger networks so as to consider presumably more adequate averaging volumes than the horizontal thin slices considered in the present work (a somewhat standard view is to consider that a REV is a cubic or spherical domain of sizes corresponding to at least 10-20 lattice spacing in each direction). Nevertheless, our results strongly support the idea that NLE models are more adapted to describe the drying process than the much more classical local equilibrium models, not only in the case of the capillary porous media, (Moghaddam *et al.* 2017), but also for hygroscopic porous materials.

Naturally, the present model relies on several simplifying assumptions, which deserve to be revisited in future works. In addition to the already mentioned viscous effects, these include the possible effects of adsorbed and capillary liquid films, (see *e.g.*, Eijkel et al. 2005), as well as the possible impact of the total gas pressure (Mainguy *et al.* 2001). The latter effect is somewhat controversial (Thiery *et al.* 2007). In this regard, PNM simulations could help settle the question, at least in the case of isothermal drying.

Acknowledgement

Financial support from joint project ‘‘Drycap’’, funded by GIP ANR (project16-CE92-0030-01) and DFG (project TS28/10-1), is gratefully acknowledged.

References

Adamson, A.W., Physical chemistry of surfaces, 5th ed., Wiley (1990).

Babalievski, F.,Cluster counting: the Hoshen-Kopelman algorithm versus spanning tree approaches, International Journal of Modern Physics C, Vol 9, No 1, p. 43-60 (1998).

Bosanquet, C.H. British TA Report BR-507 (1944).

Carey V.P, Liquid-Vapor phase change phenomena, Taylor & Francis (1992).

Chammari, A., Naon, B., Cherblanc, F., Cousin, B., Bénet, J.C., Interpreting the drying kinetics of a soil using a macroscopic thermodynamic nonequilibrium of water between the liquid and vapor phase, Drying Technology, Vol 26, p. 836-843 (2008).

Chapuis, O., Prat, M., Influence of wettability conditions on slow evaporation in two-dimensional porous media, *Phys. Rev. E, 75,* 046311 (2007)

Chauvet, F., Duru, P., Geoffroy, S., Prat, M., Three periods of drying of a single square capillary tube, Physical Review Letters, Vol 103, 124502 (2009).

Chraibi, H., Prat, M., Chapuis, O., Influence of contact angle on slow evaporation in two dimensional porous media, *Phys. Rev. E,* 79, 026313 (2009)

Eijkel, J.C.T., Dan, B., Reemeijer, H.W., Hermes, D.C., Bomer, J.G., van den Berg, A. Strongly accelerated and humidity independent drying of nanochannels induced by sharp corners. Physical Review Letters, Vol 95, 256107 (2005).

El Hannach, M., Soboleva, T., Malek, K., Franco, A.A., Prat, M., Pauchet, J., Holdcroft, S., Characterization of pore network structure in catalyst layers of polymer electrolyte fuel cells, Journal of Power Sources, Vol 247, 322-326 (2014).

Joekar-Niasar, V., Hassanizadeh, S. M., Dahle, H., Dynamic Pore-Network Modeling of Drainage in Two-Phase Flow, Journal of Fluid Mechanics, Vol 655, p. 38 -71 (2010).

Kerkhof, P.J.A.M., Geboers, M.A.M., Toward a unified theory of isotropic molecular transport phenomena. AIChE Journal 51, p. 79-21 (2005).

Krantz, W.B., Greenberg, A.R., Kujundzic, E., Yeo, A., Hosseini, S.S., Evapoporometry: A novel technique for determining the pore-size distribution of membranes Journal of Membrane Science, Vol 438, p. 153-166 (2013).

Mainguy, M., Coussy, O., Baroghel-Bouny, V., Role of Air Pressure in Drying of Weakly Permeable Materials, Journal of Engineering Mechanics, Vol 127, Issue 6, p. 582-592 (2001).

Metzger, T., Tsotsas, E., Prat, M., Pore network models : a powerful tool to study drying at the pore level and understand the influence of structure on drying kinetics, Chapter 2, in "Modern Drying Technology", Vol 1, p. 57-102 (2007a).

Metzger, T., Irawan, A., Tsotsas, E., Isothermal drying of pore networks: Influence of friction for different pore structures, Drying Technology, Vol 25, Issue 1, p. 49-57 (2007b).

Metzger, T., A personal view on pore network models in drying technology, Drying Technology, Vol 37, p. 497-512 (2019).

Moghaddam, A.A., Prat, M., Tsotsas, E., Kharaghani, A., Evaporation in capillary porous media at the perfect piston-like invasion limit: Evidence of non-local equilibrium effects, Water Resources Research, Vol 53 (12), p. 10433-10449 (2017).

Prat, M., Percolation model of drying under isothermal conditions in porous media. International Journal of Multiphase Flow, Vol 19, No. 4, p. 691-704 (1993).

Prat, M., On the influence of pore shape, contact angle and film flows on drying of capillary porous media, International Journal of Heat and Mass Transfer, Vol 50, p. 1455-1468 (2007).

Prat, M., Pore network models of drying, contact angle and films flows, Chemical Engineering Technology, Vol 34, No. 7, p. 1029-1038 (2011).

Takei, T., Chikazawa, M., Kanazawa, T., Validity of the Kelvin equation in estimation of small pore size by nitrogen adsorption, Colloid and Polymer Science, Vol 275, p. 1156-1161 (1997).

Thiery, M., Baroghel-Bouny, V., Bourneton, N., Villain, G., Stéfani, C., Modélisation du séchage des bétons, analyse des différents modes de transfert hydrique, Revue européenne de Génie Civil, Vol 11, No. 5, p. 541-577 (2007).

Whitaker, S., Simultaneous heat, mass, and momentum transfer in porous media: A theory of drying. Advances in Heat Transfer, Vol 13, p. 119-203 (1977).

Yiotis, A.G., Stubos, A.K., Boudouvis, A.G., Yortsos, Y.C, A 2-D pore-network model of the drying of single-component liquids in porous media, Advances in Water Resources, Vol 24, p.439-460 (2001).

Yiotis, A.G., Salin, D., Tajerand, E.S., Yortsos, Y.C., Drying in porous media with gravity-stabilized fronts: Experimental results. Physical Review E, Vol 86, 026310 (2012).

Membrane characterization by evapoporometry and liquid-liquid displacement porosimetry: assessment from pore network simulation

Otman Maalal[a,b], Marc Prat[a*], René Peinador[b], Didier Lasseux[c]

[a]Institut de Mécanique des Fluides de Toulouse (IMFT), Université de Toulouse, CNRS, Toulouse, France.
[b]Institut de La Filtration et des Techniques Séparatives (IFTS), Rue Marcel Pagnol, 47510, Foulayronnes, France
[c]I2M, UMR 5295, CNRS, Univ. Bordeaux – Esplanade des Arts et Métiers, 33405 Talence, CEDEX, France

[*] *Corresponding author:mprat@imft.fr (+33534322883)*

Abstract

Evapoporometry (EP) and Liquid-Liquid Displacement Porosimetry (LLDP) are two techniques aiming at characterizing the pore size distributions of porous membranes from simple macroscopic data such as the evaporation rate (EP) or flow rate and pressure measurements (LLDP). The link between the pore size distribution (PSD) and the measured data is straightforward for simple porous microstructures for which the pores are essentially straight cylindrical tubes in parallel but much less obvious for more complex microstructures with interconnected pore networks. This link is studied from numerical simulations on model pore networks for both methods. This allows a detailed analysis of the evapoporometry technique and a comparative assessment of both methods.

Keywords: Pore body size distribution; Pore throat size distribution; Membrane characterization, Pore network model; numerical simulation

1 Introduction

Pore sizes play a key role in most separation processes with membranes and the pore size distribution (PSD) is therefore one of their most important characteristics. Not surprisingly, many experimental methods aiming at the membrane pore sizes determination have been developed, as recently reviewed [23, 24]. In this context, direct and indirect methods are commonly distinguished. Direct methods include microscopy and spectroscopic techniques while measured quantities are used in indirect methods in order to determine the PSD on the basis of phyiscal modeling employing for instance the Young-Laplace equation or the Kelvin equation. The net advantage of the latter lies in their simplicity and in the fact that they generally do not require expensive dedicated equipments. However, since the extraction of the pore sizes relies on theoretical considerations together with the use of a model, the quality and accuracy of the resulting identification is necessarily highly dependent on the relevance of the model. As a simple illustrative example, the extraction of the PSD in the Liquid-Liquid Displacement Porosimetry (LLDP) technique [25], relies on the consideration of a model of cylindrical tubes in parallel. While the pore space geometry of some membranes, such as the Anopore^{TM} membrane discussed in [23] and illustrated in Fig.1 is reasonably close to a system of straight tubes in parallel, the situation for other membranes, such as the PVDF membranes also illustrated in [23] and Fig.1, can be markedly different. The latter have an irregular fibrous highly interconnected porous structure.

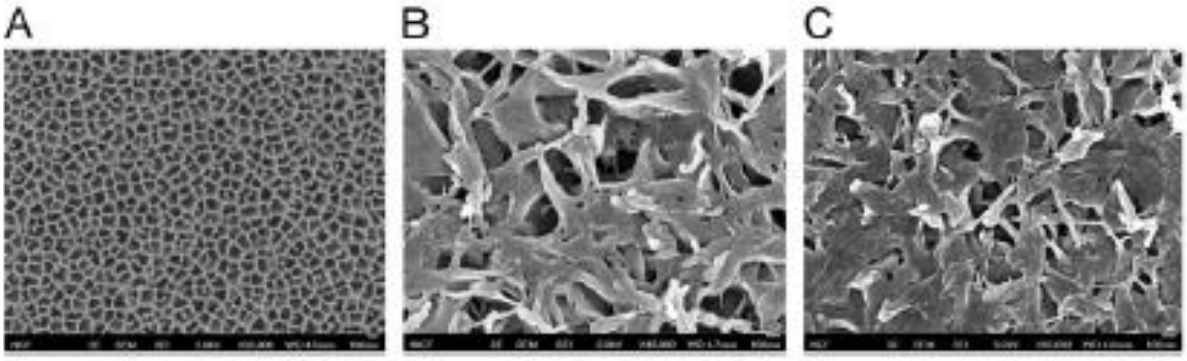
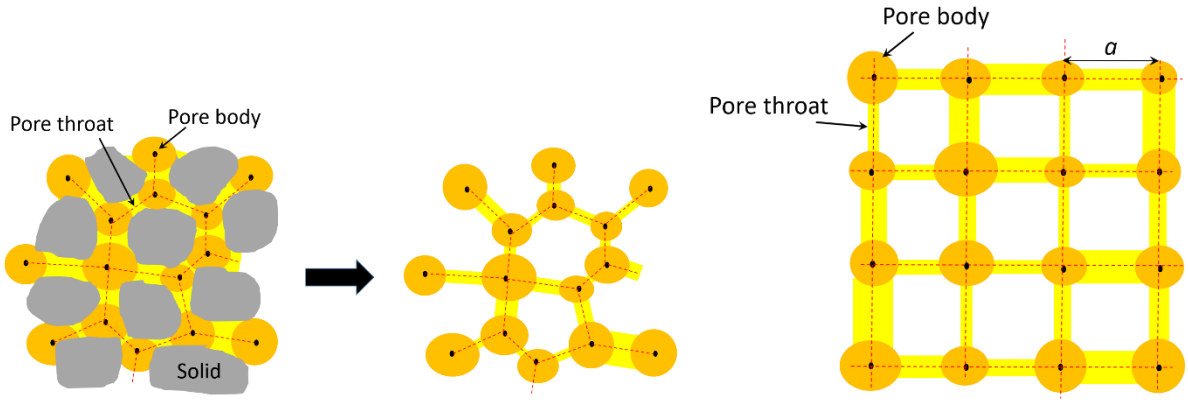


Fig. 1. Representative FESEM micrographs. (A) 100 nm AnoporeTM membrane, (B) 50 nm PVDF membrane, and (C) 20 nm PVDF membrane. The AnoporeTM membrane has a very regular non-interconnected columnar pore structure; PVDF membranes have an irregular fibrous interconnected porous structure (images and figure caption reproduced with permission from [23]).

The question then arises as to whether the LLDP PSD extraction from the consideration of a bundle of straight tubes in parallel is still valuable when the pore space is highly interconnected. With this respect, it is important to elucidate on what is really obtained from indirect methods. The focus of the present study is to bring some clarifications in this regard from numerical simulations for two indirect methods, namely the Liquid-Liquid Displacement Porosimetry (LLDP) technique [24-27], and the evapoporometry (EP) technique [23, 24]. According to the results reported in [24] for several membranes, it can be noted that the two techniques do not lead to the same PSD. An issue is therefore also to explain this situation and to evaluate both methods. The LLDP technique is based on the immiscible displacement of a wetting liquid by a non-wetting liquid (drainage) in the membrane pore space through a series of pressure steps. Two quantities are measured: the pressure in the displacing fluid at the membrane inlet and the displacing fluid flow rate through the membrane. The EP is based on the measurement of the evaporated mass of a wetting liquid initially saturating the membrane as a function of time. The present study is based on pore-scale numerical simulations of the processes occurring in both techniques. The advantage of the numerical procedure developed here is that the PSD is perfectly known a priori for the model pore structure under consideration since this is an input of the model pore structure. This PSD is referred to as the real PSD. The immiscible two-phase flow occurring in the LLDP and the evaporation process occurring in the EP are then numerically simulated in the model pore structure. From these simulations, quantities measured in LLDP and EP experiments, namely the pressure and displacing fluid flow rate for the LLDP and the evaporation rate for the EP, are computed and the PSD is extracted using interpretation procedures commonly used in the LLDP or EP. Finally, the resulting PSD are compared to the real PSD for both methods. The two-phase flow simulations with evaporation (EP) or without phase change (LLDP) in the model membrane are performed using a technique called pore network modelling (PNM), e.g. [28, 29]. As discussed in [30, 31], this technique is based on the representation of the pore space as a network of two main types of structural elements: the pore bodies and the pore throats. As schematically illustrated in Fig. 2, the pore bodies correspond to the local larger volumes in the pore space whereas the pore throats correspond to the constrictions, that is, to the narrower passages between the pore bodies. The concept of pore network is illustrated in Fig. 2a. In Fig. 2b, the simplified pore network considered for the present study is represented. It consists of a square pore network where the pore bodies are

spheres located at the nodes of a regular square grid whereas the pore throats are narrower cylindrical channels between pore bodies.



a) b)

Fig. 2. (a) Schematic partition of the pore space in pore bodies (shown in orange) and pore throats (in yellow) and extracted pore network; (b) square (2D) model pore network (the black dots correspond to the computational nodes).

This pore space partition leads to the consideration of two main distributions for characterizing the pore space: the pore body size distribution (PBSD) and the pore throat size distribution (PTSD). The latter is simply denoted by TSD in the study. As discussed in [30], it is argued that the size distribution derived from the LLDP technique should essentially correspond to the TSD because the immiscible displacements involved in the LLDP is mainly controlled by the constrictions. In any case, the distinction is made in this study between the TSD and the PBSD.

To assess the TSD and PBSD extraction from LLDP and EP simulations, the paper is organized as follows. In section 2, both characterization techniques, namely the LLDP and the EP, are briefly presented. The model membrane, a simple square pore network, is presented in Section 3 together with the LLDP drainage and EP evaporation PNM algorithms. Simulations results are presented in Section 4. A short discussion is presented in Section 5. Conclusions are drawn in Section 6.

2. Liquid-liquid displacement porosimetry (LLDP) and evapoporometry (EP)

2.1 Liquid-liquid displacement porosimetry (LLDP)

The liquid-liquid displacement porosimetry [24-27], is based on performing the immiscible displacement of a wetting liquid by a non-wetting one in the membrane, referred to as drainage in the porous media literature [32]. The membrane to be characterized is initially fully saturated with the wetting liquid. Then, a displacement by injection of a non-wetting immiscible liquid at the inlet is carried out. To do so, the pressure is increased step by step in the injected fluid at the inlet while the pressure is kept constant at the outlet. In addition to the pressure drop, ΔP, that is, the pressure difference between the inlet and the outlet, the displacing liquid volume flow-rate is measured for each pressure step after stabilization of the inlet pressure. The LLDP procedure is stopped when the flow rate starts varying linearly with the pressure drop, which indicates that no more wetting fluid can be displaced. A characteristic throat size, r_{cj}, can then be associated with each pressure step *j* assuming cylindrical pores via the Young-Laplace equation

$$\Delta P_j = \frac{2\gamma\, cos\theta}{r_{cj}} \qquad (1)$$

where θ is the contact angle of the fluid-fluid solid system under consideration (here $\theta = 0$, *i.e.*, the displaced fluid is perfectly wetting) and γ is the interfacial tension. To obtain the TSD, the number of throats of size r_{cj}, or more precisely the fraction of throats having the size r_{cj}, must be determined. This is commonly performed from the flow rate information considering the pore structure as a bundle of cylindrical straight tubes in parallel. The number of tubes being invaded at the j^{th} step is then determined from the volume flow-rate measurement using Poiseuille's law. The volume flow-rate, Q_j, at the j^{th} pressure step is expressed as the sum of all volume flow-rates in the entire set of invaded tubes which are of radius larger or equal to r_{cj},

$$Q_j = \frac{\pi \Delta P_j}{8\mu L} \int_{r_{cj}}^{\infty} r^4 f_{LLDP}(r) dr \qquad (2)$$

where μ is the dynamic viscosity of the displacing fluid, L is the tube length, r is the tube radius and f_{LLDP} is the probability density function (p.d.f.) to be characterized. Combining Eqs.(1) and (2) and deriving with respect to ΔP_j yields

$$f_{LLDP}(r_{cj}) = \frac{8\mu L}{\pi}\left(\frac{\Delta P_j}{2\gamma}\right)^5\left(\frac{dQ_j}{d\Delta P_j} - \frac{Q_j}{\Delta P_j}\right) \quad (\mathbf{3})$$

This probability density function is then normalized so that $\int_0^{+\infty} f_{LLDP}(r)dr = 1$. The TSD is thus extracted from Eqs. (1) and (3), using the measurements of the pressure difference ΔP and the volume flow-rate Q. The above development makes clear that the LLDP implies to consider a model structure in order to obtain the TSD, the structure commonly used being the parallel cylindrical tubes model.

2.2 Evapoporometry (EP)

Unlike the LLDP technique, the EP technique does not require the consideration of a geometrical model for the pore space. To begin with, it is of interest to describe the experimental procedure and the interpretation of the resulting data employed in [23]. Technically, the method consists in saturating the membrane by a volatile wetting liquid, isopropanol being the commonly used fluid. As sketched in Fig. 3, the saturated membrane is set in a cylindrical test diffusion cell. The latter is placed on an electronic microbalance placed on an anti-vibration table, [23-24]. The evaporated mass is recorded with the microbalance at a fixed time frequency (for instance every 10 s in the measurements reported in [23]). The whole equipment is set in an environmental chamber at a fixed temperature. Initially, a liquid layer is present on the upper surface of the saturated membrane. This allows determining a reference evaporation rate independent of the throat size. After a while, once this liquid film is fully evaporated, evaporation of the liquid saturating the membrane starts, first from the menisci forming at the surface of the membrane and then within the membrane. This affects the evaporation rate because the isopropanol equilibrium vapor pressure, P_{vequ}, at the surface of a curved meniscus depends on the meniscus curvature. This effect can be quantified thanks to the Kelvin relationship, which for a meniscus in a cylindrical pore can be expressed as,

$$P_{vequ} = P_{vsat}\exp\left(-\frac{M_v}{RT}\frac{2\gamma}{\rho r_{curv}}\right) \quad (4)$$

where P_{vsat} is the saturation vapor pressure, M_v is the isopropanol molecular weight, R is the universal gas constant, T is the temperature of the ambient air, ρ is the liquid density and r_{curv} is the meniscus radius of curvature.

Note that the height, *H*, of the test cell is much larger than the membrane thickness. For instance, *H* = 10.5 cm in the set-up used in [23] and 2.5 cm in the one used in [24]. Since the membrane thickness is small compared to the diffusion length *H* in the cell, it is assumed that the external mass transfer is essentially in the direction orthogonal to the membrane surface, between the top surface of the membrane and the top of the cell. By contrast, the internal mass transfer refers to the mass transfer inside the membrane pore space. The evaporation rate is thus expressed as,

$$W \approx kA\frac{M_v}{RT}P_{vequ} \tag{5}$$

where *A* is the cross-sectional area of the diffusion cell and *k* is the external mass transfer coefficient. The latter can be determined from the evaporation rate when the liquid film is present

$$W_{ref} \approx kA\frac{M_v}{RT}P_{vsat} \tag{6}$$

Note that the isopropanol vapor partial pressure at the top of the cell is very small and considered in practice to be equal to zero. Combining Eqs. (5) and (6) yields

$$\frac{P_{vequ}}{P_{vsat}} = \frac{W}{W_{ref}} \tag{7}$$

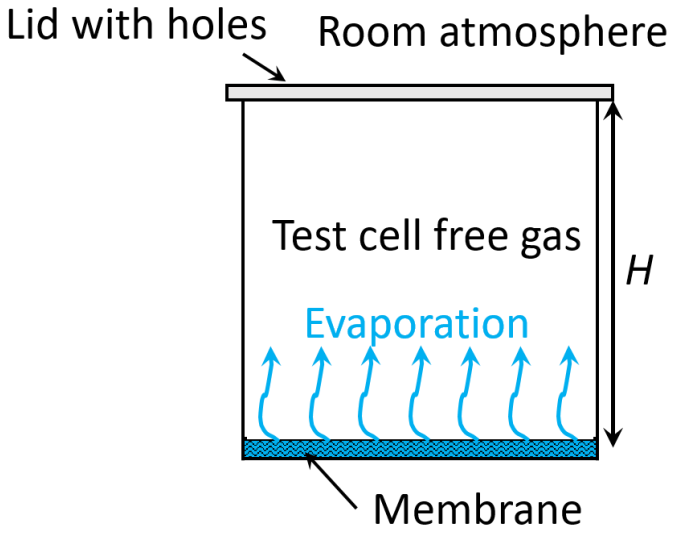


Fig. 3. Sketch of evapoporometry test cell. Scales are distorted for clarity (the membrane thickness is actually much smaller that the height *H* of the gaseous diffusion region in the test cell).

When this result is introduced in the Kelvin relationship, Eq. (4), the average meniscus radius of curvature can be expressed as a function of the evaporation rate as

$$r_{curv} = -\frac{M_v}{RT}\frac{2\gamma}{\rho \ln\left(\frac{W}{W_{ref}}\right)} \tag{8}$$

The evaporation rate is determined from the evaporated mass measurement. Consider two successive measurements of the liquid mass, m_i and m_{i+1}, corresponding to two times, t_i and t_{i+1}. The evaporation rate is then simply computed as,

$$W = \frac{m_{i+1} - m_i}{t_{i+1} - t_i} \tag{9}$$

In the EP technique, it is admitted that the radius of curvature of a meniscus is close to the element (pore body or throat) radius, r, in which the meniscus is located, thus $r \approx r_{curv}$. Assuming that during the interval $t_{i+1} - t_i$, the fraction of liquid only contained in elements (pore bodies or throats) of radius r was evaporated, the corresponding mass fraction, f_{EP}, is then simply given by

$$f_{EP} = \frac{m_{i+1} - m_i}{m_t} \tag{10}$$

where m_t is the total mass of liquid initially filling the membrane. The PSD, or more precisely the PBTSD (where PB stands for pore bodies and T for throats) is actually obtained in a discrete form. The distribution interval [r_{min}, r_{max}] is divided into n_b bins, r_{min} and r_{max} being respectively the minimum and maximum element radius present in the membrane. A radius is evaluated corresponding to each time interval of the experimental mass evaporation rate curve using Eqs. (5) and (8) and the associated fraction, f_{EP}, is determined from Eq. (10). The sum of the mass fractions corresponding to each radius contained within each bin hence leads to the determination of the fraction of elements of this bin, finally leading to the PBTSD discretized in n_b intervals.

In Fig. 4, the variation of the equilibrium vapor pressure is represented as a function of the meniscus radius of curvature for isopropanol as determined from Eq. (4). The Kelvin effect is noticeable only for radii of curvature in the submicronic range and more significantly for radii approximately below 20 - 25 nm. The EP technique is therefore only suitable for membranes with sufficiently small pores, such as the ultrafiltration membranes whose pores are typically in the range [1 - 100 nm].

However, for very small pores of radius below 2 nm, the applicability of the Kelvin relationship can be questioned [33]. Thus, one may consider that the applicability of EP is rather for membranes with pore sizes in the range [2-100 nm].

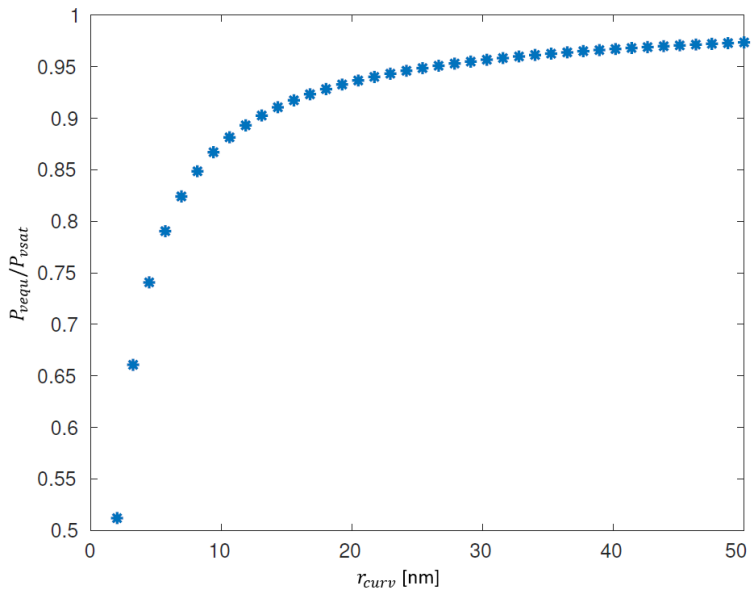


Fig.4. Equilibrium vapor pressure as a function of meniscus radius of curvature for isopropanol.

3. Pore network models

As previously stated, LLDP and EP pore scale processes are simulated in the model pore structure depicted in Fig. 2b, using pore network models (PNM). The aim of the PNM is to simulate the drainage process involved in the LLDP and the evaporation process in the case of the EP. The corresponding PNM algorithms are described in previous publications, both for the LLDP [34] and evaporation [31] simulations. A summary of these algorithms is given below.

3.1 Pore network

As illustrated in Fig. 2b, the model pore structure considered in this study is a square network. Pore bodies, *i.e.*, the local larger cavities, are located at the nodes of the square grid. The network size is the number of pore bodies in the network along each main direction. Simulations were performed on 20 × 20 networks. The distance between the centers of two adjacent pore bodies is the lattice spacing a. In the present study, a = 300 nm. The pore bodies are spheres of radius r_p. Pore body

radii are distributed randomly within a specified range [r_{pmin}, r_{pmax}] according to a given probability density function (p.d.f.). Pore throats connecting the pore bodies are cylinders of radius r_t. The throat size is randomly distributed within a specified range [r_{tmin}, r_{tmax}] according to a given p.d.f. with the constraint that a throat radius cannot be greater than the smallest radius of the two adjacent pore bodies. In this work, the pore body size distribution (PBSD) and throat size distribution (TSD) are either Gaussian or uniform. The length, l, of a throat is computed from the lattice spacing and the sizes of the neighboring pore bodies 1 and 2 as,

$$l = a - r_{p1} - r_{p2} \tag{11}$$

3.2 LLDP PNM

A drainage simulation consists in simulating the two fluids equilibrium pattern at every pressure step. The non-wetting fluid invasion is computed as follows. A capillary pressure invasion threshold is specified for each throat according to the Young-Laplace equation as

$$p_{cth} = \frac{2\gamma}{r_t} \tag{12}$$

An interfacial throat, that is a throat with a meniscus at its entrance, can be invaded only if the pressure difference between the displacing fluid and the displaced one at the considered meniscus is greater or equal to the capillary pressure invasion threshold,

$$P_{nwi} - P_w \geq \frac{2\gamma}{r_t} \tag{13}$$

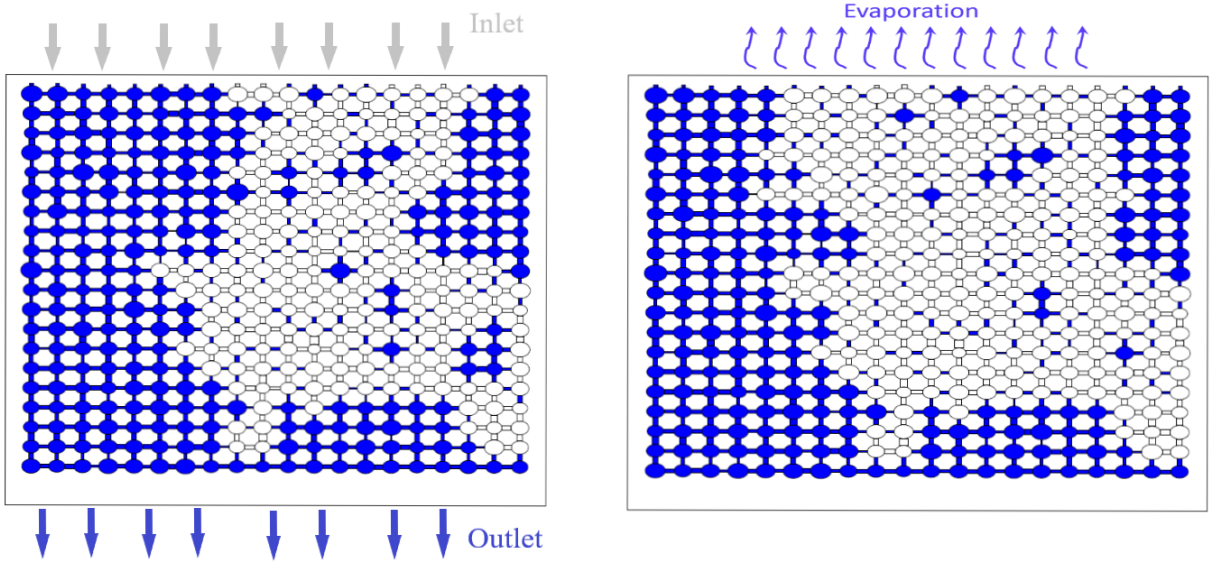
Here, P_{nwi} is the pressure in the adjacent pore body occupied by the non-wetting fluid and P_w is the pressure in the wetting fluid. The latter is assumed to be spatially uniform and equal to the outlet pressure P_{outlet}. For a given fluid configuration, the pressure field P_{nwi} is computed at each node of the network occupied by the non-wetting (displacing) fluid. This is performed by expressing the mass balance at each displacing fluid node *i* as,

$$\sum Q_{nw\,i,j} = 0 \tag{14}$$

where $Q_{nw\,i,j}$ is the non-wetting fluid volume flow rate between pore body i and adjacent pore body j. If the throat between pore bodies i and j is occupied by the wetting fluid then $Q_{nw\,i,j} = 0$. If the throat is occupied by the non-wetting fluid, then

$$Q_{nw\,i,j} = \frac{\pi r_{t\,i,j}^4}{8\mu_{nw} l_{i,j}} \Delta P_{i,j} \tag{15}$$

where $r_{t\,i,j}$ and $l_{i,j}$ are the radius and length of the throat linking the two pore bodies respectively, while $\Delta P_{i,j}$ is the pressure drop in the non-wetting phase between the two neighboring pore bodies. Taking into account the pressure boundary conditions at the inlet ($P_{inlet} = \Delta P + P_{outlet}$) and outlet ($P_{outlet} = Cte$) and the zero-flux condition imposed on the lateral faces of the network, Eqs. (14) and (15) lead to a linear system for the pressure field in the non-wetting fluid. This system is numerically solved using the conjugate gradient method. Then the interfacial throats such that Eq. (13) is verified are identified. The one with the largest relative difference $\left((P_{nwi} - P_w) - \frac{2\gamma}{r_t}\right) / \frac{2\gamma}{r_t}$ is invaded and the procedure is repeated until the equilibrium is reached, that is until $(P_{nwi} - P_w) < \frac{2\gamma}{r_t}$ for all interfacial throats. When an equilibrium is reached, the displacing fluid flow rate Q_{nw} is computed at the outlet using Poiseuille's law applied to all non-wetting fluid throats connected to the outlet. As with a LLDP experimental device, this procedure yields the functional dependence $Q_{nw}(\Delta P)$.



a) b)

Fig. 5. a) Typical drainage LLDP pattern in the network. The displacing fluid in blue is injected at the bottom. The displaced fluid is in light grey, b) EP fluid distribution in the network (liquid clusters in blue, gas phase and solid phase in white).

In Fig. 5a, a typical LLDP drainage pattern obtained with the drainage PNM algorithm is represented.

3.3 EP PNM

As discussed in [31] and illustrated in Fig. 5b, the evaporation process is characterized by the formation of liquid clusters. In order to compute the evaporation rate from each cluster, the isopropanol vapor partial pressure at each node *i* of the network occupied by the gas phase is determined from the mass balance,

$$\sum_j \phi_{ij} = 0 \tag{16}$$

Here, ϕ_{ij} is the diffusive mass flow rate between pore bodies *i* and pore *j* if both are fully occupied by the gas phase or between pore body *i* and the meniscus at the entrance of an adjacent throat if this throat is occupied by the liquid phase. The diffusive mass flow rate, ϕ_{ij}, is computed using Fick's law. For instance, between two gaseous pore bodies connected by a gaseous throat, ϕ_{ij} reads

$$\phi_{ij} = D_{eff} \frac{M_v}{RT} \pi r_{tij}^2 \left(\frac{P_{vj} - P_{vi}}{a}\right) \tag{17}$$

where the effective diffusion coefficient, D_{eff}, is computed as the harmonic mean of the vapor molecular diffusion coefficient and the Knudsen diffusion coefficient [31]. To obtain the vapor partial pressure field from Eq. (16), boundary conditions must be specified. Zero flux conditions are specified at the lateral and bottom sides of the network. The coupling with the external mass transport in the cell is performed by locating additional computational nodes in the test cell, *i.e.*, in the gas region above the membrane represented in Fig. 3. One can refer to [31] for more details. Since a key feature of EP test cell is that the membrane thickness is much smaller than the cell height, an external layer of height *H* equal to 500 *a* is considered. The network to diffusion layer thicknesses ratio is thus equal to 20 *a* / 500 *a* = 0.04 in the simulations. It is about one order of magnitude larger than in the set-up used in [24] where *H* = 25 mm and the membrane active

thickness is on the order of 10 μm. Nevertheless, this ratio can be reasonably considered as sufficiently small for the hypothesis of a unidirectional evaporation flux to be valid. A key issue is the specification of the vapor partial pressure at the boundary of each cluster, or, according to the Kelvin relationship (4), the curvature radius of the menisci forming the boundary of each liquid cluster. First, on the ground that the evaporation process is quite slow in the EP, as a result of the significant height H of the test cell, viscous effects can be neglected and, therefore, the fluid distribution evolution in the network is controlled by capillary effects only. The consequence is that the radius of curvature is the same for every meniscus at the boundary of a given cluster. Second, it is argued that the meniscus curvature at the boundary of a given cluster should adapt so that the mass flow rate from a cluster cannot be negative. By convention, the mass flow rate from a cluster is positive when there is a net evaporation. A negative mass flow rate would correspond to condensation, thus to the potential growth of the cluster and thus to a change in the meniscus curvature radius. As explained in [31], an iterative numerical procedure implying to solve repeatedly the system of equations obtained from Eq. (16) is used to determine the radius of curvature, that is, the isopropanol equilibrium vapor partial pressure at the boundary of each cluster so that there is no negative cluster mass flow rate. Once the iterative procedure reaches convergence, the evaporation rate, Φ_k, at the boundary of each cluster k present in the network can be computed. Then the procedure is similar to the one for drying PNM simulation in the absence of Kelvin effect [35]. The evaporation algorithm in the presence of the Kelvin effect can finally be summarized as follows:

(1) All liquid clusters present in the network are labelled.

(2) The interfacial element (pore body or throat) with the lowest threshold capillary pressure is identified for each cluster.

(3) The vapor partial pressure at the boundary of each cluster is computed employing the iterative procedure outlined above.

(4) The evaporation rate at the boundary of each cluster is computed.

(5) For each cluster, the mass loss corresponding to the evaporation rate determined in step (4) is assigned to the element identified in step (2).

(6) The element eventually invaded is the one which is the first to be completely drained among the elements selected in step (2).

(7) The phase distribution within the network is updated and the procedure is iterated starting from step (1).

A typical fluid distribution obtained with the above algorithm and made of many liquid clusters is represented in Fig. 5b.

In direct link with the EP, the EP PNM allows computing the mass variation as a function of time due to evaporation as well as the evaporation rate *W*. The mass is simply obtained as

$$m(t) = m(0) - \rho \sum_{i=1}^{i=n_t} S_{ti}(t) V_{ti} - \rho \sum_{i=1}^{i=n_p} S_{pi}(t) V_{pi} \tag{18}$$

where n_t and n_p are respectively the number of throats and pore bodies in the network, V_{ti} and V_{pi} the volume of throat and of pore body # *i*, S_{ti} (S_{pi} respectively) is the saturation in the throat (pore body respectively) # i. The latter is equal to 1 when the element is fully occupied by the liquid, zero when the element is empty (that is fully occupied by the gas-phase) and between 0 and 1 when the element is partially filled with liquid.

The evaporation rate, W_{PNM}, is determined from the vapor partial pressure field by summing up all the mass flow rate contributions between two horizontal adjacent rows of computational nodes in the external boundary layer using expressions similar to Eq. (17)

$$W_{PNM}(t) = -\sum_{1}^{N} D_{eff} \frac{M_v}{RT} \, a^2 \left(\frac{P_{vj} - P_{vi}}{a} \right) \tag{19}$$

In this expression, *N* is the number of computational nodes in the horizontal direction, P_{vj} and P_{vi} are the vapor partial pressures at the upper and lower rows of nodes between which the evaporation rate is computed. Then the element (pore bodies and throats) probability density function can be determined from

$$f_{EP-PNM} = \frac{W_{PNM}\left(\frac{t_i + t_{i-1}}{2}\right)(t_i - t_{i-1})}{m_t} \tag{20}$$

where t_i and t_{i-1} are two successive elapsed times in the EP PNM simulation.

Table 6 Isopropanol physical properties and temperature condition

Interfacial tension (N/m)	2.17×10^{-2}
Contact angle	0
Density (kg/m^3)	786
Molecular weight (kg/mol)	6.1×10^{-2}
Temperature (K)	293
Saturation vapor pressure (Pa)	4400
Binary diffusion coefficient (m^2/s)	1.06×10^{-5}
Dynamic viscosity (Pa.s)	2.37×10^{-3}

The evaporation rate can be also computed as in the EP procedure (Eq. (9)) from

$$W_m\left(\frac{t_i+t_{i-1}}{2}\right) = \frac{m(t_i)-m(t_{i-1})}{t_i-t_{i-1}} \tag{21}$$

where t_i and t_{i-1} are two successive elapsed times. In principle, W_{PNM} and W_m must be equal but, as will be detailed below, the EP procedure can introduce some errors due to its discrete nature, more specifically because of the fact that the evaporation rate is determined at a fixed time frequency. For this reason, it is interesting to distinguish W_{PNM} from W_m.

Then the element (pore bodies and throats) probability density function is determined from the equivalent of Eq. (10), namely,

$$f_{EP-m} = \frac{m_{i+1} - m_i}{m_t} \tag{22}$$

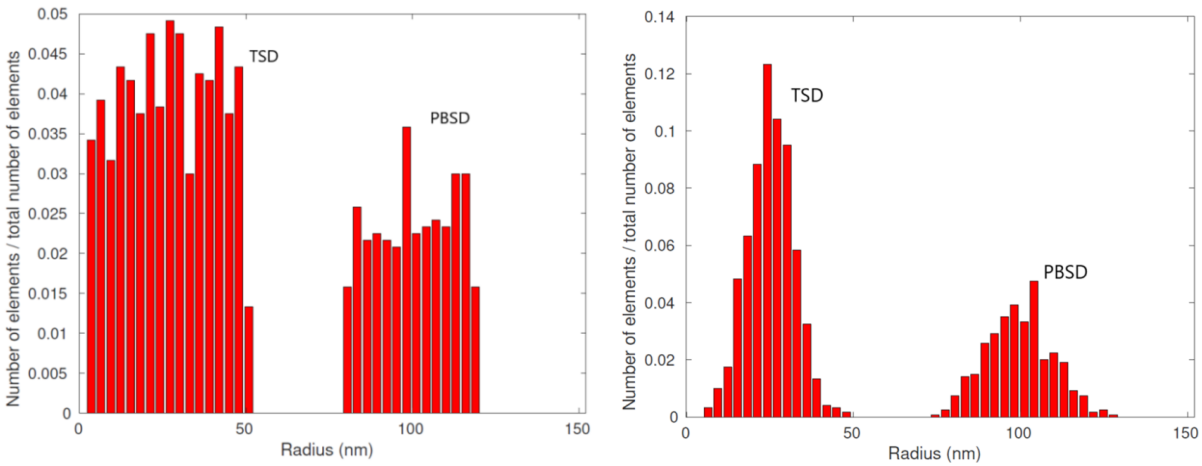
The EP PNM simulations were performed for the isopropanol physical properties summarized in Table 6

4. Results

The LLDP and EP PNM simulations were performed for a 20 × 20 network and two types of element distributions: uniform or Gaussian. Details on the distributions are given in Table 7. These distributions are the reference (also called real) TSD and PBSD; they are depicted in Fig. 6.

Table 7. Reference uniform and Gaussian TSD and PBSD.

p.d.f. type	Uniform	Gaussian
TSD	r_{tmin} = 2 nm, r_{tmax} = 50 nm	Mean: 25 nm Standard deviation: 7 nm
PBSD	r_{pmin} = 80 nm, r_{tmax} = 120 nm	Mean: 100 nm Standard deviation: 10 nm



a) b)

Fig. 6. Reference uniform (a) and Gaussian (b) TSD and PBSD.

4.1 LLDP

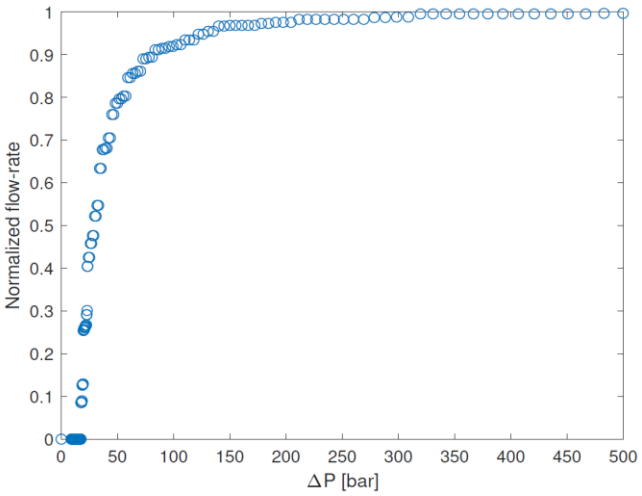
Main results are illustrated in Fig. 7. As discussed in [34] and also mentioned in [24], the LLDP technique is not adapted to determine both the PBSD and TSD but, rather, only the TSD, owing to the high dependence of the drainage process on the pore space constrictions. For this reason, only the TSD is considered in this section for the comparison with the real distributions. In Fig. 7a, the normalized flow rate obtained from the simulation of the LLDP is represented versus the applied pressure difference, ΔP, between the inlet and the outlet, in the case of the Gaussian network. The normalized flow rate is computed as

$$\chi_i = \frac{\frac{Q_i}{\Delta P_i}}{\frac{Q_{if}}{\Delta P_{if}}} \tag{23}$$

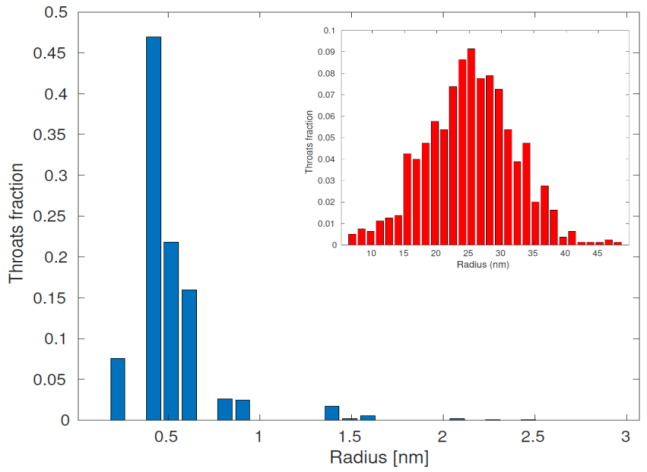
where Q_i is the displacing flow rate at the i^{th} pressure difference, ΔP_i, between the inlet and outlet, whereas Q_{if} is the flow rate obtained for the largest pressure difference, ΔP_{if}, considered in the simulation.

As illustrated in Fig. 7b and 7c, the LLDP procedure introduces a shift toward unrealistic small throat sizes. This shift, which was studied in some details in [34], is due to the displacing fluid viscous pressure drop through the membrane. Consider two throats of the same size, the first one being located near the membrane outlet, the second one near the inlet. The pressure near the inlet is $P_{inlet} = \Delta P + P_{outlet}$ while the pressure near the outlet is much lower, close to P_{outlet}. As a result, the throat near the outlet will be invaded for a much greater pressure difference across the membrane than the one close to the inlet. In other words, a different throat size is affected to two throats of identical size and the pressure needed for invading the throats near the outlet is overestimated, which leads to the wrong identification of too small throats. Also, it can be noted that the nature of the distribution, *i.e.*, Gaussian or uniform, is not correctly identified, with a more pronounced discrepancy in the case of the uniform distribution.

a)


Normalized flow-rate
ΔP [bar]
0
0.1
0.2
0.3
0.4
0.5
0.6
0.7
0.8
0.9
1
0
50
100
150
200
250
300
350
400
450
500

b)



c)

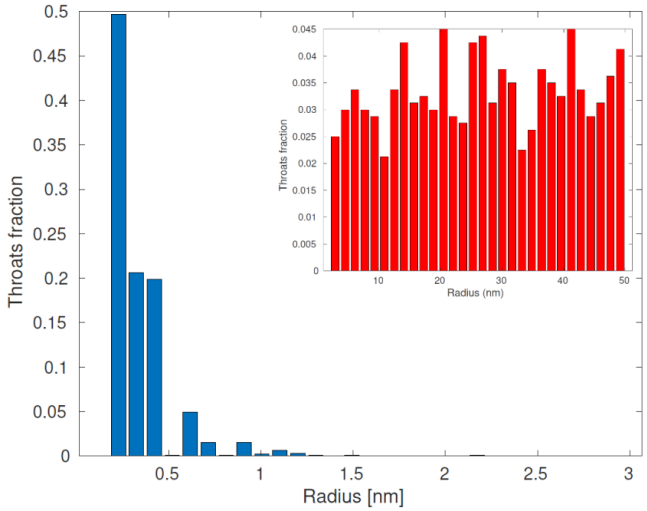
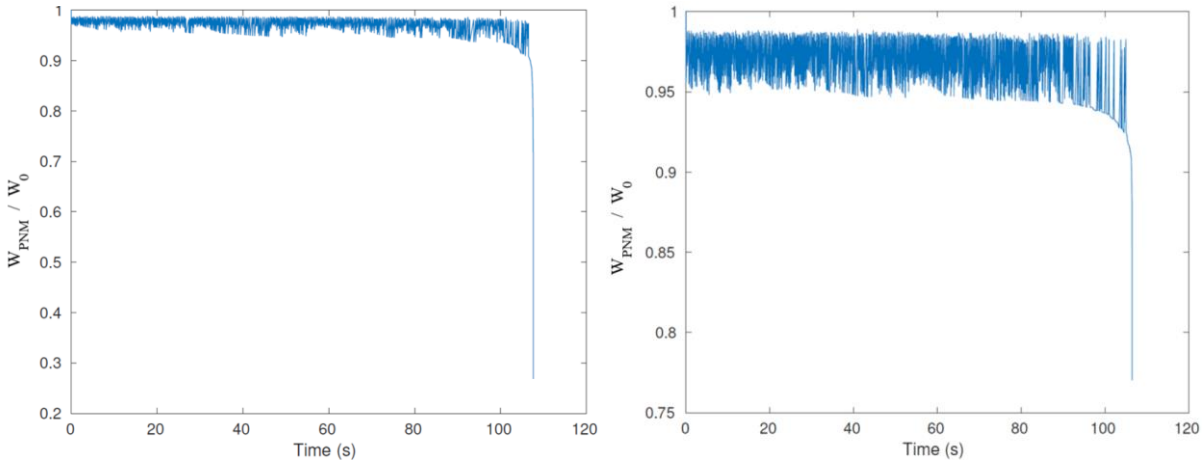


Fig. 7. a) LLDP curve: displacing fluid normalized flow rate (χ) as a function of inlet – outlet pressure difference (Gaussian distribution); TSD determined from LLDP procedure for: b) the Gaussian distribution; c) the uniform distribution. Reference TSD are represented as insets in both cases.

4.2 EP

In Fig. 8, the variation of the evaporation rate, as determined from Eq. (19), is represented versus time for the uniform and Gaussian distributions. In this figure, $W_{PNM}(t)$ is normalized by the evaporation rate, W_0, at t = 0, *i.e.*, when the network is fully saturated and the menisci at the network surface are flat. One can observe a long plateau followed by an abrupt drop in the evaporation rate. At first glance, these curves look very similar to the ones reported in the EP experimental works, [23, 24]. However, the interpretation is quite different here. In [23], the plateau is entirely attributed

to the evaporation of the liquid film standing initially at the surface of the membrane and the drop in the evaporation rate is attributed to the occurrence of evaporation in the pores. In [24], part of the plateau is attributed to the evaporation of the free-standing liquid initially present on the top of the membrane. In the present simulations, there is no film. Initially, the network is saturated and in contact with the cell test atmosphere at its top surface. Clearly, the plateau corresponds to evaporation in the pores. This is illustrated in Fig. 9, which shows the computed fluid distribution in the network at different times. This contrast is an indication that excessive care must be taken while interpreting the experimental evaporation rate curve versus time as the constant rate period may include part of the evaporation within the pores, depending on the pore structure.



a) b)

Fig. 8. Normalized evaporation rate as a function of time for the uniform (a) and Gaussian (b) TSD and PBSD.

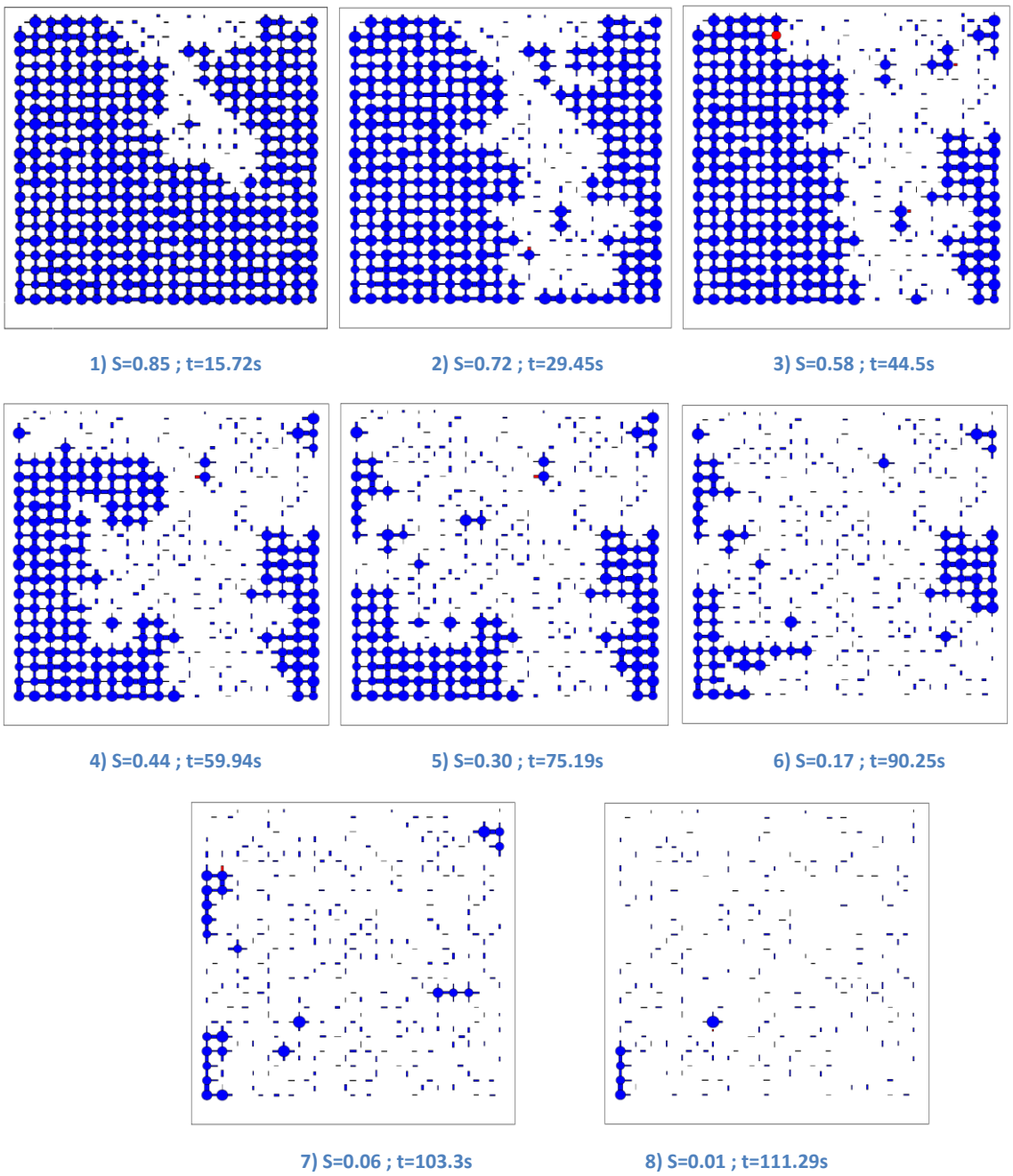


Fig. 9. Liquid (in blue) gas (in white) distributions in the network at different times for the case corresponding to Fig.8a (uniform distributions). Partially evaporated pores and throats have the red color in the figures.

It must also be noted that the evaporation rate obtained from the numerical simulations fluctuates with time. In other words, the evaporation rate can slightly increase during the drying process. This

somewhat counter-intuitive result is due to the Kelvin effect. As discussed in [31], the vapor pressure at the boundary of each cluster fluctuates because of the menisci curvature fluctuations during the drying process. As a result, when, for instance, a larger throat becomes an interfacial throat, the menisci curvature decreases and therefore the menisci vapor pressure increases according to Kelvin's relationship. This, in turn, induces a larger evaporation rate. The origin of the fluctuations can be simply illustrated with the situation depicted in Fig.10, assuming that the membrane is made here, for simplicity, of a spatially periodic arrangement of non-interconnected vertical columns of cylindrical pores of variable section. Only the top of a single column of pores is shown in Fig. 10.

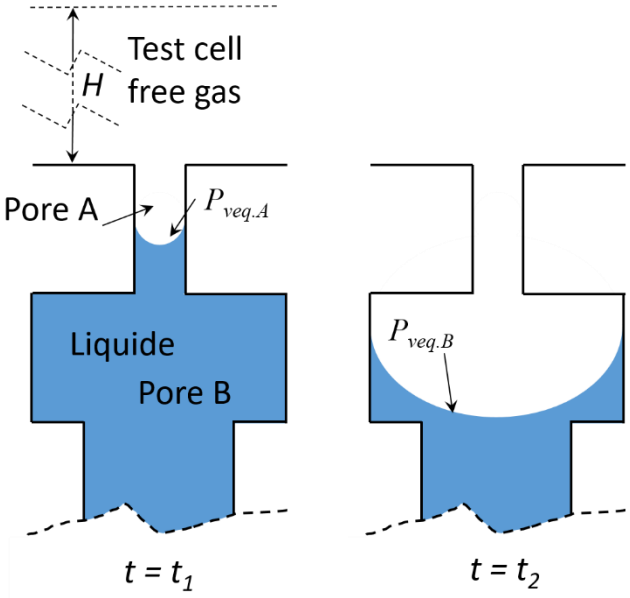


Fig. 10. Illustrative situation leading to an increase in the evaporation rate when the meniscus moves from pore A to pore B.

Since the size of pore A is smaller than the size of pore B, $P_{veq.A} < P_{veq.B}$ according to Kelvin's relationship given in Eq. (4). Then, since the membrane, and thus the distance between two pores, is very small compared to the length of the free gas region in the cell test, *i.e.*, $a << H$, the evaporation rate, when the meniscus is in pore A, is $W_A \approx kA\frac{M_v}{RT}P_{vequ\,A}$ and equal to $W_B \approx kA\frac{M_v}{RT}P_{vequ\,B}$ when the meniscus is in pore B. Since $P_{vequ\,A} < P_{vequ\,B}$, $W_B > W_A$. Thus, the

evaporation rate increases when the meniscus moves from pore *A* to pore *B*. Conversely, the evaporation rate may again decrease if the meniscus moves into a smaller pore below pore B.

As a consequence, the fluctuations, as illustrated in Fig. 8, should not be confused with possible parasitic fluctuations that might occur during mass measurement in the experimental EP operation. The fluctuations depicted in Fig. 8 are intrinsic to the drying process and it is important to capture them properly as discussed below.

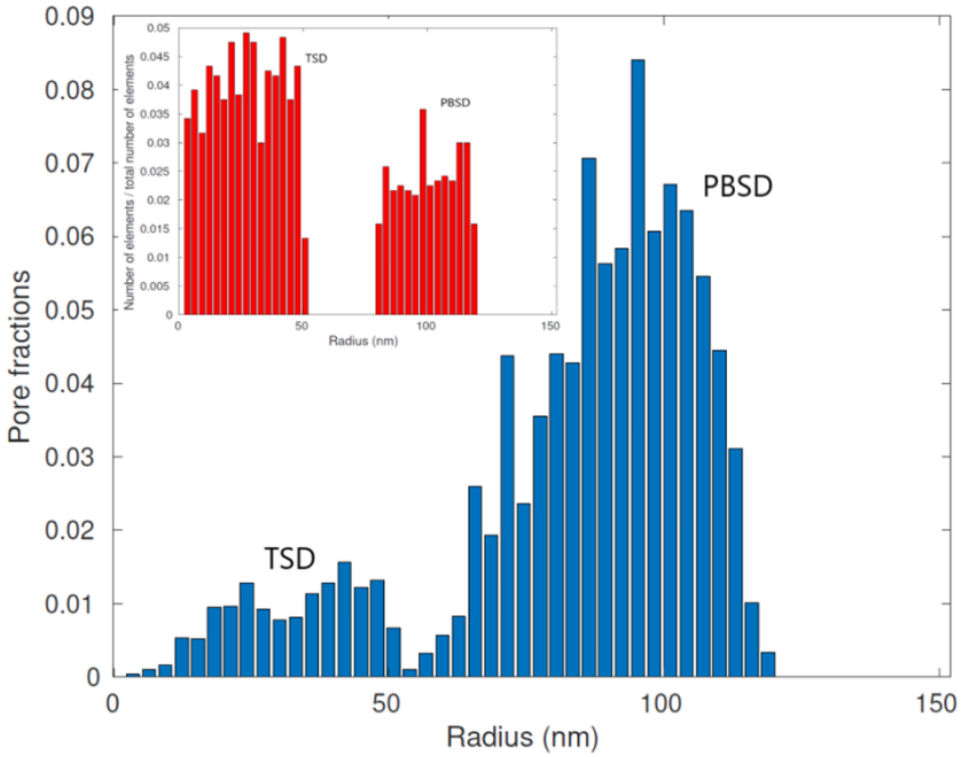


Fig. 11. TSD and PBSD obtained from EP using the W_{PNM} curve (Fig. 8) for the uniform reference distributions (shown in the inset).

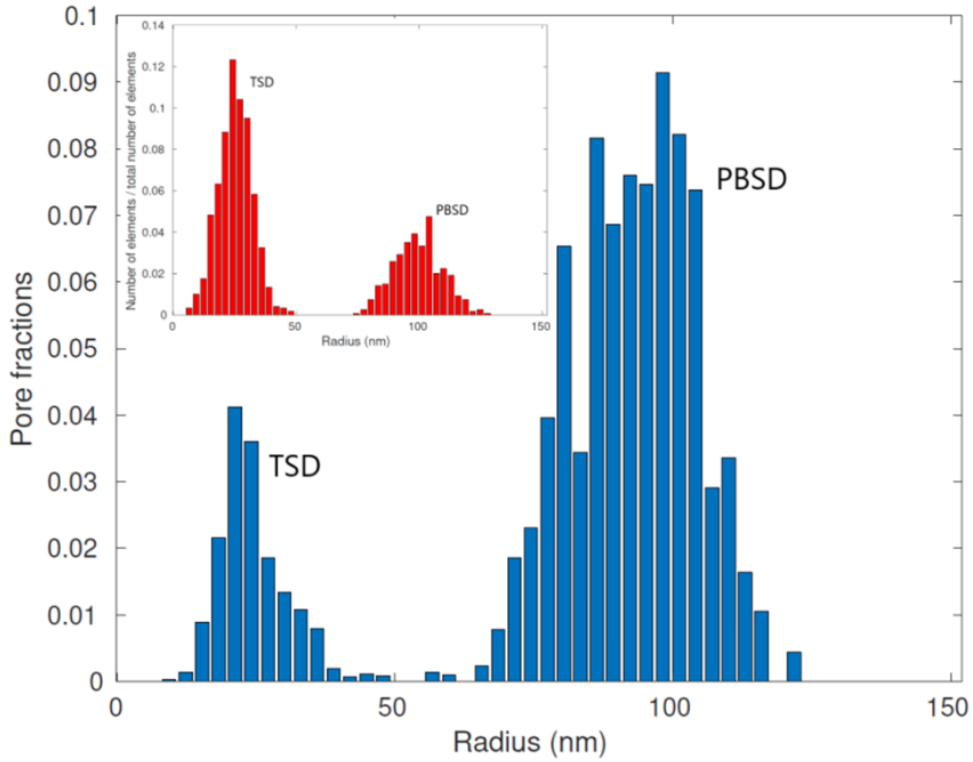


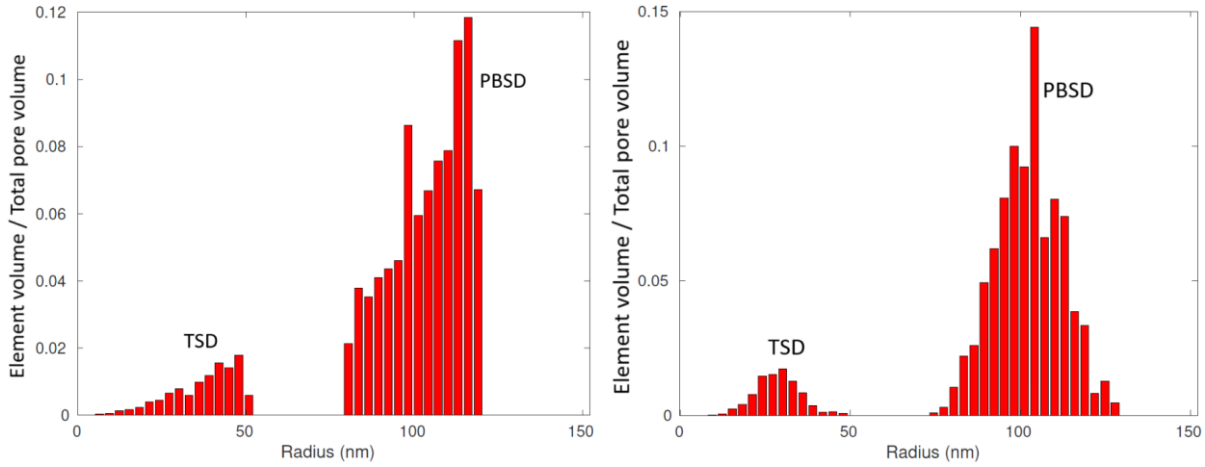
Fig. 12 TSD and PBSD obtained from EP using the W_{PNM} curve (Fig. 8) for the Gaussian reference distributions (shown in the inset).

The TSD and PBSD, obtained from the results shown in Fig. 8 and by applying Eq. (8) together with the expression of W_{PNM} given in Eq. (19), are depicted in Fig. 11 and 12 for the reference uniform and Gaussian distributions respectively.

As can be seen from Figs. 11 and 12, the results are quite appealing. Both element populations, namely the throats and the pore bodies, are retrieved. The sizes are in the correct ranges. In the case of the Gaussian distributions, the identified distributions are reasonably Gaussian-like. The identified and reference uniform distributions are also reasonably similar. However, it can be observed that the pore bodies and throats fractions are different in the extracted distributions compared to the reference ones. In brief, there are much less throats than pore bodies in the identified distributions compared with the reference distributions.

This may be explained as follows. The pore fractions presented in the distributions obtained with the evapoporometry procedure are weighted by the mass of each pore body or throat, that is, by the volume of each element. In other words, the probability densities obtained from the EP procedure represents the contribution of the throats or pore bodies to the volume of the pore space in the

membrane. As the pore bodies have volumes greater than the throats (keeping in mind that the pore body sizes are greater than the adjacent throat sizes), the extracted probabilities of pore bodies are consequently greater in comparison with the throat ones. Therefore, to make a fair comparison, the reference TSD and PBSD should represent the volume fraction of the porous void as well, rather than simply the fraction of the number of elements. For every pore body or throat, the corresponding probability density function is the volume of that pore body (sphere) or throat (cylinder) divided by the total void volume. The reference TSD and PBSD obtained after this correction is applied are reported in Figures 13.a and 13.b for the uniform and Gaussian distributions respectively.



a) b)

Fig.13. Reference uniform (a) and Gaussian (b) TSD and PBSD after consideration of throat and pores volumes.

As can be observed from the comparison between Figs. 11 and 12 and Fig. 13, the agreement between the extracted distributions (Figs. 11 and 12) and the reference distributions (Fig. 13) is quite satisfactory. The contribution of each element category, *i.e.*, pore bodies or throats, to the pore space volume is fairly well retrieved.

Clearly, these results are quite in favor of the EP technique for the identification of the pores and throats size distributions. However, it must be emphasized that the experimental EP procedure does not allow the direct measurement of the evaporation rate within the cell test, in order to obtain the equivalent of W_{PNM} in the simulations. In the experimental EP, the evaporation is actually deduced from the mass variation measurements by making use of Eq. (21). Furthermore, in the experimental

procedure, the mass is measured at a fixed time frequency, whereas in the PNM simulations, the time step depends on the volumes of the throats or pore bodies emptying over the considered time step and is therefore variable. Moreover, W_{PNM} is determined at a quite high frequency in the PNM simulation because it is determined at each time step, *i.e.*, each time an element (pore body or throat) gets completely empty in the network.

In order to make a more accurate assessment of the experimental procedure, simulations were carried out considering a constant time step Δt. This means that the liquid mass in the network was computed at constant intervals of time Δt and that the evaporation rate was computed from the resulting mass variation with time by making use of Eq. (21) in which $t_{i+1} - t_i = \Delta t$. The probability density function was extracted from Eq. (22). The element size at the considered elapsed time was then deduced from Eq. (8). This procedure was tested for three fixed time steps, $\Delta t = 0.005$ s and $\Delta t = 0.1$ s and $\Delta t = 1$ s in the case of the reference Gaussian distributions for both the pore bodies and throats. This leads to the results on the PBTSD reported in Fig. 14b-d. The result on the PBTSD, obtained when all the mass evolution information available from the simulation is employed, is represented in Fig. 14a, showing that, both the TSD and PSD are quite well retrieved (see Fig. 13b for comparison with the reference distribution) in that case.

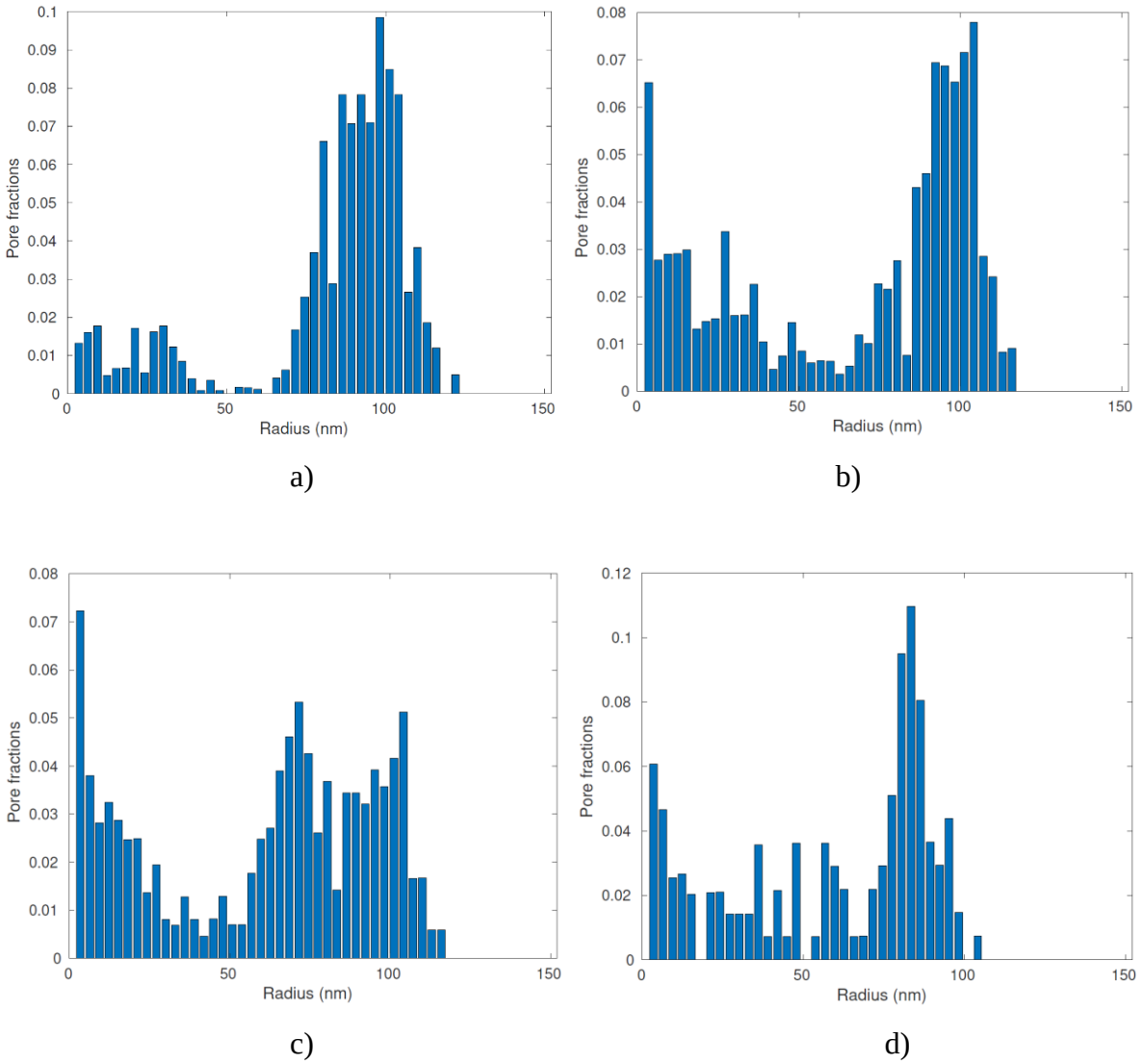


Fig. 14. PBTSD obtained from EP using the mass and evaporation rate computed at a non constant frequency (*i.e.*, at each time step of the PNM algorithm) (a) and at fixed frequencies (Δt = 0.005 s (b), Δt = 0.1 s (c) and Δt = 1 s (d)) for the reference Gaussian distributions.

When a very small fixed value of Δt is employed, namely Δt = 0.005s, the PBSD becomes easier to identify, while the TSD is poorly estimated (see Fig. 14b). When Δt is further increased, the procedure leads to a parasitic spreading of the distribution and the net separation between the TSD and PBSD is lost. Moreover, the fraction of the largest pore bodies is truncated. This can be observed from a comparison of Figs 14c (Δt = 0.1 s) and 14d (Δt = 1 s) with Fig. 13b representing the reference distributions. In other words, this procedure leads to the identification of pore sizes

which are actually not present in the network, while some others are missed. This is due to the fact that the computation of the evaporation rate from the mass tends to smooth out the evaporation rate fluctuations. Of course, the greater the time step, Δt, the greater the loss of information on the evaporation rate. In particular, when the sampling period of the mass evolution is increased, high-frequency fluctuations are filtered out. Since these high-frequency events are a signature of larger pores emptying due to the fact that the evaporation rate increases with the pore size, it explains why the fraction of the larger pore bodies is truncated when Δt is increased. This is illustrated in Fig. 14 which shows that the distribution obtained for Δt=1 s is even more different from the reference distribution depicted in Fig. 13b than for Δt=0.1 s.

In the experimental work on EP reported in [23], the evaporation rate data were averaged over seven successive measurements and the result was assigned to the time at the midpoint of the corresponding interval. From the above results, it is expected that such an averaging procedure might have an impact on the resulting PBTSD because, again, it leads to a further smoothing effect of the evaporation rate fluctuations. In order to get some insight on the impact of averaging, the Gaussian network was considered and the evaporation rate values, obtained with a time-sampling of the mass evolution Δt = 0.1 s, were averaged as indicated above. The resulting PBTSD is represented in Fig. 15. In this example, the impact is huge. The distribution is very different from the real one (depicted in Fig. 13b) and much further than the one reported in Fig. 14b obtained without an averaging procedure.

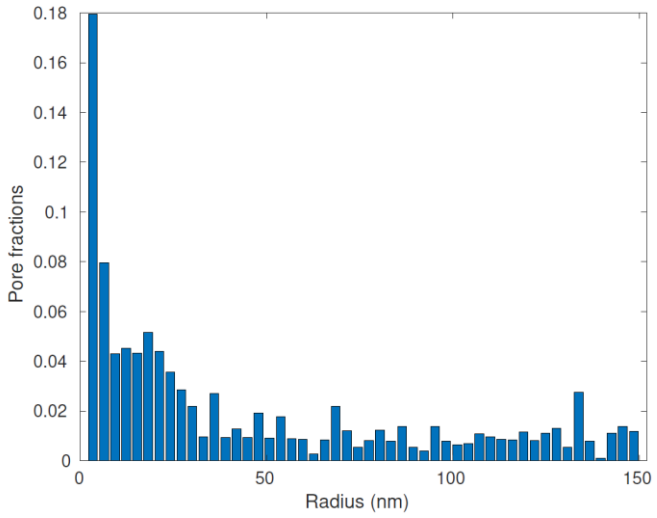


Fig. 15. PBTSD obtained from EP using the mass and evaporation rate computed at a fixed frequency (Δt=1 s) after averaging the evaporation rate data over seven successive values. Network with Gaussian distributions.

Tests were performed with the network featuring uniform reference distributions leading to the same type of results. The averaging procedure has a detrimental impact on the PBTSD extraction and the use of the evaporation rate computed from *m(t)* measured at a not enough high constant frequency introduces significant bias in the identification of the PBSD and TSD.

5. Discussion

In the previous sections, the comparison between the targets, *i.e.*, the real TSD or PBSD, and the distributions extracted from either the LLDP or the EP techniques was essentially qualitative, based on a visual comparison of the histograms. A more quantitative comparison is reported in Table 8.

Table 8 Comparison of statistical moments (mean and standard deviation) of the reference distributions (depicted in Fig. 13) and those extracted from the EP or LLDP. PBTSD refers to the whole element distribution, lumping the pore body and throat size distributions.

Technique	Reference TSD (nm)	Extracted TSD (nm)	Relative error (%)	Type of reference distributions
LLDP	Mean:25.56 Stand. Dev.: 13.82	0.42 0.2	98.4 98.6	Uniform
LLDP	Mean:24.78 Stand. Dev.: 6.89	0.61 0.23	97.5 96.7	Gaussian
Technique	Reference PBTSD (nm)	Extracted PBTSD (nm)		
EP using W_{PNM}	Mean:96.72 Stand. Dev.: 23.43	83.27 24.48	13.91 4.48	Uniform
EP using W_{PNM}	Mean:95.77 Stand. Dev.: 23.2	81.76 27.45	14.63 18.32	Gaussian
EP using W_m	Mean:95.77 Stand. Dev.: 23.2	76.23 28.54	20.4 23.02	Gaussian
EP using W_m (Δt=0.005 s)	Mean:95.77 Stand. Dev.: 23.2	68.62 29.98	28.35 29.22	Gaussian
EP using W_m (Δt=0.1 s)	Mean: 95.77 Stand. Dev.: 23.2	60.47 34.86	36.86 50.26	Gaussian
EP using W_m (Δt=1 s)	Mean: 95.77 Stand. Dev.: 23.2	54.76 35.46	42.82 52.84	Gaussian
EP using W_m with seven points averag. (Δt=0.1 s)	Mean:95.77 Stand. Dev.: 23.2	44.63 44.89	53.4 93.49	Gaussian

This comparison quantitatively confirms the results of the previous section. The LLDP technique does not allow determining the pore body sizes. Only the throat sizes can be expected to be determined. Based on the simulations carried out in this work, the method leads to a severe bias. For the network under consideration, made of highly interconnected pores in contrast with the hypothesis of cylindrical pores in parallel which underlies the LLDP interpretation, results are poor. The EP method leads to much more satisfactory results but is highly dependent on the accuracy with which the evaporation rate is determined. The results can be badly in error when the evaporation rate is too crudely estimated as a result of a too small measurement time frequency or ill-adapted averaging procedure of the mass evolution. The simulations indicate a non-monotonous variation of the evaporation rate. This means that the evaporation rate can slightly increase compared to its value at a previous time. This is a direct consequence of the Kelvin effect inducing fluctuations of the menisci radii of curvature at the boundary of the liquid clusters forming during the drying process. Results of the EP simulation suggest that the EP should allow distinguishing the throat size distribution from the pore body size distribution, but again, this possibility is highly dependent on the evaporation rate accuracy. Sampling frequency of the mass evolution during evaporation is a key parameter and simulation results presented here indicate that this frequency must be as high as possible. Improvement may be achieved by devising experiments featuring slow evaporation with an appropriate probing evaporating liquid having a small enough saturation vapor pressure.

In the work reported in [24], the LLDP and EP techniques were compared on the basis of experiments performed on the same UF membranes. The main results are somewhat disturbing since both techniques led to significantly different PBTSD. In this respect, the present study confirms this contrast. However, it does permit a full explanation of the observations reported in [24]. For instance, the average pore size in [24] is sometimes greater with the LLDP compared to the EP and sometimes smaller, depending on the membrane tested. In the simulations, the sizes identified from the LLDP correspond to the constriction (throat) sizes. Therefore, the identified average size is necessarily smaller than the average size obtained from the EP which includes both the pore bodies and the throats. Considering the viscous effects in a highly interconnected pore network even reinforces this effect which leads to the identification of unrealistic small pore throats with the LLDP. However, the results of the LLDP are highly dependent on the pore space structure. The closer the structure to a system of non-interconnected cylindrical pores in parallel, the more

representative should be the TSD as the extraction procedure from LLDP relies on this structure. Thus, the differences in the pore space structures of the various membranes characterized in [24] should partly explain the reported differences between the LLDP and the EP. It can also be noted that the membrane porosity was severely underestimated with the LLDP. This might be a consequence of the fact that the main outcome target of the method is the TSD, which is associated with only a small fraction of the porosity. Another result reported in [24], consistent with the present simulations, is that the spreading of the distribution, for a given membrane, is much wider with the EP than with the LLDP. This can be again partly explained by the fact that the interpretation of the EP experimental data allows determining both the throats and pore bodies sizes, but is sensitive to the evaporation rate extracted from the mass evolution record. As shown in Sect.4, the lack of accuracy on the evaporation rate tends to (wrongly) amplify the spreading of the identified distribution.

The simulations reported here were performed on a rather small 2D network containing 400 pore bodies (and about 800 throats). In the EP set-up used in [24], the membrane diameter in the test cell is 35 mm and the membrane active thickness is on the order of 10 μm. Considering that the mean distance between pore bodies is on the order of the mean pore diameters reported in [24], for example 100 nm, and assuming an isotropic pore structure, yields about 350 000 pore bodies over a membrane diameter and 100 pore bodies over the membrane thickness. The number of pore bodies in the real membranes is therefore several orders of magnitude larger than in the network used in this work. However, the number of pore bodies over the thickness is on the same order of magnitude (20 for the PNM against ~100 for the real membranes). Nevertheless, it would be interesting to perform the simulations over larger and 3D networks in order to explore whether the small size of the network is really an issue. Other concerns lie in the physics of drying. In the simulations, the viscous effects in the liquid phase were ignored. The evaporation rate, *W*, in the EP characterization reported in [24] is on the order of 10^{-8} kg/s. For the cell test of 35 mm in diameter (thus of cross-section surface area A = 9.6 $\times 10^{-4}$ m^2) used in this reference, this corresponds to an evaporation velocity $U_e = \frac{W}{\rho A} \approx 1.3 \times 10^{-8}$ m/s. This leads to a capillary number, *Ca*, quantifying the viscous to capillary effect ratio, given by $Ca = \frac{\mu U_e}{\gamma} \approx 10^{-9}$, which is quite small. This indicates that capillary effects are strongly dominating the transfer process and that the assumption of negligible viscous effects in the liquid clusters is quite reasonable. Another

pertaining question deals with liquid films [36-38], which were ignored in the present PNM of evaporation with Kelvin effect. In the current state of the art, it is unclear whether liquid films would indeed affect the main results obtained from the PNM simulations. Incorporating the liquid films in the model in conjunction with the Kelvin effect is a tricky task, a priori, but would certainly deserved to be addressed in the future. The liquid films considered in [36-38] are referred to as thick films, or capillary films, because their dynamics depends on capillary effects, [37]. In addition, adsorbed thin liquid films at the pore wall are likely to be present. Their presence may affect the pore size identification in particular for smaller pores when the pore opening is not large compared to the film thickness. The meniscus radius of curvature would then approximately correspond to the pore opening minus twice the film thickness and not simply to the pore opening [33]. This corresponds to pores on the order of a few nm. However, this effect is not such as to call into questions the main results of the present study.

6. Conclusions

In this study, the Evapoporometry (EP) and Liquid-liquid Displacement Porosimetry (LLDP) techniques were analyzed and compared on the basis of numerical simulations in a perfectly known model pore space structure, aiming at reproducing the evaporation process (EP) or the drainage process (LLDP) at the core of each technique. For the model pore space structure under consideration, the two techniques lead to markedly different results. The LLDP technique yields quite poor results. The pore bodies, *i.e.*, the local larger cavities, cannot be characterized and the throat sizes (the constrictions in the pore space) are shifted toward unrealistic smaller sizes. This is attributed to the highly interconnected pore space structure under consideration, which is much too different from the simplistic bundle of cylindrical pores in parallel commonly considered in the LLDP technique to extract the pore sizes. Accordingly, the LLDP technique, as it is commonly used, should be considered only for membranes with pore space structure close to straight columns of non-interconnected pores. As shown in [34], it is possible to correct the shortcomings of the LLDP technique by completing the pore size extraction model with some additional information. However, the method proposed in [34] relies on an optimization method requiring extensive numerical simulations and is much less simple than the commonly used method based on the parallel cylindrical tubes model.

In contrast, the EP technique lead to quite satisfactory results. The pore body and throat size distributions can be identified and the main distribution properties are quite well retrieved. However, the quality of the results is highly dependent on the accuracy with which the evaporation rate is determined. Relatively small errors on the evaporation rate can significantly affect the results. This can lead to an erroneous identification of non-existing pore body or throat sizes and / or to an unrealistic spreading of the size distribution. In spite of the care taken in measuring the mass in the EP set-ups, [23, 24], it is not obvious that the level of accuracy on the determination of the evaporation rate is sufficient. The technique thus would deserve further validations. Also, the impact of the Kelvin effect on the equilibrium vapor pressure is significant only over a relatively narrow range of sizes, typically between about 2 nm and 50 nm. In this respect, the LLDP technique is more versatile and can be used for characterizing porous systems with pores of much greater sizes, provided that, as indicated above, the pore size extraction model is adapted to the system under consideration.

In summary, despite these important conclusions, the study indicates that further validation studies are still needed to assess and evaluate the capabilities of the EP and LLDP techniques. Results from both procedures can be seriously in error depending on the underlying pore space structure (LLDP) or the accuracy with which the evaporation rate is determined (EP). Yet, this study relies on numerical simulations based on assumptions to model the physical processes at play in both techniques and the simulations were performed on a rather small network. Thus, a cautious conclusion is simply that the simulations suggest that both the LLDP and EP techniques still need thorough investigations. Both techniques should be compared with other experimental procedures. Pore size distributions extracted from the two techniques should be compared, for instance, to those extracted from 3D digital images of the membrane microstructure obtained by FIB-SEM (LLDP and EP) [39] or X-ray tomography (LLDP) [40].

Acknowledgements

This research was supported by the Project “PEMFC – SUDOE” – SOE1/P1/E0293 which is co-financed by the European Regional Development Fund in the framework of the Interreg Sudoe programme.

Nomenclature

Latin symbols

A	Cross sectional area of the diffusion cell [m^2]
a	Network lattice spacing [m]
D_{eff}	Effective diffusion coefficient [$m^2.s^{-1}$]
f	Probability density function [m^{-1}]
k	Mass transfer coefficient [$m.s^{-1}$]
L	Network length [m]
l	Pore throat legth [m]
M_v	Molecular weight [kg/mol^{-1}]
m	Mass of liquid in the porous structure [kg]
P	Pressure [Pa]
P_v	Vapor pressure [Pa]
P_{vequ}	Equilibrium vapor pressure [Pa]
P_{vsat}	Saturation vapor pressure [Pa]
p_{cth}	Capillary pressure threshold [Pa]
Q	Volume flow rate [$m^3.s^{-1}$]
R	Ideal gas constant (8.314 [$J.mol^{-1}.K^{-1}$])
r	Pore, throat or tube radius [m]
r_c	Characteristic throat size [m]
r_{curv}	Meniscus radius of curvature [m]
r_{max}	Maximum expected pore radius [m]
r_{min}	Minimum expected throat radius [m]
r_t	Throat radius [m]
S_p	Saturation in a pore body [-]
S_t	Saturation in a pore throat [-]
T	Temperature [K]
t	Time [s]
W	Evaporation rate [$kg.s^{-1}$]
W_{ref}	Reference evaporation rate [$kg.s^{-1}$]

Greek symbols

Δ Difference operator [-]

γ Interfacial tension [$N.m^{-1}$]

θ Contact angle [rad]

μ Dynamic viscosity [Pa.s]

ρ Liquid density [$kg.m^{-3}$]

ϕ Diffusive mass flow rate [$kg.s^{-1}$]

χ Normalized flow rate [-]

Superscript and subscript

i, j Element (pore body or throat) or time step index

w Wetting phase

nw Non-wetting phase

References

[23] W.B. Krantz, A.R. Greenberg, E. Kujundzic, A. Yeo, and S. S. Hosseini, Evapoporometry: A novel technique for determining the pore-size distribution of membranes Journal of Membrane Science, 438, 153-166 (2013).

[24] M.B. Tanis-Kanbur, R.I. Peinador, X. Hu, J.I. Calvo, J.W. Chew, Membrane characterization via evapoporometry (EP) and liquid-liquid displacement porosimetry (LLDP) techniques, Journal of Membrane Science, 586, 248-258 (2019).

[25] K.R. Morison, A comparison of liquid-liquid porosimetry equations for evaluation of pore size distribution, Journal of Membrane Science, 325, 301-310 (2008).

[26] R.I. Peinador, J.I. Calvo, P. Prádanos, L. Palacio, A. Hernández, Characterization of polymeric UF membranes by liquid-liquid displacement porosimetry, Journal of Membrane Science, 348, 238-244 (2010).

[27] J.I. Calvo, R.I. Peinador, P. Prádanos, A. Bottino, A. Comite, R. Firpo, A. Hernández, Porosimetric characterization of polysulfone ultrafiltration membranes by image analysis and liquid–liquid displacement technique, Desalination, 357, 84-92 (2015).

[28] M.J. Blunt, M.D. Jackson, M. Piri, P.H. Valvatne, Detailed physics, predictive capabilities and macroscopic consequences for pore-network models of multiphase flow, Advances in Water Resources, 25 (8-12), 1069-1089 (2002).
[29] M.J. Blunt, Flow in porous media-pore-network models and multiphase flow, Current Opinion in Colloid & Interface Science, 6, 197-207 (2001).
[30] O. Maalal, M. Prat, R. Peinador, D. Lasseux, Determination of the throat size distribution of a porous medium as an inverse optimization problem combining pore network modeling and genetic and hill climbing algorithms, submitted to Physical Review E.
[31] O. Maalal, M. Prat, D. Lasseux, Pore network model of drying with Kelvin effect, submitted to Physics of Fluids.
[32] F.A.L. Dullien, Porous Media: Fluid Transport and Pore Structure, Academic Press 1991.
[33] T. Takei, M. Chikazawa, T. Kanazawa, Validity of the Kelvin equation in estimation of small pore size by nitrogen adsorption, Colloid and Polymer Science, 275, 1156-1161 (1997).
[34] O. Maalal, M. Prat, R. Peinador, D. Lasseux, Pore network simulations of fluid-fluid displacement porosimetry for evaluation of pore size distribution, submitted to ??
[35] M. Prat, Percolation model of drying under isothermal conditions in porous media, International Journal of Multiphase Flow, 19 (4), 691-704 (1993).
[36] J.C.T. Eijkel, B. Dan, H.W. Reemeijer, D.C. Hermes, J.G. Bomer, A. van den Berg, Strongly accelerated and humidity independent drying of nanochannels induced by sharp corners, Physical Review Letters, 95, 256107 (2005).
[37] F. Chauvet, P. Duru, S. Geoffroy, M. Prat, Three periods of drying of a single square capillary tube, Physical Review Letters, 103, 124502 (2009).
[38] M. Prat, On the influence of pore shape, contact angle and film flows on drying of capillary porous media, International Journal of Heat and Mass Transfer, 50, 1455-1468 (2007).
[39] T. Prilla, C. Redenbach, D. Roldan, M. Godehardt, K. Schladitz, S. Höhn, K. Sempf, Simulating permeabilities based on 3D image data of a layered nano-porous membrane, International Journal of Solids and Structures, 184, 3-13 (2020).
[40] T. Agaesse, A. Lamibrac, F. Buechi, J. Pauchet, M. Prat, Validation of pore network simulations of ex-situ water distributions in a gas diffusion layer of proton exchange membrane fuel cells with X-ray tomographic images, Journal of Power Sources, 331, 462-474 (2016).

Identification of local contact angle distribution inside a porous medium as an inverse optimization problem

Otman Maalal[a,b], Marc Prat[a*], René Peinador[b], Didier Lasseux[c]

Institut de Mécanique des Fluides de Toulouse (IMFT), Université de Toulouse, CNRS, Toulouse, France.
Institut de La Filtration et des Techniques Séparatives (IFTS), Rue Marcel Pagnol, 47510, Foulayronnes, France
CNRS, I2M, UMR 5295 – Esplanade des Arts et Métiers, 33405 Talence, CEDEX, France

[*] *Corresponding author:mprat@imft.fr (+33534322883)*

Abstract

The local contact angle distribution within the pore space of a porous medium of mixed wettability is identified by combining pore network simulations and an optimization method. The latter is used to solve the inverse problem consisting in determining the local contact angle distribution from the capillary pressure and relative permeability curves. The inverse optimization method combines a genetic algorithm and the hill climbing algorithm. The method is illustrated considering a Boolean distribution of the local contact angle in which the pore bodies and throats in the pore space are either hydrophilic or hydrophobic.

Keywords: Porous Media; Mixed wettability; Capillary pressure curve; Relative permeability curve; Pore network model; Genetic algorithm; Hill climbing algorithm

1 Introduction

The wettability conditions inside a porous medium can be of crucial importance. Consider for instance the gas diffusion layer (GDL), [1], in the proton exchange membrane fuel cells (PEMFC), [2]. The GDL is a key component as regards the gas access to the catalyst layer and the management of the water produced as the result of the electrochemical reaction, [3]. GDLs are typically composed of two distinct layers, a substrate of graphitized carbon fibers and a micro porous layer (MPL) coated onto one side. Without treatment, the graphitized carbon fibers are hydrophilic with a static contact angle on the order of 80° [4]. GDL substrates are generally rendered hydrophobic by applying a polytetrafluoroethylene (PTFE) coating. The most commonly used technology [4,5] is to perform the coating by immersion of the GDL substrate in an emulsion containing the hydrophobic agent, drying, and sintering at 350°C. The contact angle on a PTFE flat surface is expected to be on the order of 110-115° [6]. However, it is difficult to obtain a homogeneous coating. As a result, the wettability conditions can vary within the pore space of a fresh GDL substrate. In addition, loss of PTFE during mechanical compression cycles [7-9] or due to other degradation mechanisms [10-13] modifies the PTFE distribution and the GDL substrate wettability properties. For this reason, the GDL substrate is often considered as a system of mixed wettability rather than a purely hydrophobic fibrous medium with various possible distributions of the hydrophilic and hydrophobic pores within the GDL substrate pore space. As discussed and analyzed for instance in [14-16], the change in the wettability conditions can dramatically modify the liquid water pattern from a capillary fingering pattern to a compact pattern as the wettability conditions change from hydrophobic to hydrophilic. As discussed in [6], capillary fingering allows maintaining a significant fraction of the pore space free of liquid water and thus available for the gas transport through the GDL substrate whereas a compact pattern blocks the gas access and is thus detrimental to the PEMFC operation. As a result, it is highly desirable to characterize the wettability of a fresh GDL substrate wettability as well as after some time of operation. However, the methods for characterizing the wettability of a porous substrate generally lead at best to the characterization of an “average” or apparent contact angle. A somewhat popular method is the sessile drop method, [17]. The method consists in placing a droplet of liquid water at the surface. Then, the contact angle can be measured by image processing from side images of the droplet. However, the interpretation is far from straightforward when the droplet is placed on a porous

surface, especially in the case of fibers of heterogeneous wettability. Also, the wettability at the surface is not necessarily representative of the wettability inside the porous medium. Another commonly used method is the Washburn method [18-20]. The method consists in measuring the sorption kinetics of liquid into the sample, first with a liquid of very low contact angle and then with the liquid of interest for the considered application. Obviously, the method cannot be directly applied with water and a hydrophobic material since there is no sorption in this case. However, it is shown in [19] how the Washburn method can be combined with the Owens-Wendt two parameters theory [21] to estimate the internal contact angle for water in a hydrophobic porous material. Nevertheless, as pointed out in [19], the Washburn method only allows estimating an apparent or average contact angle reflecting a statistical average of the porous material wettability properties at the pore scale level. Information on the wettability conditions at the pore scale can be gained from scanning electron microscopy (SEM) images of droplets or menisci inside the pore space, [19], but the measurement of local contact angles from the images is very difficult since the droplets are tridimensional objects [20]. In the present article, a different approach is developed in order to obtain maps of internal contact angle inside the pore space of the porous material. The method is based on two observations. First, obtaining 3D digital images of porous microstructures is increasing accessible, either by X-ray microtomography techniques [23] when the pores are in the micronic range or using other techniques such as FIB-SEM [24] when the pores are in the sub-micronic range. For instance, 3D images of GDL substrate microstructures have been obtained by X-ray tomographic microscopy [25]. It is thus assumed that 3D digital images of the porous microstructures to be characterized are available. Second, macroscopic properties, such as the capillary pressure vs. saturation curve or the relative permeability curves are sensitive to the internal wettability conditions, [14, 26]. Then, the question arises as to whether this sensitivity can be harnessed to characterize the internal wettability conditions. In other words, the idea here is to explore the possibility of characterizing the internal wettability conditions from the following data: digital images of the porous microstructures, the capillary pressure curve, the relative permeability curves. This characterization problem is addressed as an inverse optimization problem combining two-phase flow simulations within the microstructure with an optimization method combining a genetic algorithm, [27, 28], and the hill climbing algorithm [27, 29]. This type of approach has shown promising results for identifying the pore size distribution from macroscopic data such as the capillary pressure curve and / or normalized flow curves [30, 31]. Contrary to [30, 31] where

the objective is to identify the pore size distribution assuming a spatially uniform wettability throughout the pore space, the objective here is to identify the internal contact angle spatial distribution knowing the microstructure geometry and thus the pore size distribution. As in [30, 31], pore network models (PNM), [32, 33], are used for the two-phase flow simulations in the pore space. This approach is preferred to direct two-phase flow simulations, e.g. [34, 35], because of the much shorter computational times. The PNM simulations require to identify the network from the microstructure digital images. Various algorithms are available for this purpose, e.g. [25, 36, 37] and references therein. However, since the focus is on the development of a new characterization methodology, a somewhat simplified version of the internal wettability characterization problem is considered in what follows. First, the network is a given two-dimensional square network so as to speed up the simulations (compared to the typical unstructured 3D network extracted from a microstructure 3D digital image). Second, the internal contact angle can take two values, either 80° or 115°. The latter value corresponds to the contact angle of water on a fiber coated by PTFE whereas 80° corresponds to the contact angle on carbon. Thus, the particular situation considered for illustrating the characterization method is inspired from the GDL substrate wettability characterization problem. Further details on the considered model problem are given in the next section.

The present paper is organized as follows. In section 2, the model porous medium, a two-dimensional square pore network of pore bodies and throats, is presented. The algorithms used to simulate the displacement on the network and compute the capillary pressure and relative permeability curves are presented in Section 3. The inverse optimization method for determining the local contact angle distribution in the network is described in Section 4. Section 5 presents results obtained with the optimization method. A short discussion is presented in Section 6. Conclusions are drawn in Section 7.

2 Model porous medium

A simple two-dimensional square pore network is considered to test the proposed local contact angle characterization method. As illustrated in Fig. 1, the pore space is an assembly of two types of elements: the pore bodies and the throats. The pore bodies are spheres of radius r_p located at the nodes of a regular square grid. The distance between two adjacent nodes is the lattice spacing a with $a = 350$ μm in all the simulations presented below. The size of the network is the number of

nodes (pore bodies) in each direction (for example, Fig. 1 shows a 12 × 5 square network). Throats are cylindrical channels of radius r_t. The throat and pore body sizes are randomly distributed according to a given probability density function (p.d.f.). In what follows, a uniform p.d.f. is considered with r_t varying between r_{tmin} = 20 μm and r_{tmax} = 40 μm. Similarly, the pore body sizes are distributed according to a uniform p.d.f with the constraint that a pore body size is equal or greater than the largest throat to which the considered pore body is connected. In what follows, the minimum and maximum pore body sizes are respectively r_{pmin} = 80 μm and r_{pmax} = 120 μm. The model of wettability heterogeneity consists in considering that a fraction f of the pore bodies and throats in the network is hydrophilic (with a contact angle θ = 80°) whereas the complementary fraction is hydrophobic (θ = 115°). Thus, a fully hydrophobic (hydrophilic respectively) network corresponds to f = 0 (f = 1 respectively). Networks of mixed wettability correspond to intermediate values of f (0< f < 1). The hydrophilic elements are randomly selected in the network until f reaches the desired value.

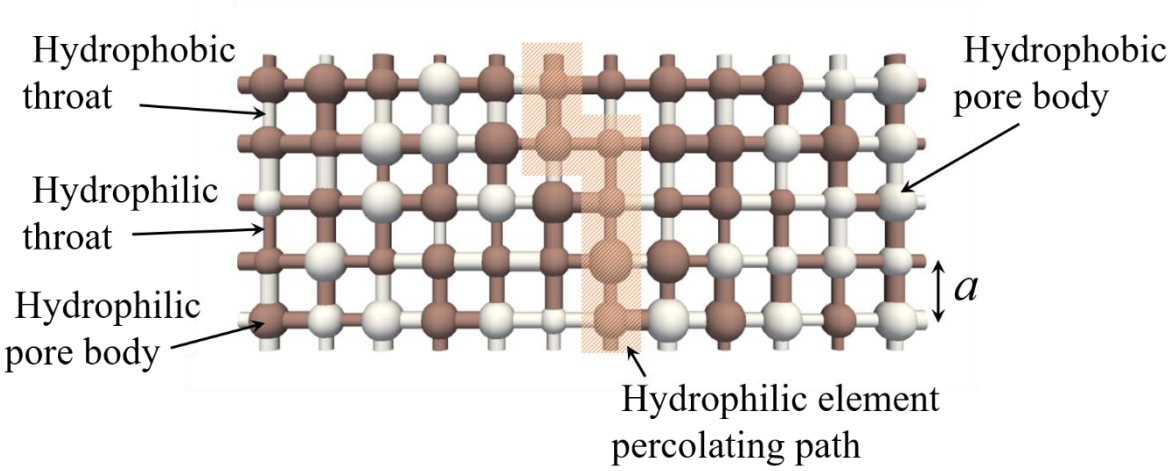


Fig.1. 12 × 5 square pore network. Throats and pore bodies in brown are hydrophilic (θ = 80°). Throats and pore bodies in grey are hydrophobic (θ = 115°).The notion of hydrophilic element percolating path between the network inlet (at the bottom) and outlet (at the top) is illustrated.

3 Capillary pressure and relative permeability curves

3.1 Local invasion rules

The PNM computation of the capillary pressure and relative permeability curves is based on the definition of local invasion rules. An invasion capillary pressure threshold (ICPT) is associated

with each element, pore body or throat, in the network. The ICPT of a throat is simply given by the Young – Laplace equation as,

$$p_c = \frac{-2\gamma\cos(\theta)}{r_t} \quad (1)$$

where γ is the surface tension. Similarly, the ICPT of a hydrophobic pore body is given by,

$$p_c = \frac{-2\gamma\cos(\theta)}{r_p} \quad (2)$$

As first shown in [38], the situation is more involved for the hydrophilic pore bodies because the invasion of such a pore body depends on the number of adjacent hydrophilic throats already filled by the liquid. This aspect can be taken into account by defining the ICPT of a hydrophilic pore body as [39].

$$p_c = \frac{-2\gamma\cos(\theta)\,[1+0.25(N_{neighbours}-1)]}{r_p} \quad (3)$$

where $N_{neighbours}$ is the number of hydrophilic adjacent throats already containing liquid water. Suppose a meniscus is located at the entrance of a pore network element of ICPT p_c. Such a meniscus can move into the element only when P_w-$P_g > p_c$,where P_w is the pressure in the liquid phase and P_g is the pressure in the gas phase.

3.2 Capillary pressure curve computation

The capillary-pressure curve $P_c(S)$, where S is the saturation of the displaced fluid, is computed using an algorithm similar to the one presented in [30] and [40], but which now takes into account the presence of hydrophilic elements. This algorithm mimics the commonly used experimental procedure [26]. The network is initially fully saturated by the gas phase. Then liquid water is injected into the network through a sequence of pressure steps. A membrane is supposed to be present at the outlet so that only the displaced fluid can exit the network. The capillary pressure as a function of S is determined for successive states of hydrostatic equilibrium corresponding to small increment dP_w in the liquid water pressure (the gaseous phase pressure, P_g, is kept constant). The

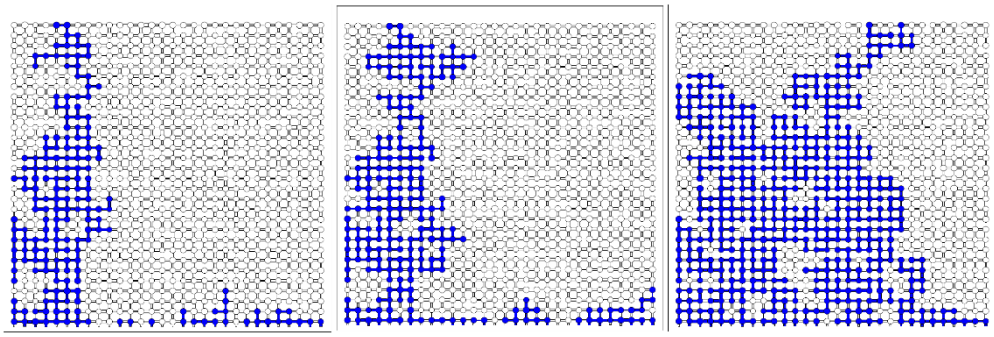
capillary pressure is by definition $P_c = P_w - P_g$. The algorithm used to determine the saturation evolution right after a pressure increment can be summarized as follows:

1. Initialization of a menisci position vector that stores all interfacial pore bodies and throats. A pore body or throat is interfacial when it is occupied by the displaced fluid (gaseous phase in our simulation) and is adjacent to an element, pore body or throat, containing the displacing fluid (liquid water).
2. Identification of the interfacial pore body or throat to be invaded first: it corresponds to the interfacial pore body or throat which has the minimum ICPT (real value calculated from Eq. 1; 2; and 3) among the interfacial pore bodies and throats with ICPT lower than the imposed pressure difference $P_w - P_g$ between the two fluids. For hydrophilic pore bodies or throats connected to liquid-gas interfaces, the ICPT is negative ($\theta = 80° < 90°$). Hence, they are the ones to be selected first. In addition, the ICPT associated with a hydrophilic throat is smaller than the hydrophilic pore bodies ICPT (recall that $r_p > r_t$), which means that hydrophilic throats are more likely to be selected (except for some cases where there exists a hydrophilic pore body connected to many hydrophilic throats, the ICPT can be smaller as dictated by Eq. (3)).
3. Invasion of the pore body or throat selected in the previous step, the vector of menisci positions is updated: interface positions are either added or deleted according to the pore body or throat invaded.
4. Steps 2 and 3 are repeated until no further interfacial pore body or throat satisfying the condition $ICPT < P_w - P_g$ can be selected.
5. Computation of overall saturation.

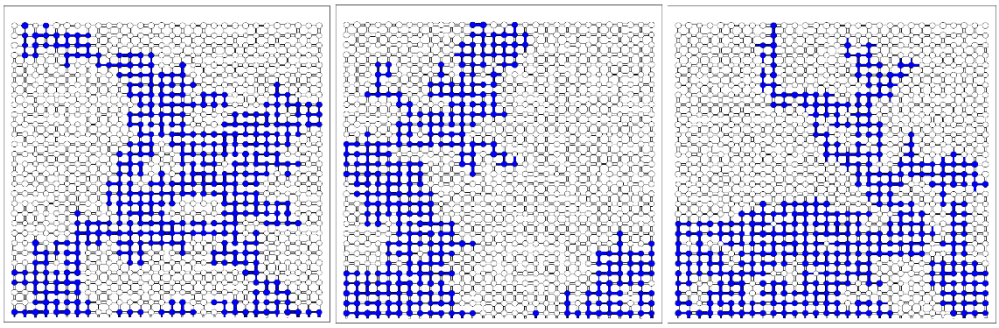
For simplicity, trapping, [16, 42], is neglected. This means that the displaced fluid in a network element, pore body or throat, is implicitly assumed to be always connected to the outlet face and can thus be always displaced when the corresponding capillary pressure invasion threshold is overcome.

Fig.2 illustrates the impact of the hydrophilic element fraction on the fluid distribution at breakthrough (the breakthrough is when the displacing fluid becomes connected to the outlet). A capillary fingering pattern is observed for $f \sim 0$ as expected for a quasi-static drainage process. A compact pattern is obtained for $f \sim 1$. The pattern obtained for $f \sim 0.4$ resembles the capillary

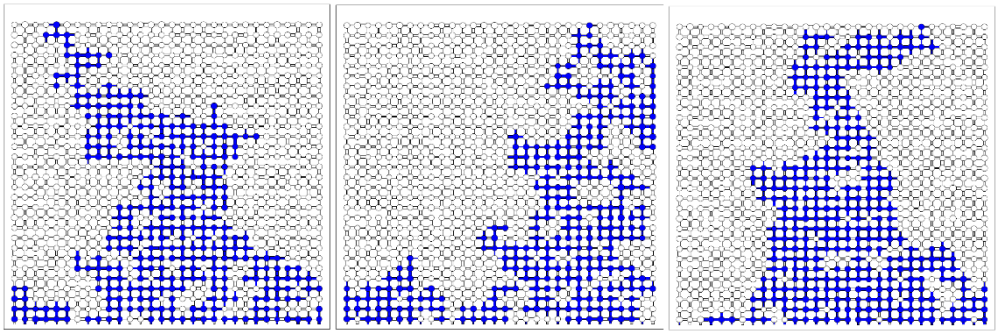
fingering pattern but actually results from the fact the percolating subnetwork formed by the hydrophilic pore bodies and throats is a percolation cluster. An invasion percolation cluster ($f \sim 0$) is about the same fractal object as the hydrophilic element percolation cluster ($f \sim 0.4$). This is why both cases ($f \sim 0$ and $f \sim 0.4$) lead to the same type of phase distribution despite the change in the local mechanisms controlling the growth of the liquid/gas interface in the hydrophobic regions and the hydrophilic ones respectively.



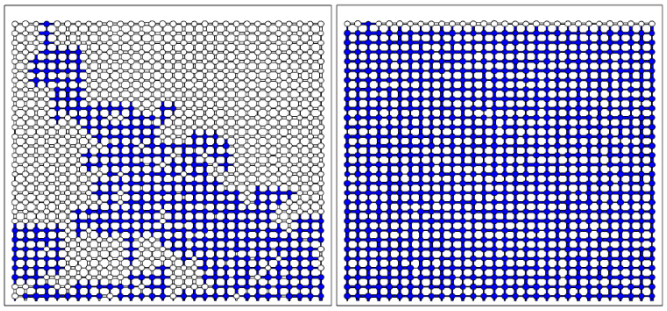
f =0 *f=0.1* *f=0.2*



f =0.3 *f=0.4* *f=0.5*



f =0.6 *f=0.7* *f=0.8*



f =0.9 *f=1*

Fig.2. Fluid distribution for various values of the hydrophilic pore body-throat fraction *f* in the 2D 30 x 30 square network (from *f*=0 to *f*=1 with a step of 0.1). The displacing fluid (in blue) is injected from the bottom using the capillary pressure algorithm. The displaced fluid (in grey) escapes from the top.

Fig.3 shows the capillary pressure curves obtained for one realization of a 30 × 30 network with the above algorithm when the fraction *f* of hydrophilic elements in the network is varied. As mentioned before the pore body and throat sizes are distributed according to uniform p.d.f. with r_{tmin}= 20 μm, r_{tmax} =40 μm, r_{pmin}= 80 μm, r_{pmax} =120 μm, a = 350 μm.

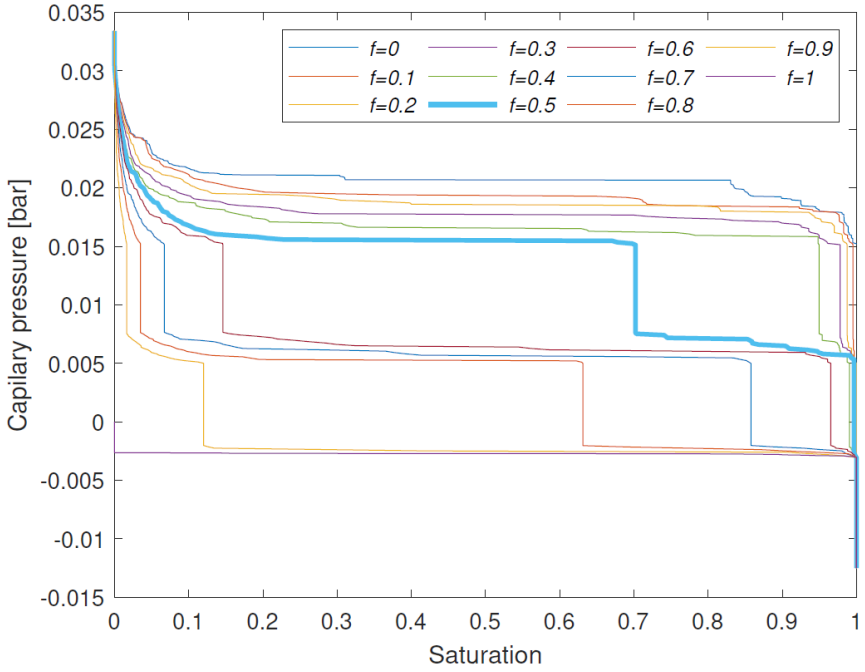


Fig.3. Capillary pressure curves computed for the 30 × 30 network for several values of the fraction *f* of hydrophilic elements in the network. The top curve corresponds to *f* = 0 (fully hydrophobic network). The bottom curve (in violet) corresponds to *f* = 1 (fully hydrophilic network). The intermediate curves are for *f* = 0.1 (red),0.2,0.3,0.4,0.5,0.6,0.7,0.8 and 0.9 (yellow). The curve corresponding to *f* = 0.5 is thicker.

Fig.3 illustrates the sensitivity of the capillary pressure curve to the hydrophilic element fraction *f*. This sensitivity is a crucial feature since it indicates a clear dependence of the considered macroscopic property with the distribution of the local contact angle. This dependence originates

from the impact on the hydrophilic element fraction on the fluid distribution illustrated in Fig.2. Based on a previous work [14], f = 0.5 approximately corresponds to the hydrophilic element percolation threshold, i.e. the minimum value of f for which the hydrophilic element forms a cluster spanning the network. The hydrophilic element percolation threshold is denoted by f_c. The value f_c. = 0.4, as discussed with the patterns (Fig.2), is however possible for a particular realization due to finite size effects. As can be seen from Fig.3, the sensitivity of the capillary pressure curve to f is greater for $f > f_c$. This is consistent with the patterns depicted in Fig.2 which shows that the transition from a fingering pattern to a compact pattern occurs for $f > f_c$

3.3 Relative permeability curve

As in [30], only the relative permeability for the invading phase is computed. One can refer to [30] for the reasons motivating this choice. An equilibrium liquid gas distribution in the network is obtained for each considered value of the capillary pressure P_c. The invading phase relative permeability is computed from the computation of the invading fluid viscous flow through the network for each equilibrium phase distribution, that is for each point of the capillary pressure curve. The computation of the displacing fluid flow rate, Q_i, is performed as follows [32]. At each saturation equilibrium, a pressure difference, ΔP, much smaller than the capillary pressure characterizing this equilibrium, is applied in the displacing fluid between the network inlet and outlet. For the resulting flow, the mass conservation equation is expressed at each invaded pore body i

$$\sum Q_{i-j,k} = 0 \tag{4}$$

where $Q_{i-j,k}$ is the displacing fluid volume flow rate between pore body j and adjacent pore body k. If the throat between pore bodies j and k is occupied by the displaced fluid, then $Q_{i-j,k} = 0$. If the throat is occupied by the displacing fluid, then

$$Q_{i-j,k} = \frac{\pi r_{t-j,k}^4}{8\mu_{nw} l_{j,k}} \Delta P_{j,k} \tag{5}$$

where $r_{t-j,k}$ and $l_{j,k}$ are the radius and length of the throat linking the two pore bodies respectively, while $\Delta P_{j,k}$ is the pressure drop in the displacing fluid between the two neighboring pore bodies.

Taking into account the pressure boundary conditions at the inlet ($P_{inlet} = \Delta P + P_{outlet}$) and outlet ($P_{outlet} = Cte$) and the zero flux condition imposed on the lateral faces of the network, Eqs. (4) and (5) lead to a linear system for the pressure field in the invading fluid. This system is numerically solved using the conjugate gradient method. Once the pressure field is obtained, Q_i can be computed at the inlet using Poiseuille's law applied to all displacing fluid throats connected to the inlet. Then, the generalized Darcy's law is applied to determine the displacing fluid relative permeability,

$$Q_i = A\frac{KK_r(P_c)}{\mu}\frac{\Delta P}{L} \tag{6}$$

where μ is the displacing fluid viscosity, A is the network cross-section surface area, L is the network length, K is the porous medium intrinsic permeability and K_r is the non-wetting fluid relative permeability. From Eq. (6), the relative permeability is computed as

$$K_r(P_c) = \frac{Q_i}{Q_{imax}} \tag{7}$$

where Q_{imax} is the displacing fluid flow rate obtained after the last pressure increment when the network is fully saturated by the displacing fluid.

Fig.4 shows the displacing fluid relative permeability obtained with the above algorithm when the fraction f of hydrophilic elements in the network is varied for the same 50 × 50 network as for the capillary pressure curves computation (Fig.3).

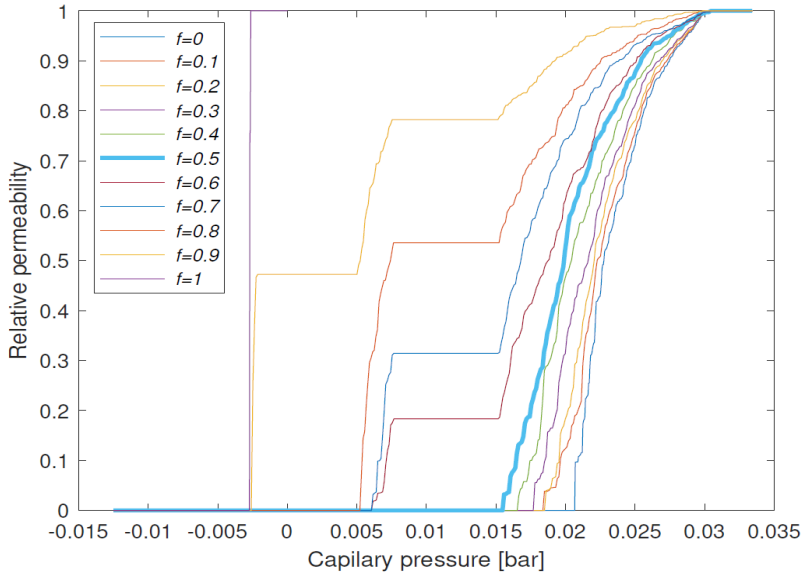


Fig.4. Displacing fluid relative permeability curves computed for the 30 × 30 network for several values of the fraction f of hydrophilic elements in the network. The curve to the far right corresponds to $f = 0$ (fully hydrophobic network). The curve to the far left (in violet) corresponds to $f = 1$ (fully hydrophilic network). The intermediate curves are for $f = 0.1$ (red), 0.2, 0.3, 0.4, 0.5, 0.6, 0.7, 0.8 and 0.9 (yellow). The curve corresponding to $f \approx 0.5$ is thicker.

As for the capillary pressure curves (Fig.3), Fig.4 illustrates the noticeable sensitivity of the considered macroscopic property, here the displacing fluid relative permeability, to the hydrophilic element fraction *f*. Again, it can be noted that sensitivity to *f* is greater for $f > f_c$ (~0.4) but noticeable all considered values of *f*. How this sensitivity is exploited is described in the next section.

4 Local contact angle distribution as an inverse optimization problem

4.1 Local contact angle distribution as an inverse problem

The problem of determining the distribution of the local contact angle in the network is addressed as an inverse optimization problem. The problem can be expressed as follows. Knowing the $K_r(P_c)$ and $P_c(S)$ curves for a given network, can the local contact angle distribution in the network be predicted? In this context, the direct problem is of course to compute the $K_r(P_c)$ and $P_c(S)$ curves of the network. As for the direct problem (Sec. 3), the inverse problem is solved using PNM. To build and test the procedure, a network is generated with a specified value of the fraction, *f*, of hydrophilic elements. This network is referenced to as the reference network. It shall be viewed as the porous medium to be characterized for which the experimental measurement of $Q_i(P_c)$ and $P_c(S)$ would have been performed in practice and which local contact angle distribution is to be determined. Since two values of the local contact angle are considered in our model problem, a wettability label 0 or 1 is assigned to each pore network element. The label is 1 when the element is hydrophilic ($\theta = 80°$) and 0 when the element is hydrophobic ($\theta = 115°$).

The inverse problem is solved using an optimization method based on a searching algorithm which is a hybrid version of the genetic and hill climbing algorithms [27-29]. The genetic algorithm is a searching algorithm based on the biological evolution laws including reproduction, mutation and natural selection. A population of individuals is first defined. In our case, the individuals are realizations of the pore network, that is random spatial distributions of the wettability label in the network (for a given fraction *f* of hydrophilic elements). Every individual has genes. A gene in the

pore network is the element wettability label. The aim of the algorithm is to identify the hydrophilic element fraction, *f*, via the minimization of a fitness function which value is estimated from a direct solution for each individual. The fitness function, denoted by $\phi(\boldsymbol{w})$, is an objective function comparing the curve obtained by direct simulation for the individuals to the reference one. $\boldsymbol{w}$ is a vector which components are the wettability labels assigned to each element, pore body or throat, in a network. The fitness function is defined as,

$$\Phi\ (\boldsymbol{w}) = \sum_{j=1}^{n} \left| K_{rn-refj} - K_{rn-indj}(\boldsymbol{w}) \right| + \sum_{j=1}^{n} \left| S_{refj} - S_{indj}(\boldsymbol{w}) \right| \qquad (8)$$

where *n* is the total number of pressure steps, $K_{rn-refj}$ and $K_{rn-indj}$ are the reference network and individual relative permeabilities corresponding to the j^{th} pressure increment, respectively;
S_{refj} and S_{indj} are the reference and individual saturations at the j^{th} pressure increment.
The algorithm main steps can be summarized as follows:
The first step consists in generating a series of N_0 parent realizations ($N_0 = 16$ in this work) of various hydrophilic element fraction, *f*, to which evolutionary laws and natural selection are applied. Since the hydrophilic element fraction is the unknown to be determined, this fraction is varied between 0 and 1 over the N_0 parent realizations.
The relative permeability and capillary pressure curves, together with the corresponding fitness function, are computed for each individual parent. After this initialization procedure, the genetic algorithm is executed according to the following steps.

1. The natural selection is performed by randomly choosing a subset of N_1 individuals among the generation of individuals (here, $N_1 = 5$). The two ones corresponding to the best fitness values are selected.

2. Two evolutionary operators, namely crossover and mutation, are applied to the two parent individuals. Crossover is the process by which the two selected parent individuals give birth to a child realization by exchanging randomly wettability labels (genes). Mutation is an operation applied separately to both selected parent realizations. It consists in altering genes (the wettability labels). Mutations are generally supposed to happen rarely. In the present case, the mutation rate is taken equal to 0.01. In our case this means for example for a 30 x 30 network containing 2640 elements (900 pore bodies and 1740 throats) that 9 pore bodies

and 17 throats are selected randomly. Then the wettability label of these 26 elements are specified randomly.

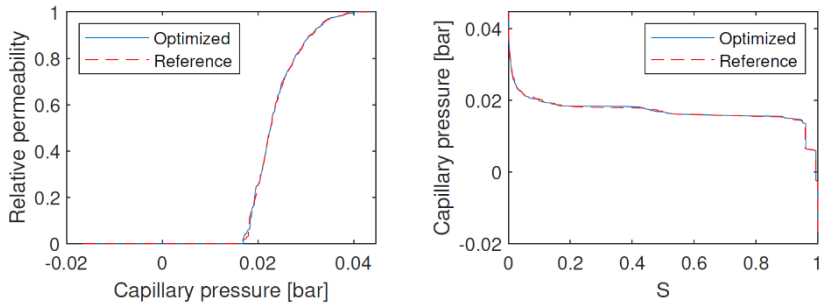
3. The $K_r(P_c)$ and $P_c(S)$ curves and the fitness values for the two children are computed and, among the four individuals (the two parents and the two children), the two individuals having the best fitness values are selected. They are kept to form the new generation.
4. Steps 1 to 3 are repeated until there are no more individuals in the parent population and a new generation of N_0 individuals is formed.
5. The process made of steps 1 to 4 is iterated until convergence is reached. By convergence, it is meant that the fitness of all the individuals from one generation to the following one does not change by more than about 0.1%.

For all the cases under study in this work, 200 generations (iterations) were enough to reach convergence at which the solution is estimated to be close to the global solution. Then a new step is performed using the hill climbing algorithm.

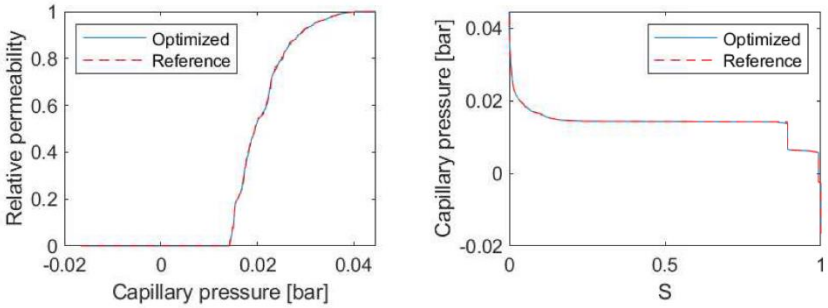
The objective of the hill climbing algorithm, which, like the genetic algorithm is a searching algorithm, is to gradually modify the wettability distribution within a single individual so as to refine the convergence toward the reference network wettability distribution. To this end, the hill climbing algorithm is operated on the best fitted individual in the population obtained at the end of genetic algorithm step. The procedure is the following. An element is randomly selected in the network. The wettability of this element is changed (from hydrophobic to hydrophilic if this element is hydrophobic or from hydrophilic to hydrophobic if the element is hydrophilic). Then fitness function is computed. If the value of the fitness function has diminished, then a small number (randomly selected between 1 and 5) of hydrophobic elements are randomly selected among the hydrophobic elements and change into hydrophilic elements. If the fitness function has further diminished, this operation is performed again: a small number of hydrophobic elements are randomly selected among the hydrophobic elements and change into hydrophilic elements. This operation is repeated until there is no further diminution of the fitness function. Then the whole hill climbing algorithm procedure is repeated over and over again until convergence (considered as obtained when the value of the fitness function does not change by more than 0.1% over 20 successive iterations).

5. Results

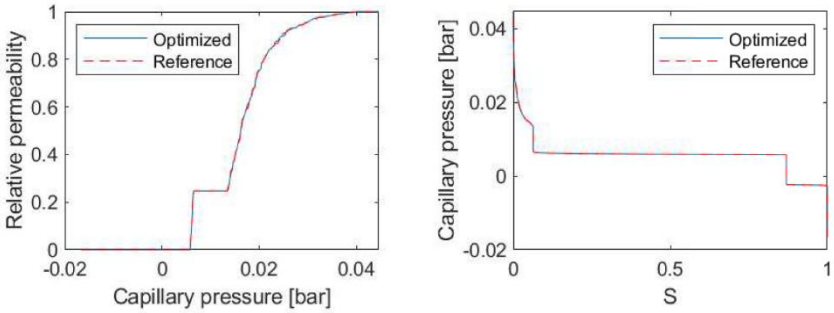
Tests were first performed for three values of the hydrophilic elements fraction in a 30 × 30 reference network, namely f = 30, 50 and 70%. The comparison between the relative permeability and capillary pressure curves for the reference network and the corresponding curves for the network resulting from the optimization procedure is shown in Fig.5.



a) f = 30 %



b) f = 50 %



c) f =70 %

Fig.5. Comparison between the relative permeability and capillary pressure curves for the reference network and the corresponding curves for the network resulting from the optimization procedure.

As can be seen, the optimization procedure leads to an excellent agreement between the curves for the reference network and the ones resulting from the optimization procedure.

The optimization procedure leads to the values of f reported in Table 1. Consistently with the excellent agreement on the relative permeability and capillary pressure curves depicted in Fig.5, the results reported in Table 1 show that the optimization procedure leads to a good estimate of the fraction of hydrophilic elements.

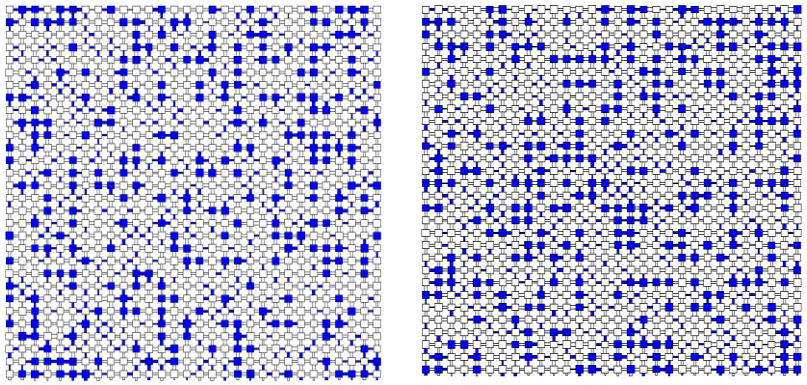
Table 1. Comparison between the fraction of hydrophilic elements in the reference network and the value identified by the optimization procedure.

f (%) (reference network)	f_o (%) (optimization procedure)	*Error (%)* $\lvert f_o - f \rvert$	*Relative error (%)* $\frac{\lvert f_o - f \rvert}{f}$
10	11.59	1.59	15.9
20	22.74	2.74	13.7
30	29.7	0.3	1
40	38.07	1.93	4.81
50	51.78	1.78	3.56
60	59	1	1.66
70	68.56	1.44	2.06
80	79.74	0.26	0.33
90	89.15	0.85	0.94

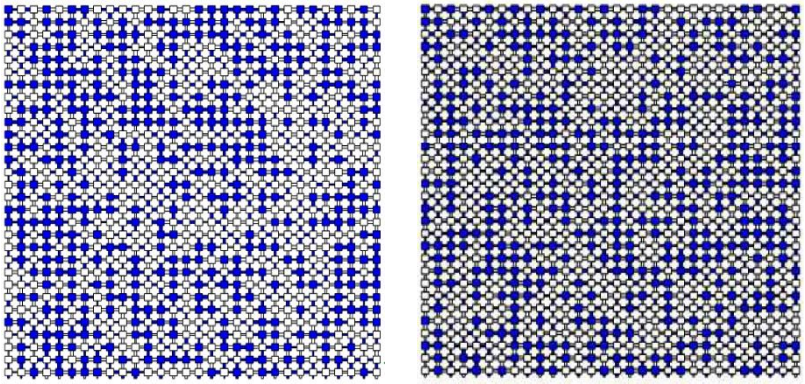
The good performance of the optimization procedure is further illustrated in Fig.6 where the distribution of hydrophilic and hydrophobic elements in the reference network and the network resulting from the optimization procedure, also referred to as the optimized network in what follows, are compared. Of course, it is not expected that the optimization procedure leads to a one-to-one matching between the localization of the hydrophilic elements in the reference network and the optimized network. The good matching must be understood in a statistical sense. In other words, the matching is good if the reference network and the optimized network can be considered as two realizations of the random process consisting here in distributing randomly the hydrophilic elements in the network. It is certainly possible to go deeper in this direction in comparing more

advanced statistical properties than simply the average, that is *f*. For instance, it could be tempting to make use of the Minkowski functionals [43]. However, this is left for a more refined work. It is our belief that predicting the fraction of hydrophilic element *f* is already a quite interesting step forward. Therefore, it should be clear that the solutions for the optimized network depicted in Fig.6 are not unique. Repeating the optimization procedure typically leads to the same value for *f* but generally to a different realization of the optimized network.

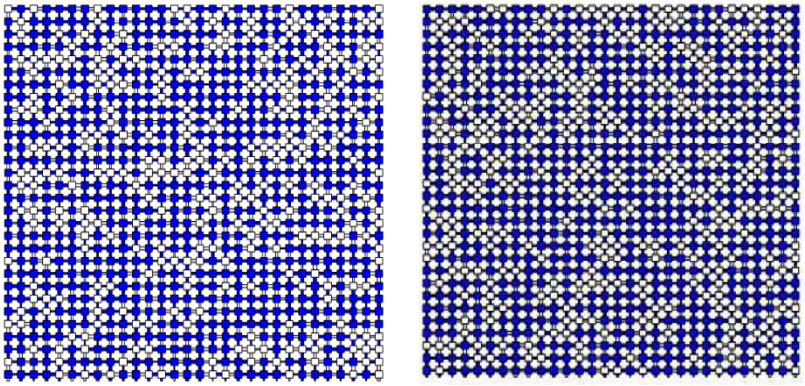
Reference network Optimized network



a) $f = 30\ \%$



b) $f = 50\ \%$



c) f = 70 %

Fig.6. Distribution of hydrophilic (in blue) and hydrophobic (in light grey) elements in the reference network (left column) and the optimized network (right column) for three values of the hydrophilic element fraction.

As reported in Table 1, the optimization procedure lead to good results not only for the values of f illustrated in Fig.6 but over the whole range of f.

6. Discussion

Two macroscopic classical data, namely the displacing fluid relative permeability and the capillary pressure curves were considered as input data for the optimization procedure. As considered in [30] in the case of the throat size distribution (TSD) determination problem, it is possible to perform the optimization procedure considering only one data, either the capillary pressure curve or the relative permeability curve. For the TSD problem, it was found that considering both data led to the best results and that the consideration of the capillary pressure curve alone led to better results than the relative permeability curve alone. For this reason, both data were considered in the present article. Nevertheless, it would be interesting to test the quality of the results when, for instance, the capillary pressure curve alone is considered. Conversely, it can be expected that considering more macroscopic data, such as for instance the displaced fluid relative permeability in addition to the displacing fluid relative permeability and the capillary pressure should improve the results.

The optimization procedure was tested considering a 2D network. Then the question arises as to whether similar results can be expected with 3D networks. Some indications on this point can be obtained from the PNM simulation results presented in [14] where computations of the capillary pressure and relative permeability are presented for a 3D cubic network for various fraction of hydrophilic pores. A crucial point is of course that the macroscopic data, the capillary pressure curve or the relative permeability curve in the present study, be sensitive to the wettability variations. In this respect, it can be seen from Figs. 3 and 4 that the curves sensitivity to f is more marked for f > 40 % than for f < 40%. A similar observation can be made as regards the 3D simulation results presented in [14] where a critical value f_c ($f_c \sim 0.48$) was introduced. Furthermore, the sensitivity to f was still less marked for $f < f_c$ than for the case considered in the present paper.

This is an indication that the local wettability characterization method could be less accurate for $f < f_c$ than for $f > f_c$. This is consistent with the results reported in Table 1 showing a somewhat greater relative error for $f < 0.4$. However, it can be seen from Table 1 that the results are still quite good in the domain of lesser sensitivity ($f < 0.4$) As discussed in some details in [14], f_c corresponds to the network percolation threshold [44]. In the context of percolation theory, the distribution of the hydrophilic elements considered in the present work is a mixed bond – site percolation problem since the wettability of both the throats (bonds) and the pore bodies (sites) is varied. The percolation threshold f_c corresponds to the smallest fraction of hydrophilic elements for which a percolating path of hydrophilic elements exists between the network inlet and outlet. According to percolation theory [44], the greater the coordination, i.e. the number of pore bodies to which a pore body is connected, the lower is the network percolation threshold. The coordination number in real porous media can be expected to be greater than the one of the square network considered in the present study (4) or the cubic network considered in [14] (6). In other words, the proposed characterization method can thus be expected to be accurate over the full range of f when applied to a real porous medium.

Another concern lies in the considered wettability distribution in term of spatial scale and in term of local contact angle distribution. In this study, a Boolean distribution was considered corresponding to only two values of the contact angle. Also, as illustrated in Fig. 2, see also [14, 16], the change in the contact angle has a significant impact of the capillary equilibrium pattern when one value of the contact angle corresponds to hydrophilicity and the other to hydrophobicity. The capillary pressure and relative permeability curves sensitivity to f is expected to be less when both contact angle values correspond to either hydrophilicity or hydrophobicity, for example θ = (20°, 60°) or (115°, 150°). In this respect, the method is likely to be more efficient when the change in the wettability is around the wettability transition marking a significant change in the displacement pattern [45] as considered in the present study. Nevertheless, it would be interesting to explore the capabilities of the method for more complex situations than the one considered in the present article. For example, in direct continuation with the present article, it would be interesting to consider the case where the local contact angle value is distributed over a given range, for instance between 80° and 115°. The latter case could correspond to a gradual change in the wettability rather than an abrupt change from 115° to 80°. Also, it has been reported that the spatial distribution of the PTFE coating can be quite heterogeneous but different from purely random with

PTFE present in the regions of the porous medium adjacent to its surface and practically to PTFE deeper in the medium [46]. In other words, strong spatial correlations can exist in the local contact angle distributions. The correlations are expected to have an impact on the relative and capillary pressure curves. Therefore, it would be interesting to test the optimization method for this type of case as well.

A somewhat crude simplification was to consider a spatially uniform contact angle at the scale of each network element. In many situations, the local contact angle can vary within a pore body or a throat. In this case, the characterization method considered in the present work could be used to determine the apparent contact angle associated with each network element. This apparent contact angle would reflect the contact angle spatial variations at the scale of the element. A much more ambitious approach would be to extent the approach considering direct simulations [33, 34] instead of PNM simulations for computing the two-phase displacements. However, this would dramatically increase the computational times. Furthermore, the computations of a quasi-static flows, i.e. two-phase flows at very low capillary number, with this type of method is still an active research area [46, 47].

It is difficult to validate the method with real porous media since the local contact angle distribution cannot be obtained from the commonly used experimental methods. An option could be to determine the contact angle distribution from the visualization of the fluid distribution and of the menisci inside the pore space [48] but regardless of the difficulty for characterizing the local contact angle from the menisci shapes [22] it is also perhaps difficult to obtain the contact angle distribution over a large region of the pore space with this method. A simpler validation test would be to use microfluidic devices of controlled patterned wettability [49].

7. Conclusion

A method considering the determination of the wettability distribution within the pore space of a porous medium as an inverse optimization problem was presented. The method combines two-phase flow pore network simulations with a genetic algorithm and the hill climbing algorithm. The method was tested on a model problem where the network elements are either hydrophilic or hydrophobic. The obtained results are promising. The hydrophilic element fraction in the network was reasonably well predicted and the determined contact angle maps judged as quite representative.

Acknowledgements

This research was supported by the Project "PEMFC – SUDOE" – SOE1/P1/E0293 which is co-financed by the European Regional Development Fund in the framework of the Interreg Sudoe programme.

References

1 S. Park, J.-W. Lee and B.N. Popov, A review of gas diffusion layer in PEM fuel cells: Materials and designs. International Journal of Hydrogen Energy, 37, 5850-5865 (2012).

2 F. Barbir, PEM fuel cells: theory and practice, Academic Press (2012)

3 Y. Wang, K.S. Chen, S.C. Cho, PEM Fuel Cells: Thermal and Water Management Fundamentals, Momentum Press (2013).

4 L. Giorgi, E. Antolini, A. Pozio, E. Passalacqua, Influence of the PTFE content in the diffusion layer of low-Pt loading electrodes for polymer electrolyte fuel cells, Electrochimica Acta, 43, 3675-3680 (1998).

5 G.G. Park, Y.J. Sohn, T.H. Yang, Y.G. Yoon, W.Y. Lee, C.S. Kim, Effect of PTFE contents in the gas diffusion media on the performance of PEMFC, Journal of Power Sources, 131, 182-187 (2004).

6 O. Chapuis, M. Prat, M. Quintard, E. Chane-Kane, O. Guillot, and N. Mayer, Two-phase flow and evaporation in model fibrous media: Application to the gas diffusion layer of PEM fuel cells, Journal of Power Sources, 178, 258-268 (2008).

7 D. Qiu, H. Janßen, L. Peng, P. Irmscher, X. Lai, W. Lehnert, Electrical resistance and microstructure of typical gas diffusion layers for proton exchange membrane fuel cell under compression, Applied Energy, 231, 127-137 (2018).

8 A. Bazylak, D. Sinton, Z.S. Liu, N. Djilali, Effect of compression on liquid water transport and microstructure of PEMFC gas diffusion layers, Journal of Power Sources, 163, 784-792 (2007).

9 V. Radhakrishnan, P. Haridoss, Effect of cyclic compression on structure and properties of a Gas Diffusion Layer used in PEM fuel cells, International Journal of Hydrogen Energy, 35, 11107-11118 (2010).

10 J. Wu, J.J. Martin, F.P. Orfino, H. Wang, C. Legzdins, X.Z. Yuan, C. Sun, In situ accelerated degradation of gas diffusion layer in proton exchange membrane fuel cell Part I: Effect of elevated temperature and flow rate, Journal of Power Sources, 195, 1888-1894 (2010).

11 S.G. Kandlikar, M.L. Garofalo, Z. Lu, Water Management in A PEMFC: Water Transport Mechanism and Material Degradation in Gas Diffusion Layers, Fuel Cells, 11, 814-823 (2011).

12 S. Yu, X. Li, J. Li, S. Liu, W. Lu., Z. Shao, B. Yi, Study on hydrophobicity degradation of gas diffusion layer in proton exchange membrane fuel cells, Energy Conversion and Management, 76, 301-306 (2013).

13 J. Park, H. Oh, T. Ha, Y. I. Lee, K. Min, A review of the gas diffusion layer in proton exchange membrane fuel cells: Durability and degradation, Applied Energy 155, 866-880 (2015).

14 S.P. Kuttanikkad, M. Prat, J. Pauchet, Pore-network simulations of two-phase flow in a thin porous layer of mixed wettability: Application to water transport in gas diffusion layers of proton exchange membrane fuel cells, Journal of Power Sources, 196, 1145-1155 (2011).

15 J. Pauchet, M. Prat, P. Schott, and S.P. Kuttanikkad, Performance loss of proton exchange membrane fuel cell due to hydrophobicity loss in gas diffusion layer: Analysis by multiscale approach combining pore network and performance modelling, International Journal of Hydrogen Energy 37, 1628-1641 (2012).

16 L. Ceballos, M. Prat, Slow invasion of a fluid from multiple inlet sources in a thin porous layer: influence of trapping and wettability, Physical Review E, 87(4), 43005 (2013).

17 D.N. Staicopolus, The computation of surface tension and of contact angle by the sessile-drop method, Journal of Colloid Science, 17, 439-447 (1962).

18 E.W. Washburn, The Dynamics of Capillary Flow, Physical Review, 18, 273-283 (1921).

19 V. Gurau, M.J. Bluemle, E.S. De Castro, Y.M. Tsou, J.A. Mann Jr, T.A. Zawodzinski Jr. Characterization of transport properties in gas diffusion layers for proton exchange membrane fuel cells: 1. Wettability (internal contact angle to water and surface energy of GDL fibers), Journal of Power Sources, 160, 1156-1162 (2006).

20 V Parry, E Appert, JC Joud, Characterisation of wettability in gas diffusion layer in proton exchange membrane fuel cells, Applied surface science, 256, 2474-2478 (2010).

21 D.K. Owens, R.C. Wendt, Estimation of the surface free energy of polymers, Journal of Applied Polymer Science, 13, 1741-1747 (1969).

22 M.J. Blunt, T. Akai, B. Bijeljic, Evaluation of methods using topology and integral geometry to assess wettability, Journal of Colloid and Interface Science, 576, 99-108 (2020).

22 V. Cnudde, M.N. Boone, High-resolution X-ray computed tomography in geosciences: A review of the current technology and applications. Earth-Science Reviews, 123, 1-17 (2013).

23 J. Joos, T. Carraro, A. Weber, E. Ivers-Tiffée, Reconstruction of porous electrodes by FIB/SEM for detailed microstructure modeling, Journal of Power Sources, 196, 7302-7307 (2011).

24 T. Agaesse, A. Lamibrac, F. Buechi, J. Pauchet, M. Prat, Validation of pore network simulations of ex-situ water distributions in a gas diffusion layer of proton exchange membrane fuel cells with X-ray tomographic images, Journal of Power Sources, 331, 462-474 (2016).

25 D.J. Fairweather, P. Cheung, D.T. Schwartz, The effects of wetproofing on the capillary properties of proton exchange membrane fuel cell gas diffusion layers, Journal of Power Sources, 195, 787–793 (2010).

26 S., Steven, The Algorithm Design Manual (2nd ed.). Springer Science+Business Media; (2010).

27 E. Unsal, J.H. Dane, and G.V. Dozier, A genetic algorithm for predicting pore geometry based on air permeability measurements, Vadose Zone Journal, 4, 389-397 (2005).

28 S.C. Su, C.J. Lin and C.K. Ting, An effective hybrid of hill climbing and genetic algorithm for 2D triangular protein structure prediction, Proteome Science, 9, (Suppl 1): S19 (2011).

29 O. Maalal, M. Prat, R. Peinador, D. Lasseux, Determination of the throat size distribution of a porous medium as an inverse optimization problem combining pore network modeling and genetic and hill climbing algorithms, submitted to Phys. Rev. E.

30 O. Maalal, M. Prat, R. Peinador, D. Lasseux, Pore network simulations of fluid-fluid displacement porosimetry for evaluation of pore size distribution, to be submitted.

31 M.J. Blunt, M.D. Jackson, M. Piri, P.H. Valvatne, Detailed physics, predictive capabilities and macroscopic consequences for pore-network models of multiphase flow, Advances in Water Resources, 25, 1069-1089 (2002).

32 M.J. Blunt, Flow in porous media-pore-network models and multiphase flow, Current Opinion in Colloid & Interface Science, 6, 197-207 (2001).

33 Z. Niu, Y. Wang, K. Jiao, ZJ. Wu, Two-Phase Flow Dynamics in the Gas Diffusion Layer of Proton Exchange Membrane Fuel Cells: Volume of Fluid Modeling and Comparison with Experiment, Journal of The Electrochemical Society, 165, F613-F620 (2018).

34 W. Chen, F. Jiang, Impact of PTFE content and distribution on liquid–gas flow in PEMFC carbon paper gas distribution layer: 3D lattice Boltzmann simulations, International Journal of Hydrogen Energy, 41, 8550-8562 (2016).

35 J.T. Gostick, Versatile and efficient pore network extraction method using marker-based watershed segmentation, Physical Review E 96 (2), 023307 (2017).

36 A.Q. Raeini, B. Bijeljic, M.J. Blunt, Generalized network modeling: network extraction as a coarse-scale discretization of the void space of porous media. Physical Review E 96, 013312 (2017).

37 R. Lenormand, C. Zarcone, Role of roughness and edges during imbibition in square capillaries, in: SPE Annual Technical Conference and Exhibition (1984).

38 V. Mani, K. Mohanty, Effect of pore-space spatial correlations on two-phase flow in porous media, Journal of Petroleum Science and Engineering, 23, 173-188 (1999).

39 M.Rebai, M.Prat, Scale effect and two-phase flow in a thin hydrophobic porous layer. Application to water transport in gas diffusion layers of PEM fuel cells, Journal of Power Sources, 192, 534-543 (2009).

40 F. Babalievski, Cluster counting: the Hoshen-Kopelman algorithm versus spanning tree approaches, International Journal of Modern Physics, 9, 43-60 (1998).

41 V. Joekar-Niasar, S.M. Hassanizadeh and A. Leijnse, Insights into the relationships among capillary pressure, saturation, interfacial area and relative permeability using pore-network modelling, Transport in Porous Media, 74, 201-219 (2008).

42 K. Mecke, Integral geometry and statistical physics. International Journal of Modern Physics, B12, 861-899 (1998).

43 D. Stauffer, A. Aharony, Introduction to percolation theory, Taylor & Francis, London, (1992).

44 M. Cieplak and M.O. Robbins, Dynamical Transition in Quasistatic Fluid Invasion in Porous Media, Physical Review Letters, 60, 2042-2045 (1988).

45 H. Ito, K. Abe, M. Ishida, A. Nakano, T. Maeda, T. Munakata, H. Nakajima, T. Kitahara, Effect of through-plane distribution of polytetrafluoroethylene in carbon paper on in-plane gas permeability, Journal of Power Sources, 248, 822-830 (2014).

46 M. Shams, A.Q. Raeini, M.J. Blunt, B. Bijeljic, A numerical model of two-phase flow at the micro-scale using the volume-of-fluid method, Journal of Computational Physics, 357, 159-182 (2018).

47 H. Si Hadj Mohand, H. Hoang, G. Galliero, D. Legendre, On the use of a friction model in a Volume of Fluid solver for the simulation of dynamic contact lines. Journal of Computational Physics, 393, 29-45 (2019).

48 M.G. Andrew, B. Bijeljic, M.J. Blunt, Pore-scale contact angle measurements at reservoir conditions using x-ray microtomography, Advances in Water Resources, 68, 24-31 (2014).

49 K. Ma, J. Rivera, G.J. Hirasaki, S.L. Biswal, Wettability control and patterning of PDMS using UV–ozone and water immersion, Journal of Colloid and Interface Science, 363, 371-378 (2011).

Conclusion

Dans cette thèse, nous avons évalué deux techniques de porosimétrie : la porosimétrie fluide-fluide et l'évaporosimétrie à partir d'une représentation de l'espace poral en terme de réseaux de pores et de techniques de simulations numériques des processus à l'œuvre dans ces deux techniques à l'échelle du réseau de pores.

La nécessité d'évaluer la porosimétrie fluide–fluide est née du constat que le modèle de tubes parallèles utilisé communément pour extraire la distribution des tailles de pores (PSD) est a priori très peu représentatif du réseau de pores fortement interconnectés rencontré dans de nombreuses membranes. Les simulations présentées dans ce travail ont mis en évidence que ce modèle de tubes parallèles pouvait alors conduire à des résultats erronés. Ceci a motivé la recherche d'une technique alternative d'extraction de la PSD basée sur une méthode d'optimisation combinant des algorithmes génétique et de hill climbing. Cette approche s'est avérée très efficace. Elle est cependant beaucoup plus lourde que l'approche quasi-analytique basée sur le modèle à tubes parallèles. Une clarification importante apportée par l'approche réseau de pores est la distinction de deux types d'objets structurants au sein du réseau de pores : les étroitures (les « pore throats ») et les élargissements (les « pore bodies »). Nos résultats indiquent que la porosimétrie liquide-liquide permet essentiellement de caractériser les tailles des étroitures.

Deux versions de la porosimétrie fluide–fluide ont en fait été étudiées. La version dite quasi-statique (Chap.1) n'est pas celle correspondant typiquement à l'utilisation du porométre fluide-fluide. Elle correspond à des montages expérimentaux classiquement utilisés pour déterminer deux propriétés importantes : la courbe de rétention (ou courbe de pression capillaire) et la perméabilité relative du fluide déplaçant. Cette première étude a permis de montrer que les pores dont la taille est supérieure à la taille critique correspondant au seuil de percolation du réseau ne pouvaient pas être identifiées en utilisant l'approche conventionnelle. Elle a permis aussi de mettre au point et de tester la méthode d'optimisation.

La porosimétrie fluide-fluide a été plus spécifiquement étudiée au Chap.2 avec la prise en compte explicite de l'impact de la perte de pression visqueuse sur le déplacement non-miscible. Les simulations indiquent alors que l'approche conventionnelle basée sur le modèle de tubes parallèles conduit à des PSD erronées avec un décalage pouvant être important vers des pores de petites tailles irréealistes. Ici encore la méthode d'extraction par optimisation conduit à de bons résultats, qui sont encore meilleurs quand les données de la porosimétrie liquide-liquide sont combinées à la mesure de la pression capillaire.

L'étude de l'évapoporosimétrie a nécessité des développements nouveaux en ce qui concerne la modélisation de l'évaporation avec une approche réseau de de pores. Le point clé a été de prendre en compte l'effet Kelvin (Chap.3). Ainsi, la simulation de l'évaporation dans un réseau de pores avec effet Kelvin a été réalisée dans la limite quasi-statique. Cet effet est important pour les tailles de pores inférieures à 100nm. La diffusion de Knudsen a aussi été prise en compte pour représenter les effets de raréfaction. Les résultats montrent que l'effet Kelvin a un impact sur les chemins d'invasion ainsi que sur le taux d'évaporation. En effet, le changement de courbure d'un lien vers un « pore body » ou vice versa a un impact direct sur l'évaporation via l'équation de Kelvin, ce qui implique que le taux d'évaporation fluctue en fonction du temps suivant son passage d'un « pore body » vers un lien ou l'inverse. Les résultats montrent aussi l'existence d'un effet de non-équilibre local, contrairement à l'hypothèse considérée dans la plupart des modèles macroscopiques classiques.

L'algorithme de simulation de l'évaporation dans un réseau de pores avec effet Kelvin a permis d'évaluer l'évapoporosimétrie (Chap.4). En partant d'un réseau dont on connait parfaitement la TSD et la PSD, la simulation de l'évaporation permet de trouver le taux d'évaporation en fonction de temps. Ensuite, par la même analyse faite en déplacement liquide-liquide, la PSD obtenue a été comparée à la PSD (et la TSD) de référence. Les résultats montrent que l'évapoporosimétrie permet de déterminer à la fois la PSD et la TSD. Cependant, cela requiert une fréquence de mesure élevée pour pouvoir déterminer la majorité des tailles de pores et de liens. Contrairement à certaines procédures expérimentales, les simulations suggèrent qu'il ne faut pas moyenner le taux d'évaporation sur un nombre de points de mesure successifs. Il faut noter aussi que le taux d'évaporation normalisé fluctue sur des valeurs proches de 1 (d'après l'équation de Kelvin) et donc il est fortement recommandé d'utiliser une micro balance très précise afin de pouvoir différencier les fluctuations du taux d'évaporation des fluctuations dues au bruit de mesure. Le niveau de précision souhaitable semble difficile à atteindre en pratique. L'analyse effectuée explique en partie les incohérences obtenues par cette technique qui apparaissent dans certaines publications.

Dans un dernier chapitre (Chap.5), nous avons présenté une approche permettant de caractériser la distribution locale de l'angle de contact au sein d'une structure poreuse. Cette approche a été mise en œuvre dans le cas des milieux poreux de mouillabilité mixte, c'est-à-dire où les pores et liens peuvent être hydrophiles ou hydrophobes. Cette approche exploite la sensibilité de la courbe de rétention et de la courbe de perméabilité relative à la distribution de la mouillabilité locale, plus exactement à la fraction de liens et de pores hydrophiles. Elle s'appuie sur une technique d'optimisation qui, comme celle développée pour l'étude de la porosimétrie fluide-fluide, combine l'algorithme génétique et l'algorithme du hill climbing. Les résultats montrent que la fraction de mouillabilité peut être correctement estimée. La cartographie de mouillabilité n'est pas déterminée de façon univoque car le problème est mal posé et la solution n'est pas unique mais est jugée statistiquement représentative de la cartographie de référence.

Enfin il est à noter que même si cette thèse est de nature exclusivement numérique, elle permet de conforter la modification du poromètre IFTS qui a consisté à adjoindre un module de mesure de la courbe de pression capillaire.

Perspectives

Cette thèse est basée sur des simulations du drainage et de l'évaporation selon l'approche réseau de pores. Un premier volet de perspectives concerne l'amélioration des algorithmes. Pour le drainage, les phénomènes de piégeage ont été négligés. Il serait intéressant de les prendre en compte. Les pores ont été supposés cylindriques ce qui élimine la prise en compte des films de fluide mouillant qu'on observe dans les pores anguleux. Cette simplification mériterait d'être reconsidérée. De même, les effets visqueux ont été totalement négligés dans le liquide déplacé. Cela peut être critiqué. On peut arguer que l'essentiel est de prendre en compte les mêmes règles du jeu dans les simulations de référence et dans les simulations intervenant dans la procédure d'optimisation. Bien que cet argument nous paraisse défendable, il n'en reste pas moins qu'améliorer la représentativité de la simulation du drainage constitue une perspective. Des comparaisons avec des expériences sur cellules microfluidiques permettant une observation directe du déplacement seraient également très utiles pour améliorer l'algorithme du drainage. Pour l'évaporation, les principales voies d'amélioration concernent la prise en compte des effets visqueux dans le liquide et celle des films liquides (de coins et adsorbés). D'un point de vue technique, il est à noter aussi que nos codes ont été développés dans l'environnement Matlab. L'implémentation dans un langage compilé (C ou Fortran) permettrait d'effectuer des simulations sur des réseaux plus grands.

Un problème évident concernant la méthode d'extraction de la PSD via la technique d'optimisation est que la taille et la structure du réseau sont exactement les mêmes pour le réseau de référence et le réseau intervenant dans la méthode d'optimisation. En pratique, le réseau d'une membrane réelle est inconnu. Il n'est pas évident que l'assimiler à un réseau cubique structuré par exemple conduise à de bons résultats. En tout cas, il est tout à fait souhaitable d'examiner la sensibilité des résultats vis-à-vis de la structure présupposée. Numériquement, une première approche peut par exemple consister à considérer un réseau de référence non-structuré (il existe des logiciels libres permettant de générer des réseaux non structurés de type « Voronoi » par exemple) et à mettre en œuvre la méthode d'optimisation avec un réseau cubique. La comparaison des PSD permettrait alors d'avoir une évaluation de l'impact de la structure du réseau. Une autre idée consiste à établir un catalogue de structures de réseaux possibles (sur la base des différentes propositions de la littérature). L'idée serait alors de choisir la structure de réseau qui parait la plus proche de celle de la membrane à caractériser. Même si des informations relativement faciles à obtenir comme des images MEB de la membrane peuvent être utiles pour guider le choix, le choix d'un réseau approprié à partir d'une banque de réseaux reste une tâche ardue.

Une approche certainement encore plus intéressante en terme de validation et d'analyse critique de la porosimétrie fluide-fluide consisterait à choisir une membrane de microfiltration avec des pores suffisamment gros pour pouvoir être imagés par tomographie X. On pourrait alors extraire le réseau de pores à partir des images 3D de la microstructure, déterminer la PSD à partir des images, la déterminer à partir de la porosimétrie fluide-fluide conventionnelle, et enfin à partir de la méthode d'optimisation. Cette procédure permettrait de confirmer (ou d'infirmer) que la porosimétrie liquide-liquide

conventionnelle, basée sur une interprétation à l'aide d'un réseau de tubes parallèles, conduit à des résultats erronés et de tester de manière probatoire, la méthode d'optimisation développée ici.

Concernant la caractérisation de la mouillabilité, ici encore des expériences avec des cellules microfluidiques seraient intéressantes pour valider la méthode de caractérisation développée dans cette thèse. Il est en effet possible de réaliser de telles cellules en distribuant la mouillabilité. Il est à noter que nous avons uniquement examiné une situation où un élément du réseau (pore body ou pore throat) est soit hydrophile, soit hydrophobe. En réalité, la situation peut être bien plus complexe en raison par exemple de variation locale de l'angle de contact à plus petite échelle (c'est-à-dire à l'intérieur d'un même pore) ou pouvant prendre plus de valeurs qu'une distribution binaire comme nous l'avons considéré. Une perspective consiste donc à tester la méthode pour des cas plus complexes.